Fotonische huid gebaseerd op integratie van optische sensoren en uitleeseenheden in polymere substraten

Photonic Skin Based on Polymer Embedding of Optical Sensors and Interrogation Units

Bram Van Hoe

Promotoren: prof. dr. ir. G. Van Steenberge, prof. dr. ir. P. Van Daele
Proefschrift ingediend tot het behalen van de graad van
Doctor in de Ingenieurswetenschappen: Elektrotechniek

Vakgroep Elektronica en Informatiesystemen
Voorzitter: prof. dr. ir. J. Van Campenhout
Faculteit Ingenieurswetenschappen en Architectuur
Academiejaar 2013 - 2014

UNIVERSITEIT GENT

ISBN 978-90-8578-636-8
NUR 959
Wettelijk depot: D/2013/10.500/69

Universiteit Gent
Faculteit Ingenieurswetenschappen en Architectuur
Vakgroep Elektronica en Informatiesystemen

Promotoren: prof. dr. ir. G. Van Steenberge
prof. dr. ir. P. Van Daele

Centre for Microsystems Technology (CMST)
Vakgroep Elektronica en Informatiesystemen
Technologiepark 914A
B-9052 Zwijnaarde

Tel.: +32-9-264.53.70
Fax.: +32-9-264.53.74

Examencomissie: prof. dr. ir. L. Taerwe – Voorzitter
dr. ir. E. Bosman – Secretaris
prof. dr. ir. F. Berghmans
prof. dr. P. Dubruel
prof. dr. D.J. Webb
prof. dr. ir. D. Van Thourhout
dr. J. Vlekken

Onderzoek gefinancierd met een specialisatiebeurs van het Instituut voor de Aanmoediging van Innovatie door Wetenschap en Technologie in Vlaanderen (IWT-Vlaanderen).

Proefschrift ingediend tot het behalen van de graad van
Doctor in de Ingenieurswetenschappen: Elektrotechniek
Academiejaar 2013-2014

Dankwoord

Het boek dat u nu vasthebt is er enkel kunnen komen door een heleboel mensen die allemaal een bijdrage hebben geleverd hiervoor op heel wat verschillende gebieden.
Ik begin bij CMST, het Centrum voor Microsysteem Technologie, waar ik na mijn masterproef als doctoraatsstudent ben begonnen. Vooreerst wil ik mijn promotoren, Geert Van Steenberge en Peter Van Daele, bedanken. Ze gaven me de kans om aan dit doctoraat te beginnen en zorgden voor veel inspiratie tijdens mijn onderzoek. Daarnaast boden ze mij de mogelijkheid om intensief betrokken te zijn bij nationale en internationale projecten, en om onderzoeksresultaten te publiceren en te presenteren op internationale conferenties.
Verder wil ik ook André Van Calster en het CMST management bedanken. Zij hebben CMST gemaakt tot wat het nu is: een onderzoeksgroep, deel uitmakend van zowel Universiteit Gent als het onderzoekscentrum Imec, en bestaande uit bijna zestig mensen met een state-of-the-art cleanroom infrastructuur en een indrukwekkende portfolio van onderzoeksprojecten.
De leden van de jury hebben veel interessante opmerkingen en commentaren aangebracht. Ik wil hen bedanken voor de tijd die ze in mijn proefschrift hebben geïnvesteerd. Erwin, Jeroen, Geert en Ann wil ik graag bedanken voor het reviewen van één of meerdere hoofstukken.
Het optische (of correcter "Polymer Photonics and Laser Technology") team van CMST hoort zeker ook in dit rijtje thuis. Geert, Erwin, Jeroen, Sandeep, Sanjeev, Kamal, Pankaj, Nuria en Ahmed wil ik bedanken voor de vele interessante discussies, nieuwe ideeën en verhelderende uitleg, in combinatie met de nodige ambiance.
Een groot deel van dit doctoraat is gebaseerd op technologische processen die worden verricht in een cleanroom omgeving met hoogtechnologische toestellen. Ik wil dan ook de mensen bedanken die voor mij of met mij verschillende processtappen hebben uitgevoerd. Steven voor het laserwerk (inclusief opstart van ons nieuw 3DMM systeem) én de liefde voor blauw-wit, Peter G. voor het uitvoeren van chip verdunning, waveguide processing, litho- en etsstappen, en vele andere probeersels. Dieter en Filip V. voor het sputteren en RIE'en, Björn voor de dispenser- en Tresky-testjes, Filip T. voor de molds en andere technische hulpmiddelen, David voor het SEM werk, en het hele CR support en EIP team voor de ondersteuning en het safety management. Dr. Tresky en Dr. Bosman wil ik

bedanken voor de hulp en het technisch vernuft bij het plaatsen van dunne chips. Ook de collega's van de smart power group ("de designers") wil ik graag bedanken voor alle hulp bij elektronicahindernissen. Jindrich in het bijzonder, voor de technische bijstand bij zeer uiteenlopende problemen, gaande van gecrashte laptops tot verbrande Ford Mondeo-ruitensproeiverwarmelementjes...
Collega's en ex-collega's van "onzen bureau", bedankt voor alle mooie herinneringen! Verder ook Katrien om altijd klaar te staan om administratieve vragen te beantwoorden en Peter S. voor de IT ondersteuning. Ik wil bij uitbreiding ook alle andere collega's van CMST bedanken voor alle hulp en de uitstekende (werk)sfeer!
Niet alleen met de collega's binnen CMST, maar ook met andere onderzoeksgroepen had ik een zeer goed contact binnen de IWT-SBO projecten FAOS en SSC, en de EU-FP7 projecten Phosfos en Actmost. Die combinatie van uiteenlopende expertise heeft niet alleen geleid tot gemeenschappelijke publicaties en nieuwe inzichten, maar ook tot een netwerk van mensen die ik graag tegenkom op projectmeetings, conferenties of workshops.
In het bijzonder wil ik de collega's van de (Ugent) Polymer Chemistry & Biomaterials Group ("den S4") vermelden voor de materiaalontwikkelingen en -karakterisatie. De PMA groep in Leuven (KUL) wil ik graag bedanken voor het werk rond de mechanische karakterisatie van de VCSEL druksensor. Ook de (Ugent) Mechanica van Materialen en Structuren onderzoeksgroep mag hier niet ontbreken, in het bijzonder Geert Luyckx, voor het gebruik van testopstellingen (o.a. elektrodynamische shaker) en demonstratoren. Verder was het Brussels Photonics Team (VUB) een onmisbare schakel in dit doctoraatsonderzoek. Vooreerst vermeld ik de Fiber Group, in het bijzonder Sanne Sulejmani, Camille Sonnenfeld, Thomas Geernaert en Francis Berghmans, voor het werk rond microgestructureerde vezelsensoren. Verder Jürgen Van Erps voor de simulaties en expertise rond optische koppelstructuren. Ook Heidi Ottevaere en de andere B-Phot collega's voor gebruik van en uitleg bij allerlei meetapparatuur. Jan Van Roosbroeck en Jo Vlekken van FBGS International wil ik graag bedanken voor de samenwerking rond ingebedde DTGs. I would also like to acknowledge the people from the Aston Institute of Photonic Technologies in Birmingham for the excellent collaboration within Phosfos. Thank you, David Webb, Kate Sugden and Graham Lee, for all your efforts on polymer optical fiber sensors and FBG interrogation systems. A special thanks to Graham, I admire your drive to achieve results and very much enjoyed working together.
Greetje Godier, Tom De Geyter en Johan Paul van Flamac voor het gebruik van de nano-intender en de ondersteuning bij experimenten. Deben Lamon en Giuseppe Melpignano voor het thesis- en stagewerk rond de VCSEL druksensor.

Bedankt studiegenoten, in het bijzonder Yannick, Deben en Kristof. Misschien herkennen jullie hier en daar wel enkele ideeën van ons hardware-ontwerpproject uit 2007.

Veel collega's zijn ondertussen goede vrienden geworden...
Ik wil Pritesh, Frederick & Adinda, Thomas & Eveline, Ann & Alwin en Fabrice bedanken voor de onvergetelijke trip naar India. Jindrich, Ann & Alwin voor de fijne roadtrip in de US. Tom voor het bijhouden van mijn oneliners ("het leven zit vol anticipaties!!"), Rik voor de *Extra Time* babbels in de gang. Erwin voor de lancering van onze DJ carrière, alsook de organisatie van vele culturele activiteiten (Hans Teeuwen-avond, boefparty, wok dynasty uitstapjes, ...).
Ook het CMST voetbalteam mag hier niet ontbreken. Het was een hele eer samen met jullie de kleuren van CMST te verdedigen. De voorzittersverkiezing met bijhorend ribbekesfestijn is elk jaar iets om naar uit te kijken. Ik heb met veel genoegen het voorzittersambt gedurende een seizoen mogen opnemen. Verder hebben ook de CMST barbecues een aantal onuitwisbare indrukken nagelaten, bedankt aan iedereen die dit evenement elk jaar tot zo'n succes maakt.
Sport en ontspanning zijn cruciaal tijdens het leven, en zeker tijdens een doctoraat. Daarom wil ook buiten CMST een aantal mensen bedanken.
Om te beginnen de kerncompetitieploeg Brildesign Deinze: ik ben er zeker van dat ons nog vele mooie seizoenen te wachten staan. Squashpartner Wim mag hier niet ontbreken, na een sabbatjaar vliegen we er volgend jaar opnieuw in! Ook de Gent Symphonic Band hoort in dit rijtje thuis. Samen musiceren en concerteren blijft iets speciaal, zelfs na bijna 20 jaar! Verder wil ik de wijnclub-bende aka de wijnzero's: Wim, Dhondt, Baeck, Ben en Cédric bedanken. Onze maandelijkse bijeenkomsten zijn altijd iets om naar uit te kijken, of er nu wijn aan te pas komt of niet...
Het is onmogelijk in dit korte dankwoord iedereen te vermelden. Een dikke merci aan alle andere vrienden voor de vele mooie momenten!

Ik wil ook graag mijn familie bedanken, in het bijzonder mijn zussen en petekind, Anke, Liesbet en Floris. Als ik jullie een cijfer moet geven, dan geef ik jullie een 11!

Mijn ouders. Er zijn niet veel momenten waarop ik jullie expliciet bedank, maar ik wil dit nu graag doen voor de perfecte zorgen gedurende al die jaren en voor de kansen die jullie me hebben gegeven.

En natuurlijk Elien. Storm, niemand anders weet zo goed wat ik voel of denk. Bedankt voor alle support die je me geeft! Van Ryhove wacht op ons!

Gent, oktober 2013
Bram Van Hoe

Table of Contents

List of Tables

List of Figures

List of Acronyms

α	linewidth enhancement factor
ADC	Analogue to Digital Converter
ASE	Amplified Spontaneous Emission
A.U.	Arbitrary Unit
CCD	Charge Coupled Device
CMST	Centre for Microsystems Technology
CTE	Coefficient of Thermal Expansion
CVD	Chemical Vapor Deposition
DBR	Distributed Bragg Reflector
DAQ	Data Acquisition
DTG	Draw Tower grating
FAOS	Flexible Artificial Optical Skin (IWT funded project)
FBG	Fiber Bragg Grating
FFP	Fiber Fabry-Pérot
FFT	Fast Fourier Transform
FP	Fabry-Pérot
FR4	Fiber Reinforced board material
FWHM	Full Width at Half Maximum
GaAs	Gallium(III)Arsenide
GPIB	General Purpose Interface Bus
IC	Integrated Circuit
ICA	Isotropic Conductive Adhesive
ICP	Inductive Coupled Plasma
Imec	Interuniversitair Micro-elektronica Centrum
IoT	Internet of Things
LD	Laser Diode
LED	Light Emitting Diode
L_{ext}	external cavity Length
MEMS	Microelectromechanical Systems
MFD	Mode Field Diameter
MM	Multimode

MMF	Multimode Fiber
MSF	Microstructured Silica Fiber
NA	Numerical Aperture
Nd:YAG	Neodymium-doped Yttrium Aluminum Garnet, Nd:$Y_3Al_5O_{12}$
NOA	Norland Optical Adhesive
OE	Optoelectronic
OSA	Optical Spectrum Analyzer
oTC	optical Thin Chip package
OTDR	Optical Time-Domain Reflectometry
PCB	Printed Circuit Board
PD	Photodiode
PDMS	Polydimethylsiloxane
PET	Polyethylene Terephthalate
Phosfos	PHotonic Skins For Optical Sensing (EU funded project)
PI	Polyimide
PMMA	Polymethyl Methacrylate
POF	Polymer Optical Fiber
POFBG	Polymer Optical Fiber Bragg Grating
R_{ext}	external (target) Reflectance
RH	Relative Humidity
RIE	Reactive Ion Etching
R_{int}	internal (mirror) Reflectance
rms	Root mean square
rpm	revolutions per minute
RT	Room Temperature
sccm	standard cubic centimeters per minute
SEM	Scanning Electron Microscope
Si	Silicon
SLED	Superluminescent Light Emitting Diode
SM	Single-Mode
SMF	Single-Mode Fiber
SMU	Source Measure Unit
SSC	Self Sensing Composites (IWT funded project)
SU-8	Negative Photoresist from MicroChem
UV	Ultra Violet
VCSEL	Vertical-Cavity Surface-Emitting Laser
WYKO	Non-contact optical profilometer from Veeco

Samenvatting

Het beginpunt van dit proefschrift zijn drie belangrijke trends binnen de hedendaagse onderzoekswereld. De eerste trend is gelinkt aan de snelle opmars van draagbare, kleine of soms zelfs onzichtbare toepassingen waarvoor steeds verder geminiaturiseerde technologische bouwblokken nodig zijn. Voorbeelden van dergelijke toepassingen vinden we onder meer in smartphones, tablets en smart TV's die de gebruiker in een oogwenk toegang verschaft tot sociale media, persoonlijke muziek en dataopslag. Ook toepassingen om allerlei functies van het menselijk lichaam te monitoren maken gebruik van deze miniaturisatietrend. Denken we maar aan applicaties om ademhaling, hartslag of spierbelasting op te meten. Naast de gebruiker kan hierbij ook de behandelende arts informatie krijgen over de toestand van de patiënt. Deze miniaturisatietrend beperkt zich niet tot de consumentenapplicaties maar reikt veel verder. Andere applicaties zijn bijvoorbeeld implanteerbare systemen, ruimtevaarttoepassingen of het monitoren van de integriteit van bruggen en gebouwen. Gebruikers van al deze toepassingen zijn steeds op zoek naar lichtere en kleinere meetsystemen.

Een tweede belangrijke pijler voor deze doctoraatsthesis is het toenemend gebruik van sensoren in allerlei soorten toepassingen. Micro's en camera's zijn enkele van de meest gekende sensorapplicaties. Recentere voorbeelden vinden we bijvoorbeeld in de automobielindustrie, zoals parkeer- of neerslagsensoren. Verder zijn ook touchscreens, RF-IDs en anti-diefstalsystemen populaire sensorapplicaties. Zulke "artificiële zintuigen" bootsen één van de vijf menselijke zintuigen na en maken tegenwoordig deel uit van ons dagelijks leven, vaak zonder dat we er ons van bewust zijn.

Een derde trend is de invoering van fotonische systemen. Deze systemen zijn gebaseerd op de propagatie van licht, door lichtdeeltjes (fotonen) te gebruiken als informatiedrager of als sensormedium. Fotonische of optische sensoren bezitten verschillende unieke eigenschappen die hen een concurrentieel voordeel opleveren ten opzichte van de traditionele, elektronische sensoren. Het meten van de sensorrespons gebeurt namelijk door een wijziging van de eigenschappen van licht dat propageert in een optisch medium, bijvoorbeeld een optische vezel. Enkele voorbeelden van deze voordelen zijn hun gevoeligheid, immuniteit voor elektromagnetische interferentie en het inerte karakter van de sensoren. Daarnaast laten hun laag gewicht, beperkte grootte (dimensies van een optische vezel zijn vergelijkbaar met een menselijk haar) en robuustheid ook toe ze in te zetten binnen omgevingen waar geen, of slechts onder zeer strikte voorwaarden, elektrische toepassingen mogen worden gebruikt (bijvoorbeeld bij hoge temperatuur of druk). Optische vezelsensoren in het bijzonder laten op een zeer eenvoudige wijze multiplexing toe en bieden de mogelijkheid tot een lagere productiekost. Het gebruik van fotonische systemen beperkt zich niet tot sensortoepassingen. Ze zijn alomtegenwoordig in dagdagelijkse toepassingen maar worden ook nog zeer intensief onderzocht in de wetenschappelijke wereld. Een aantal voorbeelden hiervan zijn verlichting, metrologie, spectroscopie, holografie, chirurgie en laser ablatie van materialen.

We vestigen nu de aandacht op geminiaturiseerde optische sensoren die met behulp van de hierboven beschreven recente technologische ontwikkelingen werden ontworpen. Deze optische sensorsystemen, en in het bijzonder de optische vezelsensoren, bieden zoals eerder vermeld een brede waaier aan voordelen die hen multifunctioneler maken tegenover hun elektronische tegenhangers. Hoewel er dus een enorm potentieel is, blijft het marktaandeel van optische sensoren echter nog steeds beperkt. Binnen dit doctoraatsonderzoek is het dan ook de bedoeling een aantal van de traditionele showstoppers weg te nemen en de toepasbaarheid van optische sensoren te vergroten. Op verschillende gebieden, onder andere optische koppeling, efficiënte overdracht van rek of andere sensorparameters, verpakking, integratie en betrouwbaarheid, kunnen nog belangrijke stappen gezet worden. De drie eerder beschreven trends worden binnen dit doctoraat gecombineerd in een doorgedreven integratie van zowel de optische sensoren als de bijhorende opto-elektronische componenten. Het integratieproces maakt gebruik van polymere materialen en beperkt zo de dimensies van het sensorsysteem tot een minimum.

Naast de bovenvermelde uitdagingen op het gebied van optische (vezel)sensoren, is er ook nood aan performante uitleeseenheden die op dit moment vaak te groot en moeilijk te bedienen zijn. Een ander struikelblok dat vaak wordt aangehaald is de complexe installatie van deze sensoren die enkel kan worden uitgevoerd door gespecialiseerd personeel. Verder is er ook sterke competitie van de geminiaturiseerde sensoren gebaseerd op Micro-Elektromechanische systemen (MEMS). Binnen dit onderzoek gaan we daarom nog een stap verder door een flexibele of zelfs rekbare folie te ontwikkelen waarin naast alle sensoren ook de aandrijf(opto-)elektronica kan worden geïntegreerd. Zo wordt een artificiële fotonische huid gecreëerd die op of rond om het even welk oppervlak kan worden aangebracht of gewikkeld. Door het multiplexen van verschillende sensorpunten in combinatie met de integratie in polymere substraten krijgt het systeem bovendien een quasi-gedistribueerd karakter.

De integratie van optische sensoren samen met de nodige optische bronnen en detectoren levert een nieuw sensorconcept op: een fotonische huid gebaseerd op optische sensoren. Voor de eerste keer worden optische sensoren gecombineerd met opto-elektronische componenten en ingebed in flexibele of rekbare polymeren. Dit sensorconcept vindt toepassingen in zeer verschillende ingenieursdomeinen zoals de automobielindustrie, robotica, gezondheidszorg etc. Door het toenemend vertrouwen in de robuustheid en betrouwbaarheid van ingebedde optische vezelsensoren vinden ze tegenwoordig ook ingang in de olie- en gasindustrie.

Na de twee eerste - inleidende - hoofdstukken komt in hoofdstuk 3 de integratie van optische vezelsensoren in polymere materialen aan bod. Het resultaat is een rigide, flexibele of rekbare sensorfolie, voorzien van een ingebedde optische vezel. Afhankelijk van de toepassing en daarmee gepaard gaande vereisten op gebied van mechanische en ruimtelijke gevoeligheid kan een inbedmateriaal met verschillende mechanische eigenschappen worden gekozen. Ormocer (een product van Micro resist technology) is een materiaal dat vaak wordt gebruikt als circulaire coating voor een optische vezel. Binnen dit doctoraat zal het worden aangewend als hard "huid" materiaal voor de fabricage van planaire sensorfolies. Als rekbaar inbedmateriaal wordt een rubberachtige silicone gebruikt, PDMS.

Standaard optische vezels zijn gemaakt van glas en worden vervaardigd met een trekproces startende van een preform. Sensoren worden vervolgens ingeschreven door een invallend interferentiepatroon van een UV bron. Het resultaat is een optische filter die een welbepaalde golflengte, variërend onder invloed van temperatuur, rek en druk, reflecteert. Ook speciale types vezelsensoren met unieke sensoreigenschappen worden gebruikt in dit proefschrift. Zo hebben polymere vezels een hogere mechanische flexibiliteit en compatibiliteit met biomedische toepassingen. Verder wordt ook een speciaal type glasvezel gebruikt gebaseerd op microstructuren (luchtgaten) rond de vezelkern. Dit type vezelsensor maakt het mogelijk de gevoeligheid van de sensor te variëren voor verschillende externe parameters. Overspraak tussen verschillende meetgrootheden kan op deze manier worden beperkt en de gevoeligheid voor transversale rek en hydrostatische druk kan merkbaar worden verhoogd.

Sensoren die worden gebruikt in biomedische toepassingen moeten worden ingebed in biocompatibele of soms zelfs implanteerbare systemen. Daarom is ook een cilindrische versie van de inbedtechnologie ontwikkeld die het mogelijk maakt om vezelsensoren te integreren in tubulaire systemen. Een typisch voorbeeld dat gebruik maakt van een dergelijke technologie vinden we bijvoorbeeld terug bij een gastroscopisch onderzoek. Bij een dergelijk onderzoek kan het monitoren van drukgolven die propageren in de slokdarm een grote bron van informatie zijn. Een sensorsysteem gebaseerd op verschillende meetpunten in een polymere vezelsensor en ingebed in een flexibel cilindrisch polymeer met een diameter van ≈ 4.5 mm wordt ook beschreven in hoofdstuk 3. Bij het vergelijken van de prestaties van deze polymere vezelsensor met de standaard glasvezelsensoren, stellen we een verhoging van de gevoeligheid met een factor 6 vast.

Net zoals elke elektronische component een elektrische voeding nodig heeft,

heeft elk optisch element een lichtbron nodig om te kunnen functioneren. Hoofdstuk 4 beschrijft de ontwikkeling van een verpakkingstechnologie voor het integreren van de nodige perifere opto-elektronische componenten. Om de mechanische flexibiliteit en compatibiliteit met fotonische huid te behouden, wordt getracht deze componenten en bijhorende verpakking zo klein en discreet mogelijk te maken. Om deze "ultra-dunne" modules te vervaardigen wordt er vertrokken van de onderzoekservaring op het gebied van het verpakken van chips, beschikbaar binnen het Centrum voor Microsysteemtechnologie (CMST) via de doctoraatsproefschriften van Wim Christiaens (ultra-dunne chip technologie), Erwin Bosman (flexibele opto-elektronische verpakking), Jeroen Missinne (aanbrengen van rekbare sensorlagen en ontwikkeling van vervormbare optische tactiele sensoren) en Rik Verplancke (verpakkingstechnologie voor rekbare microsystemen). Deze "ultra-dunne" integratiefilosofie wordt binnen dit onderzoek voor de eerste maal toegepast op chips met contactpaden op de substraatkant (achterkant van de chip). Aangezien de chips worden verdund tot 20 µm tijdens het integratieproces, wordt de achterste contactlaag ook weggenomen. Een depositie van nieuwe contactlagen met bijhorende thermische stappen is noodzakelijk om een goede werking van de chip te garanderen.

Wanneer deze opto-elektronische componenten (lasers, fotodiodes, etc.) worden gecombineerd met vezelsensoren, is het belangrijk dat de optische modestructuur overeenkomt. Daarom werden ook single-mode componenten ingebed. Een opto-elektronische verpakking met een totale dikte van 40 µm is het resultaat van dit hoofdstuk. Deze chipverpakking is voorzien van een actieve component, een heatsink en een elektrische uitwaaiering om connectie met de buitenwereld te maken.

Hoewel het gebruik van optische vezelsensorsystemen gestaag toeneemt, blijft de systeemkost één van de grootste struikelblokken die een volledige doorbraak van deze systemen belemmert. De belangrijkste factor binnen de totale kost van een dergelijk systeem is veelal gelinkt aan de *koppeling* van optische vezels of andere lichtgeleidende structuren met bronnen en detectoren. Aligneringsnauwkeurigheden van 1 µm of zelfs minder zijn vaak noodzakelijk om het optische vermogenbudget hoog genoeg te houden. Dit brengt met zich mee dat de koppeling actief moet gebeuren door het oplichten van de optische structuren tijdens het koppelproces om zo de koppelefficiëntie te maximaliseren. Het oplichten van elke individuele component bemoeilijkt uiteraard een efficiënt (bijvoorbeeld "roll-to-roll") fabricage proces. Het is met andere woorden van groot belang om de koppelingstructuur en -technologie de nodige aandacht te geven, zowel in de fase van het ontwerp, als bij het ontwikkelen van een prototype als bij de fabricage van optische systemen.

In hoofdstuk 5 wordt daarom een op maat gemaakte vezelkoppeltechnologie ontwikkeld om een kostenefficiënte, geïntegreerde koppeling te voorzien van een laser naar een optische vezel en van een optische vezel naar een detector. Naast het actieve koppelingsproces bestaat de belangrijkste uitdaging erin de compatibiliteit met de vlakke sensorfolies en de ultra-dunne laser- en detector- chipverpakkingen uit hoofdstuk 3 en 4 te behouden. Het resultaat is een koppelplug, bestaande uit PMMA materiaal, met een geïntegreerde spiegel op micrometer niveau aan de optische vezel. Een optische link bestaande uit een Verticaal Emitterende Laser (VCSEL), 2 vezelkoppelpluggen en een detector resulteert zo in een totaal verlies van 7 dB (volledig single-mode systeem). De PMMA plug heeft een dikte van 500 µm en is bijgevolg compatibel met de toepassingen die we voor ogen hebben, gebaseerd op het concept van de optische sensorhuid.

Alle technologieblokken, ontwikkeld binnen dit doctoraat, werden zo generiek mogelijk gehouden om op die manier de bruikbaarheid niet te beperken tot sensortoepassingen. De karakterisatie en testresultaten zijn echter gebaseerd op optische vezelsensorsystemen. Dergelijke volledig ingebedde systemen, bestaande uit geïntegreerde lasercomponenten, detectoren en vezelsensoren, worden beschreven in hoofdstuk 6. Een snel, kostenefficiënt en uiterst nauwkeurig interrogatiesysteem voor vezelsensoren is het resultaat (demonstratie van een dynamische sensoruitlezing aan 1 kHz en 1000 meetpunten per interrogatiecyclus). Het beperkte golflengtebereik van de lasercomponenten zorgt ervoor dat het multiplexen van verschillende sensorpunten met dit uitleessysteem de belangrijkste uitdaging blijft. Door gebruik te maken van verschillende, in parallel werkende, optische bronnen, of een speciaal type verticaal emitterend lasers (met een hoger golflengtebereik) kan dit euvel evenwel worden verholpen.

Binnen hoofdstuk 7 wordt een alternatieve optische druksensor beschreven die gebaseerd is op het meten van verticale verplaatsingen. Het principe van deze sensor is gelinkt aan het fenomeen "optische feedback" dat optreedt wanneer licht wordt teruggekoppeld in een lasercaviteit. Dit interferometrisch effect is inherent aan de laser zelf, wat ervoor zorgt dat er geen aparte sensorstructuren (bijvoorbeeld optische vezels) nodig zijn. Op deze manier wordt ook een optische koppelstructuur vermeden, wat het integratieproces merkbaar vereenvoudigt. Concreet wordt er vertrokken van ingebedde lasers (VCSELs) uit hoofdstuk 4 waar een sensor- en spiegellaag wordt aan toegevoegd. De sensorlaag is een samendrukbare PDMS laag die een extern uitgeoefende druk omzet in een verandering van de caviteitslengte van de laser. De spiegellaag zorgt voor de terugkoppeling van licht in de lasercaviteit. In dit hoofdstuk worden lasercomponenten op 850 nm gebruikt die een interferometrisch signaal voortbrengen met een periode van 425 nm. Met behulp van dit sensorprincipe wordt het bijgevolg mogelijk om verplaatsingen op nanometer schaal te visualiseren. Deze sensor kan ook worden uitgelezen met een optische detector of een spectrometer. We hebben er echter voor gekozen om de uitlezing elektronisch te doen om geen extra componenten te moeten toevoegen en zo geïntegreerde metingen mogelijk te maken. Dit resulteert in een gevoeligheid van 4.71 µm/nm. Verder laat het gebruik van laserrijen op chipniveau gemultiplexte metingen met een hoge densiteit (spatiëring tussen twee lasers is typisch 250 µm) toe. De ruimtelijke uitgestrektheid van een sensorpunt is 200 µm (overeenkomend met een halvering van de sensorrespons).

Hoofdstuk 8 besluit deze verhandeling met een oplijsting van de belangrijkste bijdrages in verschillende branches binnen de optische sensorwereld. Ook wordt een kort overzicht gegeven van de verschillende demonstratoren die werden ontwikkeld en wordt er teruggekeken naar de initieel gedefinieerde objectieven.

Summary

The starting point of this dissertation is the observation of three major trends in today's technology research. A first trend is the evolution towards ever-smaller technology building blocks providing the necessary tools to create portable, wearable and unobtrusive applications. These applications include all kinds of "smart" devices providing instant connectedness to social media, music, personal storage, etc. Also applications developed to monitor vital human functions (respiration, heart rate, muscle overload), providing feedback to the patient but also to the treating physician, make extensive use of these recent miniaturization technology advances. This miniaturization trend is definitely not limited to consumer applications but extends much further. One can for example think of implantable devices, aerospace applications or structural health monitoring of bridges and buildings continuously seeking for lighter and smaller monitoring systems.

Next to miniaturization, a second important driver for this dissertation is the tendency to add sensing intelligence to a broad range of applications. Microphones and cameras are some of the best-known sensor applications. More recent examples include humidity sensors in car windows or proximity sensors in car hoods, but also touchscreens, RF-IDs and anti-theft systems. Such "artificial senses" are mimicking one of the five human senses. Sensors have become part of our daily life and are often being used without the awareness of the user.

A third development is the introduction of photonic systems. These systems are based on the propagation of light, using it for example as an information carrier or sensor transducer. Concerning sensing applications, the optical systems typically offer several advantages over their electrical counterparts. These are mainly related to their sensitivity, immunity to electromagnetic interference, passiveness, size, weight, resistance to harsh environments, multiplexing capabilities and potentially also cost. Photonic systems are ubiquitous in our daily life as well as in the most advanced branches of science including lighting, metrology, spectroscopy, holography, surgery, laser material processing, to name a few.

We now turn our focus to the main topic of this PhD: integrated optical sensing systems and the according interrogation technologies. Owing to the abovementioned recent trends and associated technology advances, the emerging field of integrated optical sensing systems is rapidly developing. Although these optical sensing systems, mainly based on optical fiber sensors, offer several unique advantages making them more versatile than their electronic counterparts, their market share is still significantly below its potential. Within this PhD, the aim is to remove some of the traditional issues preventing these optical sensors from penetrating the market, which include packaging, optical coupling, true strain transfer, reliability, and fully-fledged system integration. Therefore, this dissertation is combining those three trends by coming up with thorough integration of optical sensors and the associated driving optoelectronic components through polymer embedding.

Other challenges impeding a full breakthrough within the (fiber) optical sensing field include the need for low-cost optical interrogation units, complex installation of fiber sensor modules requiring trained personnel and the tough competition with miniaturized electrical sensors typically based on Microelectromechanical Systems. A major objective of this PhD is therefore the development of a flexible or even stretchable foil in which all necessary optical sensing elements can be integrated and, if necessary, can include optical and electrical interrogation, powering and communication. This yields an optical skin that can be wrapped around, embedded in, attached and/or anchored to irregularly shaped and/or moving objects, that will allow quasi-distributed sensing.

Integrating optical sensors and their associated optoelectronic driving and readout components enables the fabrication of photonic skins for optical sensing. This unobtrusive photonic sensing skin is a new paradigm for optical sensors integrated in an unprecedented manner with optoelectronic and electronic circuitry in flexible and stretchable skins for applications in various engineering disciplines such as structural health monitoring, automotive industry, robotics, health care etc. Furthermore, because of their robustness, optical fibers sensors are nowadays also used in the field of oil and gas extraction.

After two introductory chapters, Chapter 3 describes the embedding of optical fiber sensors in polymer host materials resulting in rigid, flexible or stretchable sensing foils. Depending on the application and the required sensitivity, both mechanically and spatially, a different embedding material is used. Ormocer from Micro resist technology is a popular fiber coating material. This material is used in this dissertation as a rigid fiber embedding - optical skin - material. The stretchable alternative is based on PDMS, a silicone type family of materials.

Traditional optical fibers are based on silica and fabricated through a drawing process starting from a preform. Sensors based on fiber Bragg gratings are typically inscribed using an interference pattern of a UV light source. Within this dissertation also special types of fibers possessing unique sensing capabilities are used. These include *polymer* fiber alternatives offering a higher degree of mechanical flexibility and compliance with biomedical applications. Furthermore, a special type of silica fiber sensors based on microstructures (typically air holes) surrounding the fiber core is embedded enabling tuning of the sensor

response to different ambient parameters. Unwanted cross-sensitivity effects related to temperature variations can be reduced to a minimum and the transverse strain/hydrostatic pressure sensitivity can significantly be enhanced.

Especially in biomedical applications there is a growing need for embedded sensors which can be embedded in human-friendly, biocompatible or even implantable systems. The different embedding techniques therefore also include a tubular version which allows to produce embedded fiber sensors in cylindrical shapes. An application which is demanding for this technology is esophageal examination monitoring pressure waves propagating in the esophagus. This sensor concept is introduced in Chapter 2 and further discussed within Chapter 3. Within this last-mentioned chapter, technology is developed to come up with a multiplexed polymer fiber sensor embedded in a cylindrical tube with a diameter of 4.5 mm. Comparing the polymer fiber sensing tubes with the traditional silica sensors, the polymer fiber sensors outperform their silica counterparts by a factor 6 in terms of sensitivity.

Similar to electronic components needing electrical powering, all optical elements need an optical powering source and/or detecting unit. Chapter 4 reports on the development of a dedicated package to integrate these necessary peripheral (opto)electronic components. To fabricate these ultra-thin packages, technology was optimized using the research experience available within the Centre for Microsystems Technology (CMST) through the PhDs of Wim Christiaens (Ultra-Thin Chip Technology), Erwin Bosman (flexible optoelectronic packaging), Jeroen Missinne (introducing stretchable transducer layers and development of conformable optical tactile sensors) and Rik Verplancke (packaging technology for stretchable microsystems). This "ultra-thin" embedding approach is applied for the first time on chips with back-contact pads in this chapter. The optoelectronic chips (lasers, light emitting diodes, photodetectors) are thinned down to a thickness of 20 µm during the embedding process consequently also removing the contact pads on the backside. Redeposition of these back-contact layers and annealing ensure proper functioning of the thinned components. From a fiber sensing point of view, also the modal structure of laser components should be closely monitored. The embedding process was therefore also extended towards single-mode components, more specifically Vertical-Cavity Surface-Emitting Lasers (VCSELs), offering excellent compatibility with optical sensing structures. A 40 µm thick optoelectronic package incorporating an active component, heatsinking and electrical fan-out is the result of this chapter.

Although the use of optical fiber sensing systems is growing steadily, cost effectiveness is one of the biggest challenges preventing a complete breakthrough. The cost item which is generally the most important relates to the *coupling* of fibers or waveguides to optical sources (e.g. lasers) and detectors. Often alignment accuracies down to or even below 1 µm are needed implying the need for active coupling schemes. Active coupling requires lighting up the optical structures

to monitor and maximize the coupled optical power (into a fiber, waveguide or photodetector) before fixing the coupling structures preventing high throughput fabrication processes. Great care must be consequently taken when designing, prototyping and manufacturing coupling technologies for optical systems.

Within Chapter 5 a dedicated fiber coupling technology is developed to provide a cost-effective, integrated way to launch light emitted by a laser into an optical fiber and to capture the light from an optical fiber by a photodetector. Next to the active coupling process, the main challenge here is to ensure the compatibility with the planar sensing foils and ultra-thin packaged lasers and detectors from respectively Chapters 3 and 4. As a result, a PMMA based coupling plug with integrated micromirror provided on the fiber itself provides a low-loss and optical skin compatible (coupling plug thickness of 500 µm) coupling scheme for the envisaged applications. A total loss number of 7 dB is achieved for a full single-mode optical link based on a VCSEL-photodetector system and including in- and out-coupling as well as propagation losses.

Most of the technologies developed within this PhD are generic technologies which can be used for other applications than sensing. The characterization and testing results are however performed from an optical fiber sensing point of view. A fully embedded fiber sensing system is described in Chapter 6 combining integrated lasers, detectors and fibers into a high-speed, low-cost and highly accurate fiber sensor interrogation system. This system is demonstrated using a dynamic sensor read-out with an interrogation frequency of 1 kHz while measuring 1000 data points each interrogation cycle. Because of the limited wavelength range covered by the laser components used within this chapter, multiplexing different sensing points is the main challenge associated with this approach. This can be solved using a combination of optical sources or using a special type of vertically emitting sources covering a broader tuning range.

Within Chapter 7, an alternative sensor to measure pressure or vertical displacements is presented. The sensing principle is based on optical feedback in a semiconductor laser causing interferometry effects. By using this sensing principle inherent to the laser itself the need for fibers or waveguides and associated coupling schemes is avoided. Starting from the embedded components from Chapter 4, sensing intelligence is added to vertically emitting lasers (VCSELs). These sensing features include a PDMS transducer layer to convert an externally applied pressure into a displacement and a reflecting layer recoupling the light back into the laser cavity. This vertical displacement is changing the length of the laser cavity and consequently adjusting the optoelectronic characteristics of the VCSEL. Lasers emitting at 850 nm are integrated yielding an interferometric signal with a periodicity of 425 nm. Using this sensing principle it is consequently possible to visualize displacement variations on a nanometer scale. To maintain the integration advantages, optical read-out measurements requiring additional photodetector or spectrometer components, are avoided. Reading out the sensor is

therefore done electrically providing a sensitivity of 4.71 μV/nm (displacement) or 26.2 μV/mbar (pressure). The use of laser chip *arrays* enables easy and high-density multiplexing of sensing points. The spatial range of one sensor element is 200 μm (halving the sensor response).

Chapter 8 concludes this dissertation by listing the main contributions to the different optical sensing branches. A short overview of the different proof-of-principle systems is also included as well as a look back on the initially defined objectives.

1
General introduction

Important thing in science is not so much to obtain new facts as to discover new ways of thinking about them
–Sir William Bragg (1862 - 1942)

1.1 Sensors

The continuous quest to add intelligence to a wide range of different applications, leading to all kinds of "smart" devices and increasing the ambient awareness of traditionally simple devices, entails a massive increase in the use of *sensors*. Today, sensors are ubiquitous and play an important role in our modern society. Next to the use of sensors in well-known consumer electronic products such as digital cameras, smartphones, computers, also in the processing industry, material manufacturing, civil engineering, transport and energy production, sensors are becoming increasingly important to monitor the influence of physical quantities. These quantities typically include temperature, pressure, strain or force [1]. Adding sensors within a wide range of technology levels is an important trend providing a first starting point for this dissertation.

Next to the trend of adding sensing features, two other major trends are important for the rationale of this dissertation. A first trend we can identify is the need for *miniaturization*. Devices which are compact, ultra-small, sometimes even not visible to the naked eye, enable a range of new applications. The second trend is related to the working principles of sensors and datacom links which are becoming more and more complex in order to be deployed in challenging environments and monitor extreme ambient parameters. Especially the evolution towards *optical* systems, being complementary to or even replacing the traditional electrical systems, is an important motivation within the framework of this dissertation. In the next paragraphs these trends will be discussed in more detail, not limited to sensing but within a broader technological context.

1.2 Miniaturization

Miniaturization is referring to the creation of ever-smaller scales for mechanical, optical, and electronic systems and products. This miniaturization trend is pushing through in all levels of the production cycle. One of the types of end products which is the most influenced by this trend are consumer electronics. Mobile phones, laptops, MP3 players, television sets, etc. are getting thinner, smaller and lighter or are adding more intelligence or extra features in equal space. As an example, Figure 1.1 is depicting the evolution in terms of size of the OmniVision - leading developer of advanced digital imaging solutions - mobile phone cameras.

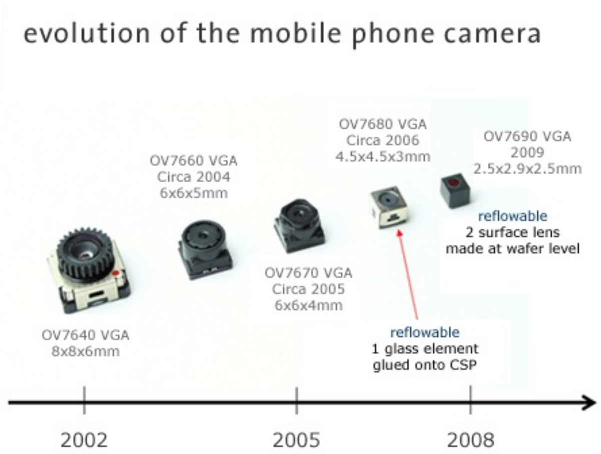

Figure 1.1 – The evolution of mobile phone cameras has experienced rapid decrease in size and cost [2]. Source: `http://www.ovt.com/`

One step back in the production process, several miniaturization examples can be found on the packaging level of (opto)electronics. Through the use of for example Surface Mount (SM), Ball Grid Arrays (BGAs) or Chip Scale Packages (CSPs), the packaging technology has a large influence on the total size of the full system. On a chip level, the best-known example of miniaturization can be found, i.e. Moore's law. This law is based on the observation that over the history of computing hardware, the number of transistors on integrated circuits doubles approximately every two years. Miniaturization is important because it can create new markets by enabling new applications through technology scaling. This technology scaling is resulting in better performance and potentially also lower cost, as illustrated in Figure 1.2.

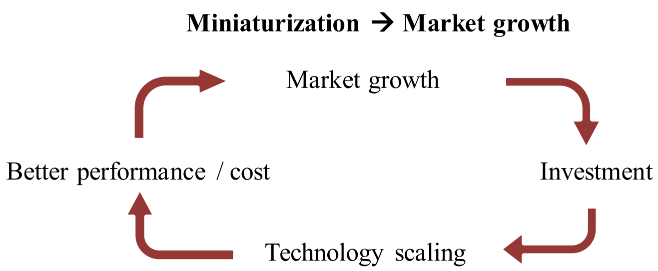

Figure 1.2 – Miniaturization leading to market growth.

1.3 Optical systems

Traditional interconnections and sensing structures are based on electrical or electromechanical working principles. A change in the electrical current level, resistance or capacitance contains the necessary information on the transmitted datasignal or sensing parameter. Electrical devices may nevertheless experience difficulties in performing properly under challenging circumstances, for example in the presence of sources of electromagnetic radiation such as high voltage lines or lightning strikes. Electrical interconnections face their fundamental limits when targeting high-speed applications, making them unsuitable for long-distance communication channels but also yielding serious challenges in short-range datacom applications. Concerning electrical sensors, their intrinsic temperature sensitivity can also disturb the sensor signal when the physical quantity of interest is measured in transient temperature regimes. Therefore, optical alternatives have been introduced both for communication and sensing purposes.

1.3.1 Optical datacommunication

Long-distance links

One of the most famous examples of a long-distance link is the transatlantic communication cable, a submarine link between Europe and North America running under the Atlantic Ocean. The first (galvanic) transatlantic telephone cable system was laid in the 1950's. The first transatlantic optical cable based on fiber optics (TAT-8) was operational in 1988, increasing the number of available channels by a factor of 10. At present, all operational transatlantic links are fiber based providing a capacity of several 10's of Tbps (Terabits per second). Optical fibers are consequently indispensable for the rapid growing internet based economy.

Currently there is a trend to provide fiber optics as close to the end user as possible. By limiting the galvanic distance, the communication speed is further maximized. Fiber-to-the-home pilot projects have also been rolled out demonstrating the possibilities to provide fiber optic interconnection inside homes. In this context, polymer optical fibers can serve as a cost-effective alternative for the silica fibers and solve fiber interconnection issues [3].

On-board or board-to-board links

Because of the increasing demand for high-speed computing power, also the developments related to on-board electrical interconnections are coming close to the fundamental limits. Therefore, optical alternatives are starting to be deployed in short-range interconnects as well. Typically these interconnects are used on printed circuit boards. Fibers are in this case too complicated (in- and out-coupling) and integrated polymer optical waveguides constitute an elegant cost-effective alternative [4, 5].

1.3.2 Optical sensing

For some applications, traditional - electrical - sensors to measure ambient parameters such as temperature, strain and pressure suffer from several disadvantages. These disadvantages include their weight, size, inherent electrical operating principle and associated need for electrical powering, sensitivity etc. Although a lot of these electrical sensors are mass produced and sometimes extremely low-cost, optical sensing alternatives are gaining a lot of interest from people from several niche application areas. Optical fiber sensors are particularly interesting because they allow for distributed measurements, have a low weight and potentially also a low cost. These unique features can fulfill the sensing needs within a broad range of application domains. Figure 1.3 is depicting the estimated revenue growth of sensors based on fiber optics. Within Figure 1.3a, the distribution of the estimated revenues over different application domains is shown whereas Figure 1.3b shows the expected revenue growth in the coming years, up to $4.0 billion in 2017.

The research domain of optical sensing is rapidly gaining interest. This trend can be demonstrated when looking to the publication trend (Web of Science), illustrated in Figure 1.4 and the patent filing trend (Espacenet), illustrated in Figure 1.5.

Note that the numbers in these figures provide evidence of an increasing interest in optical sensors *in general*, including applications outside the research scope of this dissertation, such as the development of optical detectors and Charge Coupled Devices (CCDs) or CMOS camera devices.

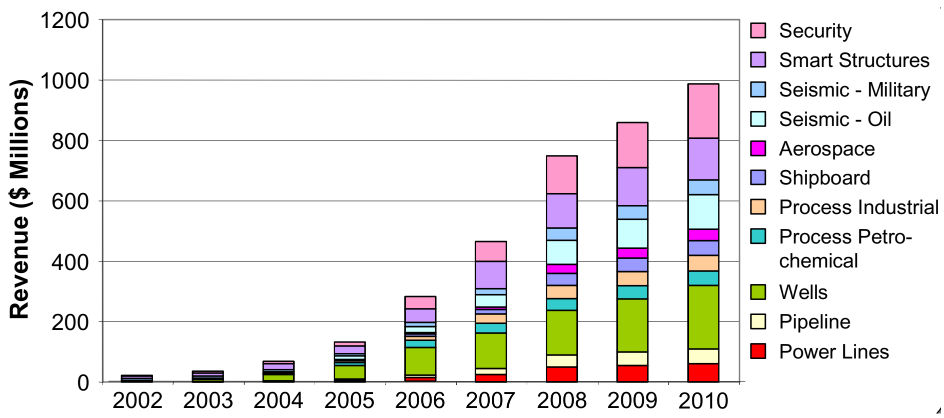

(a) Estimated total fiber optic sensors market in $ million, distributed over the different application domains. Source: Lightwave Venture, OIDA.

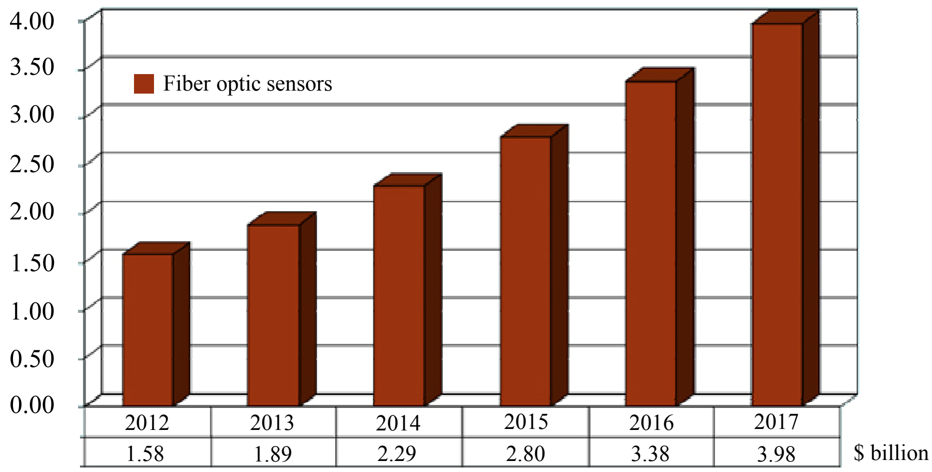

(b) The consumption value of fiber optic sensors (continuous distributed and point) will grow at an annual rate of 20.3 % from $1.6 billion (2012) to $4.0 billion (2017). Source: optics.org and ElectroniCast Consultants.

Figure 1.3 – Estimated revenues of the fiber optic sensors market from 2002 to 2017.

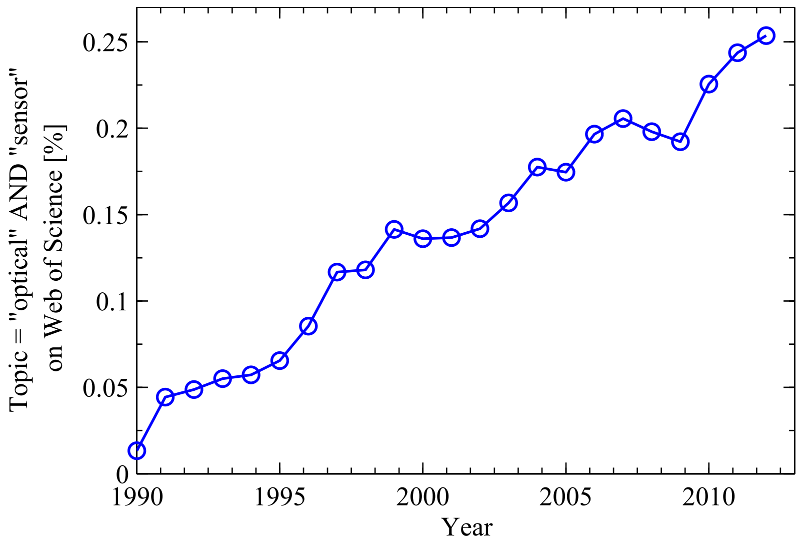

Figure 1.4 – Research publications on optical sensors (source: Web of Science).

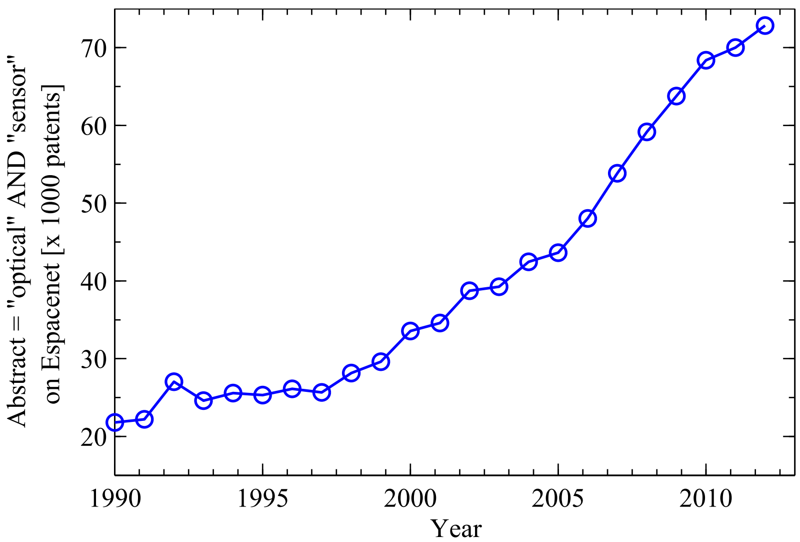

Figure 1.5 – Patents on optical sensors (source: Espacenet).

1.3.3 Combination of optical datacommunication and sensing

A unique property of the optical waveguiding structures is the fact that the fibers or waveguides can act simultaneously as a sensing element and a communication channel. The need for a specific telemetry system, required for most of the existing sensing systems, is consequently avoided. This dual characteristic of optical fibers enables a key advantage when using fiber sensors, being the possibility to perform multi-point or even distributed measurements. In the case of fiber Bragg gratings (FBGs, based on wavelength selective mirrors), reading out all different sensing points can be done in a single wavelength sweep. The different sensing points are in this case defined by wavelength-division multiplexing: all sensing points reflect a different wavelength.

Combining a thorough integration of datalinks and sensors enables a new paradigm of connectedness through the internet, referred to as the Internet of Things (IoT). The IoT vision consists of an internet in which not only *anyone* can be connected anywhere and anytime but so too can *anything*. We have always had sensors (fire alarms, thermometers), and now they are becoming smaller and more sophisticated, more efficient and more easily embeddable. Complementary technologies such as real-time monitoring for disabled, elderly, medically vulnerable people, but also environmental management open up the possibility to anticipate problems and react proactively. The ambient awareness is significantly increased by adding sensing intelligence to both people (wearable applications) and objects (sometimes on hard to reach locations), and link them through a network of sensors and actuators.

According to [6], sensor networks are indeed the most essential components of the Internet of Things. Figure 1.6 is illustrating how a layered structure constitutes the backbone of the IoT, based on the device capabilities of sensor networks. The sensor network is proposed as an extension of our central nervous system creating a vast array of sensing nodes providing an increased awareness and responsiveness. Sensing information is picked up by the different sensor nodes and sent to higher layers (Figure 1.6) for signal processing and initiation of follow-up actions. The further we go up in the layered structure (layer 1 $\rightarrow$ 6), the higher the degree of computational intelligence will be.

The application of sensors in wearable applications or harsh environments leads to an increased use of embedded optical sensors. Embedding sensors in mechanically flexible materials leads to the creation of conformable, unobtrusive systems which can be wrapped around irregularly shaped objects. Optical sensors avoid the susceptibility to electromagnetic interference and allow for remote sensing measurements in harsh, dangerous or hard to reach environments. An optical fiber is the ideal candidate to transport the sensing information from a remote location to the end user terminal. Particularly for niche applications requiring high-end sensing solutions, optical sensors constitute an interesting alternative

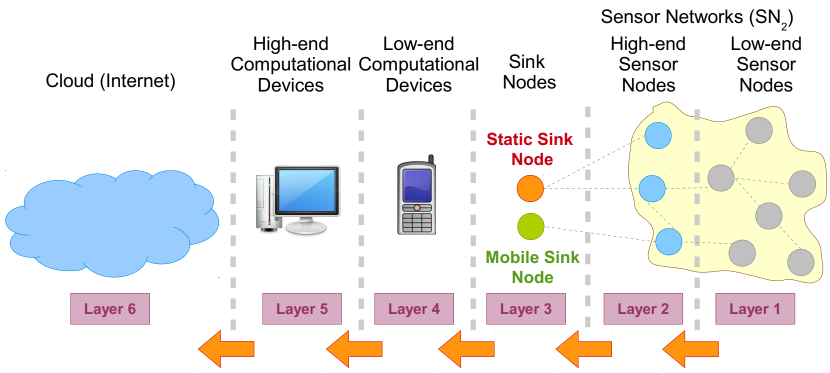

Figure 1.6 – Layered structure based on the device capabilities of a sensor network. In IoT, this layered architecture may have additional number of sub layers. Schematic diagram from Perera et al. [6].

outperforming their electrical counterparts despite their higher cost.

The polymer embedding approach is discussed in the next section. Integrating optical sensors in polymer embedding materials leads to the creation of photonic skins, discussed in Section 1.5.

1.4 Polymer embedding

As discussed earlier, the development of miniaturized sensor elements to measure physical properties such as pressure, temperature and the proximity to other objects is becoming increasingly important. This evolution has been set forward owing to the emergence of Microelectromechanical Systems (MEMS) [7]. This technology typically relies on Integrated Circuit (IC) fabrication processes using rigid substrates such as silicon and glass wafers.

The fabrication of sensors on flexible substrates offers several advantages and opens up a broad range of new applications within the field of robotics and wearable applications. Mounting rigid MEMS based sensors on flexible carriers and consequently creating rigid islands on a larger flexible substrate is an option to accomplish this. Fabricating sensor foils to cover large areas is however difficult in terms of connectivity and reliability. Alternatively, one can remove (part of) the rigid carriers of the sensors after mounting on the flexible carriers by etching. This process is however relying on IC fabrication technology, increasing the system cost to cover large areas.

The idea of sensitive skin was introduced at the 1999 NSF-DARPA Sensitive Skin Workshop [8]. The main technological challenges were identified as:

- The need for a carrier substrate of the sensors, which is compliant, and deforms with the object onto/into which it is integrated.
- The need to integrate a vast number of sensing elements onto this carrier. If these sensors are electrically wired, this generates serious challenges in massive interconnection technology and parallel signal processing capability.

Later on, a sensitive skin was defined as *a large-area, flexible array of sensors with data processing capabilities, which can be used to cover the entire surface of a machine or even a part of a human body* [9]. Within the same article, a first example of this concept was presented (Figure 1.7) containing 64 active infrared sensor pairs (LED & detector), each of which can sense objects within a narrow cone at a distance up to about 20 cm.

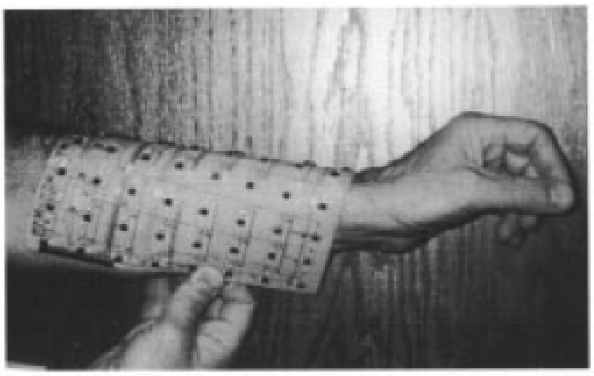

Figure 1.7 – The first sensitive skin module: 64 infrared sensor pairs on a Kapton substrate with a distance between neighboring pairs of 25 mm. Courtesy of V. Lumelsky, Robotics Laboratory, University of Wisconsin-Madison.

Over the last decade, significant progress has been made towards stretchable skin-like structures with embedded sensing features, mainly using flexible electronics leading to so-called *e-skins*. These skins are typically applied directly on top of a human skin [10]. *Optical* skin-like sensing alternatives are discussed in the next paragraph entailing several advantages such as chemical inertness, immunity to electromagnetic interference, distributed sensing possibilities and compatibility with harsh (high temperature and/or pressure) environments.

1.5 Photonic skins

In Figure 1.8, the concept of a photonic skin is presented. A photonic skin is a polymer, mechanically flexible or stretchable, sensing foil consisting of embedded optical sensors resulting in unobtrusive optical sensing systems. Depending on the envisaged application, this sensing system can provide high-density and highly accurate measurements on local thermomechanical properties or large-area measurements of ambient parameters.

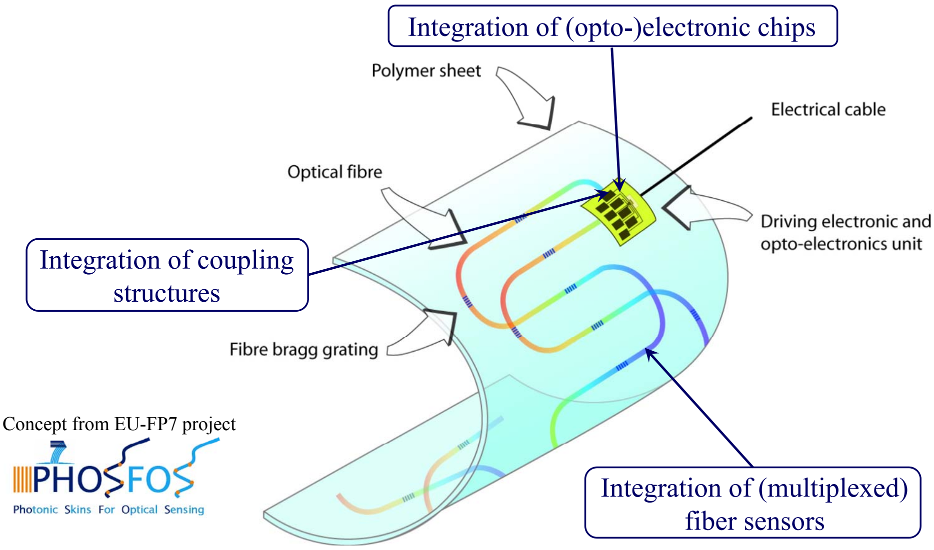

Figure 1.8 – Phosfos (Photonic skins for optical sensing) concept picture.

Optoelectronic and electronic chips are integrated using bare die chip components leading to ultra-small electrical and optical driving units. The dimensions and according mechanical properties of the photonic skin are consequently largely determined by the polymer embedding material properties. **Although alternative optical sensors will be introduced in Chapter 2 and further discussed in Chapter 7, a photonic skin typically relies on optical fiber sensor technology.** A crucial technology heavily influencing the reliability and usability of the sensing system is therefore the fiber coupling of optoelectronic components to optical fiber(s). **All technology blocks developed within this PhD dissertation need to be "skin compliant", i.e. compatible with unobtrusive, planar, mechanically flexible sensing skins with limited dimensions (especially thickness).**

A wide range of applications can be targeted with this photonic sensing skin paradigm. Two potential application domains are illustrated in Figure 1.9:

- One of the domains that could benefit from the photonic sensing skins is situated in the field of robotics. We have for example demonstrated the use of such a sensing foil with a social pet-like robot (Figure 1.9a) that is developed at the Vrije Universiteit Brussel. The fiber sensor consists of 4 or more wavelength-multiplexed FBG sensors (red dots in Figure 1.9a). This sensing concept clearly shows the possibility to integrate different sensing points in one optical fiber. Through a meandering fiber embedding design, a large-area pressure sensitive surface can be created.

- Monitoring vital human functions such as breathing movements, heartbeat, blood pressure is a second example of a photonic skin-like sensing application. Figure 1.9b is depicting a concept picture of a polymer embedded respiration monitoring vest based on a fiber Bragg grating to visualize breathing movements. Important challenges for these wearable applications include weight, size, safety and user friendliness.

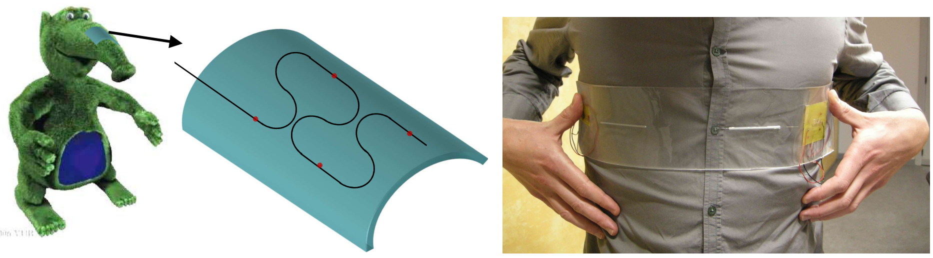

(a) An FBG based sensing skin applied to a social pet-type robot [11].

(b) Optical respiratory monitoring application based on a conformable polymer embedded sensing foil.

Figure 1.9 – Examples of photonic skins for optical sensing.

A more elaborate overview of state-of-the-art photonic skin applications is described in Chapter 2, Section 2.4. Looking back to the advantages of optical (fiber) sensors described in Section 1.3.3, an important trade-off has to be considered related to the photonic skin concept. The more compact the optical sensing system is, the closer the optoelectronic driving and read-out components will be to the optical sensing elements. Important advantages related to the optical sensors, such as the possibility to deploy them in harsh environments, may become void because of the vulnerability of these driving and coupling components embedded in close vicinity to the sensing devices. Depending on the application domain, one has to decide on the level of integration of the optoelectronic and (fiber) coupling parts.

1.6 Problem statement and objectives

State-of-the-art research has lead to significant progress on all the areas mentioned in the above discussion. The following specific objectives are defined within the scope of this PhD dissertation:

- *Polymer fiber embedding* Broaden the application domain of fiber sensors by working towards mechanically flexible and stretchable, typically polymer based, sensor host materials. Combining these materials with optical fiber sensors results in a photonic skin for optical sensing.

  Maintaining the sensing functionality of the fiber sensors after embedding is an important prerequisite. Depending on the sensor type and the embedding process, this might be a serious challenge. Accurate control on the fiber position in the sensing skin, both lateral and transversal, is a second objective within this task. The level of design flexibility is an important parameter to monitor during the fiber embedding research work. Thorough characterization of the sensing skins in terms of responsivity, sensitivity and sensing range, is an essential third objective.

- *Integration and coupling of optoelectronic chips* By miniaturizing and integrating optoelectronic (OE) components on a chip level, ultra-small laser and detector packages are created. These packages can be fiber-coupled when using them in combination with optical fiber sensors or serve as stand-alone sensing units (intrinsic sensor).

  Commercially available optoelectronic chips typically have a thickness > 100 µm. The targeted thickness of an ultra-small package is 40 µm. Thinning of optoelectronic components (down to 20 µm) while maintaining their electrical and optical properties is therefore a first objective related to optoelectronic integration resulting in mechanically flexible optoelectronic packages. A photonic skin typically has a total thickness of 1 mm or less. Standard fiber coupling techniques immediately compromise this unobtrusive photonic skin concept. The fabrication of flat, skin compatible, optical coupling parts is therefore a second objective.

- *Simple and cost-effective optical sensor interrogation systems* By simplifying and downsizing the sensing interrogation schemes, the usability and applicability of optical sensors can significantly increase.

  Combining optoelectronic components on a chip level into a functional interrogation system with a state-of-the-art measurement accuracy and resolution is one of the most important challenges within this dissertation. The ability to perform full spectral measurements when reading out optical fiber sensors, not limited to peak tracking, will enable a unique selling point of this embedded interrogation system.

- *Ultra-small integrated pressure sensors* A sensing alternative for highly accurate pressure measurements can be based on self-mixing interferometry in a laser consequently avoiding fiber sensors, coupling structures and photodetectors. By pushing the limits of the optoelectronic integration process, one can include the necessary polymer transducer layers and reflective coatings.

Starting from the embedded optoelectronic components, a first challenge is to integrate a polymer transducer layer converting an externally applied pressure into a displacement variation. Both the mechanical and optical parameters have to be investigated in order to enable reliable pressure measurement based on this optical feedback mechanism. The sensor build-up has to be optimized in order to combine the packaging, sensing and reflection layers in a proper way in terms of alignment, adhesion, stress concentrations etc.

Two proof-of-concept optical sensing systems will be described in this dissertation:

- An ultra-small integrated optical fiber sensing system.
- A photonic incremental pressure sensor based on optical feedback in a polymer embedded Vertical-Cavity Surface-Emitting Laser (VCSEL).

1.7 Research trajectory and dissertation structure

Within the Centre for Microsystems Technology (CMST) research group, the optical sensing research topic is tackled in different ways. Based on the particular needs of the application in terms of ambient parameters, size, sensitivity, range etc., a specific sensing principle and according measuring system is selected. We can distinguish respectively fiber based, waveguide based and optoelectronic based sensing systems.

Fiber based sensing systems can operate in harsh environments and allow for remote and (quasi-)distributed sensing. Waveguide based sensors can perform high-density tactile measurements and can be combined with integrated lasers and detectors. Also the combination of optical waveguides and capillary microfluidic channels is under investigation. The sensing principle within the optical waveguide can be based on a change in transmitted light intensity but also on wavelength shifts introduced by fluorescence. Optoelectronic based sensors do not require additional components for read-out purposes. They are therefore easier to integrate and potentially also more cost-effective.

In all different approaches, the end goal is to come up with a fully integrated sensing system incorporating in- and out-coupling structures as well as the necessary optoelectronic and possibly also electronic components. This sensing system is then typically embedded in a flexible or stretchable polymer host material. The first steps towards fully embedded optoelectronic components and waveguiding structures were carried out within the PhD framework of Erwin Bosman [12]. This concept was proven through a polymer, mechanically flexible optical link with datacommunication speeds $> 1\,\mathrm{Gbps}$. Therefore, thinned optoelectronic components were embedded in very thin polymer foils making them ideally suited for incorporation in flexible or stretchable skin materials, together with optical sensors. The PhD of Jeroen Missinne [13] resulted in an optoelectronic shear sensor using polymer embedding and transducer materials. Also a tactile pressure sensor was developed based on a changed coupling behavior of polymer crossing waveguides. The integration of polymer waveguide sensing structures for gas sensing applications is under investigation in the PhD of Sandeep Kalathimekkad. A foil based stand-alone sensing platform is the ultimate goal of this research. Finally, the application of optical sensors and integrated coupling structures within micro-nano biosystems is part of the PhD of Nuria Teigell Beneitez.

This dissertation is divided in 8 chapters and the structure of this book is shown in Figure 1.10. After this *General Introduction chapter*, a technical introduction to traditional optical sensors, polymer based optical sensors, interrogation techniques and embedding opportunities is presented in *Chapter 2*. These "introduction" chapters are followed by 3 subsequent "technology" chapters starting with the polymer embedding of optical fiber sensors (silica or polymer, step-index or microstructured) in *Chapter 3*. The technological work related to the miniaturization and integration of optoelectronic components needed to drive the optical sensors and read out the sensing information is described in *Chapter 4*. In order to couple optical fibers to the integrated optoelectronic components, a dedicated fiber coupling technology is developed in *Chapter 5*.

The characterization of the embedded optical fiber sensors is included in *Chapter 3*. *Chapter 6* is combining the technology related to both fiber embedding as well as component integration and fiber coupling into an ultra-small and fully embedded fiber sensing system based on a highly accurate sensor interrogation principle (introduced in *Chapter 2*). The optoelectronic components can also be used to avoid the need for optical fibers and create an optical sensor intrinsic to the optoelectronic component (*Chapter 7*). Finally, the overall conclusion and a discussion of the future work is described in *Chapter 8*.

1.8 Research context and related projects

The research leading to this dissertation was performed within the framework of the following projects:

- A personal Ph.D grant of the Institute for the Promotion of Innovation through Science and Technology in Flanders (IWT-Vlaanderen [14]).
- FAOS (Flexible Artificial Optical Skin) [15]
  SBO project, funded by the Institute for the Promotion of Innovation through Science and Technology in Flanders (IWT-Vlaanderen [14])

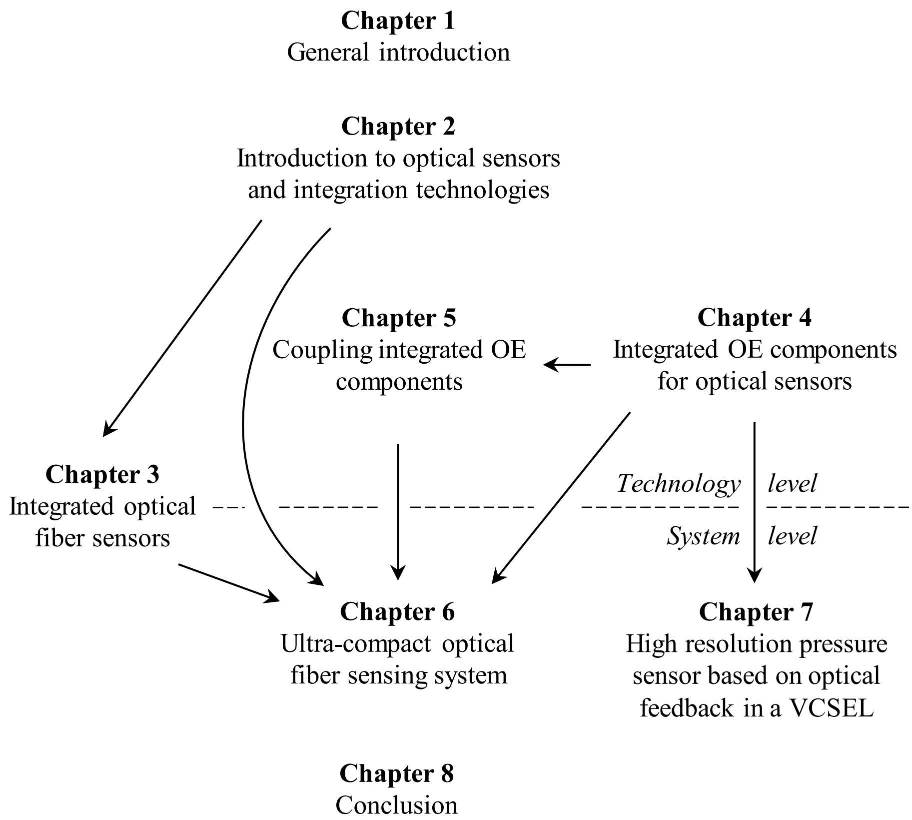

Figure 1.10 – Structure of this dissertation.

Starting date : January 1, 2007
Ending date : December 31, 2010
Project coordinator : Prof. Dr. Ir. Peter Van Daele, IMEC - Ghent University / CMST Microsystems, Technologiepark 914A, B-9052 Zwijnaarde, Belgium

FAOS aimed to develop a new paradigm for flexible optical sensors integrated with electronic modules and control circuitry. The many advantages of optical sensors, and mainly optical fiber sensors, make them very attractive for a wide range of applications. The immunity with regard to EMI (electromagnetic interferences), the resistance to harsh environments, the high sensitivity and the possibility in parallelizing the read-out all make these sensors more useful than their electronic counterparts for automotive applications, aviation, robotics and others. The use of these optical sensors however always implies the use of a light-source, detectors and electronic circuitry to be coupled and integrated with these sensors. The coupling of these fibers with these light sources and detectors is a critical packaging problem and as it is well-known that costs for packaging, especially with optoelectronic components and fiber alignment issues are huge and can rise up to 90 % of the total cost of the module. FAOS delivered a technology that offers an integrated solution to this issue by allowing the embedding of light sources, detectors and electronic circuitry inside flexible polymer materials.

- PHOSFOS (PHotonic Skins For Optical Sensing) [16]
  European ICT-Project, Framework 7
  Starting date : April 1, 2008
  Ending date : August 31, 2011
  Project coordinator : Prof. Dr. Ir. Francis Berghmans, VUB Vrije Universiteit Brussel Pleinlaan 2, B-1050 Brussels, Belgium

  PHOSFOS implemented new approaches to optical sensing, flexible materials, embedding technologies and integration concepts. The PHOSFOS project is now completed and several breakthroughs in the field of optical sensing, flexible materials, embedding technologies and integration concepts have been achieved which may be used in a wide range of applications. A first highlight of the research involves the development of a new pressure sensitive and temperature insensitive sensor. A second highlight involves Bragg grating sensors in polymer optical fibers. The PHOSFOS consortium also developed a new low-cost Polymer Optical Fiber (POF) sensor interrogator designed to work with polymer optical fibers. The sensor interrogator has been designed to operate at a wavelength around 850 nm to match the low loss transmission window of POF and to significantly reduce component costs. Using this technology a new polymer multi-point FBG sensor that can measure the pressure in various medical applications has been demonstrated. More PHOSFOS results and contact information can be obtained on the website of the project `http://www.phosfos.eu`. An introductory video about the project is available on YouTube: `http://www.youtube.com/watch?v=pGpL_icFn1c`.

The research will be further developed within the framework of the following project:

- SSC (Self Sensing Composites) [17]
  SBO project, funded by the Institute for the Promotion of Innovation through Science and Technology in Flanders (IWT-Vlaanderen [14])
  Starting date : January 1, 2013
  Ending date : December 31, 2016

Project coordinator : Dr. Ir. Geert Luyckx, Ghent University / MMS (Mechanics of Materials and Structures) Technologiepark 903, B-9052 Zwijnaarde, Belgium

The technology required to accurately and continuously monitor all critical material aspects of composites is lacking today. In collaboration with industrial partners the main limitations of current state-of-the-art monitoring systems were identified. The development of sensor systems which overcome these limitations will create a number of important economic opportunities. In order to overcome the limitations of the currently existing (embedded) sensor technologies which hinder industrial uptake and limits the deployment of composite structures up to their full potential, this project will realize several scientific breakthroughs. These breakthroughs will result from the development of optical sensors and deformable electronics with innovative and unprecedented properties and which can be integrated within all types of layered materials, with a primary focus on monitoring the structural health of composites during their complete life cycle, i.e. from fabrication to operation. Three sensor techniques are considered: micro-structured optical fiber Bragg gratings, polymer waveguide gratings in relation with deformable electronics and a capacitive sensor based on deformable electronics.

1.9 Research dissemination

1.9.1 Journal papers

- E. Bosman, G. Van Steenberge, B. Van Hoe, J. Missinne, J. Vanfleteren, and P. Van Daele, "Highly reliable flexible active optical links," *IEEE PHOTONICS TECHNOLOGY LETTERS*, vol. 22, no. 5, pp. 287–289, 2010. [Online]. Available: `http://dx.doi.org/10.1109/LPT.2009.2038797`
- E. Bosman, J. Missinne, B. Van Hoe, G. Van Steenberge, S. Kalathimekkad, J. Van Erps, I. Milenkov, K. Panajotov, T. Van Gijseghem, P. Dubruel, H. Thienpont, and P. Van Daele, "Ultrathin optoelectronic device packaging in flexible carriers," *IEEE JOURNAL OF SELECTED TOPICS IN QUANTUM ELECTRONICS*, vol. 17, no. 3, pp. 617–628, 2011. [Online]. Available: `http://dx.doi.org/10.1109/JSTQE.2010.2096407`
- J. Missinne, E. Bosman, B. Van Hoe, G. Van Steenberge, S. Kalathimekkad, P. Van Daele, and J. Vanfleteren, "Flexible shear sensor based on embedded optoelectronic components," *IEEE PHOTONICS TECHNOLOGY LETTERS*, vol. 23, no. 12, pp. 771–773, 2011. [Online]. Available: `http://dx.doi.org/10.1109/LPT.2011.2134844`

- B. Van Hoe, E. Bosman, J. Missinne, S. Kalathimekkad, G. Melpignano, T. De Geyter, G. Godier, P. Van Daele, and G. Van Steenberge, "Photonic incremental pressure sensor based on optical feedback in a polymer embedded vcsel," *IEEE PHOTONICS TECHNOLOGY LETTERS*, vol. 24, no. 13, pp. 1151–1153, 2012. [Online]. Available: http://dx.doi.org/10.1109/LPT.2012.2197678
- B. Van Hoe, G. Lee, E. Bosman, J. Missinne, S. Kalathimekkad, O. Maskery, D. J. Webb, K. Sugden, P. Van Daele, and G. Van Steenberge, "Ultra small integrated optical fiber sensing system," *SENSORS*, vol. 12, no. 9, pp. 12 052–12 069, 2012. [Online]. Available: http://dx.doi.org/10.3390/s120912052
- J. Missinne, E. Bosman, B. Van Hoe, R. Verplancke, G. Van Steenberge, S. Kalathimekkad, P. Van Daele, and J. Vanfleteren, "Two axis optoelectronic tactile shear stress sensor," *SENSORS AND ACTUATORS A-PHYSICAL*, vol. 186, pp. 63–68, 2012. [Online]. Available: http://dx.doi.org/10.1016/j.sna.2012.01.038

1.9.2 Proceedings of international conferences, with Web of Science indexation

- J. Missinne, G. Van Steenberge, B. Van Hoe, K. Van Coillie, T. Van Gijseghem, P. Dubruel, J. Vanfleteren, and P. Van Daele, "An array waveguide sensor for artificial optical skins," in *Proceedings of SPIE, the International Society for Optical Engineering*, A. Glebov and R. Chen, Eds., vol. 7221. SPIE, the International Society for Optical Engineering, 2009. [Online]. Available: http://dx.doi.org/10.1117/12.809154
- E. Ferraris, T. Van Gijseghem, C. Yan, B. Van Hoe, G. Van Steenberge, P. Van Daele, P. Dubruel, and D. Reynaerts, "Embedding of fibre optic sensors within flexible host," in *4M/ICOMM 2009 - THE GLOBAL CONFERENCE ON MICRO MANUFACTURE*. Professional Engineering Publishing ltd, 2009, pp. 351–354.
- X. Chen, C. Zhang, D. J. Webb, B. Van Hoe, G. Van Steenberge, K. Kalli, F. Berghmans, H. Thienpont, W. Urbanczyk, K. Sugden, and G.-D. Peng, "Polymer photonic sensing skin," in *Proceedings of SPIE, the International Society for Optical Engineering*, J. L. s. Santos, B. Culshaw, J. M. Ló pez Higuera, and W. N. MacPherson, Eds., vol. 7653. SPIE, the International Society for Optical Engineering, 2010. [Online]. Available: http://dx.doi.org/10.1117/12.866367
- E. Bosman, J. Bauwelinck, K. Panajotov, G. Van Steenberge, J. Missinne, B. Van Hoe, and P. Van Daele, "Characterization of flexible fully embed-

ded optical links," in *Proceedings of SPIE, the International Society for Optical Engineering*, H. Thienpont, P. Van Daele, J. Mohr, and H. Zappe, Eds., vol. 7716. SPIE, the International Society for Optical Engineering, 2010. [Online]. Available: `http://dx.doi.org/10.1117/12.854229`

- J. Missinne, G. Van Steenberge, B. Van Hoe, E. Bosman, C. Debaes, J. r. Van Erps, C. Yan, E. Ferraris, P. Van Daele, J. Vanfleteren, H. Thienpont, and D. Reynaerts, "High density optical pressure sensor foil based on arrays of crossing flexible waveguides," in *Proceedings of SPIE, the International Society for Optical Engineering*, H. Thienpont, P. Van Daele, J. Mohr, and H. Zappe, Eds., vol. 7716. SPIE, the International Society for Optical Engineering, 2010. [Online]. Available: `http://dx.doi.org/10.1117/12.854578`
- X. Chen, C. Zhang, B. Van Hoe, D. J. Webb, K. Kalli, G. Van Steenberge, and G.-D. Peng, "Photonic skin for pressure and strain sensing," in *PROCEEDINGS OF SPIE - THE INTERNATIONAL SOCIETY FOR OPTICAL ENGINEERING*, F. Berghmans, A. G. Mignani, and C. A. van Hoof, Eds., vol. 7726, no. Optical Sensing and Detection. SPIE, the International Society for Optical Engineering, 2010. [Online]. Available: `http://dx.doi.org/10.1117/12.854235`
- B. Van Hoe, G. Van Steenberge, E. Bosman, J. Missinne, T. Geernaert, F. Berghmans, D. J. Webb, and P. Van Daele, "Optical fiber sensors embedded in polymer flexible foils," in *Proceedings of SPIE, the International Society for Optical Engineering*, F. Berghmans, A. G. Mignani, and C. A. van Hoof, Eds., vol. 7726, no. Optical sensing and detection. SPIE, the International Society for Optical Engineering, 2010. [Online]. Available: `http://dx.doi.org/10.1117/12.854865`
- E. Bosman, G. Van Steenberge, J. Missinne, B. Van Hoe, and P. Van Daele, "Packaging of opto-electronic devices for flexible applications," in *Proceedings of SPIE, the International Society for Optical Engineering*, A. L. Glebov and R. T. Chen, Eds., vol. 7607. SPIE, the International Society for Optical Engineering, 2010. [Online]. Available: `http://dx.doi.org/10.1117/12.841553`
- B. Van Hoe, D. Lamon, E. Bosman, G. Van Steenberge, J. Missinne, P. Goethals, P. Krassimir, D. Reynaerts, J. Vanfleteren, and P. Van Daele, "Embedded high resolution sensor based on optical feedback in a vertical cavity surface emitting laser," in *Proceedings of SPIE, the International Society for Optical Engineering*, K. J. Peters, W. Ecke, and T. E. Matikas, Eds., vol. 7648. SPIE, the International Society for Optical Engineering, 2010. [Online]. Available: `http://dx.doi.org/10.1117/12.847647`
- J. Missinne, E. Bosman, B. Van Hoe, G. Van Steenberge, P. Van Daele, and J. Vanfleteren, "Embedded flexible optical shear sensor," in *IEEE Sensors*.

IEEE, 2010, pp. 987–990. [Online]. Available: http://dx.doi.org/10.1109/ICSENS.2010.5690919

- F. Berghmans, T. Geernaert, S. Sulejmani, H. Thienpont, G. Van Steenberge, B. Van Hoe, P. Dubruel, W. Urbanczyk, P. Mergo, D. J. Webb, K. Kalli, J. Van Roosbroeck, and K. Sugden, "Photonic crystal fiber bragg grating based sensors: opportunities for applications in healthcare," in *Proceedings of SPIE, the International Society for Optical Engineering*, J. Popp, D. Matthews, J. Tian, and C. Yang, Eds., vol. 8311. SPIE, the International Society for Optical Engineering, 2011. [Online]. Available: http://dx.doi.org/10.1117/12.901240

- E. Bosman, G. Van Steenberge, J. Missinne, B. Van Hoe, S. Kalathimekkad, and P. Van Daele, "Packaging technology enabling flexible optical interconnections," in *Proceedings of SPIE, the International Society for Optical Engineering*, A. L. Glebov and R. T. Chen, Eds., vol. 7944. SPIE, the International Society for Optical Engineering, 2011. [Online]. Available: http://dx.doi.org/10.1117/12.874959

- B. Van Hoe, E. Bosman, J. Missinne, G. Van Steenberge, P. Van Daele, W. Zhang, I. Johnson, K. Sugden, D. J. Webb, and K. Kalli, "Embedded multiplexed polymer optical fiber sensor for esophageal manometry," in *2011 IEEE Sensors*. IEEE, 2011, pp. 1499–1502. [Online]. Available: http://dx.doi.org/10.1109/ICSENS.2011.6127216

- S. Kalathimekkad, J. Missinne, J. D. Arias Espinoza, B. Van Hoe, E. Bosman, E. Smits, R. Mandamparambil, G. Van Steenberge, and J. Vanfleteren, "Fluorescence-based optochemical sensor on flexible foils," in *PROCEEDINGS OF SPIE, THE INTERNATIONAL SOCIETY FOR OPTICAL ENGINEERING*, F. Berghmans, A. G. Mignani, and P. De Moor, Eds., vol. 8439, no. 0Y-1. SPIE, 2012, pp. 84 390Y–1–84 390Y–9. [Online]. Available: http://dx.doi.org/10.1117/12.922663

- B. Van Hoe, E. Bosman, J. Missinne, S. Kalathimekkad, G. Lee, Z. Yan, K. Sugden, D. Webb, G. Van Steenberge, and P. Van Daele, "Low-cost fully integrated fiber bragg grating interrogation system," in *PROCEEDINGS OF SPIE, THE INTERNATIONAL SOCIETY FOR OPTICAL ENGINEERING*, J. Canning and G. Peng, Eds., vol. 8351. SPIE-INT SOC OPTICAL ENGINEERING, 2012. [Online]. Available: http://dx.doi.org/10.1117/12.914253

- S. Kalathimekkad, J. Missinne, J. D. Arias Espinoza, B. Van Hoe, E. Bosman, E. Smits, R. Mandamparambil, G. Van Steenberge, and J. Vanfleteren, "Foil-based optical technology platform for optochemical sensors," in *PROCEEDINGS OF SPIE, THE INTERNATIONAL SOCIETY FOR OPTICAL ENGINEERING*, J. E. Broquin and G. N. Conti, Eds., vol. 8264, no. 0R-1. Spie, 2012, pp. 82 640R–1–82 640R–9. [Online]. Available: http://dx.doi.org/10.1117/12.908182

- B. Van Hoe, E. Bosman, J. Missinne, S. Kalathimekkad, G. Van Steenberge, and P. Van Daele, "Novel coupling and packaging approaches for optical interconnects (invited paper)," in *PROCEEDINGS OF SPIE, THE INTERNATIONAL SOCIETY FOR OPTICAL ENGINEERING*, A. Glebov and R. Chen, Eds., vol. 8267. SPIE-INT SOC OPTICAL ENGINEERING, 2012. [Online]. Available: http://dx.doi.org/10.1117/12.913760
- G. C. Lee, B. Van Hoe, Z. Yan, O. Maskery, K. Sugden, D. Webb, and G. Van Steenberge, "A compact, portable and low cost generic interrogation strain sensor system using an embedded vcsel, detector and fibre bragg grating," in *PROCEEDINGS OF SPIE, THE INTERNATIONAL SOCIETY FOR OPTICAL ENGINEERING*, K. Choquette and C. Lei, Eds., vol. 8276. SPIE-INT SOC OPTICAL ENGINEERING, 2012. [Online]. Available: http://dx.doi.org/10.1117/12.907810
- J. Missinne, E. Bosman, B. Van Hoe, R. Verplancke, G. Van Steenberge, S. Kalathimekkad, P. Van Daele, and J. Vanfleteren, "Ultra thin optical tactile shear sensor," in *PROCEDIA ENGINEERING*, G. Kaltsas and C. Tsamis, Eds., vol. 25. Elsevier Science, 2012, pp. 1393–1396. [Online]. Available: http://dx.doi.org/10.1016/j.proeng.2011.12.344

1.9.3 Proceedings of international conferences, without Web of Science indexation

- G. Van Steenberge, E. Bosman, J. Missinne, B. Van Hoe, and P. Van Daele, "Flexible optical interconnects," in *Proceedings of the 2nd International Symposium on Photonic Packaging*, 2008.
- E. Bosman, B. Van Hoe, J. Missinne, G. Van Steenberge, S. Kalathimekkad, and P. Van Daele, "Unobtrusive packaging of optoelectronic devices for optical tactile and shear sensors," in *PROCEEDINGS OF THE 5TH INTERNATIONAL CONFERENCE ON SENSING TECHNOLOGY*. IEEE, 2011, pp. 504–509. [Online]. Available: http://dx.doi.org/10.1109/ICSensT.2011.6137031
- D. Barrera, I.P. Johnson, D.J. Webb, B. Van Hoe, G. Van Steenberge, and S. Sales, "Dynamic Strain Sensor using a VCSEL and a Polymer Fiber Bragg Grating in a Multimode Fiber," in *20th International Conference on Polymer Optical Fibers, Bilbao, Spain*. 2011.
- J. Missinne, B. Van Hoe, E. Bosman, S. Kalathimekkad, G. Van Steenberge, and P. Van Daele, "Compact coupling and packaging concepts for flexi-

ble and stretchable polymer optical interconnects," in *2012 IEEE Optical Interconnects Conference*. IEEE, 2012, pp. 129–130. [Online]. Available: http://dx.doi.org/10.1109/OIC.2012.6224412

- T. Geernaert, C. Sonnenfeld, S. Sulejmani, T. Baghdasaryan, G. Van Steenberge, B. Van Hoe, P. Mergo, W. Urbanczyck, M. Becker, F. Berghmans, and H. Thienpont, "Towards flexible photonic sensing skins with optical fiber sensors," in *2012 4th IEEE RAS & EMBS International Conference on Biomedical Robotics and Biomechatronics (BioRob 2012)*. IEEE, 2012, pp. 628–633. [Online]. Available: http://dx.doi.org/10.1109/BioRob.2012.6290767

1.9.4 Other international conferences, without proceedings

- G. Van Steenberge, J. Missine, B. Van Hoe, K. Van Coillie, J. Vanfleteren, and P. Van Daele, "Array waveguide sensor," in *Proceedings NEMO Scientific General Networking Meeting*, 2008.
- E. Bosman, B. Van Hoe, J. Missinne, G. Van Steenberge, and P. Van Daele, "Packaging of flexible optical interconnections," in *International Conference on Micro and Nano Engineering, 35th, Ghent, Belgium*. 2009.
- B Van Hoe, "Phosfos Embedding Technology for Integrated Sensing Solutions" in *European Commission 4th Concertation meeting on Photonics Enabled Applications, Athens, Greece*. 2009.
- C. Sonnenfeld, S. Sulejmani, T. Geernaert, F. Berghmans, H. Thienpont, N. Lammens, G. Luyckx, E. Voet, J. Degrieck, B. Van Hoe, G. Van Steenberge, P. Van Daele, W. Urbanczyk, J. Wojcik, M. Becker, and H. Bartelt, "Capteurs à fibre optique pour matériaux composites et polymères intelligents," in *Méthodes et Techniques Optiques pour l'Industrie, Toulouse, France*. 2010.
- B. Van Hoe, "Phosfos Integration Technology," in *Phosfos Industrial User Club Meeting, part of INDUSTRY MEETS ACADEMIA - SPIE OPTICAL METROLOGY, München, Germany*. 2011.
- B. Van Hoe, "Photonic Skins for Optical Sensing," in *3rd Flexible & Stretchable Electronics Workshop, Berlin, Germany*. 2011.

1.9.5 Proceedings of national conferences

- J. Missinne and B. Van Hoe, "Array waveguide sensor for artificial optical skin," in *UGent-FirW Doctoraatssymposium, 9e*. Universiteit Gent. Faculteit Ingenieurswetenschappen, 2008, pp. 202–203.

- B. Van Hoe and D. Lamon, "Embedded high resolution sensor based on optical feedback in vertical cavity surface emitting laser," in *UGent-FirW Doctoraatssymposium, 10e*. Universiteit Gent. Faculteit Ingenieurswetenschappen, 2009.
- B. Van Hoe, "Embedded fiber sensors with ultra-compact read-out," in *FEA PhD symposium, 12th*. Ghent University. Faculty of Engineering and Architecture, 2011, pp. 100–100. [Online]. Available: http://symposium.fea.ugent.be/sites/symposium.elis.ugent.be/files/phdsymposium/submission932_poster.pdf

1.9.6 Other publications

- B. Van Hoe, "Ontwikkeling van een artificial optical skin", Ugent Master Thesis, 2007. [Online]. Available: http://lib.ugent.be/fulltxt/RUG01/001/312/340/RUG01-001312340_2010_0001_AC.pdf
- B. Van Hoe, K. Van Coillie, G. Van Steenberge, J. Vanfleteren, and P. Van Daele, "Nieuwe benadering voor druksensoren: flexibele artificiële optische huid," KVIV Ingenieursprijzen, 2009.
- J. Missinne, B. Van Hoe, "Artificial skin based on flexible optical tactile sensors," in *SPIE newsroom*, Jan 2010. [Online]. Available: http://spie.org/x38859.xml?ArticleID=x38859
- B. Van Hoe, "Paving the way towards ultra-compact fiber sensing systems," in *Cohesi Sensors of the Future Symposium, Leuven, Belgium*. 2012.

1.9.7 Exhibitions and demonstrations

The technology developed within this dissertation has been demonstrated during following exhibitions:

- E. Bosman, J. Missinne, B. Van Hoe, P. Geerinck, and G. Van Steenberge, "Photonics in Motion - Stretchable optical waveguides", European Photonics Innovation Village 2010, Brussels, Belgium.
  Best Innovation by a Multilateral Project, Organisation or Company Award: 1st Runner-up.
- Phosfos, "Light feels pressure", European Commission Innovation Convention 2011, Brussels, Belgium. http://ec.europa.eu/research/innovation-union/ic2011/index_en.cfm.
- J. Missinne, B. Van Hoe, S. Kalathimekkad, E. Bosman, and G. Van Steenberge, "Flexible Photonics feel it, smell it...bend it!", Cohesi Sensors of the

Future Symposium 2012, Imec Leuven, Belgium. http://www.cohesi.be/.

1.9.8 The following patent has been filed

- G. Van Steenberge, J. Missinne, E. Bosman and B. Van Hoe, "Optical shear sensor and method of producing such an optical shear sensor," *World-wide patent*, WO/2011/128266 A1, 20 October 2011 and *US publication*, US/2013/0036829 A1, 14 February 2013.

References

[1] T. Geernaert, "Microstructured fiber bragg grating sensors: From fiber design to sensor implementation," Ph.D. dissertation, Vrije Universiteit Brussel, 2011.

[2] I-Micronews. (Accessed 2013) "omnivision readies for wafer level camera cube production". [Online]. Available: http://www.i-micronews.com/lectureArticle.asp?id=2723

[3] I. Moellers, D. Jaeger, R. Gaudino, A. Nocivelli, H. Kragl, O. Ziemann, N. Weber, T. Koonen, C. Lezzi, A. Bluschke, and S. Randel, "Plastic optical fiber technology for reliable home networking: Overview and results of the eu project pof-all," *IEEE Communications Magazine*, vol. 47, no. 8, pp. 58–68, Aug. 2009.

[4] H. Ma, A. Jen, and L. Dalton, "Polymer-based optical waveguides: Materials, processing, and devices," *Advanced Materials*, vol. 14, no. 19, pp. 1339–1365, Oct. 2002.

[5] L. Eldada and L. Shacklette, "Advances in polymer integrated optics," *IEEE Journal of Selected Topics in Quantum Electronics*, vol. 6, no. 1, pp. 54–68, 2000.

[6] C. Perera, A. Zaslavsky, P. Christen, and D. Georgakopoulos, "Context aware computing for the internet of things: A survey," *IEEE Communications Surveys & Tutorials, accepted for publication*, pp. 1–41, 2013.

[7] W. Eaton and J. Smith, "Micromachined pressure sensors: Review and recent developments," *Smart Materials & Structures*, vol. 6, no. 5, pp. 530–539, Oct. 1997.

[8] V. Lumelsky, M. Shur, and S. Wagner, "Sensitive skin workshop," *NSF, DARPA Sensitive Skin Workshop Report*, pp. 1–129, Oct. 1999, arlington, Virginia.

[9] V. Lumelsky, M. Shur, and S. Wagner, "Sensitive skin," *Sensors Journal, IEEE*, vol. 1, no. 1, pp. 41–51, June 2001.

[10] T. Someya, "Bionic skin for a cyborg you - flexible electronics allow us to cover robots and humans with stretchy sensors," *IEEE Spectrum*, Aug. 2013.

[11] Probo, a huggable robotic friend. (Accessed 2013) Project website. [Online]. Available: http://probo.vub.ac.be/

[12] E. Bosman, "Integration of optical interconnections and opto-electronic components in flexible substrates," Ph.D. dissertation, Ghent University, 2010.

[13] J. Missinne, "Development of conformable optical and optoelectronic based tactile sensors," Ph.D. dissertation, Ghent University, 2011.

[14] IWT. (Accessed 2012) Flemisch institute for the promotion of innovation by science and technology (iwt). [Online]. Available: http://www.iwt.be/

[15] FAOS Consortium. (2007) Flexible artificial optical skin (faos). [Online]. Available: http://intecweb.intec.ugent.be/faos/

[16] Phosfos Consortium. (2008) Photonic skins for optical sensing. [Online]. Available: http://www.phosfos.eu/

[17] SSC Consortium. (2013) Self sensing composites. [Online]. Available: www.selfsensingcomposites.be/

2
Introduction to optical sensors and integration technologies

In this chapter, several optical sensor concepts and working principles are introduced as well as the necessary driving and read-out techniques to interpret the optical sensing signals. Furthermore, the combination of optical sensors with polymer materials both as sensor material and as host material as well as the associated advantages are discussed. The overview presented in this chapter is by no means intended to be a complete list of the available optical sensors which can be based on or embedded in polymers. The aim is rather to provide the necessary background information before going into the technical details of the sensor concepts investigated in this dissertation.

2.1 Optical sensor principles

As discussed in the previous chapter, traditional - electrical - sensors for measuring physical quantities such as temperature, strain or pressure are mostly based on electrical working principles such as changing resistance or capacitance. The main drawbacks of these sensors are related to the sensitivity, cross-talk, non-compatibility with harsh environments and their size. Optical sensors are based on the interaction between light and the ambient environment, and constitute an interesting alternative providing several advantages. The field of optical sensors can be classified according to different characteristics [1].

A first option is the distinction whether the light is propagating in free-space or guided in a waveguiding structure (for example a fiber). A lot of conventional optical sensing systems are for example based on free-space interferometry and spectroscopy. Guided-wave sensing adds to the intrinsic advantages of optical sensing techniques the possibility of guiding the light beam in a confined and inaccessible medium, thus allowing more versatile and less perturbed measurements [2].

A second possibility is to distinguish to what extent the sensor is distributed. Point sensors can only measure certain measurands at discrete positions whereas distributed sensors provide continuous spatial measurements. A quasi-distributed measurement can be obtained using a combination of several point sensors at different locations which can be read out in parallel.

As a third option, the sensor working principle can be used to distinguish between the different types of optical sensors. The overview presented in the following paragraphs is based on this criterion. A more elaborate overview of the different working principles of (fiber) optic sensors can for example be found in [3].

2.1.1 Intensity based optical sensors

A first type of sensors are devices with a working principle based on the modulation of light intensity. The sensing information is then encoded in a change of the optical power (absolute or relative values) which is reflected or transmitted by the sensing medium to an optical photodetecting unit.

Optoelectronic based shear sensor

A second example of an intensity based optical sensor, consists of two optoelectronic components facing each other in free-space: one laser source and one detector. The working principle is based on the measurement of the light intensity which is coupled from the laser to the detector. This is an application using free-space light propagation consequently not requiring coupling of the light into an optical fiber. When the optoelectronic source and detector are perfectly aligned, the coupled optical power and associated photocurrent in the detector are maximized. Any shift in the alignment of the two components will lead to a decrease in this signal.

This intensity based working principle can be used to fabricate a highly accurate and sophisticated sensor to measure shear force. Within the PhD research of Jeroen Missinne [4], an ultra-small and mechanically flexible prototype was fabricated and characterized. The working principle is shown in Figure 2.1.

A Vertical-Cavity Surface-Emitting Laser (VCSEL) and photodiode chip are embedded in ultra-thin flexible packages. A polymer polydimethylsiloxane (PDMS)

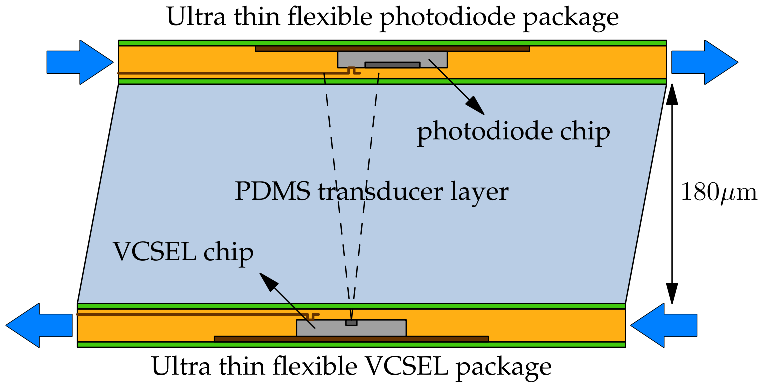

Figure 2.1 – Principle of optical intensity based shear sensor based on changing coupling behavior between a light source and a detector.

transducer layer is applied between the two packages, aligned on top of each other and irreversibly bonded. The PDMS layer is a deformable and compressible layer converting an applied shear force into a lateral displacement and thus changing the VCSEL-photodiode optical coupling efficiency. A layer thickness of 180 µm is a typical value which was used for the experimental characterization, yielding a maximum shear force sensitivity of −350 µA/N or −7 µA/kPa [5]. These responsivity values are varying when changing the thickness of the transducer layer. Tuning the mechanical properties of the transducer layer allows adjusting the sensor to the needs of a specific application in terms of sensing range, accuracy and responsivity. The size, shape and optical properties (modal properties, wavelength etc.) of the optoelectronic components are also important parameters influencing the linearity and usefulness for certain applications, requiring for example multi-directional determination of the applied shear force.

This sensing principle has been proven to exhibit only very limited cross-sensitivity to pressure. A major disadvantage of this sensor is the direct dependence on optical intensity measurements inevitably entailing challenges related to unwanted optical power fluctuations, for example due to optoelectronic aging effects or temperature variations. A possible solution is the use of reference components enabling relative measurements [6].

Distributed optical fiber sensor

The first example is based on light propagation in an optical fiber. An optical fiber can act simultaneously as optical channel and distributed transducer enabling distributed measurements along the fiber axis. The fiber can then play the role of a "nerve" for materials and structures in which the fiber is embedded [7]. The sensing mechanism is in this case inherent to the fiber and based on light scattering (Rayleigh, Raman and Brillouin scattering). One of the most popular intrinsic distributed fiber optic sensors is optical time-domain reflectometry based on Rayleigh scattering. A simple example of this sensing principle is schematically shown in Figure 2.2.

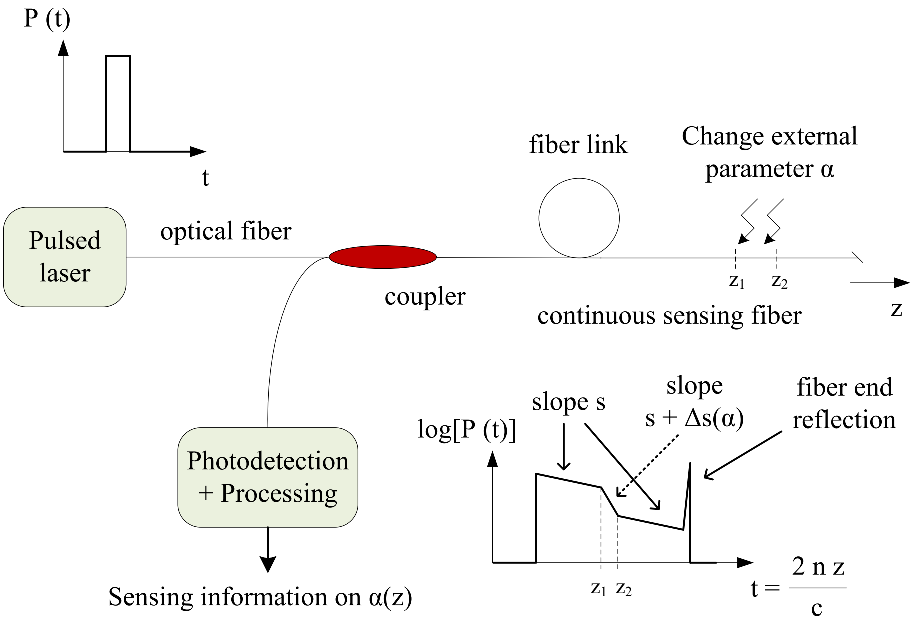

Figure 2.2 – Principle of optical time-domain reflectometry based on Rayleigh scattering.

P (t) is the optical power, z is the axis along the fiber, n is the refractive index of the fiber and c is the speed of light. When light is launched into an optical fiber, losses occur due to Rayleigh scattering that arises as a result of random, microscopic (less than the wavelength of propagated light) variations in the index of refraction of the fiber core. A fraction of the light scattered in a counterpropagation direction (180° relative to the incident direction) is recaptured by the fiber aperture and returned towards the source [8]. A narrow optical signal emitted by a pulsed laser is launched into the optical fiber (Figure 2.2) and a photodetector is capturing the reflected light. This photodetector signal is further processed to extract the sensing information. In a specific area along the optical sensing fiber (between z_1 and z_2), an external parameter α is perturbed and the local scattering coefficient is consequently changed. This spatial change can be quantified by analyzing the optical pulse which is reflected by the fiber. More specifically the slope of the logarithmic optical power versus time is an indication for the reflection coefficient as a function of distance along the fiber. Comparing the reflected optical intensity with the pulsed laser signal reflects the local fiber status and enables localization and quantification of the external perturbation. Since this sensing technique is based on detecting the back-scattered optical signal of the light pulse as a function of time, this technique is called Optical Time-Domain Reflectometry (OTDR).

An elaborate overview of the different opportunities to use optical fibers as distributed sensors including recent trends and developments can be found in [9].

2.1.2 Interferometry based optical sensors

A second type of optical sensors is based on interferometric working principles. In this paragraph interferometry in laser components, allowing for measurements not depending on light intensity, is discussed.

Laser interferometry is a well-known and widespread technique to measure displacement, velocity, vibration and distance. This technique is based on an external interferometer, an optical transducer consisting of lenses, prisms and mirrors which is typically read out by a laser. Popular applications of these techniques are the Michelson [10] and Mach-Zehnder [11] interferometers. Later, a new technique appeared, in which a fraction of the light back-reflected or back-scattered by a remote target is allowed to re-enter the laser cavity. The reflected light interferes with the light generated inside the laser, generating a modulation of both the amplitude and the frequency of the lasing field. This approach is a special case of laser interferometry, equivalently called *self-mixing*, *feedback* or *induced-modulation* interferometry, and is related to the spatial coherence length of the laser [12]. The laser source acts as a sensitive detector for the path length $2\,k\,L_{\mathrm{ext}}$ (where k is the wavenumber, and L_{ext} is the target reflector distance) traveled by the light to the target and back, exploiting so-called injection-detection [13]. The laser is in this case at the same time the optical source and the optical detector.

The first demonstrations of this principle used gas lasers to detect the Doppler shift caused by a moving remote reflector [14]. Turning point experiments were those reporting the first complete self-mixing interferometer/vibrometer [15] and the use of a Laser Diode (LD) as a source/detector [16]. Remote sensing applications based on the self-mixing effect in low-cost commercial Fabry-Pérot (FP) LDs have appeared in the scientific literature since 1986 [16, 17], demonstrating the feasibility of velocity, distance and displacement measurements [16]-[18].

According to Bosch et al. [13], some important advantages of the self-mixing sensing scheme are:

- No optical interferometer external to the source is needed, resulting in a very simple, part-count-saving and compact set-up.
- No external photodetector is required, because the signal is provided by the monitor photodiode contained in the LD package.

- The sensitivity of the scheme is very high, being a sort of coherent detection that easily attains the quantum detection regime (i.e. sub-nm sensitivity in path length is possible)
- Successful operation on rough diffusive surfaces can be achieved
- Information is carried by the laser beam and it can be picked up everywhere (also at the remote target location).

A complete analysis of laser diodes with optical feedback can be performed by using the equations first derived by Lang and Kobayashi [19].

A typical optoelectronic source which is used for optical feedback measurements is a VCSEL. **Within this dissertation an incremental pressure sensor is built based on this working principle. Starting from polymer embedded VCSEL components, polymer sensing layers are added to extend the laser cavity by introducing a compressible external cavity build-up.** A thin metal layer (the external target) on top of this external cavity is reflecting a fraction of the emitted laser light back into the laser cavity. Critical parameters in order to observe self-mixing interferometry useful for sensing measurements are a minimum threshold optical power which has to be coupled back into the laser diode cavity and an optical feedback parameter within the correct range. **A detailed discussion on this integrated VCSEL pressure sensor is provided in Chapter 7.**

2.1.3 Bragg reflection based optical sensors

A third type of optical sensors relies on wavelength selective mirrors yielding wavelength encoded sensor signals. The sensing information has to be extracted from a change in the optical wavelength reflected by this mirror, requiring spectral analysis and read-out units. The most commonly used type of optical sensor based on wavelength encoded information is a fiber sensor based on Fiber Bragg Gratings (FBGs). Optical fiber sensors are *intrinsic* sensor devices, referring to the unique feature that the optical fiber is simultaneously sensing element and communication channel. Therefore, there is no need to consider a specific telemetry system that is always required in other sensing technologies. Probably more important, this dual characteristic of the optical fiber opens the natural consideration of fiber optic sensing networks for multi-point or quasi-distributed measurement [20].

Within the following sections, the basic principles as well as the most common fabrication technologies of wavelength selective mirrors - based on Bragg reflection - in optical fibers are discussed.

Bragg grating working principle

The working principle of these mirrors is based on a modulation of the local effective refractive index of the optical fiber causing Bragg diffraction. A fiber Bragg grating sensor takes the form of a permanent *periodic spatial* modulation of the refractive index *along the core of an optical fiber*, commonly induced using ultra violet light. The reflecting Bragg wavelength is consequently related to the effective refractive index of the fiber core n_{eff} and the period of the grating structure Λ_{FBG} through following Bragg grating condition formula:

$$m\,\lambda_{\text{B}} = 2\,n_{\text{eff}}\,\Lambda_{\text{FBG}}$$

A simple visualization of a fiber Bragg grating is shown in Figure 2.3. A broadband source is used to couple light into an optical fiber. At the level of the Bragg grating, part of the light is reflected. The Bragg wavelength can be read out in reflection or transmission, respectively looking for a maximum or minimum in the optical spectrum.

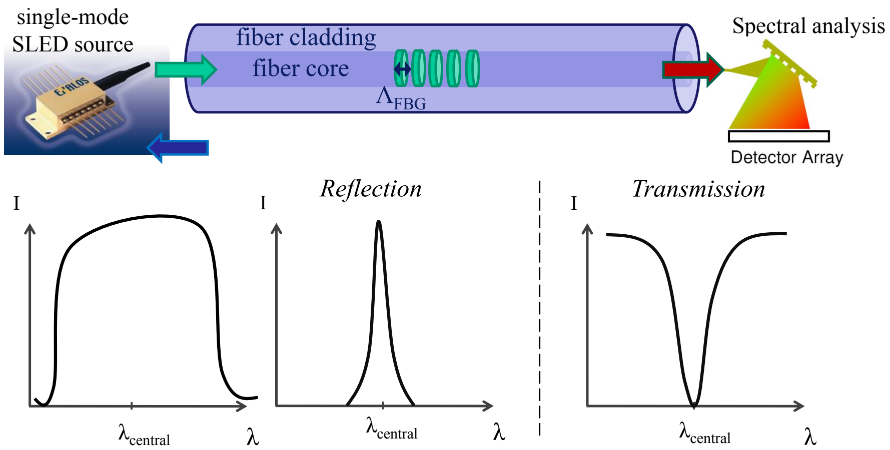

Figure 2.3 – Fiber Bragg grating working principle.

Under the influence of temperature or strain, both the period of the modulation and the mean index of the core mode change, leading to a shift in the reflected wavelength by this diffractive structure. The strain response arises due to both the physical elongation of the sensor (and corresponding fractional change in grating pitch), and the change in fiber index due to photoelastic effects, whereas the thermal response arises due to the inherent thermal expansion of the fiber material and the temperature dependence of the refractive index (thermo-optic effect). The shift in Bragg wavelength with strain and temperature can be expressed using [21]:

$$\Delta\lambda_B = 2\, n_{\text{eff}}\, \Delta \left(\left\{ 1 - \frac{n_{\text{eff}}}{2} [P_{12} - \nu(P_{11} + P_{12})] \right\} \epsilon + \left[\alpha + \frac{dn_{\text{eff}}/dT}{n_{\text{eff}}} \right] \Delta T \right)$$

where ϵ is the applied strain, P_{ij} are the coefficients of the stress-optic tensor, ν is Poisson's ratio, α is the Coefficient of Thermal Expansion (CTE) of the fiber material (e.g. silica), and ΔT is the temperature change. From the above expression the inherent cross-sensitivity to changes in temperature and strain can be calculated. This is an important challenge when using optical fiber sensors and can be tackled in various ways, for example using custom designed microstructured fibers (reduce temperature sensitivity) or polymer fiber sensors ($\alpha + \frac{dn_{\text{eff}}/dT}{n_{\text{eff}}} < 0$). These opportunities will be discussed further in the following paragraphs (Section 2.1.3, *Bragg gratings in specialty optical fibers* and Section 2.3.1).

Over the last 20 years of intensive development, silica fiber Bragg grating technology has grown increasingly mature and is now commercially exploited in a range of high-end applications such as oil and gas exploration [1]. However, back in 1997 it was already clear that the interrogation of fiber sensors based on Bragg gratings without costly and bulky laboratory equipment would be a serious challenge:

A wavelength resolution of ≈ 1 pm (0.001 nm) is required (at $\lambda_B \approx 1.3$ µm) to resolve a temperature change of ≈ 0.1°C, or a strain change of 1 µstrain. Although this wavelength resolution is attainable using laboratory instrumentation such as spectrum analyzers and tunable lasers, the ability to resolve changes on this order using small, packaged electro-optics units is a challenge, and this has been the focus of a considerable amount of research work in the grating sensor field. [21]

Within the 2008 Nature Photonics technology focus edition, Brian Culshaw pointed out another important issue impeding a full breakthrough of optical fiber sensors:

"Two other important aspects of fibre-sensor development, which many technologists under-rate, are packaging and interface. It is important to collaborate with the people who will be using their products to find out how the product should be packaged and how the interface can be designed to make it user-friendly. If the developers get this right, customers will be more likely to buy the technology." Brian Culshaw in [22].

The optical fiber sensors offer a unique set of advantages in terms of working principle, sensitivity and multiplexibility but are for many applications too innovative to be considered as an alternative. The problem is largely a lack of awareness of the technology, a shortage of regulations to establish what measurements they should be used for and ultimately a question of cost [22].

This dissertation will deliver several technology blocks to tackle these challenges related to the use of optical fiber sensors, both in terms of packaging, as well as cost and user-friendliness.

Bragg grating fabrication technologies

A short overview of the different techniques available for the fabrication of fiber Bragg gratings is presented. A more elaborate overview can be found in [23, 24].

In general the fabrication of a fiber Bragg grating is based on the photosensitivity of the fiber material (typically doped silica). Using an ultra violet source (wavelength λ_{UV}) this photosensitivity can be exploited to introduce a permanent refractive index change in the fiber core material. A Bragg grating is then created through a controlled interference pattern based on this UV source over a certain fiber length using sufficient optical power density. This is illustrated in Figure 2.4.

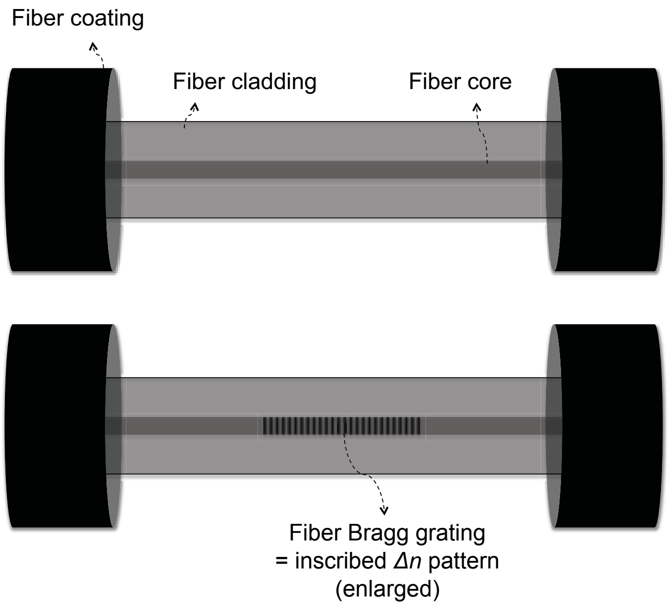

Figure 2.4 – *(top)* Optical fiber with locally stripped fiber coating (before Bragg grating inscription). *(bottom)* Resulting refractive index modulation of the fiber core (after inscription of a Bragg grating, for example using an interference pattern of a UV source). Schematic diagrams adopted from Thomas Geernaert [24].

There are different techniques available to produce fiber Bragg gratings. They can be roughly divided into three categories:

- Interferometric set-up: interfering beams of a highly coherent laser, illustrated in Figure 2.5a.
- Phase mask: interference based on diffraction, illustrated in Figure 2.5b.

- Point-by-point: direct writing using a fs pulsed laser, illustrated in Figure 2.5c.

The first Bragg gratings were fabricated using the interferometric set-up technique [25, 26]. By adjusting the rotation angle ϕ of the mirrors (Figure 2.5a), the Bragg wavelength can be tuned. Because of the beam splitting, different optical components with high alignment accuracies are needed. Phase masks offered a straightforward alternative avoiding beam splitting components by using the interference pattern that is formed between the +1 and -1 diffraction orders directly behind the phase mask [27]. The fiber is then positioned right after the phase mask (Figure 2.5b) offering a high mechanical stability. A major drawback is the necessity of a phase mask with a different period Λ_{pm} for all Bragg wavelengths. A more recent technique is direct writing of the FBG by point-to-point inscription using a pulsed laser (repetition rate f_{rep}) and a fiber mounted on a translation stage (translation speed v_{trans}). This process is illustrated in Figure 2.5c and was first reported using a femtosecond laser in [28]. An overview of the different FBG fabrication techniques as well as the associated Bragg wavelength, advantages and discomforts is presented in Table 2.1.

Table 2.1 – Overview of the different FBG fabrication techniques and associated advantages and discomforts.

Technique	λ_B	+	-
2-beam interferometry	$\frac{n_{eff}\ \lambda_{UV}}{\sin(\phi)}$	- tuning of Bragg wavelength	- need for high stability - requires highly coherent laser - bulky set-up
phase mask	$n_{eff}\ \Lambda_{pm}$	- compatibility with lasers with low temporal coherence - limited amount optical components	- fixed Bragg wavelength
point-by-point	$2\ n_{eff}\ \frac{v_{trans}}{f_{rep}}$	- tuning of Bragg wavelength - grating dimensions not limited to interference pattern	- need for fs laser - sequential writing process

The combination of different techniques is also used, for example combining a phase mask with 2-beam interferometry [23].

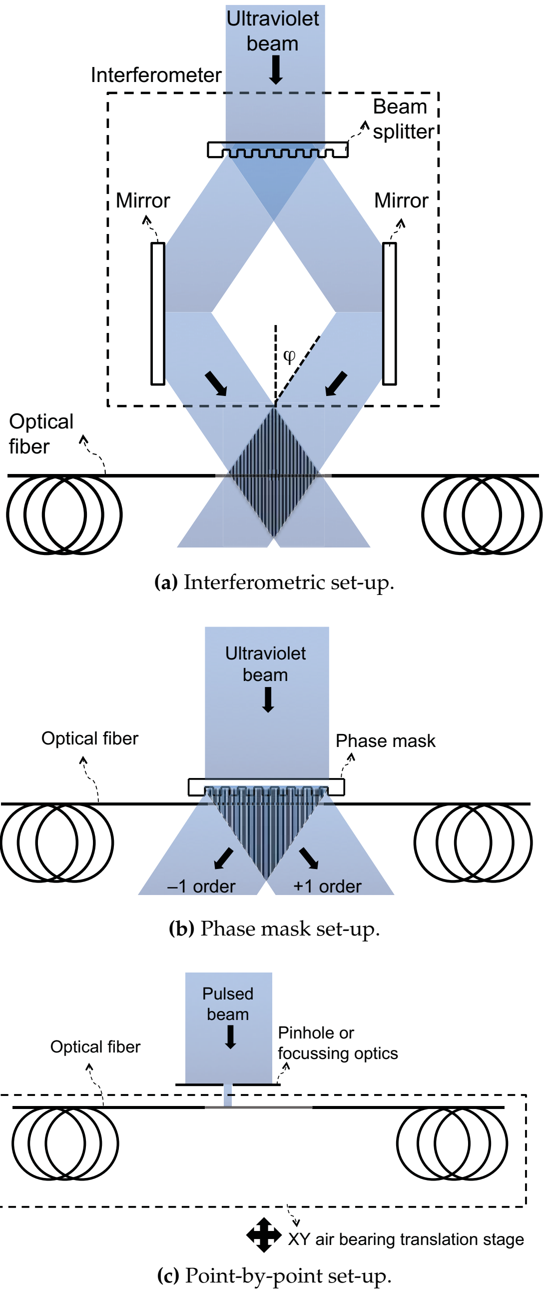

(a) Interferometric set-up.

(b) Phase mask set-up.

(c) Point-by-point set-up.

Figure 2.5 – Different techniques for FBG fabrication. Schematic diagrams adopted from Thomas Geernaert [24].

Bragg gratings in specialty optical fibers

Using fiber Bragg gratings in traditional silica fibers as sensors, some important measurement constraints are faced. One of these limitations is the cross-sensitivity for different ambient parameters such as temperature and pressure. Within this dissertation, a special type of fiber sensors is used based on highly birefringent microstructured silica fibers.

Microstructured Silica Fibers (MSFs) or photonic crystal fibers were developed as a "next-generation" optical fiber alternative. Though the traditional single-mode step-index fibers are ideally suited for telecom applications, there was a growing need for fibers that could be used for sensing, had multiple cores, had higher non-linearities or had higher birefringence [29]. The cross-section of these microstructured fibers consist of an (often periodic) arrangement of a low-index material, the microstructure, in a background (or matrix material with a higher refractive index. In most cases, the high index material is undoped silica and the microstructure consists of air holes with diameters on the order of a few µm that run along the entire length of the MSF over several kilometers. The strength of MSF technology lies in its particular design flexibility: one can adjust the shape, the dimensions and the arrangement of the microstructure and choose appropriate materials for every specific optical fiber application [24].

Standard single-mode fibers are ideally perfectly symmetric. In reality however, there is always a certain degree of ellipticity causing polarization dispersion. This effect is limiting the data rates transmitted over the optical fiber. Modal polarization dispersion can be visualized by considering the fundamental mode in a fiber consisting of two orthogonally polarized mode components. Both modal components have a different phase velocity, linked with their respective effective refractive index n_{eff}:

$$v = \frac{c}{n_{\text{eff}}}$$

with c the speed of light in vacuum. By adding a degree of asymmetry, either in the core shape or the surrounding cladding material, this effect can be used to create highly birefringent fibers. The two orthogonally polarized axes are referred to as slow and fast axis, in accordance with the naming of the polarization modes originating from their different phase velocity. The phase modal birefringence B is defined as the difference in effective refractive indices:

$$B = n_{\text{eff,slow}} - n_{\text{eff,fast}}$$

When inscribing Bragg gratings in these highly birefringent birefringent fibers, a single grating is reflecting two different wavelengths:

$$\begin{aligned}\lambda_{\mathrm{B,slow}} &= 2\, n_{\mathrm{eff,slow}}\, \Lambda_{\mathrm{FBG}}\\ \lambda_{\mathrm{B,fast}} &= 2\, n_{\mathrm{eff,fast}}\, \Lambda_{\mathrm{FBG}}\end{aligned}$$

Consequently, an additional sensing parameter based on the wavelength separation is created:

$$\Delta\lambda = \lambda_{\mathrm{B,slow}} - \lambda_{\mathrm{B,fast}} = 2\, B\, \Lambda_{\mathrm{FBG}}$$

Within the Phosfos project [30], technology was available to inscribe fiber Bragg gratings in highly birefringent microstructured optical fibers. The design of the MSFs was optimized to limit the sensitivity of temperature and axial strain on the this new sensor signal (the wavelength separation). Ideally, the Bragg wavelength separation is not depending on the ambient temperature or changing axial strain but only on (hydrostatic) pressure or transverse strain (Figure 2.6). The transverse strain and hydrostatic pressure sensitivities were significantly enhanced within Phosfos. **Within Chapter 3, Section 3.2, this sensor concept is further elaborated and cross-sections are shown of the considered MSFs. Embedding optical fiber sensors, including microstructured silica fiber sensors, is also discussed in detail in Chapter 3.**

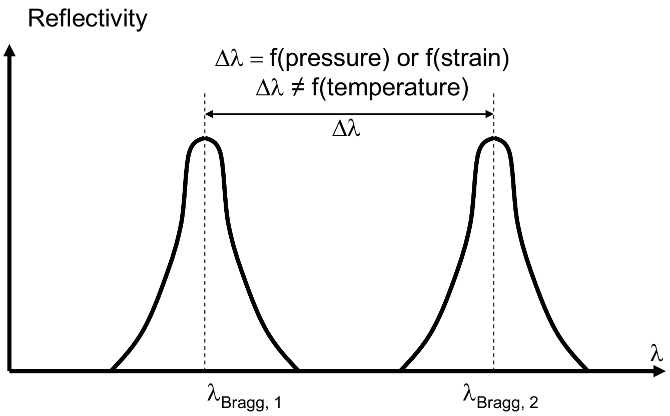

Figure 2.6 – Illustration of the sensing principle using fiber Bragg gratings in highly birefringent microstructured silica optical fibers. The measurand is encoded in the spacing between the two Bragg peaks corresponding to the two orthogonally polarized modes propagating in the fiber.

A major part of this PhD is related to the integration of optoelectronic components with optical fiber sensor elements using a modular approach, starting from separate fiber and optoelectronic building blocks. A next step towards a fully integrated system could be the integration of active optoelectronic components in the fiber structure. Similar as to the (passive) microstructure, an active metal-semiconductor heterostructure is integrated in the fiber preform. First experimental results were reported by Orf et al. [31]. A functional photodiode structure was successfully designed, fabricated and experimentally tested (Figure 2.7).

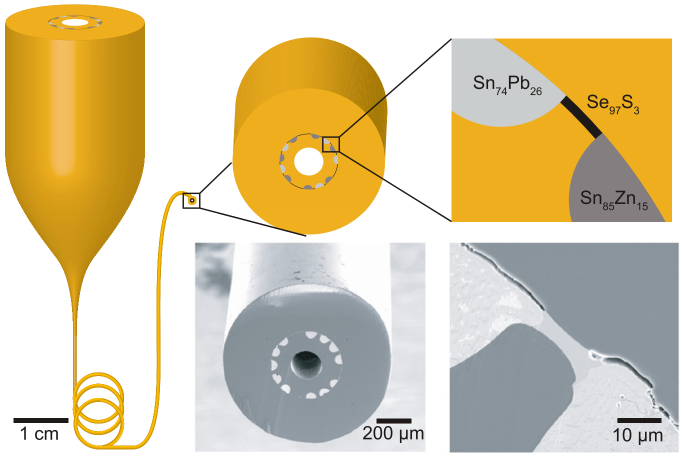

Figure 2.7 – Schematic drawings of structured preform drawn into fiber along with SEM micrographs of actual fiber and magnification of a single metal-semiconductor-metal device. Courtesy of N. D. Orf [31].

2.2 Optical sensor interrogation

An external perturbation will change the characteristics of the light guided within the optical sensor. The quality of the measurement (accuracy, resolution, speed, span, etc.) is largely determined by the interrogation mechanism. Especially optical sensors which have a working principle which is not based on light intensity require dedicated read-out solutions to extract as much sensing information as possible. In the following paragraph, an overview is given on how to interrogate the optical fiber sensors discussed in Section 2.1.3.

2.2.1 FBG sensor interrogation

Within the field of fiber sensors based on Bragg gratings, the sensing information is encoded in the shift or transformation of the FBG reflection/transmission filter characteristic (resonance wavelength, spectral width, reflectivity). There are several types of fiber Bragg gratings with specific transfer functions, but the standard structure has a reflectivity function with an approximately Gaussian shape centered at the resonance wavelength of the device and a spectral width around 0.2 nm [20]. Interrogating fiber Bragg grating sensors implies the conversion of the changes in the Bragg wavelength to an electrical signal with adequate characteristics to obtain the information about the measurand α. A general schematic view of a fiber sensor interrogation scheme is shown in Figure 2.8 (reflection measurement) and Figure 2.9 (transmission measurement).

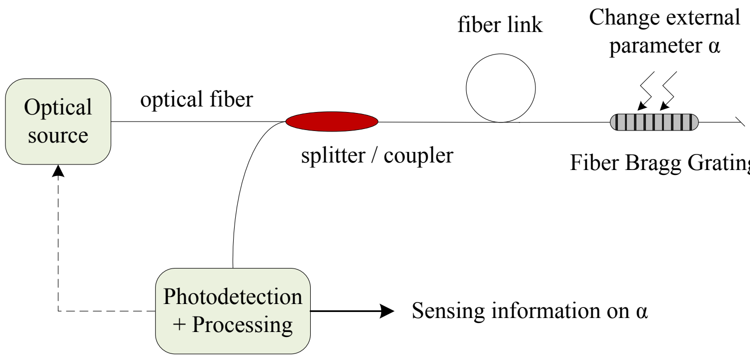

Figure 2.8 – General interrogation scheme for fiber Bragg grating sensors (reflection measurement).

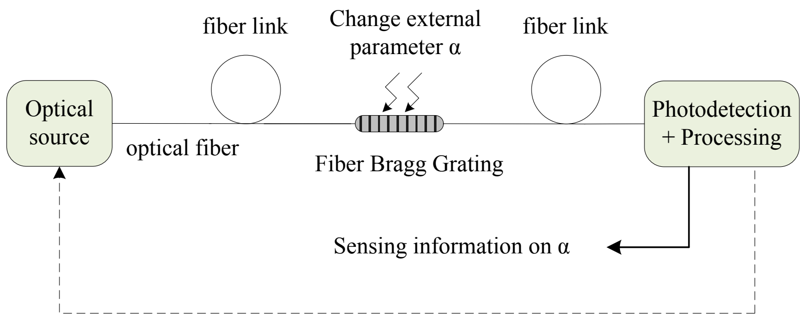

Figure 2.9 – General interrogation scheme for fiber Bragg grating sensors (transmission measurement).

An optical source couples light into an optical fiber and depending on the remoteness of the fiber sensor, an optical fiber link ranging from a few centimeters up to hundreds of kilometers is transporting the light from the optical source to the sensor point and from the sensor point to the optical detector. Depending on the interrogation technique and the associated optoelectronic source and detector, a feedback mechanism can provide the sensing information, acquired after photodetection and signal processing, back to the optical source to adjust or fine-tune the driving parameters.

Santos et al. [20] provided a clear classification of the different FBG interrogation techniques that have been proposed along the years. This overview is shown in Table 2.2. The operating and underlying physical principles are diverse, each providing specific advantages and shortcomings. Next to a reproducible transduction of the Bragg wavelength, also sensitivity, accuracy, measurement range and associated multiplexing possibilities, measurand acquisition speed, immunity to optical power fluctuations, ability to perform absolute measurements, reliability and cost are important performance indicators for the considered measuring systems. There is typically a trade-off between the wavelength measurement range (and associated multiplexing possibilities) and the measurement speed. Furthermore, a fundamental distinction should be made between interrogation systems which enable full spectral reconstruction datasets versus Bragg wavelength peak tracking systems. Peak tracking systems only provide information on the shift of the Bragg peak wavelength, excluding other effects such as peak broadening or peak splitting. Those systems on the other hand typically offer cheaper and faster spectral measurements. A trade-off between measurement speed and measurement detail consequently has to be considered.

The interrogation principles which are relevant for the remainder of this dissertation are discussed in more detail.

Bulk optics

The combination of a broadband source (LED, SLED, ASE, supercontinuum) with an optical spectrum analyzer or Charge Coupled Device (CCD) (Figure 2.10) is the most commonly used interrogation scheme within laboratory environments and research institutes. It offers full spectral reconstruction combined with a high sensitivity and a large number of sensors which can be read out simultaneously. However, high-density diffraction gratings and high precision rotation stages are needed, increasing the size and the cost of the system. An example (schematic view) of a commercially available Ocean Optics spectrometer is shown in Figure 2.11. The different building blocks of the system are listed below the figure. Note that this is already called a “miniature” spectral read-out system. Traditional Optical Spectrum Analyzer (OSA) systems are typically much more bulky.

Table 2.2 – Overview of interrogation techniques for FBG based sensors, based on [20].

Group	Principle	Configuration	References
Bulk Optics	Diffraction	Monochromator	
		Optical Spectrum Analyzer	[32, 33]
		Diffraction Grating + CCD	
		Volume Hologram + CCD	
Passive Edge Filtering	Bulk Filter	Transmissive	
	Integrated Optic Filter	Arrayed Waveguide Grating	
	Optical Fiber Filters	Biconical Filter	
		Long-Period Grating	[34, 35, 36]
		Fused Coupler	
		Chirped Bragg grating	[37, 38]
		Sagnac Loop	
	Sources/Detectors	Source Spectrum	[39, 40]
		Detector Spectral Responsivity	[41]
Active Bandpass Filtering	Bulk Optical Filters	Fabry-Pérot	[42, 43, 44, 45, 46]
		Acousto-Optic	
		Hybrid Optical MEMS	
	Optical Fiber Filters	Receiving Bragg Grating	
		WDM Coupler	
		Dynamic Long-Period Grating	
	Optical Sources	Single-mode Laser Diode	[47, 48, 49, 50, 51, 52]
		Multimode Laser Diode	[53]
	Carrier generation	Receiving Bragg Grating	
		Multimode Laser Diode	
Interferometric	Passive	Chirped Grating + Sagnac Loop	
	Homodyne	Mach-Zehnder	
	Carrier Generation	Mach-Zehnder	
	Fourier Domain	Variable OPD Scan	
	Optical Coherence Function		
Laser Sensing	FBG Laser Cavity	FBG as Cavity Mirror	
Miscellaneous	Angular Dispersion	Receiving Blazed FBG + CCD	
	OTDR		
	Wavelet Processing		

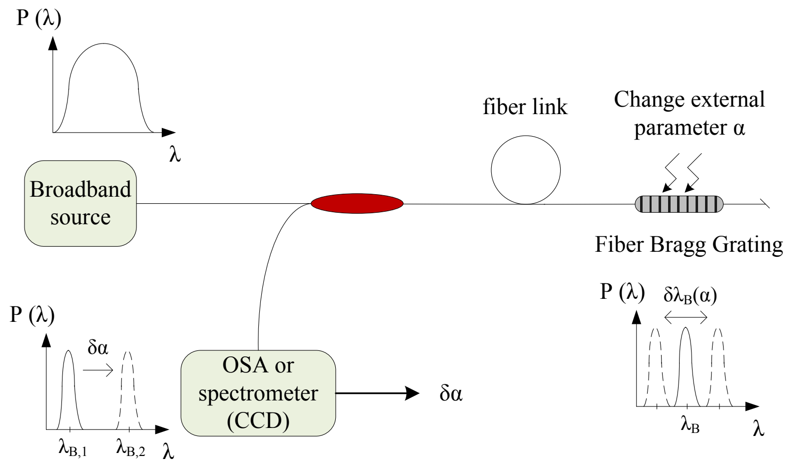

Figure 2.10 – Traditional interrogation scheme for fiber Bragg grating sensors based on a broadband source and a spectral demodulation unit (OSA or spectrometer).

Passive edge filtering

Passive edge filtering is an alternative for the expensive and large diffraction based spectrum analyzers. The basic concept is shown in Figure 2.12 and relies on an optical power measurement, captured by Photodetector 1 (V_α). This reflected light intensity is first modulated by the relative shift of the sensing Bragg grating to the filter characteristic of an optical edge filter which is applied before Photodetector 1. The wavelength information extraction is consequently based on a light intensity measurement rather than spectral demodulation. Varying losses in fibers, fiber connectors, optical source induced by temperature changes, fiber manipulation or aging phenomena are causing intensity fluctuations and are interfering with the sensing signal. Therefore, the optical sensing signal is typically bypassed to a second detector (Photodetector 2, V_{ref}) serving as a reference output to calculate the relative grating response V_α/V_{ref}. The optical edge filter can consist of a special fiber Bragg grating with a broader reflection spectrum and smoother transition edge, i.e. long-period gratings [34, 35, 36] or chirped Bragg gratings [37, 38]. Another possibility is a filter characteristic inherent to the source spectrum [39, 40] or the detector responsivity [41]. The main advantage of this passive edge filtering approach is the simplicity and low-cost whereas the main limitations are the limited possibility to read out multiplexed fiber sensors and the nullification of the main advantage of fiber Bragg gratings by converting spectrally encoded information to simple intensity measurements.

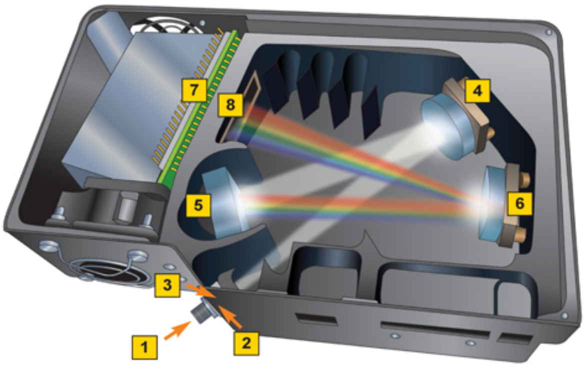

	Explanation
1	Input fiber connector
2	Entrance aperture slit
3	Long-pass absorbing filter to block second- and third-order effects or to balance color.
4	Collimating mirror matching the Numerical Aperture (NA) of the optical fiber and reflecting the light towards the grating.
5	Grating demodulating the light. The rotation of the grating determines λ_{start} and λ_{end}.
6	Focusing mirror focusing first-order spectra on the detector plane.
7	2D detector typically with thermoelectric cooling and varying integration times.
8	Filter blocking second- and third-order light from reaching the detector elements.

Figure 2.11 – Schematic view on the Ocean Optics miniature spectrometer QE65 Pro, courtesy of Ocean Optics [54].

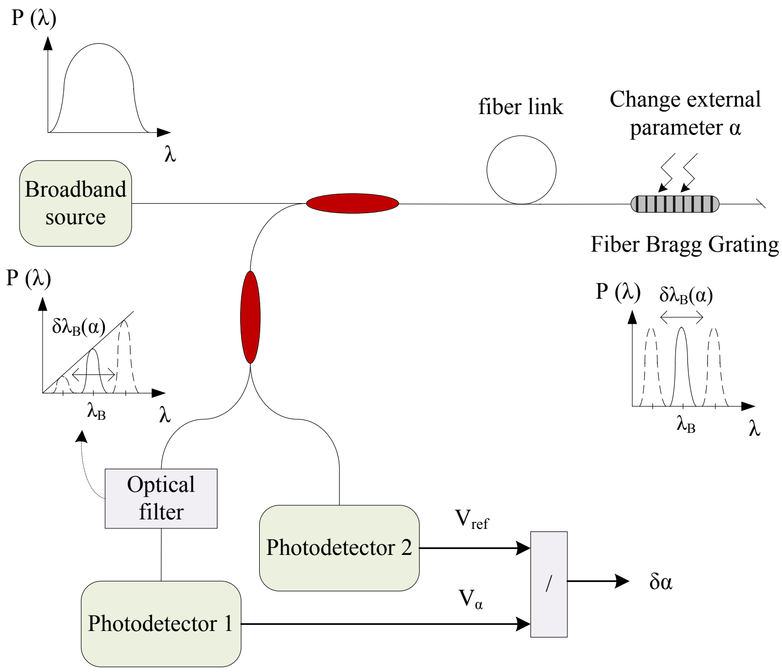

Figure 2.12 – FBG interrogation based on edge filtering based on a linearly wavelength-dependent optical filter.

Active bandpass filtering

Interrogating fiber Bragg gratings using active bandpass filtering is an important alternative for the traditional bulk optics or passive edge filtering based interrogation schemes. An example based on an Fiber Fabry-Pérot (FFP) filter is shown in Figure 2.13. The Fabry-Pérot filter consists of two partially reflecting surfaces with a spatial separation. The transmittance of light through this cavity has a periodic character (as a function of λ) due to the multiple reflections inside the cavity and interference of the multiply reflected light beams. Typically, the Fabry-Pérot filter bandwidth is comparable to the grating bandwidth (e.g. $\approx 0.3\,\text{nm}$) and the free spectral range between two transmitted wavelength windows (e.g. $\approx 50\,\text{nm}$) is larger than the operating range of the grating to avoid measurement ambiguity. The closed-loop arrangement (feedback of sensing information on FFP driving voltage) locks the Fabry-Pérot passband to the grating reflection signal [8].

Although this tracking method is applicable to the interrogation of a single grating sensor, multiple grating sensor signals can also be interrogated using the FFP by scanning the resonance wavelength. If the grating Bragg wavelengths

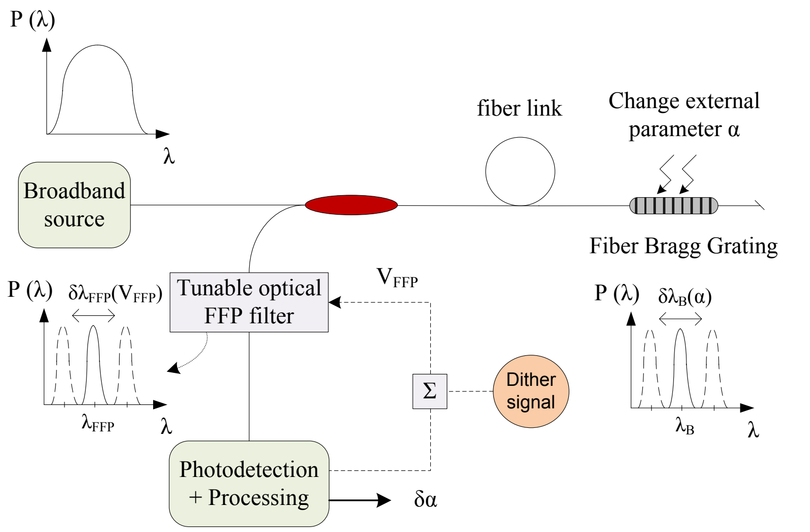

Figure 2.13 – Active bandpass filtering using a tunable Fiber Fabry-Pérot (FFP) filter. A dither signal is used to lock the filter to the grating and to circumvent the influence of optical power fluctuations.

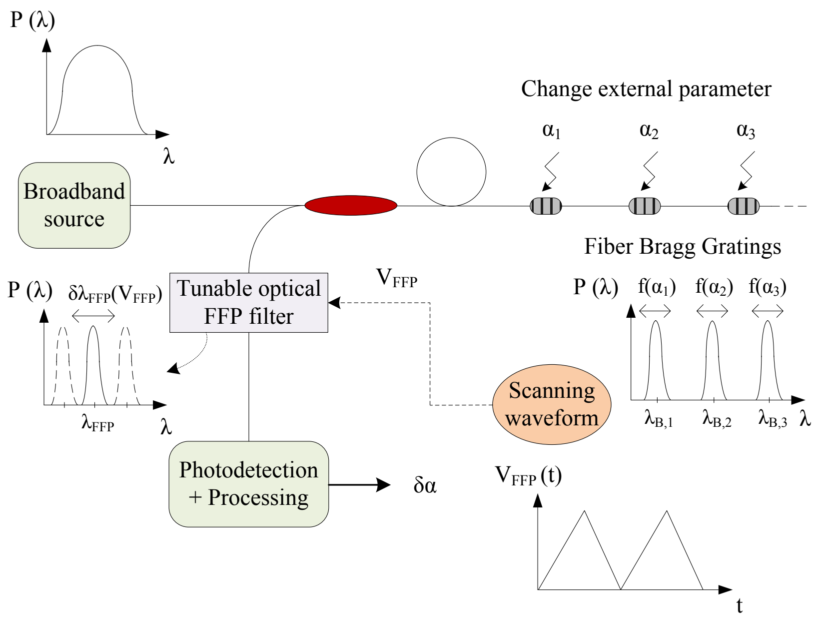

Figure 2.14 – Active bandpass filtering using a tunable Fiber Fabry-Pérot (FFP) filter. Periodically changing the tunable optical filter steering voltage enables parallel read-out of multiple sensing points.

and their ranges of change due to measurands do not overlap and yet fall within the spectral bandwidth of the light source and the free spectral range of the FFP, a number of gratings along the same optical fiber can be interrogated. Figure 2.14 shows a typical interrogation scheme using a open-loop triangle signal function.

Bandpass filtering interrogation of fiber Bragg gratings was also demonstrated when the filtering action was performed by the optical source, typically a semiconductor laser diode, either single-mode or multimode. The information about the Bragg wavelength is recovered from the level of optical power reflected by the sensor, which depends on the relative spectral position between the grating and the laser mode [20]. It is interesting to note that these laser diode based schemes, which exploit the lateral spectral filtering characteristics of the optical source/detector, can be considered to be the minimal configuration for fiber Bragg grating interrogation. A schematic view of this interrogation scheme is depicted in Figure 2.15. Alternatively, a broadband source can be actively filtered using MEMS technology. The scanning waveform (Figure 2.15) is in this case sent to the MEMS device, converting the broadband light into a smallband source [55]. It is also possible to apply the filtering function of the photodetector, moving the filter from the source to the detector side [56].

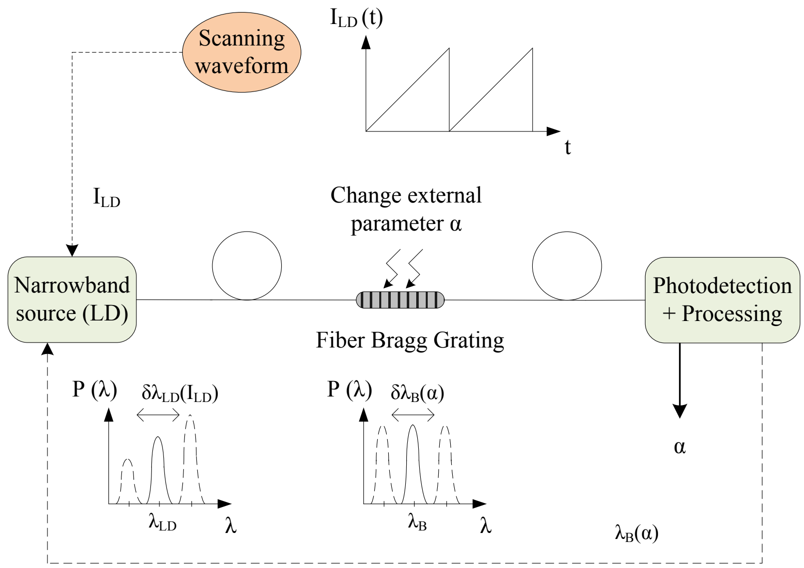

Figure 2.15 – Active bandpass filtering through optical source modulation.

2.2.2 Miniaturized FBG sensor interrogation

To tackle the optical fiber sensor challenges related to the system size, different miniaturized optical fiber sensor interrogation units have been developed by several research groups. One possibility is to introduce MEMS technology to the optoelectronic sources or detectors, reported by Peters et al. as mentioned in the previous section.

An integrated approach based on planar lightwave circuits with diffractive gratings is presented in [57]. The read-out of fiber Bragg grating sensors is based on wavelength demultiplexing the reflected light and combining the information from different photodetectors. Using this technology, the resulting spectral read-out unit can be fabricated to be of low weight providing excellent compatibility with, for example, aerospace applications. This interrogation scheme is however based on the use of a broadband light source to generate the input light.

Using a reference fiber Bragg grating or a special type of fiber interferometer is an alternative technique providing "compact all-fiber" interrogation solutions for FBG sensors. An example based on a photonic crystal fiber interferometer can be found in [58]. However, again a broadband source has to be included and the sensor read-out measurement is converted into a measurement of light intensity.

An alternative miniaturized fiber sensor interrogation approach is developed within this dissertation based on a single-mode optical source and a photodetector. Tuning the optical source is performed through electrothermal wavelength red shifting. Chapter 6 includes a detailed description of this miniaturized FBG interrogation unit which can be fabricated ultra-small including both driving and read-out optoelectronic units.

2.3 Polymer optical sensors

The optical sensors which were discussed in the first part of this chapter are based on semiconductor components combined with free-space propagating light or fiber sensors based on silica optical fibers. Silica fibers are mostly used as fiber optical fiber sensors because of the low optical losses and the compatibility with telecom equipment. Over the last 20 years of intensive development silica fiber Bragg grating technology has grown increasingly mature and is now commercially exploited in a range of applications such as oil and gas exploration [1]. We will see however that for certain applications polymers offer interesting alternative advantages.

2.3.1 Polymer fiber sensors

Polymer fibers have many advantages in common with the traditional silica fibers for sensing applications. These include immunity to electromagnetic interference, low weight and multiplexing possibilities [59]. They also possess some important additional advantages over their traditional silica counterparts such as a lower cost (in general) and improved safety (for biomedical applications). The initial drivers for the development of these polymer optical fibers were consequently the need for a low-cost, easy to use and install optical fiber alternative for short-range optical interconnects, for example in local area networks or automotive applications. In contrast to the low optical losses and the technical complexity to make reliable, low-loss silica fiber connections, the polymer fibers typically offer a large-core (0.1 to 1 mm diameter) higher loss alternative which is easy to install.

From a sensing point of view, polymers offer other, more important, advantages mainly related to their intrinsic material properties. These advantages are due to their mechanical strength (high elastic strain limits, high fracture toughness, high flexibility) and their sensitivity (high strain sensitivity and negative thermo-optic coefficient). Because the multimode large-core character of the polymer fibers, the measurement accuracy and resolution was generally rather low. Recently, single-mode polymer optical fibers are becoming available on a research scale enabling increased measurement reliability and a more precise read-out. The high optical losses, especially in the traditional telecom wavelength windows, remains a challenge in many applications (see Figure 2.16 for attenuation losses of typical polymers used for POF).

Polymer Optical Fiber Bragg Gratings (POFBG) sensors date back only a little over 10 years [61] and represent therefore a much less mature technology compared to the silica fiber Bragg grating technology. Because of their specific advantages over silica in certain situations, their use continues to increase. Firstly, POF has an elastic modulus roughly 25 times smaller than silica; consequently, although the strain sensitivity of POFBGs is only marginally higher than their sil-

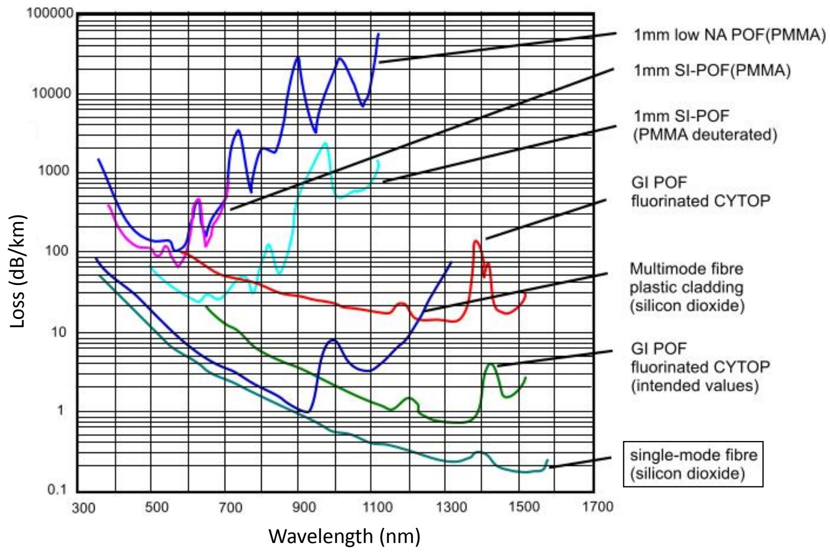

Figure 2.16 – Attenuation loss of common optical polymer fiber materials vs. silica as a function of wavelength. Graph from [60].

ica counterparts, the stress sensitivity is more than an order of magnitude higher. Secondly, for in vivo applications, when using glass fibers great care must be taken to guard against a fiber break which could exhibit a serious sharp hazard. A more elaborate overview on polymer fiber Bragg gratings can be found in [62] and [1], Chapter 11.

Within Chapter 3, both single-mode and multimode polymer optical fiber sensors will be combined with polymer host materials exploiting their excellent compatibility with organic materials, giving them great potential for biomedical applications. The polymer fiber sensors typically only transmit an optical signal over a few (tens of) centimeters and are glued to silica fibers for proper interrogation and interfacing with read-out equipment, further discussed in Chapter 3.

2.3.2 Polymer waveguide sensors

During the last years, polymer waveguide technology was developed as a means to apply printed circuit board-level optical interconnects in high-end computing systems. Waveguides offer important complementary advantages over fibers for board-level optical interconnects such as integrated processing, simplified handling and assembly. From an optical sensing point of view, polymer waveguide

(Bragg) gratings offer several advantages over FBGs: they are more compact. have a more cost-effective batch process, exhibit greater ease of tuning optical properties and offer potential integration with other components, such as light sources and detectors.

Various techniques and polymers have been developed to fabricate polymeric waveguide gratings. The fabrication of the corrugation structure usually involves using either a phase mask or two-beam interference on photosensitive polymer materials. The process usually involves three steps: (I) deposition of waveguide materials and waveguide dimension patterning; (II) creating a grating mask, typically through interference or phase mask techniques on a photoresist; and (III) transferring the gratings onto the waveguide core layer using either Reactive Ion Etching (RIE) or ion milling. Electron beam lithography can be a straightforward alternative way of transferring the grating structure but is relatively costly and slow. Other grating fabrication techniques have been reported using unconventional lithography techniques: a nanoimprint technique to fabricate the grating for an inverted rib waveguide grating device and a soft-lithography technique to fabricate a grating reflector-on-slab waveguide. Alternatively, solvent-assisted micro-contact molding (SAMIM) has been employed to fabricate rib waveguides and grating structures.

An overview of the state-of-the-art polymer waveguide sensor technologies, listing the different polymer materials, grating inscription techniques and grating characteristics, is shown in Table 2.3 (research institutes) and continued in Table 2.4 (sensor technologies developed by the research institutes listed in Table 2.3).

In a major part of the above-mentioned polymer waveguide gratings, the waveguide and grating structures are fabricated through UV induced refractive index modification. The photochemical material modification process is nevertheless rarely studied thoroughly. An interesting example of a more detailed investigation of different ways to change the optical properties such as the refractive index of polymers can nevertheless be found in [63].

The use of polymeric waveguide gratings reach beyond sensing applications. A more general use of waveguide gratings as tunable wavelength filters is a first possible alternative application. In [64] for example, the polymer waveguide gratings are integrated with electrodes yielding a tunable optical filter with a tuning range outreaching 10 nm. They are also used to fabricate distributed feedback lasers, for example using a soft-lithography (microcontact printing and replica molding) approach [65, 66]. Polymer waveguide grating couplers to couple light into planar waveguiding structures is another interesting application [67].

Polymer layers can also be applied directly on embedded laser components to increase their functionality. An example of an SU-8 layer acting as a diffraction grating and processed on a VCSEL can be found in [68].

Alternatively, a SiO_2 or glass waveguide can be used and a polymer can act as a transducer layer. This is for example discussed in [69], in which a PDMS layer is put on top of an open-top ridge waveguide Bragg grating resulting in a pressure or touch sensor. When gratings are fabricated in the PDMS material itself, they can also act as a resonant optical grating reflecting or transmitting the incident light. An example of such a membrane-embedded resonant optical PDMS grating is described in [70].

Table 2.3 – Overview of polymer waveguide sensors, continued in Table 2.4.

	Research institute / Company
1	University of Rome, Italy
2	Laser-Matter Interaction Labs Inc., Albuquerque, USA
3	Electronics and Telecommunications Research Institute, Taejon, Korea
4	AlliedSignal Inc. (Honeywell), USA
5	Faculty of Engineering, Dept. of Chemistry, Shizuoka Univ., Japan
6	Dept. of Electr. Eng., City Univ. of Hong Kong, Hong Kong
7	Dept. of Materials Science and Engineering, Kwangju Institute of Science and Technology, Korea
8	Devices and Materials Laboratory, LG Electronics Institute of Technology, Korea
9	Türk Telekom Bilkent Laboratory, Bilkent University, Turkey
10	Dept. of Applied Photonics System Technology, Chitose Institute of Science and Technology, Japan
11	Dept. of Electr. Eng., Pusan National Univ., Korea
12	School of Inform. & Comm. Eng., Sungkyunkwan Univ., Korea
13	Dept. of Electr. Eng., Southern Taiwan Univ. of Technology, Taiwan, ROC
14	Dept. of Mechanical Engineering, University of Washington, Seattle, USA

Table 2.4 – Overview of polymer waveguide sensors.

	Year	Waveguide material	WBG inscription technique	λ_B [nm]	WBG strength (transmission)	Refs
1	1993	4-dialkylamino-4′-nitro-stilbene (DANS) substituted polymer	- 2-beam interference 442 nm HeCd laser on photoresist - ion-milling in a Freon atmosphere onto glass - spin-coating polymer on glass	1540	-	[71]
2	1995	PMMA	- 2-beam interference 364 nm Ar ion-laser - RIE to transfer pattern	424	11 dB	[72]
3	1998	core: fluorinated poly(arylene ethers) grating: phenol-formaldehyde polymer	- phase mask using Hg mask aligner lamp - O_2 RIE to transfer pattern	1550	25 dB	[73, 64]
4	2000	high contrast specialty polymers (not disclosed)	photochemical (phase mask or direct 2-beam interference)	1550	> 40 dB	[74]
5	2002	diazo-dye-substituted PMMA	- single pulse 2-beam interference on PI master mold - replica molding/embossing	-	-	[75]
6	2003	MicroChem Corp. epoxy Novolak resin	e-beam lithography direct writing	1540	25 dB	[76, 77]
7	2003	fluorinated poly(arylene ether sulfide)	- 2-beam interference 488 nm Ar^+ laser - O_2 RIE to transfer pattern	1536	15 db	[78]
8	2005	ZPU12 (-445/-460) from ChemOptics (cladding/core)	- interference litho on photoresist - RIE to transfer pattern	1570	30 dB	[79]

	Year	Waveguide material	WBG inscription technique	λ_B [nm]	WBG strength (transmission)	Refs
9	2006	Epoxy Technology OG 146 (grating) and BCB (waveguide)	- e-beam lithography and RIE on Si wafer - PDMS casting on Si wafer - capillary filling of OG146	1530	20 dB	[80]
10	2007	polysilane	2-beam interference (Lloyd's mirror), annealing at 350 °C	1530	15 dB	[81]
11	2008	ZPU polymer from ChemOptics	- interference litho on photoresist - RIE to transfer pattern	1550	17 dB	[82, 83, 84]
12	2009	LFR polymer from ChemOptics	Inductive Coupled Plasma (ICP) RIE	1560	20 dB	[85, 86]
13	2009	Epoxy Technology OG146 and OG154	- interference litho on photoresist - PDMS casting on photoresist - stamping PDMS mold into OG146 cladding	1550	17 dB	[87, 88, 89]
14	2010	SU-8	- 2-beam interference 442 nm HeCd laser on AZ1518 (positive photoresist) - PDMS master mold fabrication - Solvent-assisted microcontact molding [90] in SU-8	1545	17 dB	[91]

2.4 Polymer embedded optical sensors: applications

2.4.1 Flexible sensing skins

As discussed in Chapter 1, Section 1.4, there is a growing need for embedded optical sensors in planar substrates leading to the creation of photonic skins for optical sensing (Chapter 1, Section 1.5). The state-of-the-art in the area of tactile sensing skins is extensive. Dario et al. suggested that the artificial skin should possess the intrinsic properties of human skin, like extensibility, flexibility and compliance [92]. A major part of these state-of-the-art tactile sensitive skins however is based on piezoresistive or capacitive force sensing technologies. Unfortunately, most of these structures suffer from various limitations such as low spatial resolution, limited read-out resolution, expensive manufacturing processes and complicated interconnection schemes because of the discrete nature of the sensor.

Much of the work in literature focuses on sensing devices developed for robotic tactile sensor systems. Specific reviews can for example be found in Lee et al. [93]. Back in 1995, Kolesar et al. already showed an 8 x 8 tactile sensor matrix with a linear response for loads up to 1.35 N for robotic applications [94]. Different examples of extensions of these tactile sensing skins towards artificial sensing skins are available. The first prototypes of an artificial sensing skins showed electrical sensors, mounted on a flexible polyimide substrate. Recently, a platform to fabricate ultra-thin and ultra-flexible electronics based on polymer foils (substrate thickness is typically 1 µm) was reported [95]. These electronic circuits are light and conform to their ambient, dynamic environment enabling for example matrix-addressed tactile sensor foils for health care and monitoring, thin-film heaters, and temperature and infrared sensors. To circumvent the limitations on electrical connectivity, the replacement of electrical sensors by optical sensors clearly offers a solution. Moreover, if these optical sensors could be integrated not only in a flexible, but ultimately in a stretchable substrate carrier, this would mean an additional important step towards optimal solutions for artificial skin applications. Optical sensors also offer a sensing alternative not susceptible to electromagnetic interference and enable high resolution combined with high-speed measurements.

Different research groups have published skin-like sensor foils based on optical sensors. The focus in this overview is on large-area sensing skins using fiber Bragg gratings:

- Although the inherent bare fiber *pressure* sensitivity of FBGs is rather limited, functional pressure sensing devices can be fabricated using polymer fiber coatings significantly enhancing this sensitivity [96]. An experimental pressure sensitivity of -3.41 10^{-3}/MPa is reported, approximately 1720 times higher than can be achieved with a bare FBG.

- In [97], a flexible multiplexed force sensor platform is presented based on fiber Bragg gratings for tactile sensing applications. A wavelength shift of 1.0 nm for 9.81 N at λ_B = 1550 nm measured using a ball load cell and an OSA is reported. A more elaborate description can be found in [98]. Figure 2.17 shows a 3 x 3 array sensor example. A conformable optical keyboard is a potential application.

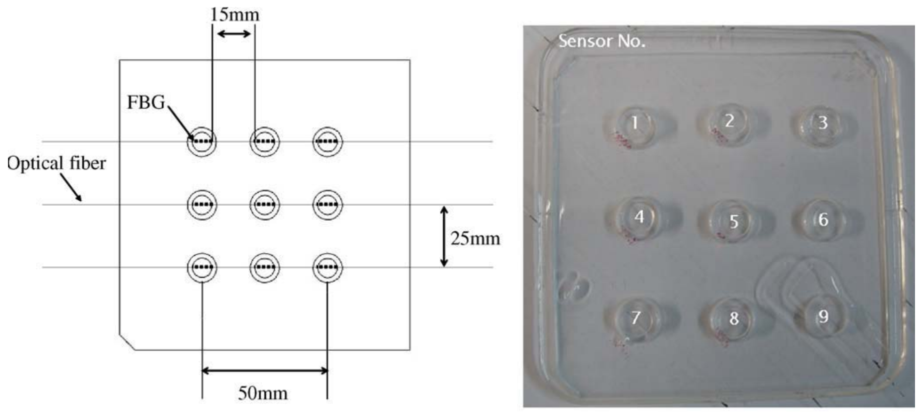

Figure 2.17 – 3 x 3 array sensor consisting of 3 embedded multiplexed fiber sensors. Courtesy of J.-S. Heo [98].

- An interesting alternative manufacturing technology for flexible optical sensing foils is based on an integration process in which optical waveguides and sensing elements are integrated "in line" during the manufacturing process of the substrate itself. This artificial and flexible optical sensing foil can then be applied to regular or irregular surfaces, resulting in a quasi-distributed strain map [99]. The embedding technique was applied to perform simultaneous cardiac and respiratory frequency measurements based on a single fiber Bragg grating sensor [100]. Figure 2.18 shows a prototype example. These prototypes were tested using a BraggMeter unit from FiberSensing [101] and FBGs with a typical length of 8 mm and resonance wavelength of 1548 nm.

- Kanellos et al. [102] presented a sensing skin based on PDMS embedded fiber Bragg gratings with a typical sensitivity of 80 pm/N at a Bragg wavelength of 1540 nm corresponding with a pressure sensitivity of 5.2 10^{-6}/kPa. The interrogation unit was an I-MON 80D from Ibsen.

- A thin and mechanically flexible alternative for the traditionally rigid tactile "touchscreen" sensors, for example to be used in keyboards, was developed

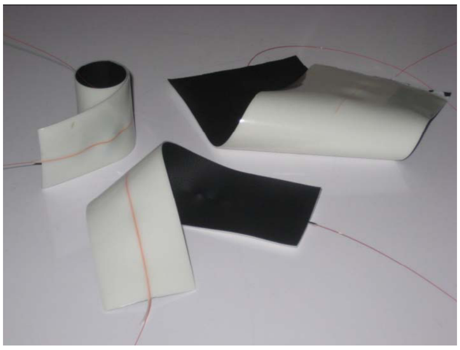

Figure 2.18 – Fabricated prototypes of FBGs embedded in polymer foils for cardiac and respiratory measurements. Courtesy of A.F. Silva [99].

by Takamatsu et al. [103]. Their approach is based on an electrical working principle (capacitance change) but integrated in a flexible fabric keyboard with conductive polymer coated fibers.

- The integration of optical sensors in *textiles* can be an interesting alternative for wearable applications. The OFSETH project [104], funded within EU-FP6, investigated how measurements of various vital parameters such as cardiac, respiratory rates and pulse oximetry can be performed using fiber Bragg gratings sensors and near infrared spectroscopy. These techniques could also, in a longer term, suit for non-invasive pH or glucometry measurements.

The photonic sensing systems presented in this overview all rely on standard silica fiber sensors and commercially available interrogation units. Important challenges limiting the applicability of these systems are related to the size, cost and accuracy of the interrogation devices as well as the limited sensitivity and inevitable cross-sensitivity of the optical fiber sensors. **Within the remainder of this dissertation, both these challenges will be tackled through:**

- **The introduction of polymer optical fiber sensors and specialty silica fiber sensors within flexible and stretchable sensing skins.**

- **The development of a fully integrated, low-cost interrogation system which will be applied on photonic sensing systems.**

A final application which could greatly benefit from the (quasi-)distributed character of fiber sensors compressed in a single read-out signal, are intelligent mattresses monitoring the position of the body and pressure distributions to improve the sleeping quality. Medical beds could even help patients that are bed-bound move without assistance [105]. Traditionally, sensing intelligence is added through electrical devices but different companies start to look into optical (fiber) alternatives [106]. The next-generation mattress will be created by adding sensing fibers which are based on optical working principles, solving potential safety issues. Moreover, these sensing fibers can be multiplexed, solving the interconnection challenges, and they can be embedded in a stretchable skin, ensuring proper functioning during complicated manipulation.

2.4.2 Esophageal manometry

A biomedical example which can benefit highly from the recent developments of optical sensors and polymer embedding, is situated within the field of manometry. Manometry measures pressure within the esophageal lumen and sphincters and is performed to investigate the cause of functional dysphagia, unexplained non-cardiac chest pain, and in the pre-operative work up of patients referred for antireflux surgery [107]. There is an increasing demand for patient-friendly, highly sensitive and biocompatible pressure sensors, embedded in cylindrical tubes, which can easily be multiplexed. The duration of the measurement, the mechanical flexibility of the sensor and the amount of pressure sensing points integrated in one sensing tube are key parameters for esophageal sensors. Traditional systems include sensors based on solid-state catheters or MEMS technology [108]. A typical read-out graph of an esophageal measurement is shown in Figure 2.19. This spatiotemporal plot presents a three-dimensional plot of the pressure along the esophagus. Time is on the x-axis and distance from the nares is on the y-axis. Each pressure is assigned a color (legend on the left). A peristaltic wave is passing distally down the esophagus.

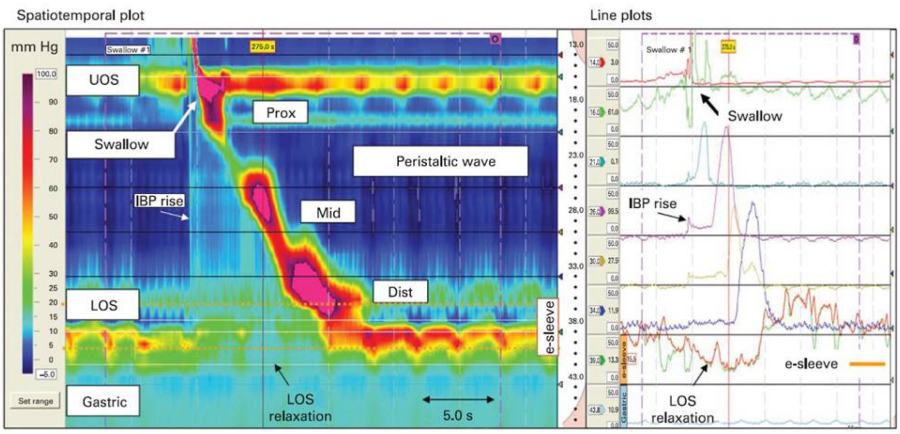

Figure 2.19 – High resolution manometry depicting esophageal pressure activity from the pharynx to the stomach. Courtesy of M.R. Fox [107].

Recently, also silica fiber optic alternatives, providing an increased usability of the esophageal sensing systems, are looked into yielding multiplexing possibilities and fast real-time measurements [109, 110]. Furthermore, a fiber optic sensor based high resolution manometry system is currently available and commercialized by MMS [111] and Unisensor AG [112], who have licensed the technology developed at CSIRO (Australia) [113]. **Within Chapter 3 of this dissertation, an embedding approach to come up with cylindrical polymer sensing tubes, based on multiplexed polymer fiber sensors, is presented. A response to a radial pressure almost 6 times that of a comparable silica fiber based sensor is obtained.**

2.4.3 Combining polymer sensing layers with other materials

Monitoring the structural integrity of bridges and large buildings typically requires the combination of sensors and concrete structures in challenging environments (high temperature, pressure). Embedded sensors based on fiber Bragg gratings are therefore increasingly being used within structural health monitoring applications [114].

Strain monitoring in wind turbine blades for example can significantly extend the life time of these structures. Nowadays they are often replaced as a precaution because monitoring strain and other aging effects is not possible using the traditional electrical sensors. Monitoring the structural health of wind turbine blades using optical sensors is therefore another important application leading to an increase in cost efficiency and a reduced environmental impact [115]. From an environmental point of view, the weight of the total sensing system integrated in a host material is of major importance, especially in transport (e.g. airplane) applications. Miniaturizing and integrating the read-out equipment within the composite structures is therefore also extensively studied, for example in the EU-FP7 projects SmartFiber [116] and Phosfos [30].

Optical sensors embedded in a polymer layer can be combined within other materials to monitor for example pressure or strain. An application which is recently gaining interest, is the combination of polymer or polymer embedded optical sensors with composite materials (combination of two or more constituent materials with significantly different physical or chemical properties). These polymer (embedded) optical sensors enable the introduction of a full sensing layer in between the different composite layers with a high sensitivity.

2.5 Conclusion

Optical sensors provide interesting sensing alternatives for applications which have limited compatibility with sensors based on electrical working principles.

Embedding optical sensors in polymer host materials allows to fabricate photonic skins. Such a mechanically flexible and stretchable sensing foil with a typical thickness below 1 mm will enable applications within the field of robotics, structural health monitoring and healthcare. To circumvent the traditional limitations of optical silica fiber sensors related to cost, sensitivity, biocompatibility, etc. several alternative fiber types (draw tower gratings, polymer optical fibers, microstructured optical fibers), each possessing their specific advantages (see Chapter 3), will be used in this dissertation.

Bulky and expensive interrogation systems often limit the applicability of optical fiber sensors in commercial applications. Within this PhD, an ultra-small interrogation system is developed based on low-cost optoelectronic components embedded in ultra-thin packages resulting in photonic skin compatible driving units. One of the crucial points to come up with such a scheme is a dedicated fiber coupling technology, compatible with this compact fiber sensing approach (Chapter 5). To avoid this delicate fiber coupling part, an alternative sensing approach will be considered based on self-mixing interferometry in lasers (Chapter 7).

References

[1] L. Thévenaz, *Advanced fiber optics : concepts and technology*. EFPL Press, 2011.

[2] G. Righini, A. Tajani, and A. Cutolo, *An Introduction to Optoelectronic Sensors*. World Scientific, 2009.

[3] S. Yin, P. Ruffin, and F. T. Yu, *Fiber Optic Sensors - second edition*. CRC Press, 2008.

[4] J. Missinne, "Development of conformable optical and optoelectronic based tactile sensors," Ph.D. dissertation, Ghent University, 2011.

[5] J. Missinne, E. Bosman, B. Van Hoe, G. Van Steenberge, S. Kalathimekkad, P. Van Daele, and J. Vanfleteren, "Flexible shear sensor based on embedded optoelectronic components," *IEEE Photonics Technology Letters*, vol. 23, no. 12, pp. 771–773, June 2011.

[6] J. Missinne, P. Kostov, B. Van Hoe, E. Bosman, W. Gaber, H. Zimmerman, and G. Van Steenberge, "Ultra-thin multi-axial shear stress sensor based on a segmented photodiode," 2013, Conference Paper, abstract submitted: IEEE Photonics Conference, Washington, USA, SEP 2013.

[7] J. M. López-Higuera, L. Rodríguez, A. Quintela, and A. Cobo, "Currents and trends on fiber sensing technologies for structural health monitoring," 2010, the 2nd Mediterranean Photonics Conference, Eilat, Israel, NOV 2010.

[8] F. T. Yu and S. Yin, *Fiber Optic Sensors*. CRC Press, 2002.

[9] X. Bao and L. Chen, "Recent progress in distributed fiber optic sensors," *Sensors*, vol. 12, no. 7, pp. 8601–8639, July 2012.

[10] P. Kwiat, W. Vareka, C. Hong, H. Nathel, and R. Chiao, "Correlated 2-photon interference in a dual-beam michelson interferometer," *Physical Review A*, vol. 41, no. 5, pp. 2910–2913, Mar. 1990.

[11] R. Heideman, R. Kooyman, and J. Greve, "Performance of a highly sensitive optical wave-guide mach-zehnder interferometer immunosensor," *Sensors and Actuators B-Chemical*, vol. 10, no. 3, pp. 209–217, Feb. 1993.

[12] C. Quay, I. Maxwell, and J. Hudgings, "Coherence collapse and redshifting in vertical-cavity surface-emitting lasers exposed to strong optical feedback," *Journal of Applied Physics*, vol. 90, no. 12, pp. 5856–5858, Dec. 2001.

[13] G. Giuliani, M. Norgia, S. Donati, and T. Bosch, "Laser diode self-mixing technique for sensing applications," *Journal of Optics A-Pure and Applied Optics*, vol. 4, no. 6, pp. S283–S294, Nov. 2002.

[14] M. Rudd, "A laser doppler velocimeter employing laser as a mixer-oscillator," *Journal of Physics E-Scientific Instruments*, vol. 1, no. 7, pp. 723–&, 1968.

[15] S. Donati, "Laser interferometry by induced modulation of cavity field," *Journal of Applied Physics*, vol. 49, no. 2, pp. 495–497, 1978.

[16] S. Shinohara, A. Mochizuki, H. Yoshida, and M. Sumi, "Laser doppler-velocimeter using the self-mixing effect of a semiconductor-laser diode," *Applied Optics*, vol. 25, no. 9, pp. 1417–1419, May 1986.

[17] G. Beheim and K. Fritsch, "Range finding using frequency-modulated laser diode," *Applied Optics*, vol. 25, no. 9, pp. 1439–1442, May 1986.

[18] S. Donati, G. Giuliani, and S. Merlo, "Laser-diode feedback interferometer for measurement of displacements without ambiguity," *IEEE Journal of Quantum Electronics*, vol. 31, no. 1, pp. 113–119, Jan. 1995.

[19] R. Lang and K. Kobayashi, "External optical feedback effects on semiconductor injection-laser properties," *IEEE Journal of Quantum Electronics*, vol. 16, no. 3, pp. 347–355, 1980.

[20] J. Santos, F. L.A., and F. Araújo, *Fiber Bragg Grating Interrogation Systems*, A. Cusano, A. Cutolo, and J. Albert, Eds. Bentham Science Publishers Ltd., 2011, *chapter from "Fiber Bragg Grating Sensors: Recent Advancements, Industrial Applications and Market Exploitation"*.

[21] A. Kersey, M. Davis, H. Patrick, M. LeBlanc, K. Koo, C. Askins, M. Putnam, and E. Friebele, "Fiber grating sensors," *Journal of Lightwave Technology*, vol. 15, no. 8, pp. 1442–1463, Aug. 1997.

[22] O. G. Nadya Anscombe, "Technology focus, optical-fibre sensors, great potential," *Nature Photonics*, vol. 2, no. 3, pp. 141–158, 2008.

[23] K. Sugden and V. Mezentsev, *Fiber Bragg Gratings: Advances in Fabrication Process and Tools*, A. Cusano, A. Cutolo, and J. Albert, Eds. Bentham Science Publishers Ltd., 2011, *chapter from "Fiber Bragg Grating Sensors: Recent Advancements, Industrial Applications and Market Exploitation"*.

[24] T. Geernaert, "Microstructured fiber bragg grating sensors: From fiber design to sensor implementation," Ph.D. dissertation, Vrije Universiteit Brussel, 2011.

[25] K. Hill, Y. Fujii, D. Johnson, and B. Kawasaki, "Photosensitivity in optical fiber waveguides - application to reflection filter fabrication," *Applied Physics Letters*, vol. 32, no. 10, pp. 647–649, 1978.

[26] G. Meltz, W. Morey, and W. Glenn, "Formation of bragg gratings in optical fibers by a transverse holographic method," *Optics Letters*, vol. 14, no. 15, pp. 823–825, Aug. 1989.

[27] K. Hill, B. Malo, F. Bilodeau, D. Johnson, and J. Albert, "Bragg gratings fabricated in monomode photosensitive optical fiber by uv exposure through a phase mask," *Applied Physics Letters*, vol. 62, no. 10, pp. 1035–1037, Mar. 1993.

[28] A. Martinez, M. Dubov, I. Khrushchev, and I. Bennion, "Direct writing of fibre bragg gratings by femtosecond laser," *Electronics Letters*, vol. 40, no. 19, pp. 1170–1172, Sept. 2004.

[29] P. S. J. Russell, "Photonic-crystal fibers," *Journal of Lightwave Technology*, vol. 24, no. 12, pp. 4729–4749, Dec. 2006.

[30] Phosfos Consortium. (2008) Photonic skins for optical sensing. [Online]. Available: http://www.phosfos.eu/

[31] N. D. Orf, O. Shapira, F. Sorin, S. Danto, M. A. Baldo, J. D. Joannopoulos, and Y. Fink, "Fiber draw synthesis," *Proceedings of the National Academy of Sciences of the United Stated of America*, vol. 108, no. 12, pp. 4743–4747, Mar. 2011.

[32] L. Blair and S. Cassidy, "Wavelength division multiplexed sensor network using bragg fiber reflection gratings," *Electronics Letters*, vol. 28, no. 18, pp. 1734–1735, Aug. 1992.

[33] M. Xu, L. Reekie, Y. Chow, and J. Dakin, "Optical in-fiber grating high-pressure sensor," *Electronics Letters*, vol. 29, no. 4, pp. 398–399, Feb. 1993.

[34] J. Meissner, W. Nowak, V. Slowik, and T. Klink, "Strain monitoring at a prestressed concrete bridge," in *12th International Conference on Optical Fiber Sensors. Technical Digest. Postconference Edition*. Opt. Soc. America; IEEE/Lasers & Electro-Opt. Soc, 1997, Conference Paper, pp. 408–11, proceedings of 12th International Conference on Optical Fibre Sensors (ISBN 1 55752 515 3), Williamsburg, VA, USA, OCT 1997.

[35] R. Fallon, L. Zhang, L. Everall, J. Williams, and I. Bennion, "All-fibre optical sensing system: Bragg grating sensor interrogated by a long-period grating," *Measurement Science & Technology*, vol. 9, no. 12, pp. 1969–1973, Dec. 1998.

[36] G. M. Rego, H. M. Salgado, and J. L. Santos, "Interrogation of a fiber bragg grating using a mechanically induced long-period fiber grating," *IEEE Sensors Journal*, vol. 6, no. 6, pp. 1592–1595, Dec. 2006.

[37] E. Udd, K. Corona, J. Dorr, and K. Slattery, "A low cost fiber grating sensor demodulator using a temperature compensated fiber grating spectral filter," ser. Proceedings of the Society of Photo-Optical Instrumentation Engineers (SPIE), E. Udd and C. Jung, Eds., vol. 3180. Blue Road Res; Soc Photo Opt Instrumentat Engineers, 1997, pp. 63–66, 3rd Pacific Northwest Fiber Optic Sensor Workshop, Troutdale, OR, MAY 1997.

[38] R. Romero, O. Frazao, P. Marques, H. Salgado, and J. Santos, "Fibre bragg grating interrogation technique based on a chirped grating written in an erbium-doped fibre," *Measurement Science & Technology*, vol. 14, no. 11, pp. 1993–1997, Nov. 2003.

[39] L. Ferreira and J. Santos, "Demodulation scheme for fibre bragg sensors based on source spectral characteristics," *Pure and Applied Optics*, vol. 5, pp. 257–61, May 1996.

[40] S. Kang, H. Yoon, S. Lee, S. Choi, and B. Lee, "Real-time measurement for static and dynamic strain using a fiber bragg grating and the ase profile of edfa," ser. Proceedings of the Society of Photo-Optical Instrumentation Engineers (SPIE), B. Kim and K. Hotate, Eds., vol. 3746, 1999, pp. 530–533, 13th International Conference on Optical Fiber Sensors and Workshop on Device and System Technology Toward Future Optical Fiber Communication and Sensing, Kyongju, South Korea, APR 1999.

[41] T. Coroy and R. Measures, "Active wavelength demodulation of a bragg grating fibre optic strain sensor using a quantum well electroabsorption filtering detector," *Electronics Letters*, vol. 32, no. 19, pp. 1811–1812, Sept. 1996.

[42] A. Kersey, T. Berkoff, and W. Morey, "Multiplexed fiber bragg grating strain-sensor system with a fiber fabry-perot wavelength filter," *Optics Letters*, vol. 18, no. 16, pp. 1370–1372, Aug. 1993.

[43] C. Ye, S. Staines, S. James, and R. Tatam, "A polarization-maintaining fibre bragg grating interrogation system for multi-axis strain sensing," *Measurement Science & Technology*, vol. 13, no. 9, pp. 1446–1449, Sept. 2002.

[44] G. Fusiek, P. Niewczas, and J. McDonald, "Extended step-out length fiber bragg grating interrogation system for condition monitoring of electrical submersible pumps," *Optical Engineering*, vol. 44, no. 3, Mar. 2005.

[45] S. Vohra, M. Todd, G. Johnson, C. Chang, and B. Danver, "Fiber bragg grating sensor system for civil structure monitoring: Applications and field tests," ser. Proceedings of the Society of Photo-Optical Instrumentation Engineers (SPIE), B. Kim and K. Hotate, Eds., vol. 3746, 1999, pp. 32–37, 13th

International Conference on Optical Fiber Sensors and Workshop on Device and System Technology Toward Future Optical Fiber Communication and Sensing, Kyongju, South Korea, APR 1999.

[46] P. Henderson, D. Webb, D. Jackson, L. Zhang, and I. Bennion, "Highly-multiplexed grating-sensors for temperature-referenced quasi-static measurements of strain in concrete bridges," ser. Proceedings of the Society of Photo-Optical Instrumentation Engineers (SPIE), B. Kim and K. Hotate, Eds., vol. 3746, 1999, pp. 320–323, 13th International Conference on Optical Fiber Sensors and Workshop on Device and System Technology Toward Future Optical Fiber Communication and Sensing, Kyongju, South Korea, APR 1999.

[47] A. Kersey, M. Davis, and T. Tsai, "Fiber optic bragg grating strain sensor with direct reflectometric interrogation," in *OFS-11. Eleventh International Conference on Optical Fiber Sensors - Advanced Sensing Photonics*. Japan Soc. Applied Phys.; IEICE of Japan; IEE of Japan; Soc. Instrum. & Control Eng., Japan, 1996, Conference Paper, pp. 634–7 vol.1, 11th International Conference on Optical Fiber Sensors, Sapporo, Japan, MAY 1996.

[48] B. Lissak, A. Arie, and M. Tur, "Highly sensitive dynamic strain measurements by locking lasers to fiber bragg gratings," *Optics Letters*, vol. 23, no. 24, pp. 1930–1932, Dec. 1998.

[49] N. Takahashi, K. Tetsumura, K. Imamura, and S. Takahashi, "Fiber-bragg-grating wdm underwater acoustic sensor with directivity," in *Fiber Optic and Laser Sensors and Applications: Including Distributed and Multiplexed Fiber Optic Sensors VII*, ser. Proceedings of the Society of Photo-Optical Instrumentation Engineers (SPIE), J. Dakin, A. Kersey, and D. Paul, Eds., vol. 3541. SPIE-Int Soc Opt Engn, 1999, pp. 18–26, conference on Fiber Optic and Laser Sensors and Applications, Boston, MA, NOV 1998.

[50] A. Arie, B. Lissak, and M. Tur, "Static fiber-bragg grating strain sensing using frequency-locked lasers," *Journal of Lightwave Technology*, vol. 17, no. 10, pp. 1849–1855, Oct. 1999.

[51] D. Hjelme, L. Bjerkan, S. Neegard, J. Rambech, and J. Aarsnes, "Application of bragg grating sensors in the characterization of scaled marine vehicle models," *Applied Optics*, vol. 36, no. 1, pp. 328–336, Jan. 1997.

[52] D. Jackson, A. Kersey, M. Corke, and J. Jones, "Pseudoheterodyne detection scheme for optical interferometers," *Electronics Letters*, vol. 18, no. 25-2, pp. 1081–1083, 1982.

[53] L. Ferreira, E. Diatzikis, J. Santos, and F. Farahi, "Demodulation of fiber bragg grating sensors based on dynamic tuning of a multimode laser diode," *Applied Optics*, vol. 38, no. 22, pp. 4751–4759, Aug. 1999.

[54] Ocean Optics. (Accessed 2013) Company website. [Online]. Available: http://www.oceanoptics.com/

[55] S. Schultz, W. Kunzler, Z. Zhu, M. Wirthlin, R. Selfridge, A. Propst, M. Zikry, and K. Peters, "Full-spectrum interrogation of fiber bragg grating sensors for dynamic measurements in composite laminates," *Smart Materials & Structures*, vol. 18, no. 11, Nov. 2009.

[56] T. Vella, S. Chadderdon, R. Selfridge, S. Schultz, S. Webb, C. Park, K. Peters, and M. Zikry, "Full-spectrum interrogation of fiber bragg gratings at 100 khz for detection of impact loading," *Measurement Science & Technology*, vol. 21, no. 9, SI, Sept. 2010.

[57] G. Xiao, N. Mrad, F. Wu, Z. Zhang, and F. Sun, "Miniaturized optical fiber sensor interrogation system employing echelle diffractive gratings demultiplexer for potential aerospace applications," *IEEE Sensors Journal*, vol. 8, no. 7-8, pp. 1202–1207, Aug. 2008.

[58] J. Villatoro, V. Finazzi, V. P. Minkovich, and G. Badenes, "Compact all-fiber interrogation unit for fbg sensors," pp. 2884–2886, conference on Optical Fiber Communications/National Fiber Optic Engineers Conference, San Diego, CA, FEB, 2008.

[59] K. Peters, "Polymer optical fiber sensors-a review," *Smart Materials and Structures*, vol. 20, no. 1, Jan. 2011.

[60] J. Zubia and J. Arrue, "Plastic optical fibers: An introduction to their technological processes and applications," *Optical Fiber Technology*, vol. 7, no. 2, pp. 101–140, Apr. 2001.

[61] Z. Xiong, G. Peng, B. Wu, and P. Chu, "Highly tunable bragg gratings in single-mode polymer optical fibers," *IEEE Photonics Technology Letters*, vol. 11, no. 3, pp. 352–354, Mar. 1999.

[62] D. Webb and K. Kalli, *Polymer Fiber Bragg Gratings*, A. Cusano, A. Cutolo, and J. Albert, Eds. Bentham Science Publishers Ltd., 2011, *chapter from "Fiber Bragg Grating Sensors: Recent Advancements, Industrial Applications and Market Exploitation"*.

[63] P. Henzi, D. G. Rabus, Y. Ichihashi, M. Bruendel, and J. Mohr, "Photonic integrated polymer components and circuits by uv-induced refractive index modification - art. no. 618502," in *Micro-Optics, VCSELs, and Photonic Interconnects II: Fabrication, Packaging, and Integration*, ser. Proceedings of the Society of Photo-Optical Instrumentation Engineers (SPIE), H. Thienpont, M. Taghizadeh, P. Daele, and J. Mohr, Eds., vol. 6185, 2006, p. 18502, conference on Micro-Optics, VCSELs, and Photonic Interconnects II, Strasbourg, France, APR 2006.

[64] M. Oh, H. Lee, M. Lee, J. Ahn, S. Han, and H. Kim, "Tunable wavelength filters with bragg gratings in polymer waveguides," *Applied Physics Letters*, vol. 73, no. 18, pp. 2543–2545, Nov. 1998.

[65] J. Rogers, M. Meier, and A. Dodabalapur, "Distributed feedback lasers produced using soft lithography," in *56th Annual Device Research Conference Digest*. IEEE Electron Devices Soc, June 1998, Conference Paper, pp. 134–5, 56th Annual Device Research Conference Digest, Charlottesville, VA, USA, JUN 1998.

[66] J. Rogers, A. Dodabalapur, and M. Meier, "Using printing and molding techniques to produce distributed feedback and bragg reflector resonators for plastic lasers," *Applied Physics Letters*, vol. 73, no. 13, pp. 1766–1768, Sept. 1998.

[67] Y. Dong, X. Yu, Y. Sun, Y. Li, X. Hou, and X. Zhang, "Polymer waveguide grating fabricated by two-photon initiated photopolymerization and its application as an input coupler," *Optical Materials*, vol. 30, no. 6, pp. 935–938, Feb. 2008.

[68] A. Gracias, N. Tokranova, and J. Castracane, "Su8-based static diffractive optical elements: Wafer-level integration with vcsel arrays," in *PHOTONICS PACKAGING, INTEGRATION, AND INTERCONNECTS VIII*, ser. PROCEEDINGS OF THE SOCIETY OF PHOTO-OPTICAL INSTRUMENTATION ENGINEERS (SPIE), A. Glebov and R. Che, Eds., vol. 6899, 2008, p. J8990, conference on Photonics Packaging, Integration, and Interconnects VIII, San Jose, CA, JAN 2008.

[69] X. Dai, S. J. Mihailov, and C. Blanchetiere, "Optical evanescent field waveguide bragg grating pressure sensor," *Optical Engineering*, vol. 49, no. 2, Feb. 2010.

[70] S. Foland, K. Liu, D. MacFarlane, and J.-B. Lee, "High-sensitivity microfluidic pressure sensor using a membrane-embedded resonant optical grating," in *IEEE SENSORS*, 2011, pp. 97–100, 10th IEEE Conference on Sensors, Limerick, Ireland, OCT 2011.

[71] S. Aramaki, G. Assanto, G. Stegeman, and M. Marciniak, "Realization of integrated bragg reflectors in dans-polymer wave-guides," *Journal of Lightwave Technology*, vol. 11, no. 7, pp. 1189–1195, July 1993.

[72] N. Mukherjee, B. Eapen, D. Keicher, S. Luong, and A. Mukherjee, "Distributed bragg reflection in integrated waveguides of polymethylmethacrylate," *Applied Physics Letters*, vol. 67, no. 25, pp. 3715–3717, Dec. 1995.

[73] M. Oh, M. Lee, J. Ahn, H. Lee, and S. Han, "Polymeric wavelength filters with polymer gratings," *Applied Physics Letters*, vol. 72, no. 13, pp. 1559–1561, Mar. 1998.

[74] L. Eldada and L. Shacklette, "Advances in polymer integrated optics," *IEEE Journal of Selected Topics in Quantum Electronics*, vol. 6, no. 1, pp. 54–68, 2000.

[75] S. Shibata, O. Sugihara, Y. Che, H. Fujimura, C. Egami, and N. Okamoto, "Formation of channel waveguide with grating in polymer films based on simultaneous photobleaching and embossing," *Optical Materials*, vol. 21, no. 1-3, pp. 495–498, Jan. 2003, international Conference on Photo-Responsive Organics and Polymers (ICPOP 2001), Cheju Isl, South Korea, AUG 2001.

[76] W. Wong, E. Pun, and K. Chan, "Electron beam direct-write tunable polymeric waveguide grating filter," *IEEE Photonics Technology Letters*, vol. 15, no. 12, pp. 1731–1733, Dec. 2003.

[77] W. Wong and E. Pun, "Polymeric waveguide wavelength filters using electron-beam direct writing," *Applied Physics Letters*, vol. 79, no. 22, pp. 3576–3578, Nov. 2001.

[78] J. Kang, M. Kim, J. Kim, S. Yoo, J. Lee, D. Kim, and J. Kim, "Polymeric wavelength filters fabricated using holographic surface relief gratings on azobenzene-containing polymer films," *Applied Physics Letters*, vol. 82, no. 22, pp. 3823–3825, June 2003.

[79] S. Ahn, K. Lee, D. Kim, and S. Lee, "Polymeric wavelength filter based on a bragg grating using nanoimprint technique," *IEEE Photonics Technology Letters*, vol. 17, no. 10, pp. 2122–2124, Oct. 2005.

[80] A. Kocabas and A. Aydinli, "Polymeric waveguide bragg grating filter using soft lithography," *Optics Express*, vol. 14, no. 22, pp. 10 228–10 232, Oct. 2006.

[81] S. Kobayashi, M. Sawada, T. Suda, K. Ogura, and H. Tsushima, "Narrow tunable polysilane optical waveguide bragg grating filters," *IEEE Photonics Technology Letters*, vol. 19, no. 5-8, pp. 363–365, 2007.

[82] K.-J. Kim and M.-C. Oh, "Flexible bragg reflection waveguide devices fabricated by post-lift-off process," *IEEE Photonics Technology Letters*, vol. 20, no. 1-4, pp. 288–290, 2008.

[83] K.-J. Kim, J.-W. Kim, M.-C. Oh, Y.-O. Noh, and H.-J. Lee, "Flexible polymer waveguide tunable lasers," *Optics Express*, vol. 18, no. 8, pp. 8392–8399, Apr. 2010.

[84] K.-J. Kim, J.-K. Seo, and M.-C. Oh, "Strain induced tunable wavelength filters based on flexible polymer waveguide bragg reflector," *Optics Express*, vol. 16, no. 3, pp. 1423–1430, Feb. 2008.

[85] H.-R. Park, I.-S. Jeong, J.-A. Park, and M.-H. Lee, "Compact waveguides with bragg gratings in the middle of a core layer," in *Lasers & Electro-Optics & the Pacific Rim Conference on Lasers and Electro-Optics, Vols 1 and 2*. Chinese Opt Soc; Chinese Inst Elect; Chinese Phys Soc; Natl Nat Sci Fdn China; Opt Soc Amer; Opt Soc Korea; japan Soc Appl Phys; IEEE Photon Soc; Australian Opt Soc; IEICE, Elect Soc; IEICE, Commun Soc, 2009, pp. 170–171, 8th Pacific Rim Conference on Lasers and Electro-Optics, Shanghai, China, AUG 2009.

[86] I.-S. Jeong, H.-R. Park, S.-W. Lee, and M.-H. Lee, "Polymeric waveguides with bragg gratings in the middle of the core layer," *Journal of the Optical Society of Korea*, vol. 13, no. 2, pp. 294–298, June 2009.

[87] W. C. Chang, K. F. Yarn, and W. C. Chuang, "Polymer nano-bragg grating waveguide using mems process," *Digest Journal of Nanomaterials and Biostructures*, vol. 4, no. 1, pp. 199–204, Mar. 2009.

[88] W. Chuang, C. Ho, and W. Wang, "Fabrication of a high-resolution periodical structure using a replication process," *Optics Express*, vol. 13, no. 18, pp. 6685–6692, Sept. 2005.

[89] W. Chang, W. Chuang, C. Ho, and K. Yarn, "High-resolution periodical structure on polycarbonate using holographic interferometry and electroforming process," *Journal of Optoelectronics and Advanced Materials*, vol. 8, no. 3, pp. 1243–1246, June 2006.

[90] E. Kim, Y. Xia, X. Zhao, and G. Whitesides, "Solvent-assisted microcontact molding: A convenient method for fabricating three-dimensional structures on surfaces of polymers," *Advanced Materials*, vol. 9, no. 8, pp. 651–654, June 1997.

[91] C.-S. Huang, Y.-B. Pun, and W.-C. Wang, "Su-8 rib waveguide bragg grating filter using composite stamp and solvent-assisted microcontact molding technique," *Journal of Micro-Nanolithography MEMS and MOEMS*, vol. 9, no. 2, 2010.

[92] L. Ventrelli, L. Beccai, V. Mattoli, A. Menciassi, and P. Dario, "Development of a stretchable skin-like tactile sensor based on polymeric composites," in *VOLS 1-4*, 2009, pp. 123–128, iEEE International Conference on Robotics and Biomimetics (ROBIO), Guilin, China, DEC 2009.

[93] M. Lee and H. Nicholls, "Tactile sensing for mechatronics - a state of the art survey," *Mechatronics*, vol. 9, no. 1, pp. 1–31, Feb. 1999.

[94] E. Kolesar and C. Dyson, "Object imaging with a piezoelectric robotic tactile sensor," *Journal of Microelectromechanical Systems*, vol. 4, no. 2, pp. 87–96, June 1995.

[95] M. Kaltenbrunner, T. Sekitani, J. Reeder, T. Yokota, K. Kuribara, T. Tokuhara, M. Drack, R. Schwoediauer, I. Graz, S. Bauer-Gogonea, S. Bauer, and T. Someya, "An ultra-lightweight design for imperceptible plastic electronics," *Nature*, vol. 499, no. 7459, pp. 458–465, July 2013.

[96] Y. Zhang, D. Feng, Z. Liu, Z. Guo, X. Dong, K. Chiang, and B. Chu, "High-sensitivity pressure sensor using a shielded polymer-coated fiber bragg grating," *IEEE Photonics Technology Letters*, vol. 13, no. 6, pp. 618–619, June 2001.

[97] J. Heo and J. Lee, "Development of flexible force sensors using fiber bragg grating for tactile sensing and its evaluation," ser. PROCEEDINGS OF THE SOCIETY OF PHOTO-OPTICAL INSTRUMENTATION ENGINEERS (SPIE), C. Quan, F. Chau, A. Asundi, B. Wong, and C. Lim, Eds., vol. 5852, no. 1&2, 2005, pp. 372–378, 3rd International Conference on Experimental Mechanics/3rd Conference of the Asian-Committee-on-Experimental-Mechanics, Singapore, Singapore, NOV-DEC 2004.

[98] J. Heo, J. Chung, and J. Lee, "Tactile sensor arrays using fiber bragg grating sensors," *Sensors and Actuators A - Physical*, vol. 126, no. 2, pp. 312–327, Feb. 2006.

[99] A. F. Silva, F. Goncalves, L. A. Ferreira, F. M. Araujo, N. S. Dias, J. P. Carmo, P. M. Mendes, and J. H. Correia, "Manufacturing technology for flexible optical sensing foils." IEEE Ind Elect Soc, pp. 1770–1773, 35th Annual Conference of the IEEE-Industrial-Electronics-Society (IECON 2009), Porto, Portugal, NOV 2009.

[100] A. F. Silva, J. P. Carmo, P. M. Mendes, and J. H. Correia, "Simultaneous cardiac and respiratory frequency measurement based on a single fiber bragg grating sensor," *Measurement Science & Technology*, vol. 22, no. 7, July 2011.

[101] FiberSensing. (Accessed 2013) Company website. [Online]. Available: http://www.fibersensing.com/

[102] G. T. Kanellos, G. Papaioannou, D. Tsiokos, C. Mitrogiannis, G. Nianios, and N. Pleros, "Two dimensional polymer-embedded quasi-distributed fbg pressure sensor for biomedical applications," *Optics Express*, vol. 18, no. 1, pp. 179–186, Jan. 2010.

[103] S. Takamatsu, T. Imai, T. Yamashita, T. Kobayashi, K. Miyake, and T. Itoh, "Flexible fabric keyboard with conductive polymer-coated fibers," in *IEEE*

SENSORS, 2011, pp. 659–662, 10th IEEE Conference on Sensors, Limerick, Ireland, OCT 2011.

[104] Ofseth Consortium. (2006) Optical fibre sensors embedded into technical textile for healthcare. [Online]. Available: http://www.ofseth.org/

[105] Spalding, Natural Sleep. (Accessed 2013) Company website. [Online]. Available: http://www.spaldin.com/

[106] Custom8 NV sensor mats. (Accessed 2013) Company website. [Online]. Available: http://www.custom8.be/

[107] M. R. Fox and A. J. Bredenoord, "Oesophageal high-resolution manometry: moving from research into clinical practice," *GUT*, vol. 57, no. 3, Mar. 2008.

[108] Y. Haga and M. Esashi, "Biomedical microsystems for minimally invasive diagnosis and treatment," *Proceedings of the IEEE*, vol. 92, no. 1, pp. 98–114, Jan. 2004.

[109] S. Voigt, M. Rothhardt, M. Becker, T. Lüpke, C. Thieroff, A. Teubner, and J. Mehner, "Homogeneous catheter for esophagus high-resolution manometry using fiber bragg gratings," ser. Proceedings of SPIE-The International Society for Optical Engineering, I. Gannot, Ed., vol. 7559. SPIE, 2010, conference on Optical Fibers and Sensors for Medical Diagnostics and Treatment Applications X, San Francisco, CA, JAN 2010.

[110] M. Becker, M. Rothhardt, K. Schröder, H. Bartelt, S. Voigt, A. Teubner, T. Lüpke, and C. Thieroff, "Fiber-optical high-resolution esophagus manometry based on drawing-tower fiber bragg gratings," O. Frazao, Ed. Univ. do Algarve, Conference Paper, pp. 41–4, advances in Sensors, Signals and Materials. 3rd WSEAS International Conference on Sensors and Signals (SENSIG 2010). 3rd WSEAS International Conference on Materials Science (MATERIALS 2010), Faro, Portugal, NOV 2010.

[111] MMS International - Medical Measurement Systems. (Accessed 2013) Company website. [Online]. Available: http://www.mmsinternational.com/

[112] Unisensor AG - Customized Sensor Solutions. (Accessed 2013) Company website. [Online]. Available: http://www.unisensor.ch/

[113] J. W. Arkwright, N. G. Blenman, I. D. Underhill, S. A. Maunder, N. J. Spencer, M. Costa, S. J. Brookes, M. M. Szczesniak, and P. G. Dinning, "A fibre optic catheter for simultaneous measurement of longitudinal and circumferential muscular activity in the gastrointestinal tract," *Journal of Biophotonics*, vol. 4, no. 4, pp. 244–251, Apr. 2011.

[114] T. Chan, L. Yu, H. Tam, Y. Ni, W. Chung, and L. Cheng, "Fiber bragg grating sensors for structural health monitoring of tsing ma bridge: Background and experimental observation," *Engineering Structures*, vol. 28, no. 5, pp. 648–659, Apr. 2006.

[115] K. Schroeder, W. Ecke, J. Apitz, E. Lembke, and G. Lenschow, "A fibre bragg grating sensor system monitors operational load in a wind turbine rotor blade," *Measurement Science & Technology*, vol. 17, no. 5, pp. 1167–1172, 17th International Conference on Optical Fibre Sensors, Brugge, BELGIUM, MAY, 2005.

[116] SmartFiber Consortium. (2010) Miniaturized structural monitoring system with autonomous readout micro-technology and fiber sensor network. [Online]. Available: http://www.smartfiber-fp7.eu/

3
Integrated optical fiber sensors

In this chapter optical fiber sensors are used to measure ambient parameters such as temperature and humidity but also other physical properties such as (contact) pressure, (axial or transverse) strain and bending. The deployment of optical fiber sensors typically requires a fixture of the optical fiber on the object which is to be examined. Using polymer host materials not only provides a robust way to embed optical fibers, it also entails several other advantages such as mechanical flexibility or even stretchability enabling the combination of these sensors with irregularly shaped objects. Typical applications include robotics, biomedics and structural health monitoring.

3.1 Introduction

Fiber Bragg grating sensors and their working principles were introduced in Chapter 2. They are essentially based on wavelength selective mirrors inscribed in optical fibers by a periodic (period in the range of hundreds of nm) change of the effective refractive core index. The fundamentals of Fiber Bragg Gratings (FBGs) are described in the following reference articles [1, 2]. Depending on the inscription process and the application, the fiber Bragg gratings can also be chirped (aperiodic refractive index modulation), tilted (refractive index variation at an angle to the optical axis) or long-period (period of hundreds of µm). However, these types of FBGs are not used within this chapter.

This chapter focuses on the embedding of optical fibers in flexible and stretchable polymer host materials. Different approaches were under investigation for embedding the fiber sensors, including injection molding, laser structuring and soft-lithography. The different embedding techniques have their specific advantages and drawbacks. Based on the specific needs of the considered application, the most appropriate embedding technique can be identified.

The optical fiber sensors which are used in this chapter are ranging from commercially available Draw Tower Gratings (DTGs) to single- or multimode Polymer Optical Fiber (POF) sensors and Microstructured Silica Fiber (MSF) sensors. Comparing the performance of these special types of fiber sensors is always performed using "standard" single-mode silica fiber sensors.

Regardless of the application, the first step is to check the influence of the embedding process on the properties of the optical fiber sensors. This influence is checked by monitoring the spectral characteristics of the sensors before, during and after the embedding process. Not only the material properties (CTE, Young's modulus, etc.), but also the curing process of the polymer (UV or thermally curable, curing time, temperature, pressure) can significantly affect or disturb the embedded fiber sensor in terms of sensitivity, sensing resolution and measurement reliability. Furthermore, the exact position of the optical fiber in the polymer host material can have a thorough influence on the measurement capabilities, for example in terms of bending measurements. A good understanding of the embedding sequences is indispensable to match the sensor responsivities to the application's needs. Moreover, by changing the appropriate processing parameters, one can tune the characteristics to avoid unwanted effects and increase the sensor's usability.

Optical fiber sensors have been embedded both in planar sensing foils but also in cylindrical tubes for biomedical applications. The resulting embedded fiber sensors have been characterized in terms of temperature, humidity, (contact) pressure, strain and bending measuring capabilities.

Most of the characterization tests have been performed within the framework of Phosfos and at different university labs. The characterization of the polymer fiber sensors was mainly performed at the Aston Institute of Photonic Technologies (Aston University, Birmingham, UK). The experimental characterization of the embedded microstructured silica fiber sensors has largely been performed by the Brussels Photonics Team (B-Phot, Vrije Universiteit Brussel, Belgium). Characterizing the embedded DTGs was performed at FBGS International (formerly FOS&S, Geel, Belgium).

First, the different types of fiber sensors and their specific advantages are briefly discussed. Next, the embedding techniques and associated polymer host materials are described in detail. Characterizing the embedded fibers is subsequently discussed according to the fiber sensor type (DTG - POF - MSF).

3.2 Optical fiber sensors selection

Different types of fiber sensors based on fiber Bragg gratings have been embedded and tested. An overview can be found in the next paragraphs.

3.2.1 Draw Tower Gratings

Draw Tower gratings (DTG®s) are a special type of fiber Bragg gratings in single-mode silica fibers. They are produced using a process that combines the drawing of the optical fiber with the writing of the grating [3]. An Ormocer® fiber coating is applied after grating inscription. As such, the commonly used stripping and recoating process of standard FBGs is not necessary and the pristine fiber strength is maintained during the DTG manufacturing process. FBGS International [4] masters this innovative highly automated production process and is investigating the possibility of making optical strain gage patches using fiber Bragg gratings in hard skin materials. For this purpose, standard FBGS silica draw tower gratings with Ormocer coatings are used.

The DTGs have some important advantages over the classical silica fiber Bragg gratings:

- Fully automated production process
- Reduced costs
- Highly reliable
- High strength: 5 % strain compared to 1 % for conventional FBGs
- Highly adhesive (compared to traditional acrylate based coating materials) coating (Ormocer®)
- High temperature resistance (200 °C)
- Batch Control & calibration possible
- Spliceless arrays (programmable)

These DTGs can be used within various sensing application domains including civil engineering, aerospace, oil and gas industry but also medical instrumentation [5].

3.2.2 Polymer Optical Fiber sensors

Polymer optical fiber sensors provide an interesting alternative for certain applications because of some specific advantages mainly related to the material properties. As mentioned in Chapter 2, great care must be taken when using glass fibers to protect against a fiber break which could exhibit a serious sharp hazard, especially for in vivo applications. Polymer fibers are an interesting alternative in this application domain as they do not suffer from this disadvantage. Moreover, POF has an elastic modulus roughly 25 times smaller than silica; consequently although the strain sensitivity of POFBGs is only marginally higher than their silica counterparts, the stress sensitivity is more than an order of magnitude higher.

Two different types of POF were available for embedding through Aston University (Aston Institute of Photonic Technologies) within the framework of the Phosfos project. During the optimization of the embedding process and the characterization of planarly embedded fiber sensors, a single-mode step-index fiber was used, whereas for the tubular embedding work, a multimode microstructured polymer fiber was used.

The single-mode step-index POF, supplied by Prof. Gang Ding Peng of the University of New South Wales, Australia, has a core diameter of 9.5 µm and a cladding diameter of 200 µm. The FBGs were inscribed at Aston University using 30 mW of continuous wave light at 325 nm obtained from a HeCd laser (Kimmon model IK5652R-G). With the fiber mounted horizontally in a V-groove, the 1.8 mm diameter beam was focused vertically down onto the fiber axis using a cylindrical lens of focal length 10 cm. A phase mask with period 1057 nm was placed on top of the fiber to generate a periodic intensity modulation in the core region. The laser beam was scanned 6 mm along the phase mask during the 30 min recording time. For further details of the inscription arrangement, see [6]. The inscription process was monitored by butt coupling the angle-cleaved end of a single-mode silica fiber coupler to the POF using a drop of index matching oil, the end of the POF having previously been cleaved using a razor blade on a hot plate at 80 °C.

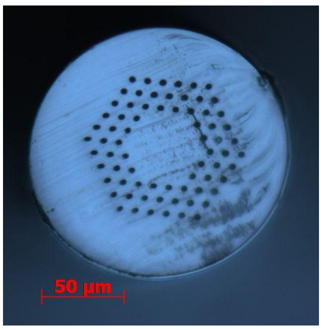

Figure 3.1 – Microscope cross-section image of microstructured POF used for POFBG inscription.

The multimode microstructured POF was obtained from Kyriama (Australia) and is a microstructured fiber with a 50 µm core surrounded by three rings of holes, see Figure 3.1. The fiber was manufactured from nominally pure poly(methyl methacrylate).

POFBGs can again be recorded in this fiber using 325 nm light from a HeCd laser [6]. For this work either two or three gratings were recorded at Aston University in a 20 cm length POF, separated by 2 cm. The gratings had a length of approximately 2 mm and were fabricated by exposing the fiber for approximately 50 min to the 30 mW laser beam after it had passed through a phase mask. In the case of the two grating sensor, two masks were used designed to produce gratings at 861 nm and 827 nm. For the three grating device, a grating was recorded at 861 nm and then the fiber was annealed at 70 °C for 24 h which reduced the Bragg wavelength by 16 nm [7]. Following the procedure, a second and third grating were recorded as described above. The end of the POF was glued to a 50 µm step-index silica pigtail, with the joint protected using a metallic tube filled with silicone. Figure 3.2 is showing a typical spectral reflection response of a multiplexed multimode POF sensor.

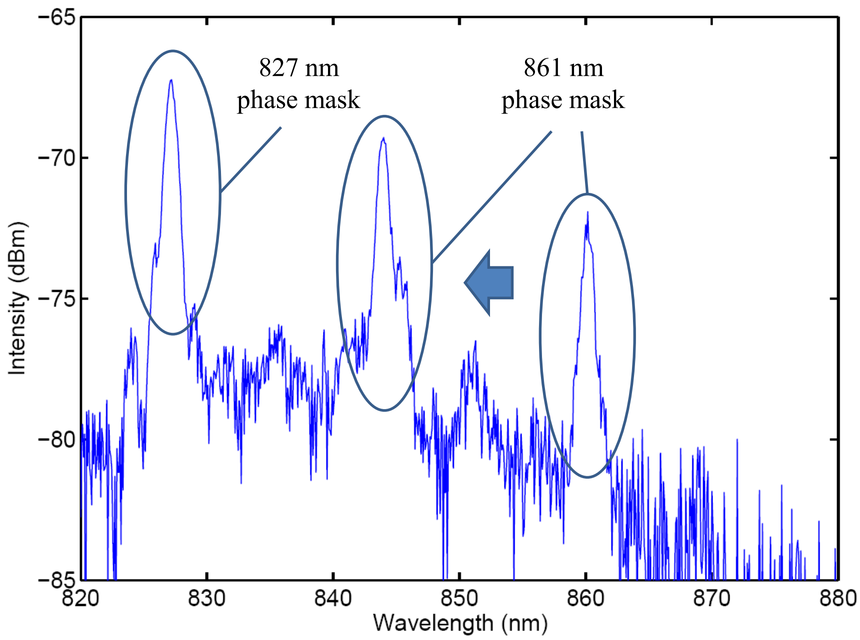

Figure 3.2 – Spectral response of a multiplexed polymer fiber sensor (3 POFBGs) fabricated using two different phase masks in combination with thermal annealing.

Interrogation of the POF is done using a coupler and a broadband light source covering the range 1530 nm to 1610 nm (Thorlabs, broadband ASE light source) while monitoring the reflection spectrum using an Optical Spectrum Analyzer

(OSA, HP86142A). In all experiments, a silica FBG was used as a reference and consequently each time embedded using the same embedding approach. The silica FBG was recorded in Single-Mode Fiber (SMF) at a Bragg wavelength of 1549 nm using a frequency-doubled argon ion laser with a 1071.9 nm period phase mask. The laser beam was scanned along the phase mask once to produce a grating 3 mm in length.

3.2.3 Microstructured Silica Fiber sensors

As discussed in Section 2.1.3, light is guided in the core of MSF by holes, typically filled with air. By modifying the air hole microstructure, i.e. by changing the hole diameter "d", or the distance between the air holes "Λ" and their location in the fiber cross-section, one can tailor the guiding properties of the fiber for specific applications and enhance its sensitivity to particular physical quantities [8]. The air hole topology of the MSFs under consideration has already demonstrated a high sensitivity to hydrostatic pressure [9]. Moreover, the phase modal birefringence in these MSFs is inherently insensitive to temperature as reported in [9] which helps avoiding complex temperature compensation systems.

Three different types of highly birefringent (HiBi) MSFs were available for embedding through Vrije Universiteit Brussel (VUB, Brussels Photonics Team) and Wroclaw University of Technology (WRUT) within the framework of the Phosfos project. The Scanning Electron Microscope (SEM) images of their cross-sections are shown in Figure 3.3. These MSFs were specifically designed to have a high transverse mechanical sensitivity and a low thermal response. They are based on a triangular lattice microstructure with some holes enlarged or missing. The MSF designs are briefly summarized in the following paragraphs.

The MSF type 090524P2 was designed by WRUT and is meant to have a high mechanical sensitivity. Due to the highly asymmetric microstructure the core itself is asymmetric and this will contribute to the total birefringence B_{modal} of the MSF. Moreover, the core is also weakly enclosed by air holes along the slow axis resulting in a low air-filling fraction d/Λ. This implies that higher-order modes will escape the core very easily along this direction, ensuring single-mode behavior but possibly also introducing high bending losses. A particular feature of this MSF is the hexagonal outer cladding, which could simplify orientation of the fiber during the embedding process.

The other two MSFs of type 090109P2 and 091023 were designed by VUB and are also designed to have a high transverse mechanical sensitivity. This is again achieved by making the microstructure highly asymmetric which also resulted in an asymmetric shaped core. The guided modes in these MSFs are better confined by air holes (large air filling factor), resulting in low bending losses. However, the tight confinement indicates that higher-order modes can be trapped in the core region. From the SEM images it is also clear that maintaining exact circular air holes or a circular outer cladding becomes increasingly difficult for more complex microstructures.

The cross-section of the silica fiber typically contains a doped GeO_2 core along the fiber length. The function of the germanium doped fiber core is to allow using conventional ultra violet fiber Bragg grating inscription methods. The FBGs were written with pulses of UV radiation originating from a KrF laser operating at 248 nm and with an interferometric Talbot system [10]. The writing of Bragg gratings in the germanium doped core of MSFs using this inscription technique has been reported in [11]. Average bare fiber temperature sensitivities for the different types of MSFs are listed in Table 3.1. Table 3.2 provides a similar overview for the pressure sensitivities. These values are based on [12, 13].

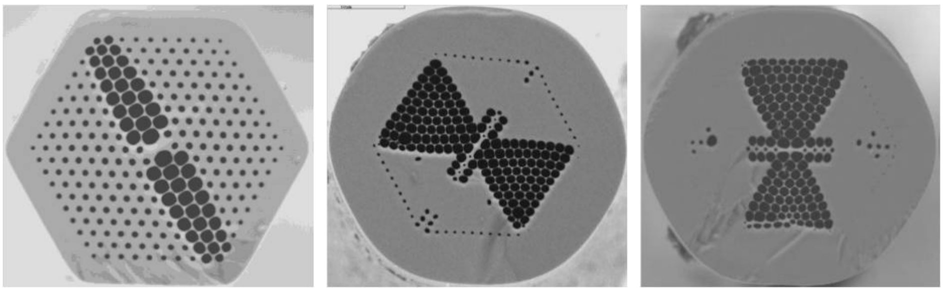

(a) WRUT design, type 090524P2 **(b)** VUB design, type 090109P2 **(c)** VUB design, type 091023

Figure 3.3 – SEM images of the cross-sections of the HiBi MSFs.

Table 3.1 – Bare fiber temperature sensitivities for the MSF sensors used within this chapter.

pm/°C	090524P2	090109P2	091023
fast axis		9.09	9.09
slow axis		9.02	9.02
peak separation		-0.07	-0.07

Table 3.2 – Bare fiber pressure sensitivities for the MSF sensors used within this chapter.

pm/bar	090524P2	090109P2	091023
fast axis	0.94	0.99	
slow axis	-0.22	-0.48	
peak separation	-1.16	-1.47	

3.3 Embedding techniques

The integration of optical fiber sensors in polymer host materials requires dedicated embedding techniques depending on the type of material and the desired shape of the embedded sensors.

3.3.1 Materials

Depending on the envisaged application, a different fiber embedding material is selected. In collaboration with the Polymer Chemistry and Biomaterials Group (PBM - Ghent University), the characteristics of the polymer materials can be further fine-tuned by carefully selecting the compounds which are added. Tuning can be performed in terms of mechanical flexibility, hardness, etc. [14]

A thermally curable polydimethylsiloxane (PDMS) material, Sylgard®184 from Dow Corning [15], has been selected as a first flexible and stretchable embedding material. Polydimethylsiloxane (commonly referred to as "silicone") is a linear polymer material with a -Si-O- backbone (a chain of siloxane units) and methyl side groups attached to every silicon atom, see Figure 3.4 [16]. The types of silicone considered in this dissertation are supplied as 2-component systems consisting of a liquid "base polymer" and a "curing agent" that polymerize by means of an addition-cure reaction. These 2 parts are mixed in a certain ratio (typically 10:1 or 1:1) to initiate the cross-linking or "curing" process.

(a) siloxane **(b)** polydimethylsiloxane

Figure 3.4 – Formula for siloxane and polydimethylsiloxane: if "R" is "CH_3" in the basic siloxane unit, it is named polydimethylsiloxane.

Sylgard®is a popular embedding material, enabling for example integrated electronics leading to smart textiles [17]. However, embedding optical fibers in this stretchable host material is a relatively new application (prior art see Chapter 2, Section 2.4). It is difficult to list exact mechanical properties of PDMS materials as they strongly depend on the preparation (e.g. amount of curing agent), application and curing parameters [18]. An estimation for a few important mechanical and optical parameters is nevertheless listed in Table 3.3. For a detailed discussion on the mechanical and optical properties of PDMS, we refer to the PhD dissertation of Jeroen Missinne [19] (Chapter 2, Sections 2.3 and 2.4). The curing process typically consists of mixing the silicone product with a curing agent (ratio 10:1). A slow thermal curing process at 60 °C for 2 h is typically applied.

Table 3.3 – Sylgard®184 material parameters

Parameter	Value
CTE	310 ppm/°C
Young's modulus	0.7-3.7 MPa
Poisson coefficient	0.46
Refractive index @ 589 nm[1]	1.413

As an alternative embedding material, Ormocer from Micro resist technology [20] has been selected, because of its compatibility with the Ormocer coating of the FBGS Draw Tower Gratings. Ormocer is an example of an inorganic/organic material developed by the Fraunhofer Institute [21]. The first step of the Ormocer synthesis is a hydrolysis/condensation reaction of functionalized alkoxysilanes and leads to the formation of organically modified inorganic nanoscale oligomers. After the addition of photoinitiator, the second processing step consists of a polymerization reaction, leading to a fully cross-linked three dimensional network. This is one of the reasons for the good structure accuracy up to temperatures of 270 °C in comparison to conventional thermoplastic materials. The Ormocer materials have been developed to come as ready-to-use photosensitive mixtures. Figure 3.5 shows the structural composition of the material.

Relevant thermal, mechanical and optical parameters are shown in Table 3.4. The curing process consists of a UV exposure, depending on material thickness, ranging from 5 s to 60 s at 10 mW/cm^2. A hard bake on a hot plate (typically 1 h at 150 °C) is applied resulting in a fully cured and flat Ormocer skin.

Table 3.4 – Ormocer material parameters

Parameter	Value
CTE	100-130 ppm/°C
Young's modulus	2.5 GPa
Poisson coefficient	0.45
Refractive index @ 635 nm	1.538

[1] PDMS cured on a hot plate for 2 h at 60 °C and refractive index n_d measured using an Abbe refractometer (21 °C).

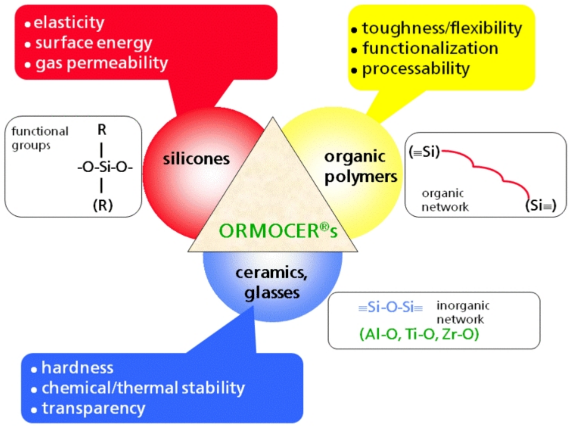

Figure 3.5 – Chemical structure of Ormocer, as developed by the Fraunhofer Institute [21].

3.3.2 Planar sensing foils

Molding

The first embedding technique is injection molding using a polymethyl methacrylate (PMMA) mold. In this approach, the fiber is temporarily fixed in channels on the edge of the mold. A slow curing (gradual temperature increase, starting at room temperature) and cooling process (cooling down to room temperature) is needed in order not to expose too much stress on the embedded fiber caused by the CTE mismatch (for example 310 ppm/°C for Sylgard®184 versus 0.55 ppm/°C for a standard silica fiber). The result of an injection molding process is illustrated in Figure 3.6a. To make not only straight embedded fibers but also other designs (e.g. horseshoe shape, see below), a design of a dedicated mold is needed. The fiber has then to be fixed not only on the edges of the mold but along the full mold design. A major drawback of this embedding technique is consequently the necessity of a new mold for every new design.

A similar approach, using glass molds and release foils can be used to fabricate embedded fiber sensors based on UV curable host materials. An example of a POF embedded in a UV curable resin is depicted in Figure 3.6b using the embedding approach shown in Figure 3.7.

Laser ablation

Laser ablation can be an alternative to easily adapt the fiber embedding design. Starting from a fully cured sheet, a track can be ablated to embed the fiber in.

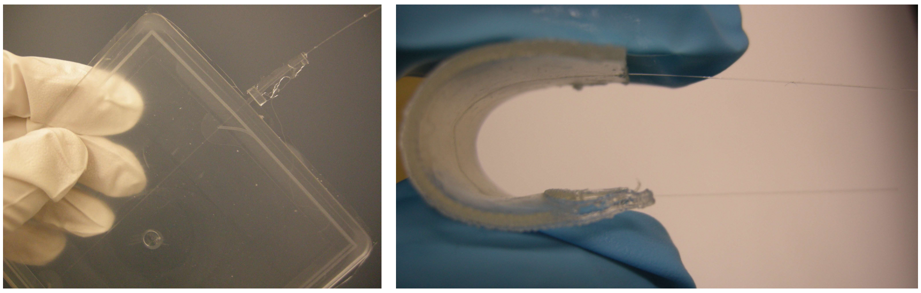

(a) molded silica fiber in Sylgard®184. **(b)** POF embedded in UV curable resin.

Figure 3.6 – Results of the injection molding process.

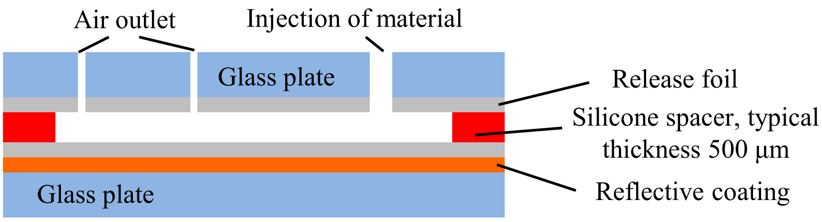

Figure 3.7 – Schematic view of the glass mold used for fiber embedding using UV curable host materials.

Three different laser sources have been evaluated for this purpose: a KrF Excimer laser (λ = 248 nm), a frequency-tripled Nd:YAG laser (λ = 355 nm) and a CO_2 laser (λ = 10.6 µm). The Optec laser system available at CMST and consisting of these three integrated lasers is shown in Figure 3.8.

Table 3.5 provides an overview of the most important parameters of the CMST Optec laser set-up.

Table 3.5 – Overview of the Optec laser system available at CMST.

	Excimer	Nd:YAG	CO_2
Wavelength	248 nm	355 nm	10.6 µm
Pulse duration	3-7 ns	35 ns	70 ns
Max. pulse energy	18 mJ	500 µJ	400 mJ
Max. pulse frequency	300 Hz	100 kHz	150 Hz

Due to the small spot size, the Nd:YAG laser was found to be less suited. Both Excimer and CO_2 could yield proper results in terms of ablation depth and width,

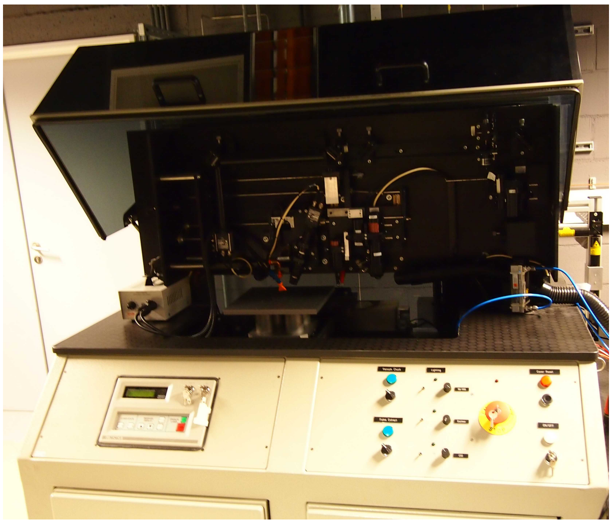

Figure 3.8 – Optec laser set-up installed at CMST.

depending on the absorption of the the flexible foil material at the specific laser wavelength. For Sylgard®184, the CO_2 laser provided the best results using a pulse frequency of 100 Hz, a typical ablation speed of 10 mm/s and varying laser fluences. After ablating tracks in the silicone material, a glue layer (Norland Optical Adhesive or instant adhesive) is needed to fix the fiber within these tracks.

The main advantage of using laser structuring is the straightforward definition of new embedding designs. Any CAD file can easily be exported to a laser drilling file. Results of silica fibers embedded into laser structured PDMS are shown in Figure 3.9.

Soft-lithography approach

An advanced fiber embedding technique has been investigated to control the fiber position on the optical skin even more accurately. The technique is based on a soft-lithography process which essentially consists of the transfer of a polymer master mold in the PDMS host material. A schematic view of the process flow is shown in Figure 3.10. As a master mold carrier, a silicon wafer is used but this can be any other substrate which has a low surface roughness. SU-8, a spin-coatable and photodefinable epoxy, is used as polymer master mold material. SU-8 is developed by MicroChem [22] and ideally suited for producing high-aspect ratio ($>$ 1:10) and thick (more than 200 µm) polymer structures. This material is optimized for permanent applications where it is left on the substrate after processing, making it ideal for creating master molds which can be used

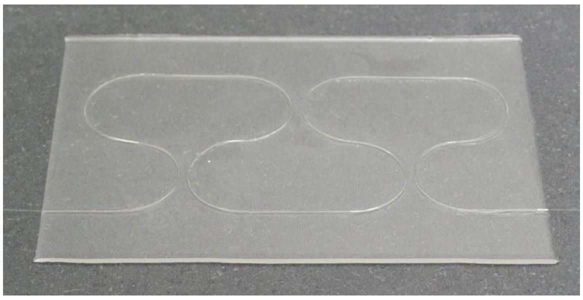

(a) Silica fiber.

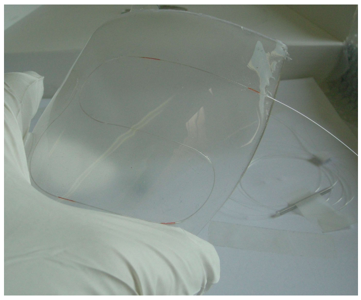

(b) Multiplexed microstructured silica fiber sensor.

Figure 3.9 – Fiber embedding using laser ablation to define meandering structures.

multiple times for replicating the structures [19].

An SU-8 100 layer is spin-coated and patterned by UV contact lithography (Figure 3.10a). This polymer structure will serve as a negative mask for the PDMS material. After a hard bake step of the SU-8, a controlled amount of PDMS material is poured on the silicon wafer and cured at 60 °C (Figure 3.10b). The bad adhesion between the UV patterned polymer and the cured PDMS enables a smooth release of the PDMS material once it is fully cured. The result is a patterned PDMS layer with U-shaped grooves (up to a thickness of 150 µm), Figure 3.10c.

The next step is placing, aligning and fixing of the fiber (Figure 3.10d). Depending on the track width and height, this can be done by either pressing the fiber into the tracks or by using an UV glue. This last technique ensures proper fixation of the fiber but has the disadvantage of introducing a hard, non-flexible intermediate layer between the fiber and the host material. The top layer thickness can be controlled by the use of a hot embossing press: by controlling the embossing pressure and temperature, the fiber embedding tracks can be filled up and the top layer thickness can be adjusted. A liquid (not cured) PDMS layer serves as a glue layer between the bottom layer including the embedded fiber and the (half cured) top layer (Figure 3.10e). An example of a microstructured silica fiber embedded in Sylgard®184 is shown in Figure 3.10f.

Next to the accurate fiber positioning, other advantages are the possibility to reuse the SU-8 mold and the convenience to adapt the fiber embedding pattern (also enabling meandering tracks in the PDMS material) by changing the mask design for the UV patterned master mold.

In the final process flow, the bottom and top PDMS layers are spin-coated on a temporary PEN or PET foil, a low-cost polymer substrate with bad adhesion to PDMS enabling release of the PDMS stack at the end of the process. After spin-coating, these layers are half cured before the next liquid, uncured layer is applied

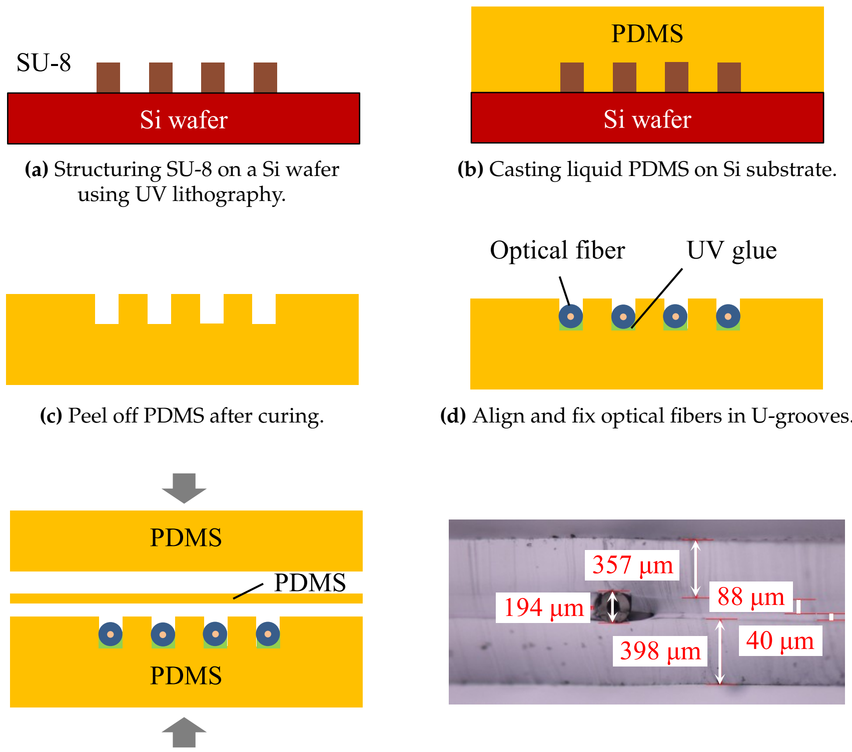

(a) Structuring SU-8 on a Si wafer using UV lithography.

(b) Casting liquid PDMS on Si substrate.

(c) Peel off PDMS after curing.

(d) Align and fix optical fibers in U-grooves.

(e) Embossing top PDMS layers (controlled temperature and pressure).

(f) Cross-sectional view on embedded microstructured silica fiber.

Figure 3.10 – Soft-lithography based fiber embedding process flow.

to enhance the adhesion between the different PDMS layers. Rather than casting PDMS on the rigid SU-8 wafer, the wafer is in this flow used as an imprint tool in an uncured layer. During this imprint, a full cure step for the PDMS is applied. An overview of this final process flow is presented in Table 3.6. By using similar process parameters for the top and bottom layer, the fiber can be embedded in the middle of the PDMS stack, as illustrated in Figure 3.11. Figure 3.11b and 3.11c show cross-sectional pictures of PDMS embedded POF.

Alternative techniques

An alternative method for embedding fibers within thermally or UV curable polymers is the use of an iron frame. The fiber is fixed under the iron frame and the polymer can simply be poured on the surface defined by this frame. This way the surface of the polymer including the embedded fiber is not covered by any mold. The mechanical manipulation of the optical fiber is consequently kept to a minimum. This process flow is particularly interesting for high viscosity embedding materials.

Table 3.6 – Process parameters for symmetrically embedding optical fiber sensors using soft-lithography approach.

Step	Description	Parameters
	Bottom sample	
(a)	Process SU-8 100 on silicon wafer	[22]
(b)	Spin Sylgard®184 on temporary PET foil	1 min at 250 rpm
(c)	Cure step 1 (sticky, half cured)	40 min at 60 °C on hot plate
(d)	Spin Sylgard®184	1 min at 250 rpm
(e)	Emboss silicon wafer with SU-8 pattern and cure Sylgard®184 using a press	90 min at 60 °C and 1 bar
(f)	Release PDMS stack from Si wafer	manually
(g)	Position optical fibers in PDMS tracks	
	Top sample	
(a)	Spin Sylgard®184 on temporary PET foil	1 min at 250 rpm
(b)	Cure step 1 (sticky, half cured)	40 min at 60 °C on hot plate
(c)	Spin Sylgard®184	1 min at 500 rpm
	Bonding top and bottom sample using press	
(a)	Place top sample (wet PDMS) on bottom sample preserving the position of the optical fibers	
(b)	Emboss wet PDMS layer and cure Sylgard®184 using a press	90 min at 60 °C and 1 bar
(c)	Release temporary PET foils from both sides	manually

3.3.3 Cylindrical sensing tubes

As an alternative for the planar sensing foils, cylindrical sensing tubes are needed for some specific applications such as esophageal manometry. For this purpose, typically polymer optical fiber sensors are used. The tubular embedding process of a multiplexed polymer fiber sensor is schematically shown in Figure 3.12.

The metal tube, protecting the glue joint between the POF and silica fiber connection, perfectly fits in the sensing tube. Dow Corning Silastic®Medical Grade Tubing (outer diameter of 4.65 mm and inner diameter of 3.35 mm) is used as a cylindrical tube and Sylgard®184 is again used as a flexible and stretchable em-

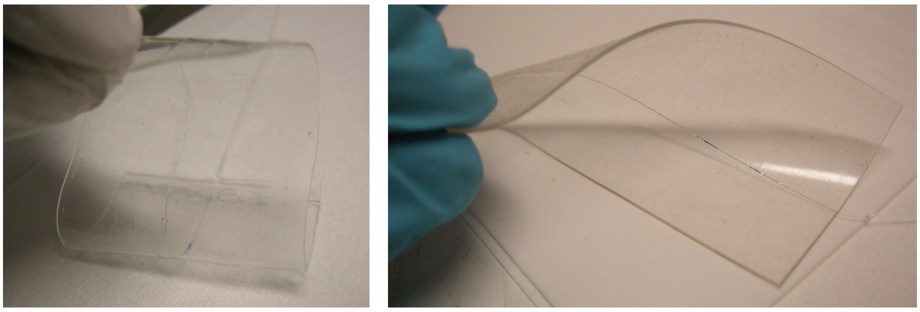

(a) POF embedded in PDMS using soft-lithography approach.

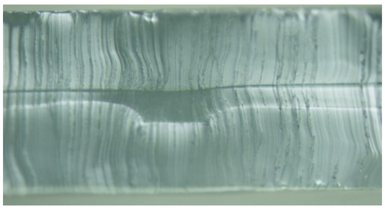

(b) Cross-section of soft-lithography based PDMS stack (without fiber).

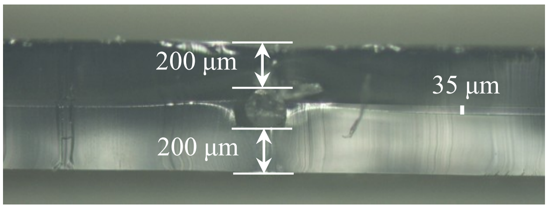

(c) Cross-section of soft-lithography based PDMS stack (with POF).

Figure 3.11 – Result of soft-lithography based PDMS embedding based on Table 3.6.

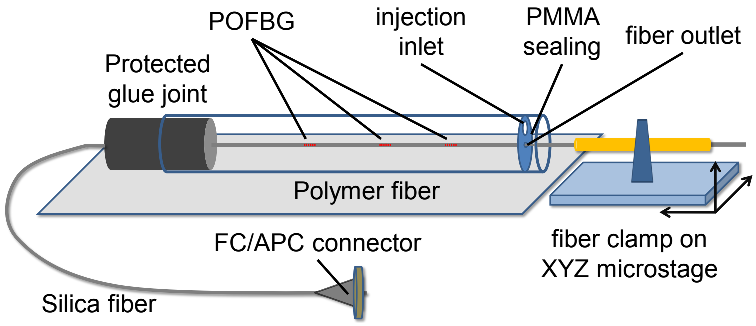

Figure 3.12 – Schematic view of the tubular POF embedding set-up.

bedding material. The tube is sealed on one end with a circular PMMA barrier accommodated with an injection inlet and a fiber outlet. This host material is injected in a liquid state via the injection inlet. By using a fiber clamp on a microstage, one can adjust the position of the fiber in the tube and prestrain the fiber before the final curing process is initiated. This way the fiber can be mounted in the middle of the tube and the position of the Bragg gratings can be accurately controlled.

Figure 3.13 is depicting a flexible polymer sensing tube and the PMMA sealing is shown in Figure 3.14a. Cross-sectional views (after fully curing the injected material) show a smooth interface between the fiber and the injected PDMS material (Figure 3.14b) as well as a good filling of the tube (Figure 3.14c). Similar tubes with silica fiber sensors are fabricated as a reference for characterization measurements (see below). An example of such a tube is shown in Figure 3.15. When illuminating the POF sensing tube with a 635 nm light source, the position of the gratings can be seen within the tube (shown in Figure 3.16).

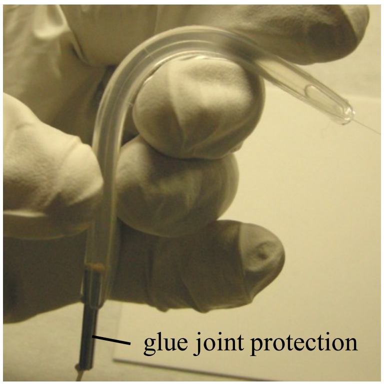

Figure 3.13 – Flexible polymer fiber sensing tube.

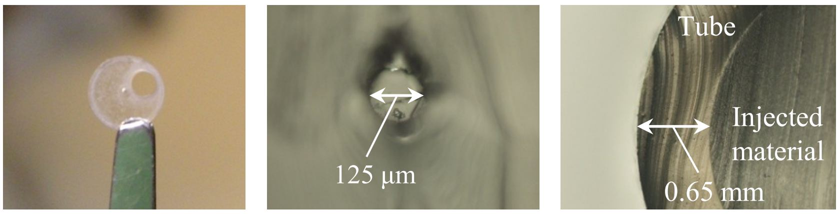

(a) PMMA sealing plate with fiber and injection inlet.

(b) Cross-section of an optical fiber in a sensing tube.

(c) Cross-section of the tube edge.

Figure 3.14 – Tubular embedding of polymer optical fibers.

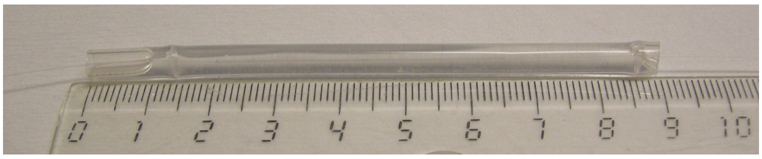

Figure 3.15 – Silica fiber sensing tube.

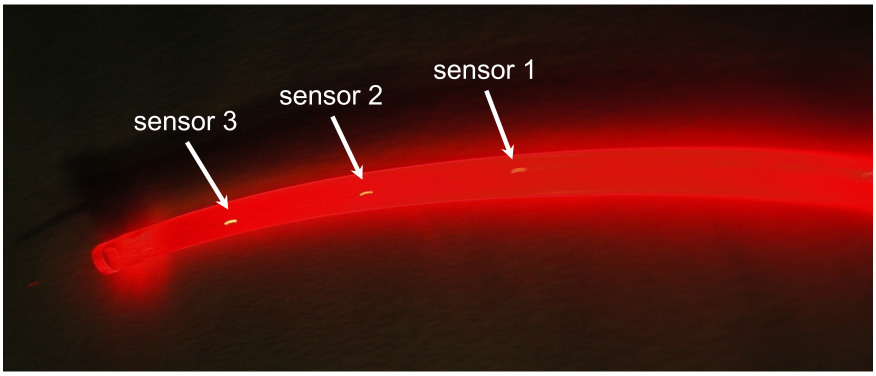

Figure 3.16 – Multiplexed embedded polymer fiber sensing tube illuminated with a 635 nm light source.

3.4 Integrated Draw Tower Gratings

The embedding and initial verification of the DTGs was performed by the PhD candidate. Most of the temperature and strain characterization tests however were performed at FBGS International (formerly FOS&S, Geel, Belgium).

DTGs have been embedded using a glass mold and Ormocer as a polymer host material (straight embedding design). The polymer skin is in this case a hard material to create a robust fiber optic strain gage patch. A result is shown in Figure 3.17a. Some samples have suffered from initial peak deformation. This can be seen in Figure 3.17b.

3.4.1 Temperature characterization

The first tests which have been carried out are the investigation of the temperature influence. The applied temperature cycles and the resulting peak wavelength shifts are shown in Figure 3.18. The peak wavelength drops; this is less pronounced in the second cycle but still visible.

Two possible explanations for the wavelength drop are:

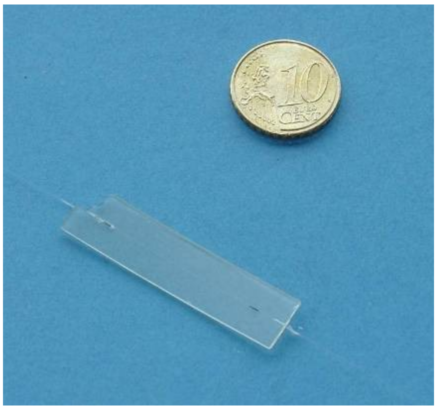

(a) Fiber optic strain gage patch.

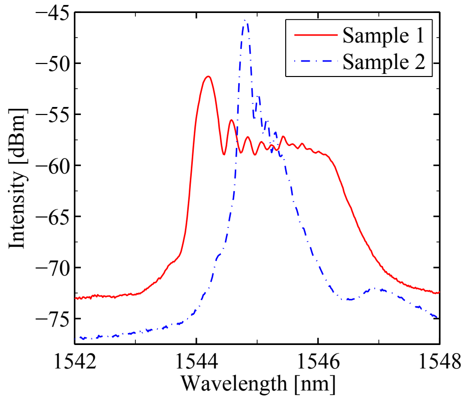

(b) Initial peak deformation, varying from sample to sample.

Figure 3.17 – DTG embedded in Ormocer.

- Relaxation of the Ormocer embedding material.
- Slippage of the fiber through the embedding material.

The resulting sensitivity is 111 pm/°C whereas the intrinsic DTG sensitivity is 10 pm/°C [2]. Consequently, the thermal expansion of the Ormocer is 84 $\mu\epsilon$/°C. In detail investigation shows a reduced peak deformation at elevated temperatures and an increased deformation at lower temperatures. We can conclude that the deformation is a result of the shrinkage of the Ormocer. A proper transfer of changing ambient conditions from the Ormocer embedding material to the Ormocer coated fiber is on the other hand a clear advantage.

3.4.2 Strain characterization

An embedded DTG is glued onto a metal plate which was 3 times stretched to 0.1 %ϵ (first time slightly more than 0.1 %ϵ, the second and third time slightly less than 0.1 %ϵ). The reference strain measurement was performed using an electrical extensometer (Figure 3.19a). The results are shown in Figure 3.19b and show the following remarkable features:

- During the first load cycle, the relation between strain and wavelength is not perfectly linear. The reason for this behavior is not fully clear. A potential explanation can be found in a mechanical setting of either the adhesive, the polymer or the fiber in its coating or skin embedding material. Dur-

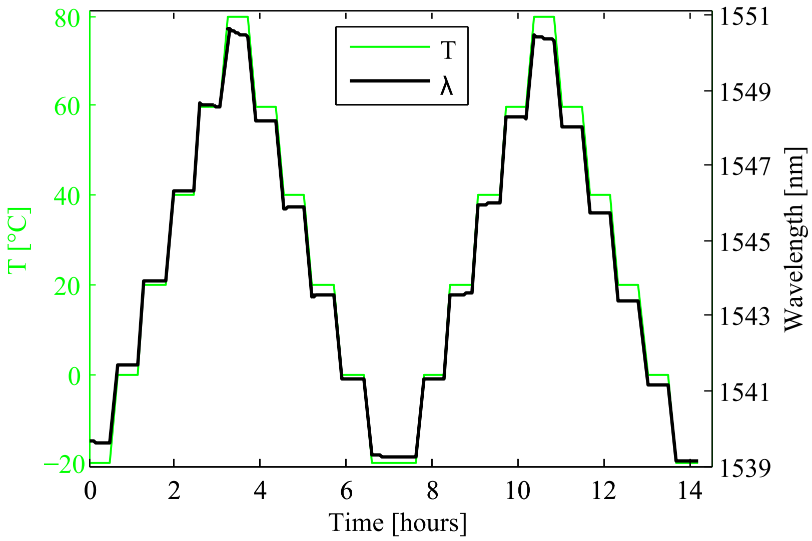

Figure 3.18 – Temperature cycle: temperature and wavelength shift versus time.

ing the second and third load cycle, the behavior is linear, which will allow reliable strain measurements.

- The strain sensitivity of the embedded fiber is about 9 nm/%ϵ, which is slightly lower than the free standing fiber (12 nm/%ϵ [2]). This can be attributed to the thin layer of Ormocer material in between the metal plate and the fiber, which does not fully transfer all strain from metal to fiber.
- The peaks are slightly deformed due to the embedding, but the shape remains nearly identical during the different load cycles. This indicates a good adhesion between fiber and Ormocer coating.

3.4.3 Meandering fiber embedding

In Figure 3.9a an example was shown of a fiber sensor embedded in Sylgard®184 using a meandering fiber embedding design. Both the optical power transmission characteristics as well as the strain induced wavelength shifts are influenced by this design. The most important parameter determining these properties is the radius of curvature. A radius of 2 cm yields a strain sensitivity of 0.31 nm/%ϵ whereas straight embedded fiber sensors in a similar stack provide a sensitivity of 4.84 nm/%ϵ. A more detailed discussion can be found in [23].

As mentioned in Chapter 1, the meandering fiber embedding concept is particularly interesting for pressure sensing applications on large-area substrates. A

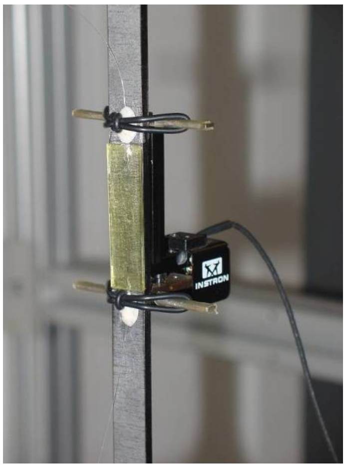

(a) Set-up.

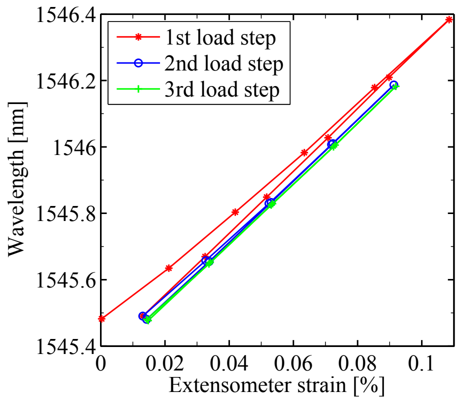

(b) Result of different loading steps.

Figure 3.19 – Ormocer embedded DTG strain characterization test.

single fiber can contain several sensing points at different Bragg wavelengths enabling quasi-distributed sensing. The spatial responsivity of the individual fiber Bragg gratings is related to the fiber embedding material.

3.5 Integrated Polymer Optical Fiber sensors

The integration and characterization of POFBGs in optical skin materials was performed in close collaboration with the Aston Institute of Photonic Technologies (Aston University, Birmingham, UK). In terms of workload distribution, the embedding and initial verification of the POFBGs was performed by the PhD candidate. The main part of the characterization tests was carried out by the Aston Institute of Photonic Technologies.

In this section, the experimental characterization results on the embedded POF samples are presented. The performance of the POF samples is often compared with that of embedded silica FBG samples to illustrate the increased level of sensitivity that POFBGs offer.

3.5.1 Planar

Effects of embedding

Following the inscription of the POFBG the fiber was glued to a silica fiber pigtail using UV curable adhesive (Loctite 3525). The reflection spectra of the FBGs were monitored before and after embedding in the optical skin, with the results being shown in Figure 3.20. The embedding was done using thermally curable PDMS material (Sylgard®184) and the iron frame technique (see Section 3.3.2). The use of the iron frame is minimizing the mechanical manipulation of the polymer fiber sensor and the fragile polymer - silica fiber interface. Embedding polymer fibers in flexible and stretchable PDMS materials ensures the preservation of the main advantage of POF which is its mechanical flexibility.

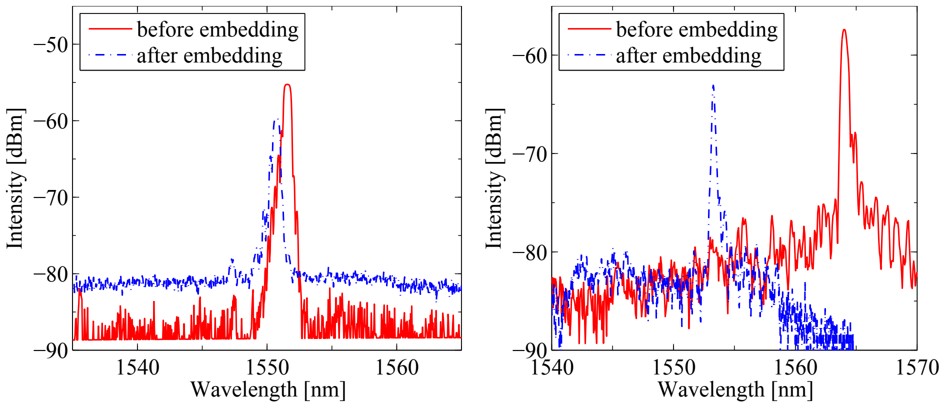

(a) Silica FBG **(b)** POFBG

Figure 3.20 – Reflection spectra of the FBGs before and after embedding in the polymer skin.

In the case of the reference silica FBG the embedding process induced a decrease in the Bragg wavelength of 0.8 nm (Figure 3.20a), probably caused by shrinkage of the polymer during the polymerization process. This wavelength shift corresponds to a compressive axial strain of 662 $\mu\epsilon$ [1]. By contrast, the POFBG displayed a decrease in wavelength of 10.8 nm (Figure 3.20b). This order of magnitude larger value is likely to be the result of two factors. Firstly, due to the much lower Young's modulus value for PMMA than silica (3 GPa [24] vs. 72 GPa [25], respectively), any compressive forces provided by the shrinking polymer skin will lead to a greater strain in the POF. Secondly, it has been shown that when FBGs in POF are taken for the first time above about 50 °C, there can be a large permanent blue shift in the Bragg wavelength associated with a shrinkage of the fiber length as residual axial strain induced during the drawing process relaxes out [26]. Heat generated during the polymerization of the skin (heat curing at 60 °C) may have been responsible for this effect.

Temperature

The temperature characterization of the POFBG sensing skins was carried out in an environmental chamber at constant humidity. The resulting graphs are shown in Figure 3.21 and the derived linear sensitivities are listed in Table 3.7. The comparison between silica FBGs and POFBGs is performed at 50 % RH. Varying the humidity for the characterization of embedded POFBGs (Figure 3.21b) results in constant linear sensitivities.

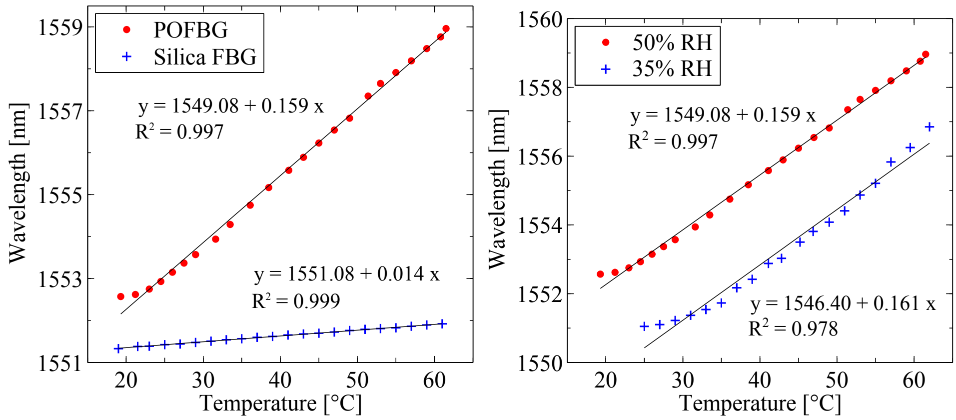

(a) Thermal sensing @ 50 % RH: POFBG vs. silica FBG

(b) Thermal sensing POFBG: 50 % RH vs. 35 % RH

Figure 3.21 – Thermal response of polymer embedded FBGs.

Table 3.7 – Temperature sensitivities POFBG characterization.

Bare fiber sensitivity		Skin sensitivity	
POFBG	Silica FBG	POFBG	Silica FBG
−43 pm/°C	10 pm/°C	159 ± 2 pm/°C	13.9 ± 0.1 pm/°C

The differences between the embedded and bare fibers are attributable to the skin material. As mentioned in Section 3.3, Sylgard®184 has mechanical properties that depend on the amount of curing agent used, the curing parameters etc. As a reference, the Young's E modulus can be approximated by 2 MPa and the CTE is 310 ppm/°C. In the case of the silica fiber, which has a much lower CTE but much higher Young's modulus, the fiber resists the thermal expansion of the surrounding skin and only exhibits a small increase in sensitivity. For the POF, the more elastic fiber follows the large expansion experienced by the skin more closely leading to a change of sign in the Bragg wavelength shift.

Humidity

POFBG humidity sensors are based on the affinity for water of PMMA, leading to a swelling of the fiber and an increase of refractive index. Both effects contribute to an increase in the Bragg wavelength of the FBG written in the fiber [27]. The humidity characterization of the sensing skins was carried out in an environmental chamber at constant temperature. The results are shown in Figure 3.22 and the derived sensitivities are listed in Table 3.8.

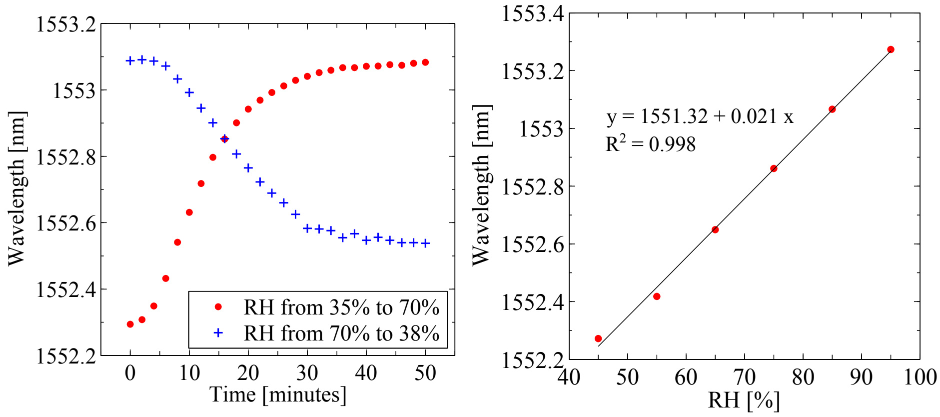

(a) Response to step changes in humidity **(b)** Humidity sensitivity

Figure 3.22 – Humidity response of polymer embedded POFBGs.

Table 3.8 – Humidity sensitivities POFBG characterization.

Bare fiber sensitivity		Skin sensitivity	
POFBG	Silica FBG	POFBG	Silica FBG
38 pm/%	0 pm/%	20.5 ± 0.5 pm/%	0.3 pm/%

The time response for the POFBG skin observed in Figure 3.22a of about 30 min is not significantly different compared to the bare fiber. The sensitivity to humidity observed in Figure 3.22b is roughly half that of the bare fiber, probably indicating that the PDMS host material (Sylgard®184) is acting to resist the humidity induced expansion of the fiber. The PDMS embedding material as such is also less sensitive to water absorption induced swelling than the POF material [28, 29], averaging the humidity effect at the interface between the embedding material and the polymer fiber.

Silica FBGs are not sensitive to humidity. However, in subsequent experiments a very small sensitivity of 0.3 pm/% was measured for silica FBGs. A potential explanation for this effect is the fact that those FBGs had been recoated before with a polymer to protect the fiber from mechanical damage.

Axial strain

The strain sensitivity of the skins was characterized using the apparatus shown in Figure 3.23.

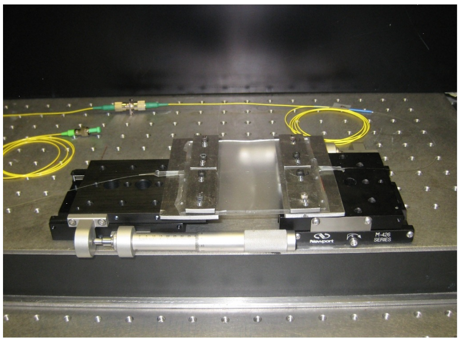

Figure 3.23 – Set-up for determining the strain sensitivity.

The skin was fixed to the translation stages by melting 8 holes (5 mm diameter) in the skin through which bolts could pass to clamp the skin between an aluminium plate and the stage. Initially a 5 mm gap was left in the clamp where the fiber was embedded to try to ensure that the fibers themselves were not directly strained, but rather that they were allowed to respond to the strain induced in the skin.

Figure 3.24 shows results up to 2 % relative strain for silica FBG (Figure 3.24a) and POFBG (Figure 3.24b). The silica fiber behaves very poorly even at modest strains of tens of millistrain. There is evidence of slip and slide behaviour leading to a considerable amount of hysteresis (1 % relative strain hysteresis when straining up to 2 %). Interestingly, even in the quasi-linear ranges, the strain sensitivity is only about 0.03 pm/$\mu\epsilon$, which is roughly a factor of 40 less than the sensitivity of the bare fiber (1.21 pm/$\mu\epsilon$) [2]. This proves that the strain transfer from the elastic skin to the stiff silica fiber is very poor. Extending the clamping area to the full width of the optical skin including the fiber to enhance the strain transfer produced no signficant increase in the strain sensitiviy. The POFBG exhibits a much more linear response ($R^2 > 0.999$) with very little hysteresis (Figure 3.24b, 0.05 % relative strain hysteresis when straining up to 2 %) and displays a sensitivity of 1.0 pm/µϵ. This is much closer to the bare fiber value of 1.5 pm/µϵ [30], but the difference is significant and demonstrates the disparity between the elastic moduli of the POF and the Sylgard material.

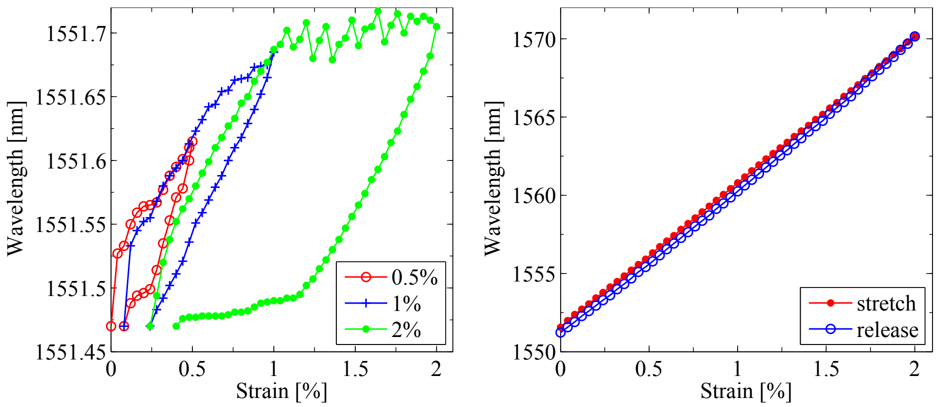

(a) Silica FBG **(b)** POFBG

Figure 3.24 – Strain response (up to 2 %) of polymer embedded FBGs.

In order to accurately control the fiber positioning in the optical skin, the soft-lithography approach (see Section 3.3) was used to produce alternative optical skins based on 850 nm microstructured multimode POF. Figure 3.25 shows the strain characterization results for a silica FBG and POFBG up to 5 %. The corresponding sensitivities are 0.098 ± 0.001 pm/µϵ for the silica FBG @ 1550 nm and 0.417 ± 0.002 pm/µϵ for the microstructured POFBG @ 865 nm.

Within [23], silica FBGs were embedded in Sylgard®184 using the laser ablation technique resulting in a sensitivity of 0.244 pm/µϵ at a wavelength of 1535 nm (not clamping fiber itself). Table 3.9 is summarizing the different axial strain sensitivities after referencing the values to their respective Bragg wavelengths λ_B.

Table 3.9 – Strain sensitivities $\delta\lambda_B/\lambda_B$ silica vs. POFBG characterization.

Bare fiber sensitivity (/ϵ)		Skin sensitivity (/ϵ)				
		iron frame		soft-lithography		laser ablation
POFBG	Silica FBG	POFBG	Silica FBG	POFBG	Silica FBG	Silica FBG
0.97 [30] 0.86 [31]	0.78 [2]	0.64	0.019	0.48	0.066	0.16

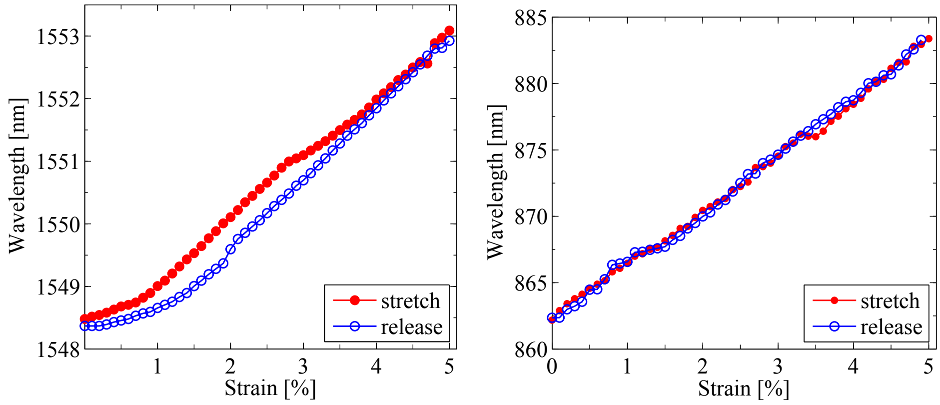

(a) Silica FBG

(b) POFBG

Figure 3.25 – Strain response (up to 5 %) of polymer embedded FBGs.

Especially for the silica FBGs, there is a clear dependence of the strain sensitivity on the embedding technique. There is no conclusive explanation for this effect. The iron frame technique consists of a one-step embedding approach providing only limited height control on the fiber embedding position. The soft lithography approach involves fiber clamping channels (see above, Section 3.3.2) and probably ensures a better fixation of the fiber in the optical skin material. The laser ablation approach requires the use of an adhesive (typically Norland Optical Adhesive) to fix the sensing fiber in the laser ablated tracks. This glue is presumably providing a more robust interface between the fiber and the embedding host material (PDMS - fiber vs. PDMS - glue - fiber) limiting fiber slippage. Extensive calibration measurements of the optical skin are in any case indispensable to interpret functional measurement data afterwards.

Contact pressure

Sensitivity to contact pressure was measured with the skin lying on a hard flat surface, using a cylindrical post (74 g, 12 mm diameter) on which additional weights could be placed in various positions relative to the FBG, centered at (0,0). This is shown in Figure 3.26a. The spatial sensitivity of the embedded POFBG to pressure is indicated in Figure 3.26b. Significant pressure signals are recovered up to a weight distance of 3 cm from the grating position (the wavelength shift value at (0,0) is omitted to increase the visibility of the lower values).

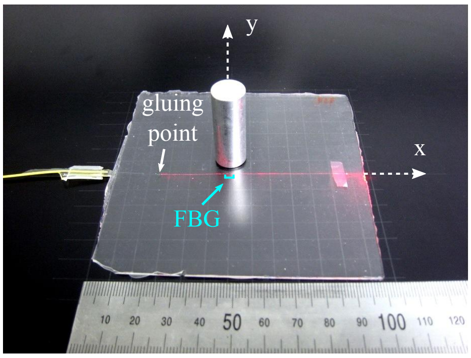

(a) Experimental set-up.

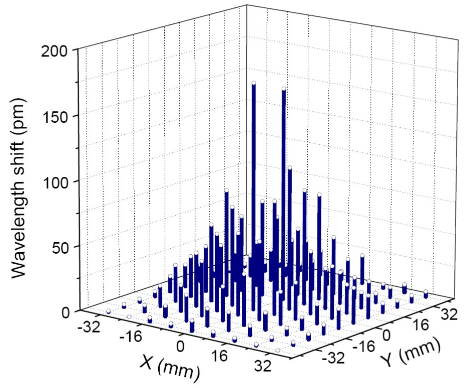

(b) Positional response of embedded POFBG to 74 g weight, (0,0) reading is omitted.

Figure 3.26 – POFBG: contact pressure characterization.

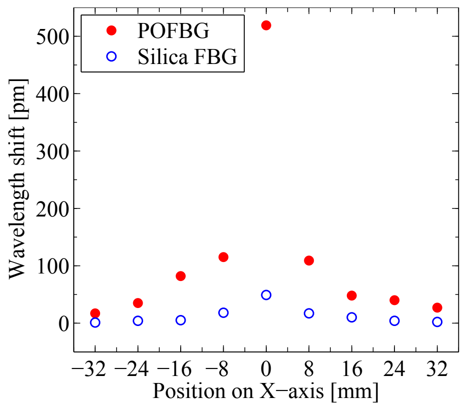

(a) Response of embedded silica and POFBGs to pressure along the fiber axis.

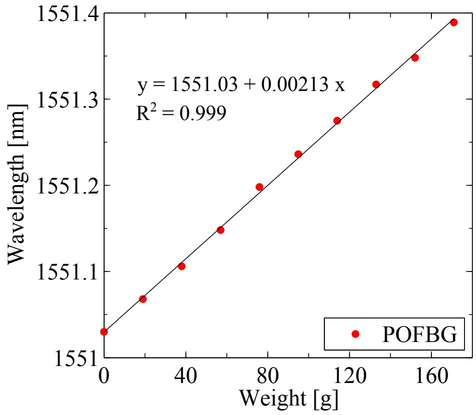

(b) POFBG sensitivity to a load at an 8 mm lateral offset from the grating position.

Figure 3.27 – POFBG: contact pressure characterization (continued).

The response to pressure along the fiber axis for both silica and POF sensors is shown in Figure 3.27a. It can be seen that the lower Young's modulus of the POF results in a sensitivity approximately 10 times greater than the silica FBG. Figure 3.27b shows the linear relationship between the Bragg wavelength and the applied weight at a lateral offset position of 8 mm for the POFBG. A sensitivity of 2.13 ± 0.03 pm/g corresponding with 24.2 ± 0.3 pm/kPa is obtained. High density tactile sensing applications typically require a pressure resolution of 0.5 kPa, easily obtainable using this photonic skin. Large area tactile sensing devices have a typical spatial resolution $\geq$1 cm (linear distance between 2 sensing points). The spatial responsiveness of the photonic skin is therefore also relevant for these applications.

Curvature

Unless deliberately made asymmetric in some way, FBGs are not sensitive to bending and curvature can only be monitored by locating the FBG away from the neutral axis of the structure under test. In this case bending results in a certain amount of strain in the fiber core. Depending on the exact position of the fiber in the optical skin, it is consequently possible to perform curvature measurements and tune the corresponding sensitivity. Respiratory monitoring is a typical application example requiring bending measurements. This example will be further discussed in Sections 5.4 and 6.4.

Figure 3.28 shows the curvature response for an embedded POFBG. Clearly the device posses significant curvature sensitivity, indicating the FBG is not in the middle of the skin. A sensitivity of $0.91 \pm 0.01\,\mathrm{nm/m^{-1}}$ is obtained. The grating strength is decreasing when the bending radius is getting smaller.

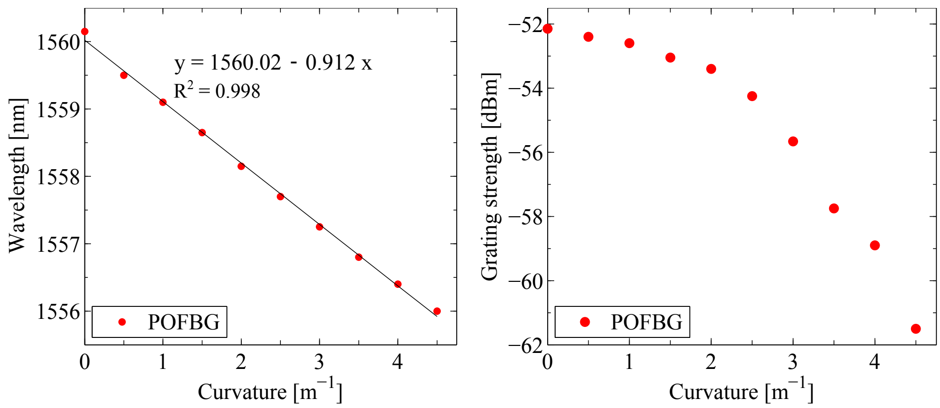

(a) Peak wavelength shift vs. curvature.

(b) Dependence of grating strength on curvature (noise level ≈ -70 dBm).

Figure 3.28 – POFBG: curvature characterization.

3.5.2 Tubular

The aim of tubular embedding optical fiber sensors is to come up with a biocompatible sensing device including different sensing points along the fiber axis. To achieve this, preferably polymer materials are used, both as a sensor and host material. Using the technology described in Section 3.3.3 multiplexed multimode POFBGs (Section 3.2.2) were embedded. The characterization results are listed in the following paragraphs.

Effects of embedding

Spectral analysis was performed before and after embedding the fiber sensors in the tubes. The resulting characteristics are shown in Figure 3.29a for the silica reference FBG and in Figure 3.29b for the multiplexed POF sensors. Curing of the PDMS material is done at 60 °C for the silica fiber and at room temperature for the polymer fiber in order to avoid further annealing of the Bragg gratings. The wavelength shift of the silica grating is because of the CTE mismatch between the PDMS (~300 ppm/°C) and silica (~0.55 ppm/°C). The wavelength shift of the polymer gratings is due to a fiber prestraining step after the PDMS injecting to have the fiber positioned as straight as possible.

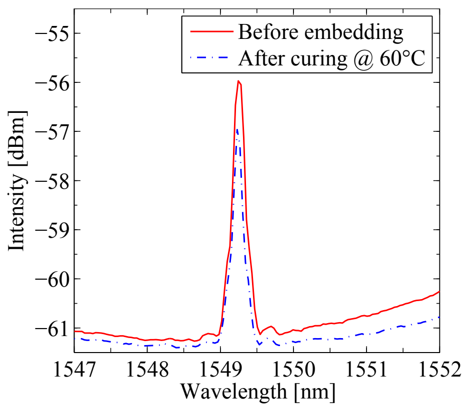

(a) Silica FBG

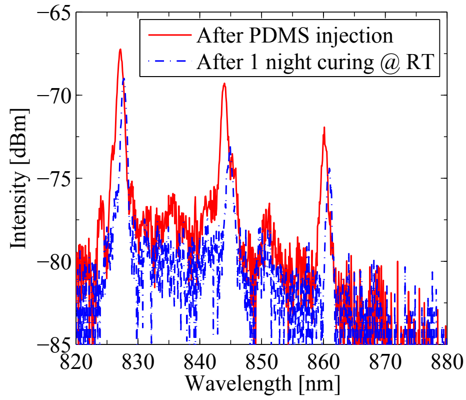

(b) POFBG

Figure 3.29 – Reflection spectra of the FBGs before and after embedding in the polymer tube.

Transverse loading

To quantify the sensor performance, two compliant sensing tubes were placed on a metal plate. One of the cylinders is embedded with the silica SMF grating of 1549 nm, the other is embedded with an array of two POFBGs of 827 nm and 861 nm. A metal beam with a width of 10 mm was placed on these two cylinders. The cylinders were carefully aligned so the silica FBG and one of the POFBGs were just lying under the beam for test. Weights were gradually applied onto the beam to simulate the radial squeezing, as shown in Figure 3.30. Since both cylinders have the same diameter the pressure can be equally applied to the gratings under test.

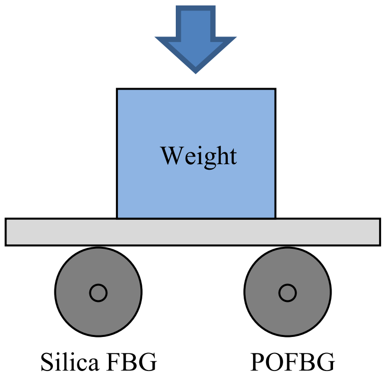

Figure 3.30 – Pressure characterization arrangement for the transverse loading of the sensing cylinders.

As the weights were gradually applied the transverse force caused an elongation of the cylinder as a result of Poisson's ratio. The Bragg wavelengths of the gratings vary with the applied transverse force. Figure 3.31 shows the response of a POFBG and the silica FBG to small loads. It may be seen that the wavelength shifts obtained are much greater in the case of the POFBG, a total wavelength shift of 336 pm, vs. 65 pm for the silica FBG. There is however more noise visible in the data from the POFBG sensing device.

The response of the device was also tested with larger forces, see Figure 3.32. It may be seen that the response of the POFBG (85.4 ± 7.1 pm/N) is a factor of 85.4/27.2 = 3.1 times greater than the silica device (27.2 ± 0.8 nm/N). It should be noted though that because of the different wavelengths of the two devices, the same strain would produce a wavelength shift in the silica device larger than that in the POF by the ratio of the wavelengths, namely 1.8. Consequently in terms of normalized sensitivity, the POF device is a factor of 3.1 x 1.8 = 5.6 greater than that based on silica fiber.

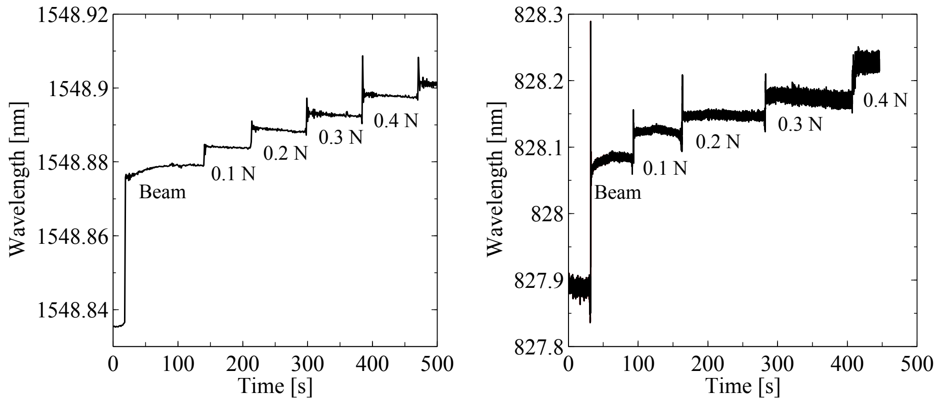

(a) Tubular embedded silica FBG **(b)** Tubular embedded POFBG

Figure 3.31 – Response of silica and POF sensors to small forces on the beam.

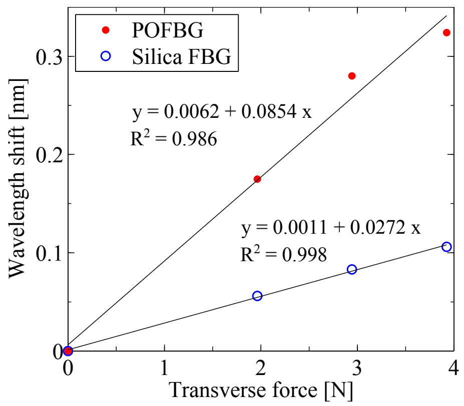

Figure 3.32 – Response of silica and POF sensors to larger forces on the beam.

Typical esophageal calibration measurements are performed with applied loads between 0 and 2 N [32]. End user requirements typically include a pressure range of 40 kPa and a resolution of 130 Pa. Also the amount of multiplexed sensors has to be further increased to 10 sensors separated by a typical distance of 2 cm.

3.6 Integrated Microstructured Silica Fiber sensors

The integration and characterization of MSFs in optical skin materials was performed in close collaboration with the Brussels Photonics Team (B-Phot, Vrije Universiteit Brussel, *Belgium). The embedding and initial verification of the MSFs was performed at CMST. The in-depth characterization tests were carried out by the B-Phot team, in particular within the master thesis of Sanne Sulejmani [13].*

In the following paragraphs the results of the experimental characterization of the embedded silica MSF samples are presented. The tested fibers were specially designed to have a high transverse mechanical sensitivity. This was achieved by introducing an asymmetry into the microstructure of the fiber by enlarging and removing air holes at specific locations. However, this dedicated design implies that the transverse load sensitivity of the fiber is orientation dependent.

3.6.1 Planar

Effects of embedding

Two MSFs of type 090109P2 and 090524P2 were embedded in a PDMS Sylgard®184 optical skin using the soft-lithography embedding approach. During the embedding process an attempt was made to fix the orientation of the MSF such that the direction that is most sensitive to mechanical loading was parallel to the skin surface. The final orientation could however not be checked after skin fabrication as this required a destructive test. The reflection spectra of the MSFs before and after embedding are shown in Figure 3.33.

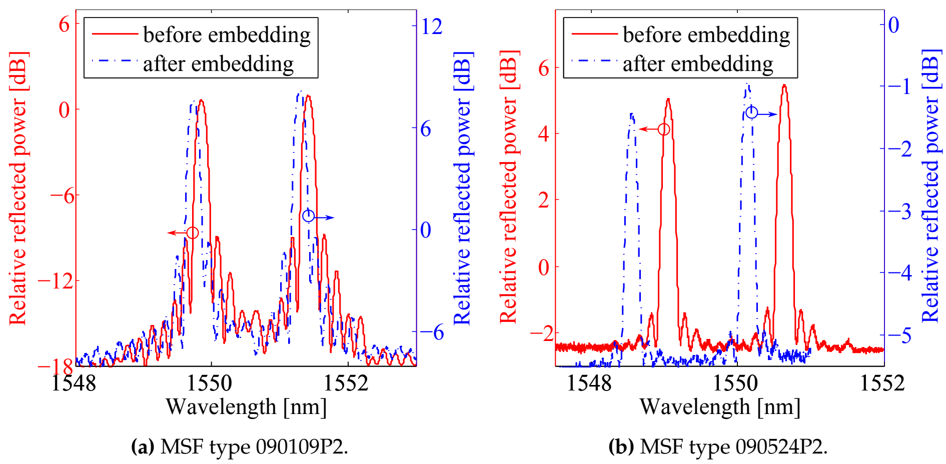

(a) MSF type 090109P2. **(b)** MSF type 090524P2.

Figure 3.33 – Reflection spectra of the FBG sensors fabricated in MSF before and after embedding in a PDMS skin.

Due to the embedding of MSF type 090109P2 the spectrum shifted about 120 pm to shorter wavelengths (Figure 3.33a), but well maintained its shape, and the

Bragg peak separation decreased only slightly by 8 pm. The overall shift of the spectrum is probably again the result of shrinkage of the polymer, but since the peak separation barely changed, we can conclude that this shrinkage is almost evenly distributed over the cross-section of the fiber. After embedding the MSF of type 090524P2 in the PDMS skin, its reflection spectrum shifted about 500 pm to shorter wavelengths (Figure 3.33b), while the Bragg peak separation decreased by 20 pm. Although the effects of polymer shrinkage seem to have a larger influence on this type of fiber, the spectrum has not deformed and both Bragg peaks are still well distinguishable.

Two MSFs of type 090109P2 and two MSFs of type 090524P2 were embedded in an Ormocer skin sample of 1 cm by 4 cm using the injection molding technique. Again efforts were made to fix the orientation of the fibers in the optimal position, but this could not be checked without destroying the samples. Figure 3.34 shows the reflection spectra of two different types of fiber before and after they are embedded in Ormocer.

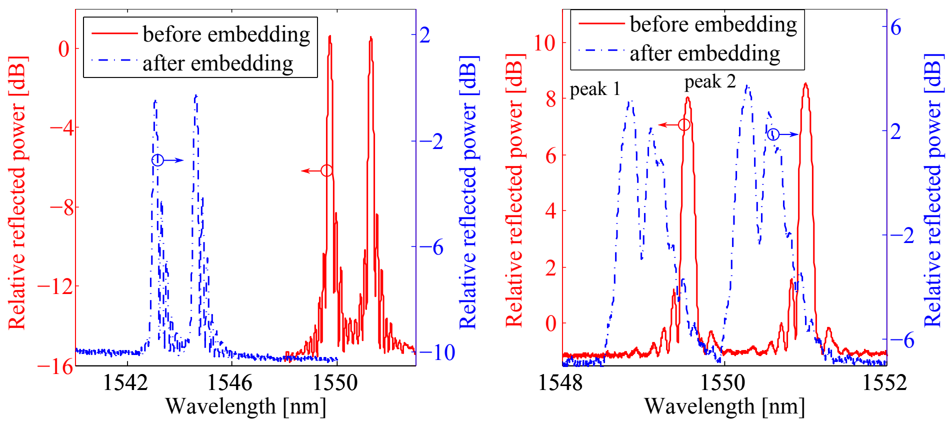

(a) MSF type 090109P2. **(b)** MSF type 090524P2.

Figure 3.34 – Reflection spectra of the FBG sensors fabricated in MSF before and after embedding in an Ormocer skin.

Embedding the MSFs of type 090109P2 led again to a shift of the spectrum to shorter wavelengths (Figure 3.34a). The overall shift is about 6.67 nm, indicating that the shrinkage of Ormocer (typically a few %) has a larger influence on the embedded fiber. The Bragg peak separation however only decreased by 14 pm, again proving that the polymer shrinkage is almost evenly distributed along the cross-section of the MSF. Due to a bad optical connection, the second sample fabricated with this type of fiber could not be tested. For both samples with MSF of type 090524P2 embedded, the spectra after embedding was heavily deformed and Bragg peak detection was difficult. There is again a shift of the spectrum to shorter wavelengths, but also significant peak splitting. Only one of these two fabricated samples could be tested and the monitored Bragg peaks are indicated in Figure 3.34b. The deformation of the spectra after embedding MSF type 090524P2 can indicate that this type of fiber is indeed more heavily influenced by polymer shrinkage, but can also be the result of embedding defects such as asymmetric strain distributions.

Finally, a MSF of type 091023 with an array of 4 FBGs inscribed was embedded in an Ormocer skin of 8 cm by 8 cm using the injection molding technique. The 4 FBGs are laid out parallel to each other, 1 cm apart. During embedding the orientation of the fiber was not taken into account, as this is difficult for arrays of FBGs.

Temperature

The two fibers embedded in the PDMS skin and the array of 4 sensors embedded in Ormocer were subjected to a temperature test. They were placed in an oven and temperature was increased from 28 °C up to 49 °C. During the test, their Bragg peak wavelengths were monitored with an OSA (Figure 3.35).

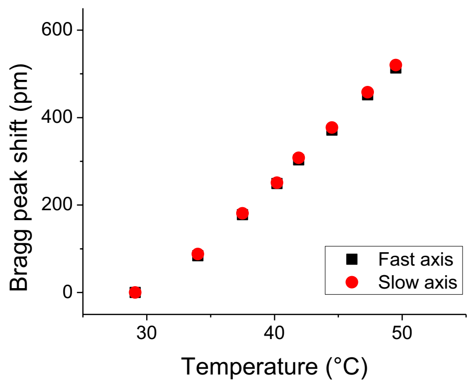

Figure 3.35 – Wavelength shift for temperature tests on a PDMS skin with a MSF 090109P2 embedded.

Table 3.10 summarizes linear fits of the recorded Bragg peak wavelength shifts. Comparing the results of the 090524P2 fiber and the 090109P2 fiber both embedded in PDMS, one clearly identifies a much larger temperature sensitivity for the individual Bragg peaks in the case of MSF type 090524P2. The sensitivity of the Bragg peak separation is however much lower (0.16 pm/°C vs. 0.30 pm/°C) but these values are still an order of magnitude higher than the temperature sensitivity of the Bragg peak separation of the bare MSFs (see Section 3.2.3, Table 3.1).

Table 3.10 – Temperature sensitivities (pm/°C) MSFs embedded in an PDMS or Ormocer skin. Standard error values (σ) reflect the variations between different experiments.

MSF type 090524P2 embedded in PDMS

	fast axis		slow axis		peak separation	
pm/°C	linear fit	σ	linear fit	σ	linear fit	σ
FBG1	47.09	1.86	47.25	1.80	0.16	0.07

MSF type 090109P2 embedded in PDMS

	fast axis		slow axis		peak separation	
pm/°C	linear fit	σ	linear fit	σ	linear fit	σ
FBG1	25.86	0.87	26.17	0.86	0.30	0.07

MSF type 091023K2 embedded in Ormocer (array of 4 FBGs)

	fast axis		slow axis		peak separation	
pm/°C	linear fit	σ	linear fit	σ	linear fit	σ
FBG1	7.83	0.43	8.22	0.51	0.38	0.10
FBG2	7.65	0.55	8.26	0.58	0.61	0.06
FBG3	7.48	0.68	8.07	0.68	0.59	0.07
FBG4	8.35	0.48	8.53	0.51	0.18	0.06

A wavelength multiplexed array of FBGs inscribed in the MSF of type 091023K and embedded in Ormocer has much lower temperature sensitivity of the individual Bragg peaks. This large difference between the two different host polymer materials is due to the higher CTE of PDMS over Ormocer (see Section 3.3). The temperature sensitivity of the Bragg peak separation for this sample was again rather low ranging between 0.18 pm/°C and 0.61 pm/°C. The different sensitivities monitored for the different FBGs inscribed in the same fibers are likely the result of different orientations of the fiber sensors. A different orientation of the fiber will influence the effect of thermally induced stresses. These values for the Bragg peak separation nevertheless confirm that the embedding process has a considerable impact on the temperature insensitivity of the sensor elements.

Contact pressure

The PDMS skin sample with two different types of fibers embedded is subjected to different types of pressure tests. The skin is placed on a hard flat surface, while loads are applied at different positions. A pressure experiment was performed with a load of 0.5 N that was applied with a metal ball with a diameter of 18 mm, as shown in Figure 3.36a. First, the shift of the individual Bragg peaks was monitored when the load was applied on several positions along a line that crosses the FBG sensor. The corresponding Bragg peak shifts for the FBG sensor fabricated in the MSF of type 090109P2 are shown in Figure 3.36b. A Gaussian fit was applied to the results and the details are summarized in Table 3.11. The maximum peak shift for the mode polarized along the fast axis (33 pm) is 2 pm higher than that of the mode polarized along the slow axis (31 pm). This implies a very small change in Bragg peak separation when the load is directly placed on top of the FBG sensor. The same experiment was performed on the MSF of type 090524P2 and the results are also summarized in Table 3.11. The maximum wavelength shift is larger for this sample, but no change in peak separation was observed. For both experiments, the Gaussian fits have a Full Width at Half Maximum (FWHM) ranging between 1.4 mm and 1.5 mm. This is an indication for the distance over which the embedded FBG sensor can still detect an applied load.

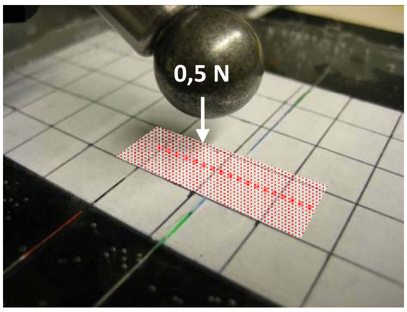

(a) Experimental set-up to apply a load to the optical skin using a metal ball.

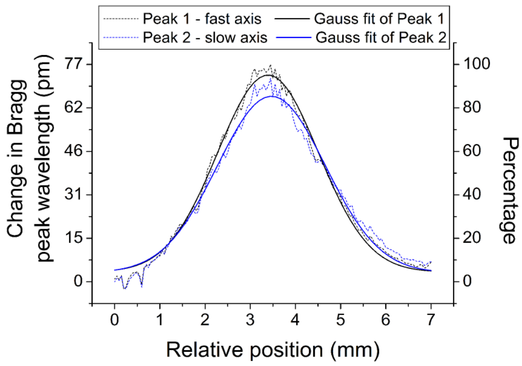

(b) Individual Bragg peak shifts of a PDMS embedded 090109P2 MSF induced by the loading along a line that crosses the FBG.

Figure 3.36 – Contact pressure characterization of embedded MSFs.

Table 3.11 – Gaussian fits of the results of the Bragg peak shifts of PDMS embedded MSFs.

	MSF type 090524P2		MSF type 090109P2	
	fast axis	slow axis	fast axis	slow axis
Max. peak shift (pm)	94	94	33	31
FWHM (mm)	1.44	1.54	1.41	1.44

This experiment was extended to scan the sensitivity of the skin over a larger area. Pressure was applied on more positions in an area of 6 mm x 13 mm, and for each position the wavelength shifts were monitored. The result is shown in Figure 3.37. Although we again see an increased sensitivity of the individual Bragg peaks at the position of the FBG, the influence of an applied load on the Bragg peak separation is minimal.

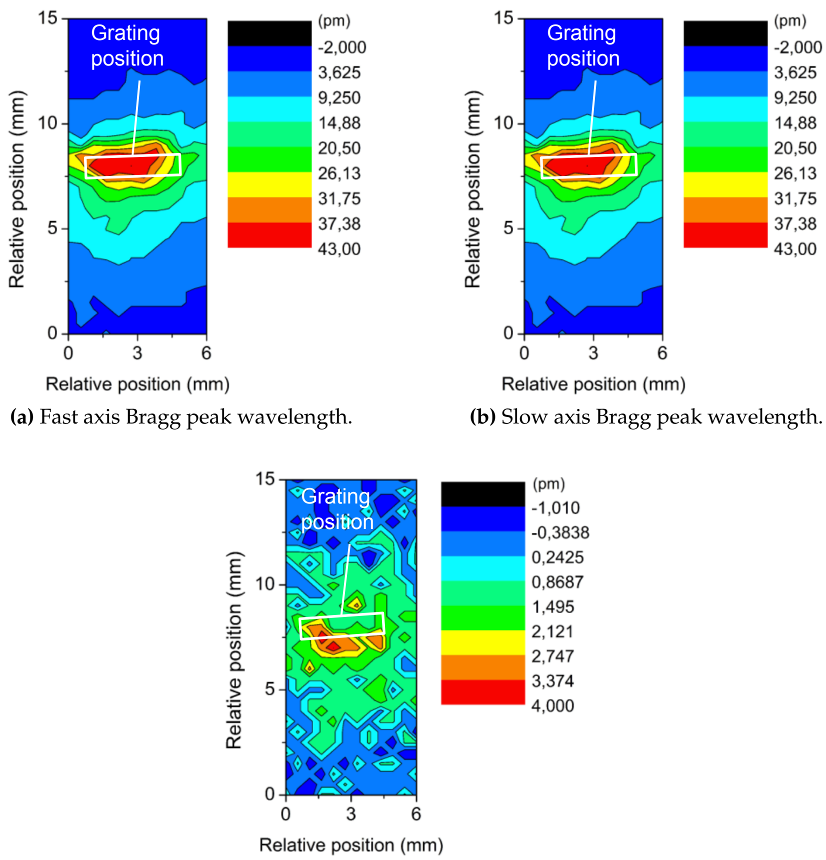

(a) Fast axis Bragg peak wavelength.

(b) Slow axis Bragg peak wavelength.

(c) Bragg peak wavelength separation.

Figure 3.37 – Contact pressure characterization of a PDMS skin with a 090109P2 MSF embedded. Color plots showing the wavelength change when a load of 0.5 N is applied at different locations.

The same experiment was carried out but with the load increased up to 5 N. Although this higher pressure led to larger wavelength shifts, it also caused the reflection spectra to deform when the skin was loaded directly or nearby the embedded FBG. When using a cylindrical load of 9 N and a larger flat contact surface (diameter 26 mm), these deformations did not take place. This is an indication that contact areas with dimensions comparable to that of the FBG (typically few mm) can lead to spectrum deformations.

Other experiments focused on the fibers embedded in Ormocer skins. First a load of 0.5 N was applied along a line on the skins that measures 1 cm by 4 cm. The experimental set-up was shown in Figure 3.36a. One of the contact pressure results of an embedded MSF type 090109P2 sample is shown in Figure 3.38 and the details of the Gaussian fits are listed in Table 3.12. For all three tested skins a different maximum Bragg peak shift is observed for the modes polarized along the fast and the slow axis. This results in a shift in the Bragg peak separation when the load is applied on top of the FBG, albeit a small shift. The shift of the individual Bragg peaks is again highest for the MSF of type 090524P2, as was the case for the PDMS skins. The FWHM of the Gaussian fits ranges between 2 mm and 2.4 mm, indicating that sensors embedded in Ormocer skins can detect pressures over a larger area than sensors embedded in PDMS skins.

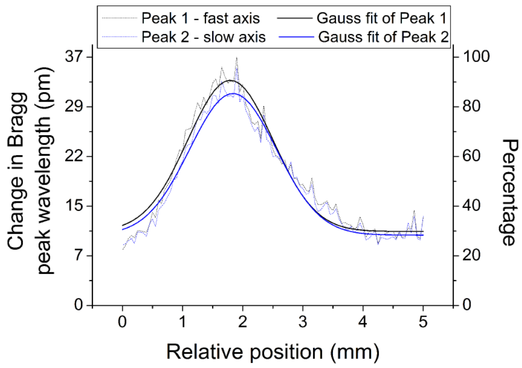

Figure 3.38 – Individual Bragg peak shifts of an Ormocer embedded 090109P2 MSF induced by the loading along a line that crosses the FBG.

Table 3.12 – Gaussian fits of the results of the Bragg peak shifts of Ormocer embedded MSFs.

	MSF type 090524P2 Sample 1		MSF type 090109P2 Sample 1		Sample 2	
	fast axis	slow axis	fast axis	slow axis	fast axis	slow axis
Max. peak shift (pm)	120	117	74	66	50	37
FWHM (mm)	2.16	2.16	2.23	2.39	2.33	2.04

The Ormocer skin with the array of FBGs embedded was tested with the same experimental set-up, but the load was increased to 5 N and a larger area was scanned. For each position where a load was applied, the Bragg wavelengths shifts were recorded and the results are shown in Figure 3.39. We see again an increased sensitivity of both the individual Bragg peaks as the peak separation nearby the location of the FBG. However, the reflection spectra deformed heavily when the load was applied on top or close to the FBG. No reliable results were consequently obtained for these positions and they are therefore left blank in Figure 3.39. It can be concluded that the practical applicability of the MSF sensors is limited using the polymer embedding technology in its current state.

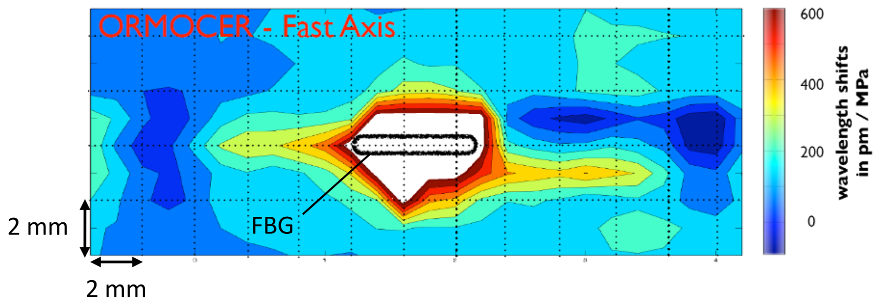

(a)

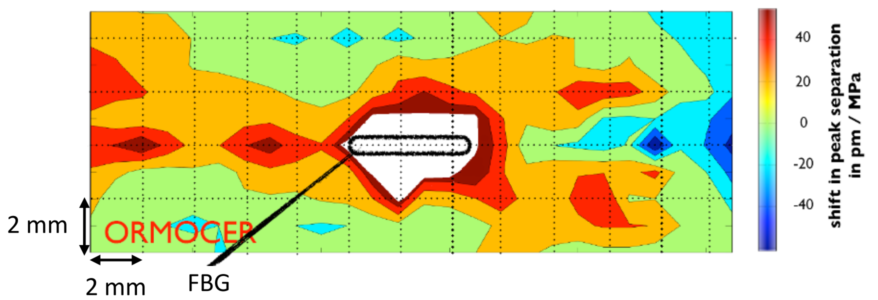

(b)

Figure 3.39 – Contact pressure characterization of an Ormocer skin with a 091023 MSF embedded. Color plots showing the wavelength change when a load of 5 N is applied at different positions.

3.6.2 Macrostructuring to enhance pressure sensitivity

In the previous section only small or moderate contact pressure sensitivities were achieved for the Bragg peak separation of the MSFs embedded in either a PDMS or an Ormocer skin. In this paragraph, an approach is presented to overcome the current limitations and increase the contact pressure sensitivity of the sensor elements via the use of *macrostructuring*.

The experimental contact pressure skin results indicated that the transverse mechanical sensitivity of the polymer embedded MSF system is significantly lower compared to the bare MSF's high transverse mechanical sensitivity. This is due to the mismatch between the transducer layer (PDMS or Ormocer) and the silica fiber limiting the portion of stress transferred to the embedded Bragg grating. To fully exploit the benefits of the microstructured fiber sensors, it is important to investigate how physical quantities can be best transformed into a parameter that can be sensed locally by the fiber grating.

To increase the compatibility between the embedding host material and the optical fiber, one possibility is to use the polymer optical fibers (Section 3.5). As an alternative, it is possible to introduce a structure that maximizes the stresses present in the region surrounding the optical fiber. This is investigated in detail within the PhD research of Sanne Sulejmani [13]. Figure 3.40 provides an overview of a few macrostructuring possibilities and the theoretical increase of the peak separation pressure sensitivity.

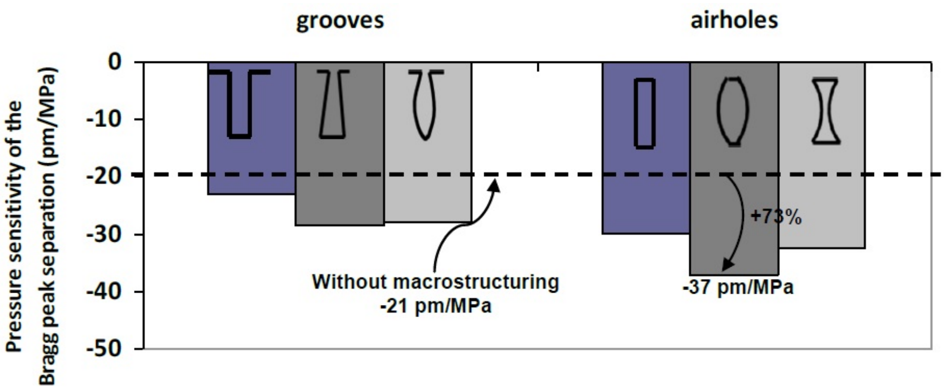

Figure 3.40 – Overview of the possible improvement to the pressure sensitivity when different types of macrostructures are applied.

Experimental work to fabricate these macrostructured grooves was performed by using a CO_2 laser (λ=10.6 µm). Scanning different parameters (Figure 3.41) provided fabrication parameters for different groove widths and depths.

First experimental results using macrostructuring grooves of almost 500 µm wide

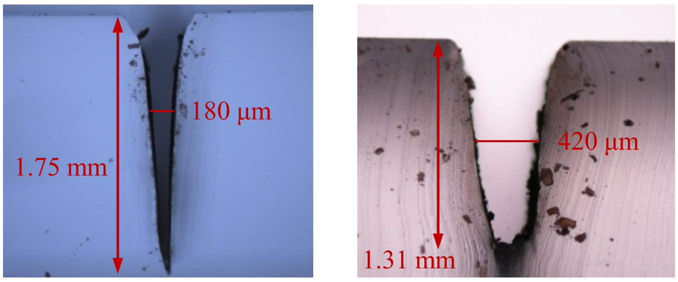

(a) Ablating 1 groove at 0.8 mm/s

(b) Ablating 4 adjacent grooves with 100 µm spacing at 2 mm/s

Figure 3.41 – Defining macrostructuring grooves by CO_2 laser ablation using a pulse repetition frequency of 100 Hz, 0° attenuator, a circular mask with 4000 µm diameter and 10x lens demagnification.

and 1.75 mm deep yielded a peak separation sensitivity of 55 pm/MPa. A sample with a similar embedded MSF without grooves provided a reference sensitivity value of 25 pm/MPa.

3.7 Advanced fiber embedding

3.7.1 Locally embedded

Instead of full planar sensing layers, there is often a need for locally pressure sensitive islands. This way the application of an external strain or pressure is localized on the fiber Bragg grating, enhancing the sensitivity of the fiber sensor, especially in the case of MSF, and avoiding cross-talk between the different sensor points.The interconnection between different sensing points is then based on (uncoated or coated) bare fiber. Using a dedicated mold, these pressure sensitive islands can be fabricated. An example of such a mold is shown in Figure 3.42 including fiber alignment tracks, material inlet and air outlet channels.

Figure 3.43 is depicting an example of silica fiber Bragg gratings locally embedded in MED-6015, a PDMS material from Nusil [33] as well as a cross-sectional view on the embedded silica fiber (with fiber coating, total diameter 250 µm).

3.7.2 Stacking optical skins

For respiratory monitoring applications, bend sensors are typically required. One option is to mount two separate gratings symmetrically either side of the neutral axis in an optical sensing skin. With such an arrangement, the difference between

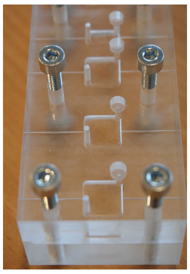

(a) Top view.

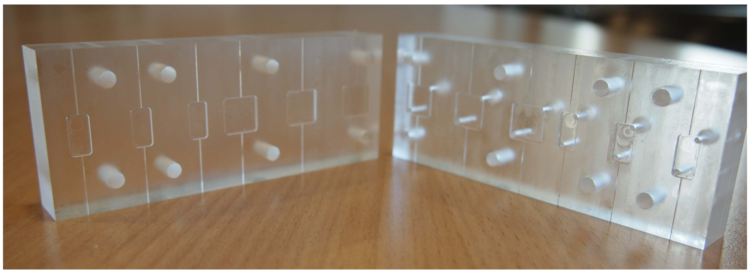

(b) 6 pressure sensitive islands can be molded in parallel.

Figure 3.42 – Dedicated mold to fabricate locally embedded fiber Bragg grating sensors.

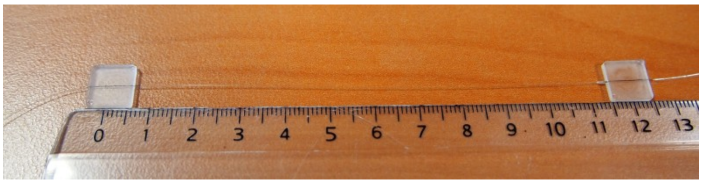

(a) Locally embedded sensor islands.

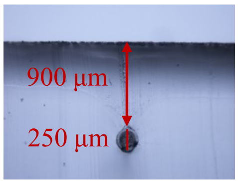

(b) Cross-sectional view - coated fiber.

Figure 3.43 – Silica fiber embedded in Nusil MED-6015 using dedicated mold.

the two Bragg wavelengths is sensitive to bending but not sensitive to common mode strain or temperature. The stacking of two optical skins, each containing a single FBG, was achieved by plasma activating both optical skin surfaces, followed by an aligning and dry bonding step using an air plasma generator (Diener Pico, 0.8 mbar, 24 s, 190 W, 40 kHz). Figure 3.44a depicts a schematic view on this bonding process. Aligning the two optical skins before bringing them into contact is done using a mask aligner system (SET MG1410) which was modified by placing an adapter plate containing an extra vacuum chuck in the mask holder (holding Optical skin A in Figure 3.44b). Optical skin B was fixed in place on the substrate table of the aligner, using another adapter plate and the standard vacuum connection. Using the available positioning table and microscope of the aligner system, it was possible to align both optical skins. Once aligned, the PDMS layers were brought into contact, creating an irreversible bond of the plasma treated layers.

First prototypes of stacked silica and polymer fiber sensors are shown in Figure 3.45. In the case of POFBG stacking, it is important to position the silica - POF glue joints sufficiently separated from each other.

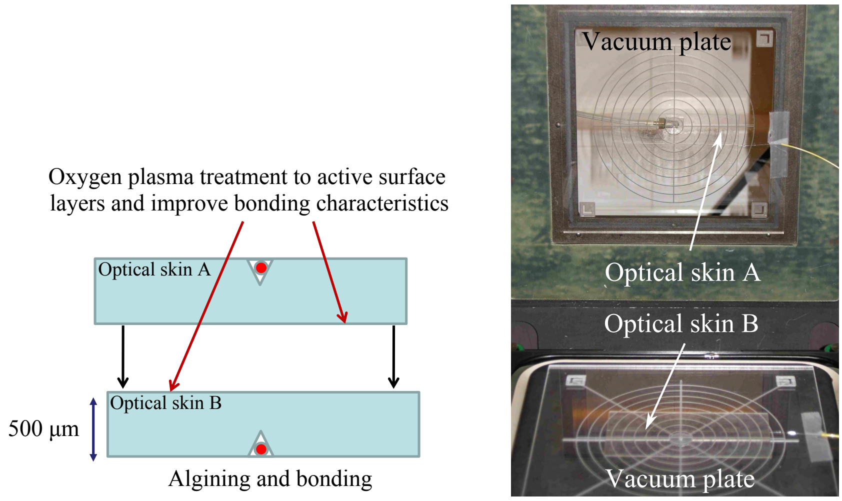

(a) Schematic view.

(b) Aligning two optical skins using a modified mask aligner set-up.

Figure 3.44 – Stacking two optical skins through aligning and dry bonding through plasma surface treatment.

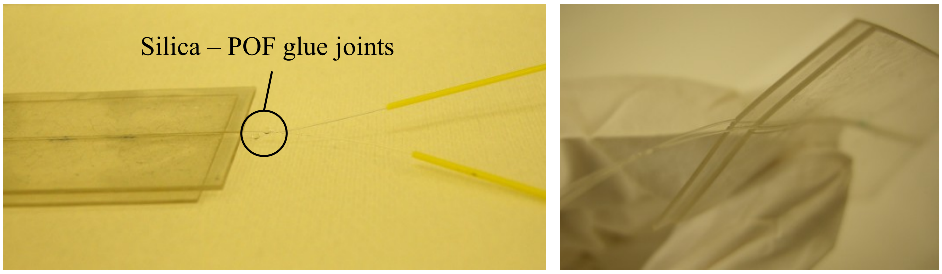

(a) POFBG.

(b) Silica FBG.

Figure 3.45 – Stacking optical skins to perform bending/respiratory measurements.

3.8 Conclusion

Different fiber embedding techniques were developed in this chapter. Depending on the application need, a soft or more stiff material can be chosen as a host material. Several embedding techniques were investigated: molding, laser ablation and soft-lithography, each possessing their specific advantages.

The sensing elements used within this chapter are based on either Draw Tower

Gratings, Polymer Optical Fiber Gratings or Microstructured Silica Fiber Gratings. The DTGs offer a commercially available and highly reliable sensor option whereas the MSFs allow for tuning the sensor response to certain parameters (increased transverse mechanical sensitivity, limit temperature cross-sensitivity). The POFBGs provide a safe alternative for potential sharp hazards when using silica fibers. Mainly because of the excellent compatibility with polymer embedding materials, they also offer a much higher sensitivity for mechanical loading.

Next to the planar optical skin foils, multiplexed POFBGs were also embedded in tubular devices to enable pressure measurements in the esophagus.

The responsivity of planar embedded MSFs was rather limited because of a complicated transfer from the applied load to the actual sensing fibers. More specifically, the polymer host material is acting as a transducer material transferring but also affecting the applied mechanical loads to the MSF. Temperature variations are introducing asymmetric stresses and transverse strains are partially redistributed. There are different solutions to solve this problem. One option is to create locally embedded fiber sensors to limit the spatial distribution of the applied loads. An alternative is macrostructuring the optical skin material to locally maximize the externally applied strain or pressure. Both embedding technologies are under investigation.

Stacking different optical skins on top of each other can provide additional opportunities for integrated fiber sensing such as respiration monitoring through bending measurements.

An overview of the different sensitivities measured throughout this chapter is listed in Table 3.13. For the MSFs, the sensitivity of the individual peaks is an average value for the fast and slow axis (split values can be found in Section 3.6.1).

Table 3.13 – Relative sensitivities of the planar embedded fiber sensors $\delta\lambda_B/\lambda_B$.

Fiber type	Embedding material	Temperature (10^{-6}/°C)	Pressure (10^{-6}/N)	Axial strain (/ϵ)
DTG	Ormocer	72		0.58
SMF	PDMS	9.0	44	0.02 - 0.16[2]
POFBG	PDMS	103	461	0.48 & 0.64[3]
MSF - individual peaks	PDMS	17 & 30[3]	41 & 121[3]	
MSF - peak separation[4]	PDMS	0.10 & 0.19[3]	≈ 0	
MSF - individual peaks	Ormocer	5.2	73 & 154[3]	
MSF - peak separation[4]	Ormocer	0.28	14 & 3.9[3]	

[2]Highly dependent on embedding process.
[3]Dependent on fiber type.
[4]Dependent on fiber orientation.

The aim of this chapter was to come up with a sensing skin based on polymer embedded fiber sensors. Depending on the application, a different embedding approach and fiber type can be selected. The tubular embedded polymer fiber sensors proved to be compatible with esophageal measurement requirements. Embedded MSF sensors are typically used within harsh (high temperature and pressure) environments. Further research is needed however to maintain the functionality of these sensing systems once embedded in a polymer host material. Polymer optical fiber sensors have a relatively low reflectivity, limiting the options for fully embedded interrogation systems. For the remainder of this dissertation, the main focus is therefore on silica fiber sensors (DTG or other) in order to come up with a proof-of-principle fiber sensing system. An outlook will be provided towards specialty fiber sensors and polymer fiber sensors.

References

[1] A. Kersey, M. Davis, H. Patrick, M. LeBlanc, K. Koo, C. Askins, M. Putnam, and E. Friebele, “Fiber grating sensors,” *Journal of Lightwave Technology*, vol. 15, no. 8, pp. 1442–1463, Aug. 1997.

[2] K. Hill and G. Meltz, “Fiber bragg grating technology fundamentals and overview,” *Journal of Lightwave Technology*, vol. 15, no. 8, pp. 1263–1276, Aug. 1997.

[3] FBGS International - DTG. (Accessed 2012) Draw tower grating® technology. [Online]. Available: http://www.fbgs.com/technology/dtg-technology

[4] FBGS International. (Accessed 2012) Company website. [Online]. Available: http://www.fbgs.com/

[5] E. Lindner, J. Moerbitz, C. Chojetzki, M. Becker, S. Brueckner, K. Schuster, M. Rothhardt, R. Willsch, and H. Bartelt, “Tailored draw tower fiber bragg gratings for various sensing applications,” ser. Proceedings of SPIE, J. Canning and G. Peng, Eds., vol. 8351, 2012, 3rd Asia Pacific Optical Sensors Conference (APOS), Sydney, Australia, JAN-FEB 2012.

[6] H. Dobb, D. Webb, K. Kalli, A. Argyros, M. Large, and M. van Eijkelenborg, “Continuous wave ultraviolet light-induced fiber bragg gratings in few- and single-mode microstructured polymer optical fibers,” *Optics Letters*, vol. 30, no. 24, pp. 3296–3298, Dec. 2005.

[7] I. P. Johnson, D. J. Webb, and K. Kalli, “Utilisation of thermal annealing to record multiplexed fbg sensors in multimode microstructured polymer optical fibre,” ser. Proceedings of SPIE, W. Bock, J. Albert, and X. Bao, Eds., vol. 7753, 2011, 21st International Conference on Optical Fiber Sensors, Ottawa, Canada, MAY 2011.

[8] P. S. J. Russell, “Photonic-crystal fibers,” *Journal of Lightwave Technology*, vol. 24, no. 12, pp. 4729–4749, Dec. 2006.

[9] T. Martynkien, G. Statkiewicz-Barabach, J. Olszewski, J. Wojcik, P. Mergo, T. Geernaert, C. Sonnenfeld, A. Anuszkiewicz, M. K. Szczurowski, K. Tarnowski, M. Makara, K. Skorupski, J. Klimek, K. Poturaj, W. Urbanczyk, T. Nasilowski, F. Berghmans, and H. Thienpont, “Highly birefringent microstructured fibers with enhanced sensitivity to hydrostatic pressure,” *Optics Express*, vol. 18, no. 14, pp. 15 113–15 121, July 2010.

[10] M. Rothhardt, C. Chojetzki, and H. Mueller, “High mechanical strength single-pulse draw tower gratings,” ser. Proceedings of the Society of Photo-Optical Instrumentation Engineers (SPIE), J. Armitage, R. Lessard, and

G. Lampropoulos, Eds., vol. 5579, no. Part 1-2, 2004, pp. 127–135, international Conference on Applications of Photonics Technology, Ottawa, Canada, SEP 2004.

[11] T. Geernaert, M. Becker, P. Mergo, T. Nasilowski, J. Wojcik, W. Urbanczyk, M. Rothhardt, C. Chojetzki, H. Bartelt, H. Terryn, F. Berghmans, and H. Thienpont, "Bragg grating inscription in geo2-doped microstructured optical fibers," *Journal of Lightwave Technology*, vol. 28, no. 10, pp. 1459–1467, May 2010.

[12] Phosfos Consortium. (2008) Photonic skins for optical sensing. [Online]. Available: http://www.phosfos.eu/

[13] S. Sulejmani, *Simulation, fabrication and characterization of bragg gratings in microstructured fibers for sensing purposes.* Master thesis, Vrije Universiteit Brussel, 2010.

[14] E. Ferraris, T. Van Gijseghem, C. Yan, B. Van Hoe, G. Van Steenberge, P. Van Daele, P. Dubruel, and D. Reynaerts, "Embedding of fibre optic sensors within flexible host," in *4M/ICOMM 2009 - The Global Conference on Micro Manufacture*, 2009, pp. 351–354, international Conference on Mult-Material Micro Manufacture/ International Conference on Micro Manufacting, Karlsruhe, Germany, SEP 2009.

[15] Dow Corning. (Accessed 2013) Company website. [Online]. Available: http://www.dowcorning.com/

[16] B. Ratner, *Biomaterials science: an introduction to materials in medicine*, ser. Academic Press. Elsevier Academic Press, 2004.

[17] F. Bossuyt, T. Vervust, and J. Vanfleteren, "Stretchable electronics technology for large area applications: Fabrication and mechanical characterization," *IEEE Transactions on Components Packaging and Manufacturing Technology*, vol. 3, no. 2, pp. 229–235, Feb. 2013.

[18] F. Schneider, T. Fellner, J. Wilde, and U. Wallrabe, "Mechanical properties of silicones for mems," *Journal of Micromechanics and Microengineering*, vol. 18, no. 6, June 2008, 18th European Workshop on Micromechanics (MME 07), Univ Minho, Guimaraes, Portugal, SEP 2007.

[19] J. Missinne, "Development of conformable optical and optoelectronic based tactile sensors," Ph.D. dissertation, Ghent University, 2011.

[20] Micro resist technology GmbH. (Accessed 2013) Company website. [Online]. Available: http://www.microresist.de/

[21] Ormocers. (Accessed 2013) Product website. [Online]. Available: http://www.ormocer.de/

[22] MicroChem. (Accessed 2013) Su-8 100 datasheet, available on company website. [Online]. Available: http://microchem.com/

[23] B. Van Hoe, G. Van Steenberge, E. Bosman, J. Missinne, T. Geernaert, F. Berghmans, D. Webb, and P. Van Daele, "Optical fiber sensors embedded in polymer flexible foils," ser. Proceedings of SPIE-The International Society for Optical Engineering, F. Berghmans, A. Mignani, and C. Hoof, Eds., vol. 7726, 2010, conference on Optical Sensing and Detection, Brussels, Belgium, APR 2010.

[24] S. Kiesel, K. Peters, T. Hassan, and M. Kowalsky, "Behaviour of intrinsic polymer optical fibre sensor for large-strain applications," *Measurement Science & Technology*, vol. 18, no. 10, pp. 3144–3154, Oct. 2007, 18th International Conference on Optical Fibre Sensors, Cancun, Mexico, OCT, 2006.

[25] N. Hawkes, "Laby, Th. - Tables of physical and chemical constants and some mathematical functions," *Nature*, vol. 213, no. 5076, pp. 555–&, 1967.

[26] K. E. Carroll, C. Zhang, D. J. Webb, K. Kalli, A. Argyros, and M. C. J. Large, "Thermal response of bragg gratings in pmma microstructured optical fibers," *Optics Express*, vol. 15, no. 14, pp. 8844–8850, July 2007.

[27] W. Zhang, D. J. Webb, and G. D. Peng, "Investigation into time response of polymer fiber bragg grating based humidity sensors," *Journal of Lightwave Technology*, vol. 30, no. 8, pp. 1090–1096, Apr. 2012.

[28] J. Barrie and B. Platt, "The diffusion and clustering of water vapour in polymers," *Polymer*, vol. 4, no. 3, pp. 303–313, 1963.

[29] J. Lee, C. Park, and G. Whitesides, "Solvent compatibility of poly(dimethylsiloxane)-based microfluidic devices," *Analytical Chemistry*, vol. 75, no. 23, pp. 6544–6554, Dec. 2003.

[30] G. Peng and P. Chu, "Polymer optical fiber photosensitivities and highly tunable fiber gratings," *Fiber and Integrated Optics*, vol. 19, no. 4, pp. 277–293, 2000.

[31] I. P. Johnson, K. Kalli, and D. J. Webb, "827 nm bragg grating sensor in multimode microstructured polymer optical fibre," *Electronics Letters*, vol. 46, no. 17, pp. 1217–U74, Aug. 2010.

[32] C. Russell, N. Bright, G. Buthpitiya, L. Alexander, C. Walton, and G. Whelan, "Esophageal propulsive force and its relation to manometric pressure," *GUT*, vol. 33, no. 6, pp. 727–732, June 1992.

[33] Nusil Silicone Technology. (Accessed 2013) Company website. [Online]. Available: http://www.nusil.com/

4

Integrated optoelectronic components for optical sensors

Optoelectronic components are needed to drive, read out and interpret the optical sensors and the according sensing information. Within this chapter, a technology is developed to embed these necessary driving and read-out elements for optical sensors in ultra-thin optoelectronic packages based on polymer materials. A thorough selection of suitable optoelectronic components is performed, studying both the compatibility with the optical sensing elements and the possibility to embed these components using polymer based integrated packages. Although this embedding technology is providing a generic optoelectronic packaging process, the intended application is the integrated interrogation of optical fiber sensors. The selection of the appropriate components is therefore based on this criterion.

4.1 Introduction

When using sensors based on optical working principles, the optomechanical properties of the sensing medium are changing when certain environmental parameters are adjusted (as was discussed in Chapter 2). To read out and visualize these changes, a light source and mostly also a detector are needed. Depending on the sensing and interrogation principle (extensively discussed in Chapter 2, Sections 2.1 and 2.2), the type of source and detector can seriously differ.

For all sensing systems within this dissertation, a major objective is an extensive integration through embedding and miniaturization of the sensors and the according interrogation systems. In this chapter, the necessary technology is developed to address this objective in terms of the *optoelectronics*. Depending on the sensor type, additional dedicated technology blocks may be required. In the case of fiber sensing systems, separate technology building blocks are necessary for the *fibers* (Chapter 3) and the *coupling* of the fibers and the optoelectronics (Chapter 5). Sensors based on a working principle inherent in the optoelectronic components, such as the shear sensor discussed in Section 2.1.1 or the pressure sensor discussed in Section 2.1.2, are not involving any light guiding structures. They can consequently rely on only the optoelectronics integration technology.

When fabricating traditional optoelectronic semiconductor active chip packages, one typically has to chose between several technology options. These technology choices are related to the interconnection technology, such as face up placement (wire bonding) or flip chip (solder bumps, ball grid arrays), and the packaging technology, such as Dual In-Line (DIL) or Multi-Chip Modules (MCM). The resulting packages are mounted on a carrier substrate such as a rigid Printed Circuit Board (PCB) or a flexible substrate. The thickness and size of such modules can be a limiting factor when using these chip packages for example in wearable systems, for biomedical purposes (such as minimally invasive surgery) or within structural health monitoring applications. In this chapter, a technology is described to come up with an ultra-thin, unobtrusive and mechanically flexible optoelectronic package. Light emitting III-V components and detectors are therefore integrated in a spin-coated polymer stack consisting of epoxy and/or polyimide materials.

The integration challenges strongly depend on the component type (metalization, light emitting area, heatsinking etc.). A selection of the most promising optical sources and detectors is consequently imposed. As we will see later on, there are several trade-offs to be considered in this context including for example sensor interrogation speed versus interrogation accuracy and multiplexing possibilities versus system cost.

4.1.1 Ultra-thin packaging

By making the driving elements and associated peripheral materials as thin and small as possible, it is possible to come up with an unobtrusive alternative for the traditional PCB technology which is typically combined with surface-mounted devices. The optoelectronic components are therefore manipulated on a bare die level. Bare dies are typically used in high-end systems where conventional packaging might result in unacceptable levels of degradation in electrical, mechanical or thermal performance [1]. In this chapter, the optoelectronic bare die components are thinned down and embedded in an ultra-thin optical package. This chip level integration enables a high degree of mechanical flexibility and formability.

4.1.2 Polymer embedding

Using polymers as embedding host material and consequently avoiding the traditional PCB laminates is further limiting the dimensions of the total chip package. The main driver behind the use of materials from the polymer family is however the possibility to make non-toxic, human-friendly or potentially even biocompatible applications.

4.1.3 Wavelength selection

This chapter has to enable the combination of the optoelectronics with optical fibers and fiber sensors. Fiber Bragg gratings typically have reflecting wavelengths in the range of 850 nm or 1550 nm. The main advantage of the 1550 nm components is the compatibility with off-the-shelf telecom equipment (sources, fibers, detectors). In terms of cost, the 850 nm devices provide a good alternative because of the possibility to work with Silicon (Si) or Gallium Arsenide (GaAs) devices. At a wavelength of 850 nm, optical losses in polymer based fibers or waveguides are also significantly lower than at 1550 nm. When selecting the appropriate wavelength, one has to take into account these different pros and cons.

4.2 Selection of optoelectronic components

The necessary optoelectronics for optical fiber sensors have to meet certain requirements:

- Availability of the component in an *unpackaged - bare die - version*.
- *Wavelength compatibility* with the fiber Bragg grating wavelengths.
- Minimum level of in-fiber *optical power budget*.
- *Modal behavior* allowing for an unambiguous fiber sensor read-out.

Within this PhD research and related projects (Chapter 1, Section 1.8), several types of unpackaged semiconductor optoelectronic sources were obtained as bare dies, both in the 850 nm and 1550 nm wavelength range. An overview of the optoelectronic components (bare die) available for further integration is provided in Table 4.1. The price/die values mentioned in this table are only indicative.

All components were then investigated to check their suitability for use with fiber sensors. To perform this comparison, they were not yet integrated in a polymer package but rather mounted as bare die on a rigid carrier.

Table 4.1 – Overview of the available (bare die) optoelectronic sources.

	edge-emitting		*top-emitting*			
	LD	SLED	LED	VCSEL	VCSEL	VCSEL
	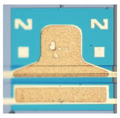		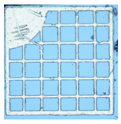		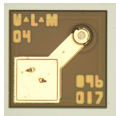	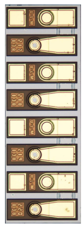
Company	Roithner	Exalos	Roithner	BeamExpress	ULM Photonics	ULM Photonics
Reference	[2]	[3]	[2]	[4]	[5]	[5]
Price/die	€ 10	€ 250	€ 2	€ 50	€ 11	€ 6
λ_{central}	1550 nm	850 nm 1550 nm	1550 nm	1550 nm	850 nm	850 nm
Modes	SM/MM	SM	MM	SM	SM	MM
$P_{\text{optical, total}}$	6 mW	10.5 mW 20 mW	2.5-5 mW	1.2 mW	2.5 mW	1.5 mW
Bandwidth	3-5 nm	50 nm 65 nm	130 nm	0.15 nm	0.1 nm	0.3 nm

4.2.1 LED

A Light Emitting Diode (LED) is a very low-cost optoelectronic source candidate offering a broad spectral output range. A 1550 nm surface emitting unpackaged LED (ELC-1550-17) from Roithner [2] was mounted on a substrate and wire bonded to copper tracks. A 3D translation stage was used to position a bare fiber end of a 50 µm core multimode pigtail close to the LED in order to maximize coupling. The remote end of the pigtail was connected to either an OSA or power meter. The optical power measured in the fiber is very low, never reaching 1 µW. Furthermore there is a non-linear relationship between power and current at higher drive currents, possibly because of the device overheating due to lack of heatsinking. The spectral width is very wide (FWHM of 145 nm) but this width in combination with the very low power in-fiber means that the power reflected from any sensing grating would be insufficient for any practical application. The reflected power needed would of course depend on the specific application and its associated signal-to-noise requirements, but is always likely to be above a few µW which is already greater than the optical power this source would provide. The low in-fiber power is due to the fact that the LED emission angle is very large.

Figure 4.1a shows the far field beam profile of the LED, measured with a beam profiler (Photon Inc. goniometric radiometer, available at B-Phot, VUB).

4.2.2 LD

An edge-emitting unpackaged Laser Diode (LD, chip 1550-5) from Roithner [2] was mounted and monitored in a similar fashion to the LED. The power vs. current curve displays typical laser behavior with a well defined threshold current (at I = 12 mA). Power in the multimode fiber is over a mW, and this coupled with the narrow spectral profile would lead to a good signal-to-noise ratio when interrogating a grating. Figure 4.1b shows the measured beam profile of the Roithner laser diode. As expected, the coupling of the laser diode light beam is much more efficient than for the LED. There is however a pronounced modal structure visible in the beam profile. This is more problematic since during interrogation of a grating the peaks in the modal structure of the source can essentially be mistaken for the peak in the grating reflectivity.

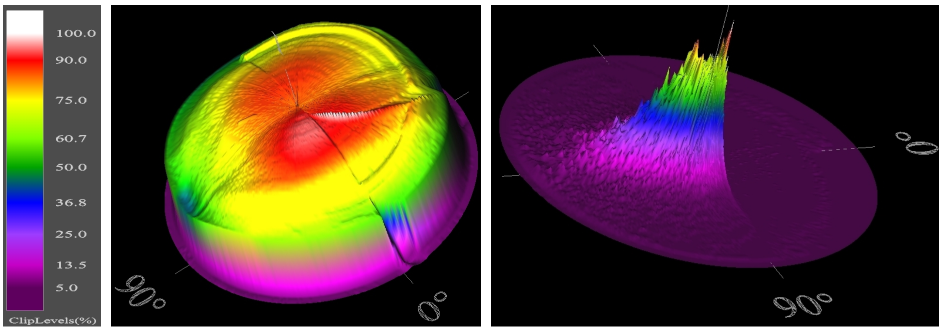

(a) Roithner LED. **(b)** Roithner laser diode.

Figure 4.1 – Measured beam profiles using a goniometric radiometer.

4.2.3 SLED

An edge-emitting unpackaged Superluminescent Light Emitting Diode (SLED, EXS1510) from Exalos [3] was mounted and monitored in a similar fashion to the LED and LD. The optical output that we expect from this component is in the range of 5 mW-20 mW, while the actual measured optical power is in the range of µWs. The reason for this can be found in the thermal heating of the chip. No active cooling is present with the given mounting set-up, only passive heatsink cooling. The driver current range of the SLED is up to 300 mA, which is considerably higher compared to the other components (typical driving currents of about 1 mA-20 mA). This is causing the bad optical behavior of the wire bonded component, driven with a continuous electrical current.

In cooperation with the SLED provider (Exalos [3]), this effect was investigated in more detail. Analyzing the SLED behavior resulted in the observation of a thermal roll-over causing a spectral collapse with strong red shifting (up to 60 nm, Figure 4.2b) near the ASE threshold (driving current of 150 mA, Figure 4.2a). We have however shown the possibility to drive the components with a modulated driving current to lower the duty cycle and avoid the thermal overheating effects. The resulting optical power coupled to a fiber increases in this case to 3 mW. The optical power values are still significantly lower than expected and normal spectral behavior is shifted to lower driving currents, still indicating a higher chip temperature. To guarantee continuous wave operation and/or full power pulsed operation of the SLED and avoid thermal problems, the thermal mass has to be increased and the thermal resistance of the n-contact has to be reduced. This can be done for example by using thicker copper traces or heat pipes in combination with multi-layer heat-spreading PCBs. These solutions are evidently severely limiting the integration possibilities of this component.

4.2.4 VCSEL

An unpackaged Vertical-Cavity Surface-Emitting Laser (VCSEL, 1550 nm) from BeamExpress [4] was mounted and monitored in a similar fashion to the LED and LD. The VCSEL displays a well defined threshold current of 1.9 mA. The power available in-fiber is good (Figure 4.3a shows the measured beam profile of the BeamExpress 1550 nm VCSEL to confirm the excellent coupling opportunities) and later experiments with higher currents and better adjustment achieved in-fiber power over 1 mW. The beam profile shows an average beam divergence of 8.15° (FWHM). Equally good is the source spectrum, which consists of a single emission peak of less than 0.2 nm width. Electrothermal tuning of the BeamExpress VCSEL central wavelength, necessary to drive a fiber sensor, is possible to a limited extent (Figure 4.3b). Depending on the fiber type and the application (transducer material, parameter range), a wavelength range of 1 nm up to a few nm is needed to interrogate a single fiber Bragg grating sensor. The wavelength resolution of commercially available (OSA or peak tracking) systems is typically ranging from a few 10 pm down to 1 pm.

Depending on the fiber sensor wavelength, also 850 nm VCSEL components are used. The characteristics of these components are similar to the 1550 nm devices and are not shown here. Detailed beam profile analysis of these components will be discussed in view of fiber coupling possibilities within Chapter 5.

Only the VCSELs and SLEDs are consequently retained for the remainder of this chapter.

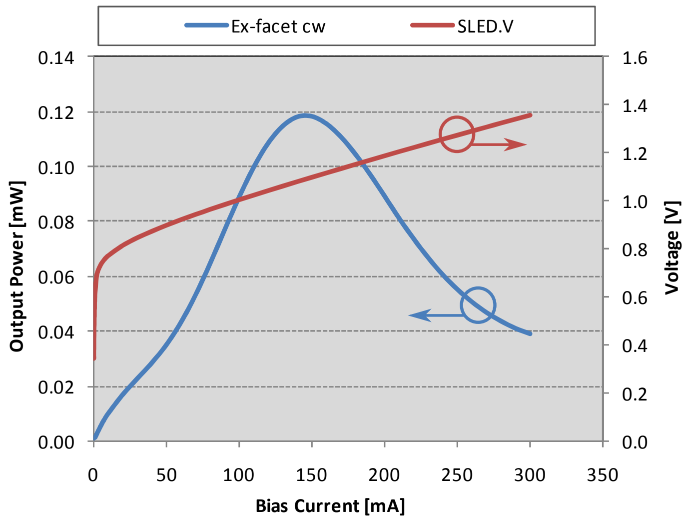

(a) Low optical output power and thermal roll-over near ASE threshold.

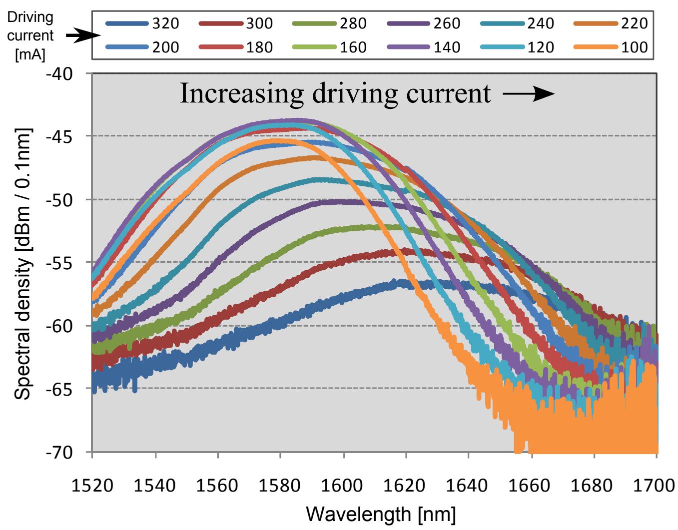

(b) Spectral collapse with strong red shifting starting at 150 mA indicating a huge thermal problem.

Figure 4.2 – Continuous wave characterization of a 1550 nm wire bonded SLED, performed at Exalos.

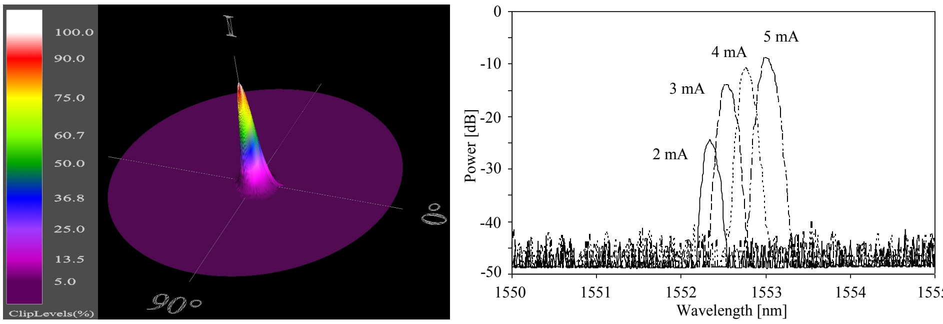

(a) Measured beam profile using a goniometric radiometer.

(b) Modal structure and electrothermal tuning effects.

Figure 4.3 – 1550 nm wire bonded VCSEL characterization.

4.3 Chip thinning and back contacting

Typical chip thicknesses of the available optoelectronic components range between 100 µm and 150 µm. Aiming for an ultra-thin optoelectronic package based on thin-film processing steps, the individual optoelectronic chips are thinned down to 20 µm. Thinning down optoelectronic components typically consists of several lapping and polishing steps. This thinning procedure was previously optimized for several types of (opto)electronic components, such as microcontrollers (PhD Wim Christiaens [6], Chapter 6), multimode 850 nm VCSEL arrays and GaAs photodetector arrays (PhD Erwin Bosman [7], Chapter 5).

Within this dissertation also active optoelectronic components at 1550 nm are used. The substrate material is in this case not Si or GaAs but mostly Indium Phosphide (InP), an even more brittle material. Therefore the thinning technology was thoroughly investigated for InP substrates. An additional challenge on thinning down the different available components is the fact that some components have a top and a bottom contact. Because the thinning process physically removes a large part of the chip backside bulk material, the back-contact metalization layer is completely removed after this thinning process. These two challenges are now discussed in more detail. Table 4.2 gives an overview of the substrate materials and contact structures of the different investigated optoelectronics.

4.3.1 Thinning InP substrates

The technology to thin down GaAs VCSELs and Photodiodes (PDs) was taken as a starting point to introduce the thinning of InP substrates (SLEDs/VCSELs). All

Table 4.2 – Overview of the contact and bulk information of the different investigated optoelectronics.

Component	Substrate material	Electrical contacts
1550 nm single-mode SLED	InP	Top-Bottom
1550 nm single-mode VCSEL	InP	Top-Top
850 nm single-mode VCSEL	GaAs	Top-Bottom
850 nm multimode VCSEL	GaAs	Top-Top

lapping and polishing work of optoelectronic chips is consequently performed on the Logitech PM5 Precision Lapping & Polishing Machine installed in the CMST cleanrooms. InP in general is even more fragile than GaAs, which is translated to a more delicate thinning process. The technology to thin down InP substrates was developed using dummy substrates. In order to prepare dummy InP chips, a sample (1 cm x 1 cm) from an InP wafer (thickness 500 µm) was thinned down to 125 µm and was cleaved into smaller pieces, matching the dimensions of the SLEDs (1500 µm x 500 µm). The dummy components were mounted onto the temporary rigid glass carrier with wax for further lapping and polishing to a final thickness of 30 µm. Fine-tuning of the different process parameters was required:

- The wax for fixation of the dies to the temporary carrier: glycophtalate.
- A minimal load on the dies with support of large InP dummy samples.
- The lapping step is done using a suspension of 3 µm Al_2O_3 grains on a glass lapping plate. This results in a fast removal rate (4 min to thin the die from 125 µm to 40 µm) with low surface damage after lapping using a plate rotation speed of 10 rpm.
- The polishing step consists of mechanical polishing with very fine 0.3 µm Al_2O_3 on a soft cloth resulting in a low edge roundness and low surface roughness. The polishing process is much slower and takes about 20 min to thin the dies further from 40 µm to 30 µm. Again a plate rotation speed of 10 rpm is used.

Figure 4.4 shows the roughness of the backside of an InP die after lapping and polishing measured with a non-contact optical profilometer (WYKO) indicating an average roughness less than 3 nm on a 120 µm x 92 µm surface. The technology is ready-to-use on functional devices.

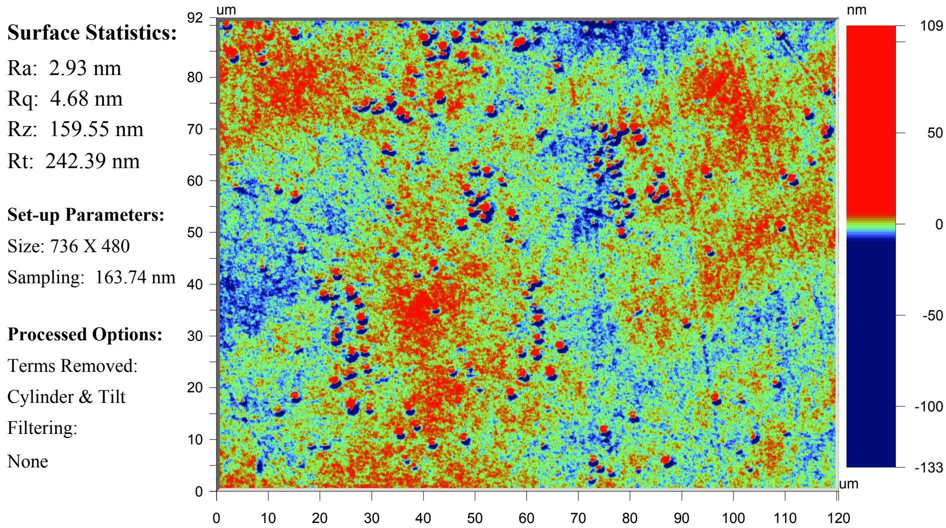

Figure 4.4 – An optical profiler scan (WYKO NT3300) of the InP substrate after lapping and polishing.

4.3.2 Applying a back-contact layer

In order to enable the application of a new back-contact layer, an additional smaller carrier substrate is used during the lapping and polishing process (Figure 4.5). The reason for this is twofold: firstly, the application of a back-contact will be done using sputtering and Chemical Vapor Deposition (CVD) in a vacuum chamber with limited dimensions requiring a small carrier. Secondly, the big carrier substrate associated with the Logitech PM5 Precision Lapping & Polishing Machine can easily be reused as no metalization or annealing steps are applied on this substrate.

After releasing the small carrier *(Carrier 2)* from the mother carrier *(Carrier 1)*, a new back-contact metalization layer AuGeNiAu stack is deposited by evaporating (AuGe and Au) and sputtering (Ni) consecutively 150 nm AuGe, 60 nm Ni and 200 nm Au. When releasing the chips from the wax, the complete metalization layer will be attached to the chip. To enable the release of the individually mounted components, the thin metal layer is therefore first removed around the chip using laser ablation. More specifically, a 355 nm Nd:YAG laser (86 mW, 10 kHz, dynamic: 1 mm/s) is used to remove the AuGeNiAu stack on a path around the optoelectronic chip. Dissolving the mounting wax in acetone releases the individual chips with a typical thickness of 20-30 µm. As a final step, a thermal annealing step (fast alloy up to 440° in 10 % H_2-N_2 forming gas environment) is applied to produce an ohmic contact.

This process was developed to apply back-contact layers to thinned individual chips and is in its current state not suitable for large quantities of optoelectronic components. It nevertheless provides a way to thin, embed and test back contacted chips within the CMST cleanrooms.

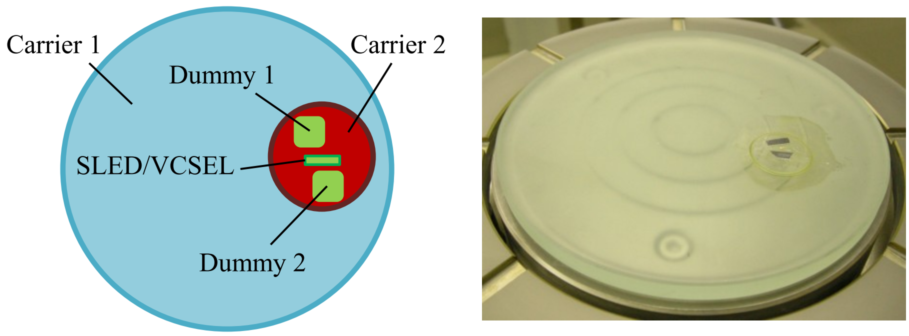

Figure 4.5 – Introducing an extra carrier *(Carrier 2)* which is released from *Carrier 1* after lapping and polishing.

4.3.3 Thinning of functional devices

The different types of functional components listed in Table 4.2 are now thinned down to a thickness of a few 10 µm. **This mechanical thinning process based on individual die thinning is applied for the first time on SLEDs,** 1550 nm **VCSELs and** 850 nm **single-mode VCSELs.**

850 nm **ULM Photonics multimode VCSELs**

Thinning multimode 850 nm VCSELs from ULM Photonics was optimized and extensively discussed within the PhD of Erwin Bosman [7] and is therefore not repeated here. This thinning process formed the basis for the thinning technology developed within this chapter. The material substrate is GaAs and all contact pads are situated on the top surface of the chip.

1550 nm **BeamExpress VCSELs**

The 1550 nm BeamExpress VCSELs were thinned down to 40 µm thickness (original thickness is 125 µm). Figure 4.6a shows a picture of the thin VCSEL and Figure 4.6b shows the measured VI curve of the chip after gluing the thinned component to a substrate and wire bonding the contacts to contact lines on the substrate. The measured characteristics are the same as for the unthinned components (reference graph included in Figure 4.6b).

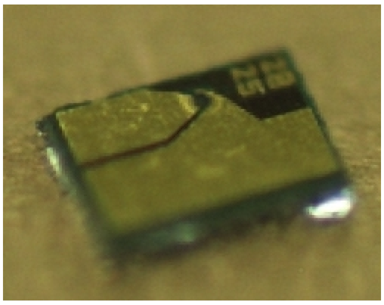

(a) Stereozoom picture.

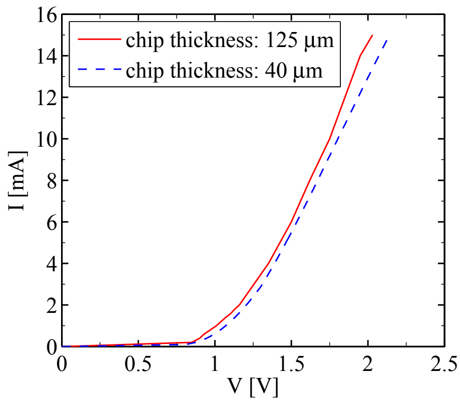

(b) Electrical characterization.

Figure 4.6 – Characterization of the 1550 nm BeamExpress VCSEL.

1550 nm **Exalos SLEDs**

SLEDs are much larger components (1500 µm x 500 µm) than the VCSELs (350 µm x 250 µm for the 1550 nm VCSELs). Together with the fact that InP is the most brittle material, we can say that the thinning process for the SLED is the most delicate. Applying the thinning process to these SLEDs however results in good backside surface quality and no chip damage. Figure 4.7 shows pictures of the backside of an SLED after lapping (a), after polishing (b) and after backside metalization (c).

Figure 4.8a shows pictures of the SLED top surface after thinning and metalization (40 µm thick). The VI curves of the SLED in unthinned and in thinned status are compared in Figure 4.8b. A small deviation in the curves is observed. The impact of this deviation in the optical output of the SLED could not be measured at this moment since the DC-driving of the component results in unusual behavior of the chip due to overheating by the lack of active cooling. Modulated driving of the chip, using a limited current duty cycle (10 % at 100 kHz), has proven to solve this problem, but is not implemented in this section.

850 nm **ULM Photonics single-mode VCSELs**

A WYKO 3D profile of the top surface of a thinned and back contacted 850 nm single-mode VCSEL is shown in Figure 4.9. This optical profilometer plot shows that the gold bump surrounding the active area is about 8 µm (reference plane = top surface of chip). This resulted in an extra challenge for the thinning and embedding process. When the components are wax-mounted on the temporary glass carrier before the thinning procedure, a weight is put on the dies to uni-

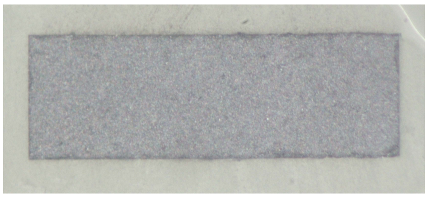

(a) After lapping.

(b) After polishing.

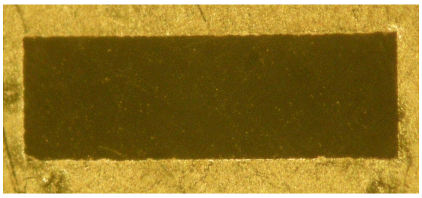

(c) After back contacting, before laser cutting and release.

Figure 4.7 – Thinning and back contacting single-mode 1550 nm Exalos SLEDs.

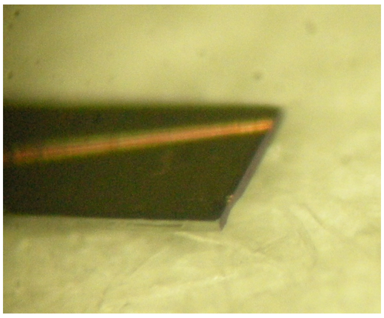

(a) Picture of the top surface after thinning and metalization (40 µm thick).

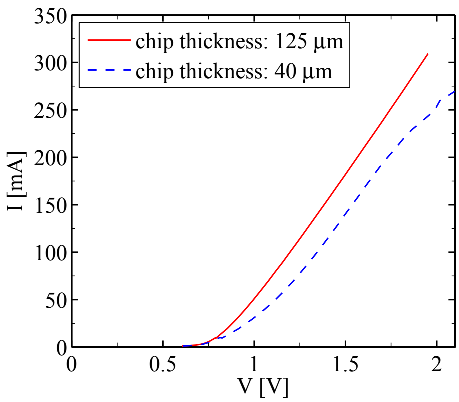

(b) Electrical behavior before and after chip thinning.

Figure 4.8 – Characterization of the 1550 nm SLED.

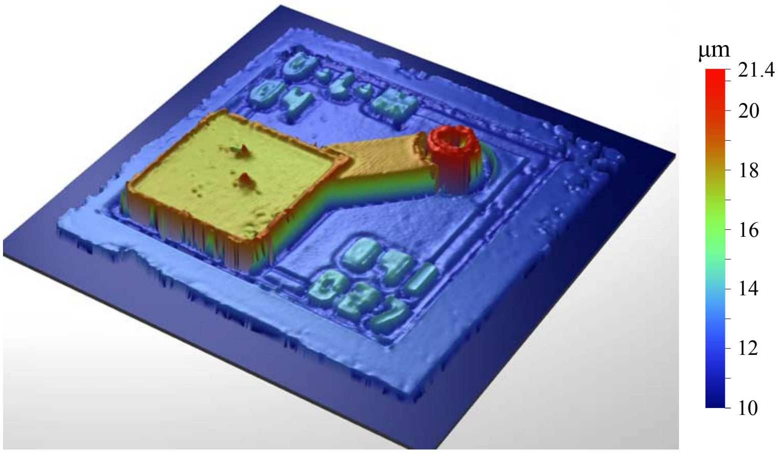

Figure 4.9 – WYKO non-contact optical profilometer plot of a single-mode 850 nm VCSEL.

formly spread out the wax layer underneath the chip. The protruding gold bump around the active area will however carry most of the weight. When the slightest horizontal shift of the dies in the molten wax occurs, the gold bump will be deformed and spread out over the active area. Figure 4.10a shows an extreme case of this deformation, resulting in a completely covered active area of the VCSEL. This problem was solved by dropping down the weight on top of the dies in a very controlled way to avoid any horizontal movement of the weight during the lowering of the weight. No deformation of the gold bump was observed since then.

After lapping and thinning of the dies, they are kept inside the wax layer on the temporary glass carrier and the back-contact metalization is applied. The wax protects the sides of the chip to be metalized and avoids the creation of a short to the top active layers of the chip. Figure 4.10b shows a picture of the laser cut back-contact layer before release of the chips. After release of the chip by removing the wax with acetone, it is glued on a copper substrate with electrical conducting glue and wire bonded to copper tracks on the same substrate. The measured VI and LI curves of the original non-thinned and thinned devices are included in the graphs in Figure 4.11. The curves are almost identical which guarantees a successful back contacting after the thinning process.

4.3.4 Conclusion

The thinning and back contacting technology for OE components is available. We will now turn our focus towards the embedding of the thinned optoelec-

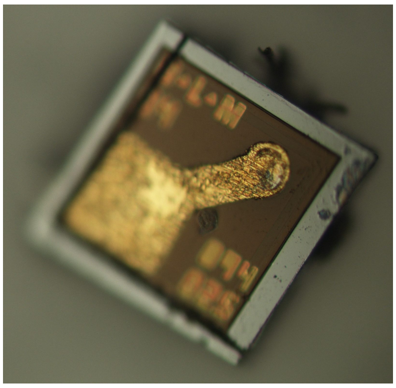

(a) Picture of a clearly deformed gold bump around the active area, covering the complete active area.

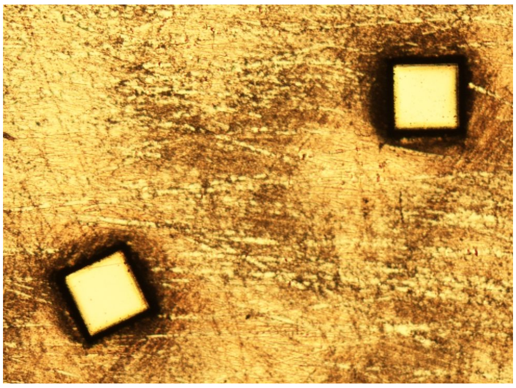

(b) Picture of the laser cut metal layer before releasing the chip.

Figure 4.10 – Thinning, back contacting and releasing single-mode VCSEL chips.

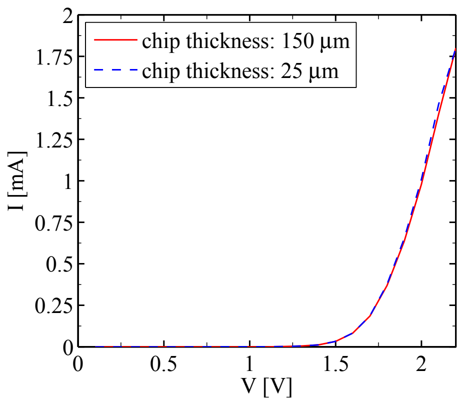

(a) Electrical characterization.

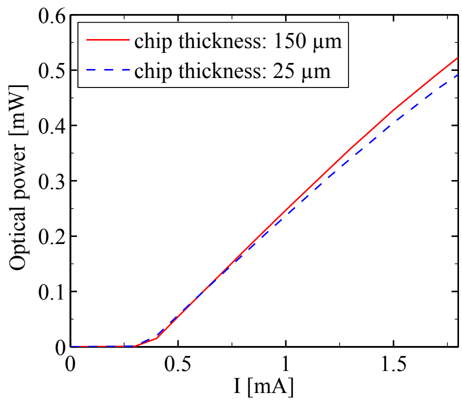

(b) Optical characterization.

Figure 4.11 – Characterization of an unthinned vs. a thinned (thickness of 25 µm) 850 nm single-mode ULM Photonics VCSEL.

tronic dies in polymer packages. Because of higher driving currents and limited heatsink possibilities, the SLEDs are challenging to integrate. The development of the integration technology is therefore focused on a VCSEL - top-emitting - approach. As an example, we take a single-mode 850 nm VCSEL from ULM Photonics and a photodetector from Albis. Two approaches have been investigated and are discussed in detail in the following sections.

4.4 SU-8 based flat optoelectronic package

Two types of packages have been investigated: the first type is based on an epoxy embedding material, SU-8, a negative photoresist from MicroChem [8]. The second type is based on a polyimide embedding material, PI-2611 from HD Microsystems [9]. Each process flow has its specific advantages and shortcomings.

The main advantage of the first approach is the possibility to work with a single chip embedding layer matching the thickness of the chip. This results in a *flat* optoelectronic package providing an easy fiber coupling interface for optoelectronic components with vertically oriented active areas (VCSEL, PD). Also other important advantages are associated with this approach. They include for example the possibility to reliably stack different chip packages on top of each other (outside the scope of this dissertation).

4.4.1 Process flow

Embedding optoelectronic components in ultra-thin flexible packages was first investigated within the PhD dissertation of Erwin Bosman. The end result was an SU-8 based package enabling integrated flexible optical datacom links. This process flow ([7], Chapter 6, Sections 6.2 and 6.4) was used as a starting point and optimized from an optical sensing point of view to enable the embedding of (back contacted) single-mode optoelectronic components and facilitate fiber coupling (minimize the optical path length). The detailed process flow is schematically shown in Figure 4.12. As a result, an optoelectronic component is embedded in an ultra-thin polymer package. When bending and manipulating this ultra-thin package, the highest stresses in the polymer optoelectronic stack can be found in the outer layers. By applying layers of polyimide on both sides of the stack as physical supporting layers, we can spread the high stress inside the outer polymer layer over a larger area than just the manipulated area. Polyimide has a high strength and flexibility which makes it the ideal support material.

The fabrication of the ultra-thin optical chip package starts on a rigid temporary glass carrier on which a thin (8 µm thickness) and mechanically strong polyimide layer (PI-2525, HD Microsystems [9]) is spin-coated. Since there is no adhesion of this layer with the glass carrier, it can easily be released after completing the

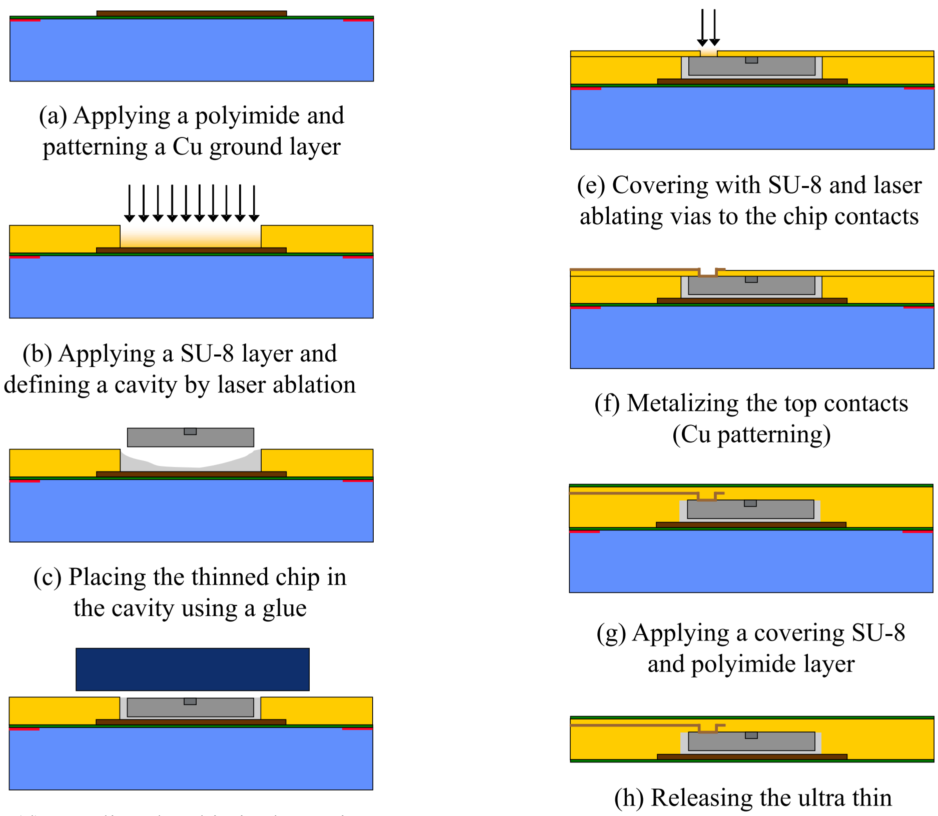

(a) Applying a polyimide and patterning a Cu ground layer

(b) Applying a SU-8 layer and defining a cavity by laser ablation

(c) Placing the thinned chip in the cavity using a glue

(d) Leveling the chip in the cavity

(e) Covering with SU-8 and laser ablating vias to the chip contacts

(f) Metalizing the top contacts (Cu patterning)

(g) Applying a covering SU-8 and polyimide layer

(h) Releasing the ultra thin optical package

Figure 4.12 – Schematic overview of the SU-8 based flat optoelectronic package process flow.

fabrication. To ensure sufficient adhesion during the process, an adhesion promoter (Pyralin VM652) is applied on the edges of the glass carrier. A 1 µm copper heatsink layer, which can also function as a back contacting layer, is sputtered on top of the PI layer and, if needed, electro-plated up to the desired copper thickness. Next, this metal layer is structured using a wet etch $CuCl_2$ process (a). An SU-8 embedding layer is spin-coated on top and, using a 10.6 µm CO_2 and 248 nm KrF Excimer laser, a chip embedding cavity is ablated (b) to mount (c), level (d) and fix an optoelectronic chip. The thickness of this SU-8 layer is approximating the thickness of the chip increased with $\approx 5\,\mu m$ (thickness of glue layer underneath the chip). Depending on the contact pad structure, a thermally conductive glue (U 8449-9, Namics Corporation) or an Isotropic (thermally and electrically) Conductive Adhesive (ICA), CE3103 WLV from Emerson & Cuming is used.

The result of the chip leveling is measured using a non-contact optical profilometer. Measuring 10 embedded single-mode VCSELs, an average of 0.77° with a standard deviation of 0.57° is obtained after leveling and after glue curing.

A thin (few µm) SU-8 covering layer is applied on top of the chip and microvias are drilled using an Excimer laser to access the chip contact pads (e). A top contacting 1 µm Cu layer is sputtered and structured (f) and again a thin polymer SU-8 layer is spin-coated on top to protect the metal contact pads (g). The final processing layer consists of applying a thin polyimide layer identical to the starting polyimide layer. To make contact with the outside world, the polymers covering the chip contact fan-out pads are locally removed using laser ablation (CO_2 and KrF Excimer). The flexible optoelectronic package with a total thickness of 40 µm is now ready for release (h). **To the best of our knowledge, such PI/SU-8 ultra-thin flexible optoelectronic packages including single-mode and back contacted laser chips are reported for the first time.**

This generally described embedding process can be used to embed several types of optoelectronic components including VCSELs and PDs. As mentioned before, the optical out-coupling facet quality is guaranteed in the case of vertically emitting or accepting components (surface quality of top surface is defined by the final spin-coating step). When combining this integration process with edge-emitting components however, one should provide an optical facet on the side of the package (surface quality of side surface is defined by the release method) with a roughness which is low enough for coupling purposes. In the remainder of this section, this process flow is applied on single-mode VCSELs at 850 nm and GaAs photodetectors for fiber sensing purposes. Figure 4.13 is depicting a few examples of single-mode VCSELs integrated in a PI/SU-8 package.

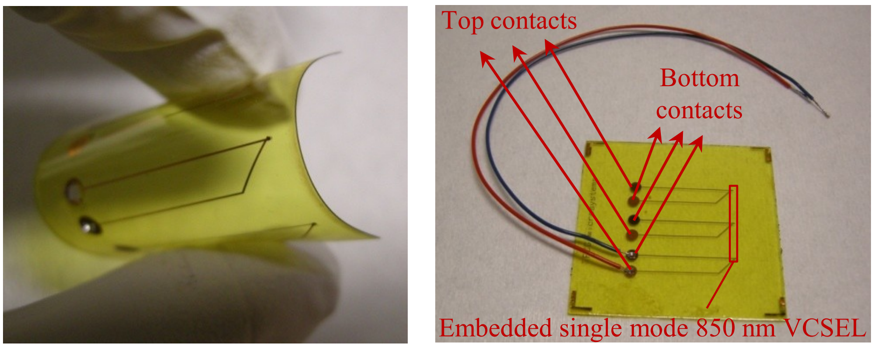

Figure 4.13 – Single-mode 850 nm VCSELs embedded in a PI/SU-8 package.

The embedded single-mode VCSELs are now characterized in detail, both electrically and optically, in order to check their functionality and compatibility with fiber sensing applications. Next to the preservation of single-mode behavior after chip thinning, polishing and embedding, efficient and optical skin compliant (i.e. compatible with planar sensing layers) fiber coupling of the VCSELs is also an important prerequisite for the envisaged application. This will be tackled in a dedicated chapter (Chapter 5).

4.4.2 Characterization

In this section, we investigate the influence of three important parameters on the electrical and optical characteristics of the SU-8 embedded single-mode VCSELs:

- Substrate material. Processing the ultra-thin polymer stack on a rigid PCB (FR4) board is compared with the polyimide supported flexible package, processed on a glass carrier.
- Chip thickness. The thickness of the chip is varied and the influence is studied ("chip: xx µm" is referring to the embedded chip thickness).
- Heatsink layer thickness. An important parameter for the thermal resistance of the optoelectronic package are the dimensions of the heatsink layer beneath the chip. The thickness of this layer is varied ("Cu: xx µm" is referring to the heatsink layer thickness).

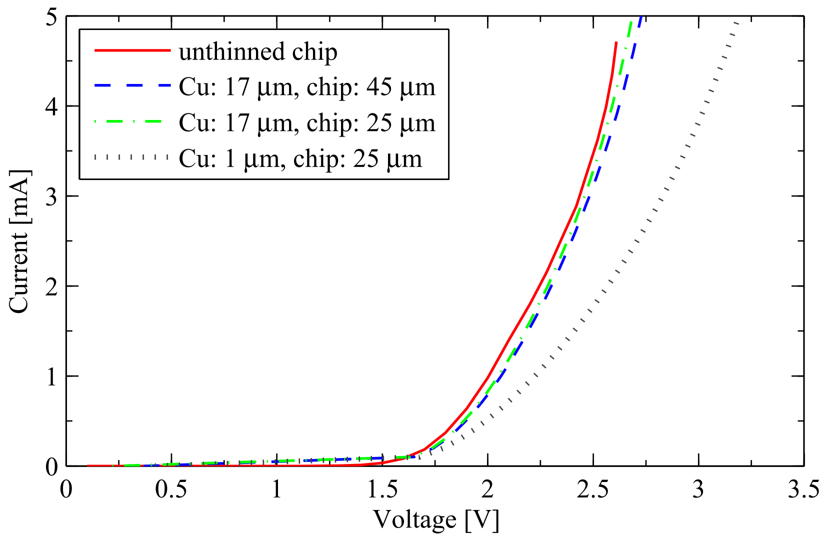

Figure 4.14 – Electrical characterization of SU-8 embedded optoelectronic single-mode VCSELs on a rigid FR4 substrate with varying Cu heatsink thickness and chip thickness.

The electrical characterization results for the PCB substrates are depicted in Figure 4.14. The results are typically averaged over two packages. These curves correspond nicely with the data in Figure 4.11a from the original (not-embedded, unthinned) components. The deviation in the "Cu: 1 µm, chip: 25 µm" case is probably due to the fact that there was only 1 package measured for this case.

The electrical characterization results for the PI on glass substrates are depicted in Figure 4.15 again showing averaged values. These curves correspond nicely with the data in Figure 4.11a from the original (not-embedded, unthinned) components.

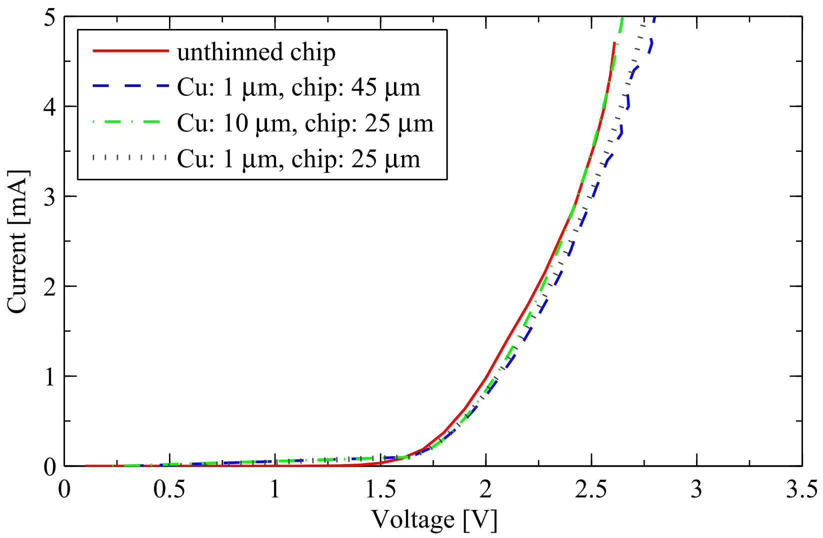

Figure 4.15 – Electrical characterization of SU-8 embedded optoelectronic single-mode VCSELs on a PI ground layer with varying Cu heatsink thickness and chip thickness.

The optical characterization results for the PCB substrates are depicted in Figure 4.16 again showing averaged values. These curves are in line with the data in Figure 4.11b from the original (not-embedded, unthinned) components. The difference in absolute optical power values is probably due to the inherent chip-to-chip variation. Bare chip LI slope efficiencies are varying between 0.3 W/A and 0.7 W/A according to the datasheet. Also the alignment of the Newport 818 series optical power detector used for these measurements can have an influence on the absolute power values. A saturation effect can however be noticed in all package types indicating potential thermal problems when using high DC driving currents.

The optical characterization results for the PI on glass substrates are depicted in Figure 4.17 again showing averaged values.

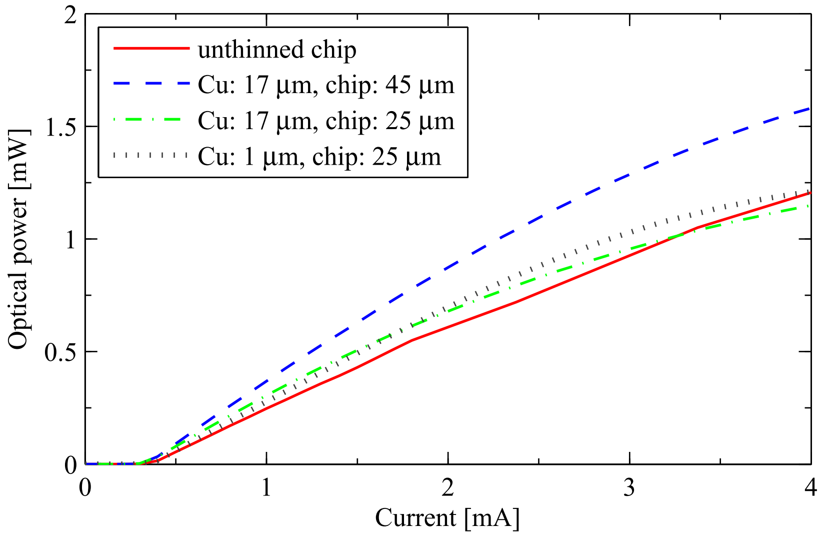

Figure 4.16 – Optical characterization of SU-8 embedded optoelectronic single-mode VCSELs on a rigid FR4 substrate with varying Cu heatsink thickness and chip thickness.

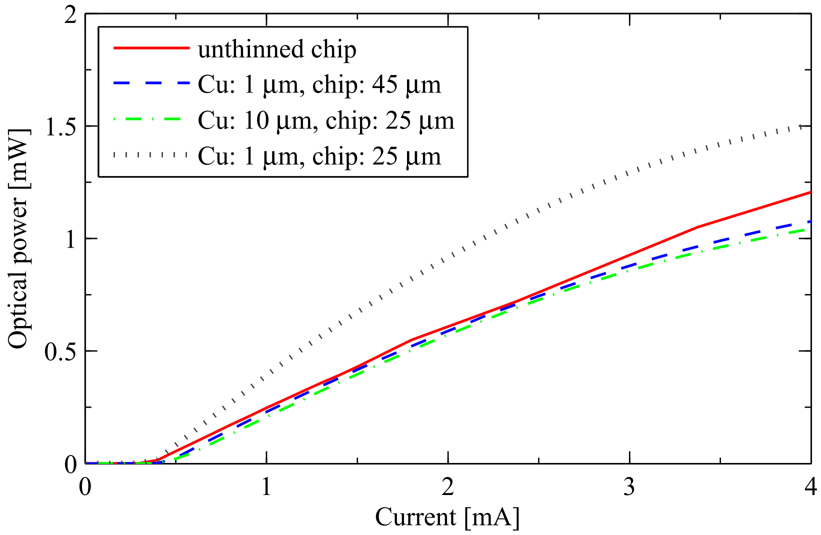

Figure 4.17 – Optical characterization of SU-8 embedded optoelectronic single-mode VCSELs on a PI ground layer with varying Cu heatsink thickness and chip thickness.

These curves are again in line with the data in Figure 4.11b from the original (not-embedded, unthinned) components. The difference in absolute optical power values is also probably due to the inherent chip-to-chip variation. A saturation effect can nevertheless again be noticed in all package types indicating potential thermal problems when using high DC driving currents.

Besides the LI (optical power versus electrical driving current) characteristics, also the electrothermal wavelength tunability will be an important property when using the VCSELs in combination with fiber sensors. This effect is also measured (DC driving) and shown in Figure 4.18 for the PCB substrates and Figure 4.19 for the PI on glass substrates. A more detailed discussion, including dynamic measurements, is included in Chapter 6, Section 6.6.

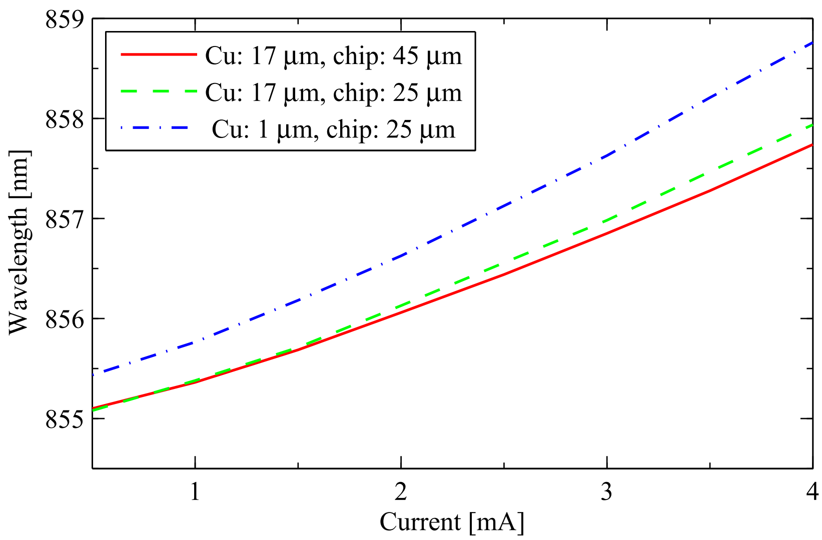

Figure 4.18 – Wavelength tuning of SU-8 embedded optoelectronic single-mode VCSELs on a rigid FR4 substrate with varying Cu heatsink thickness and chip thickness.

An overview graph depicting the differences in wavelength tunability (nm/mA), both in terms of substrate, chip thickness and heatsink thickness, is shown in Figure 4.20. The wavelength tuning effect is largely based on an electrothermal heating of the chip imposing a difficult trade-off between optimal heat dissipation and maximum wavelength tuning. The thin PI based package provides a more efficient heat dissipation compared to the FR4 substrate resulting in lower wavelength tuning ranges. Tuning ranges are significantly higher for reduced chip thickness and heatsink thickness values indicating an increased electrothermal effect and higher peak temperatures. There is consequently an additional trade-off between a minimized total thickness of the chip package leading to a higher degree of mechanical flexibility combined with higher wavelength tuning ranges, and an optimal heat management build-up.

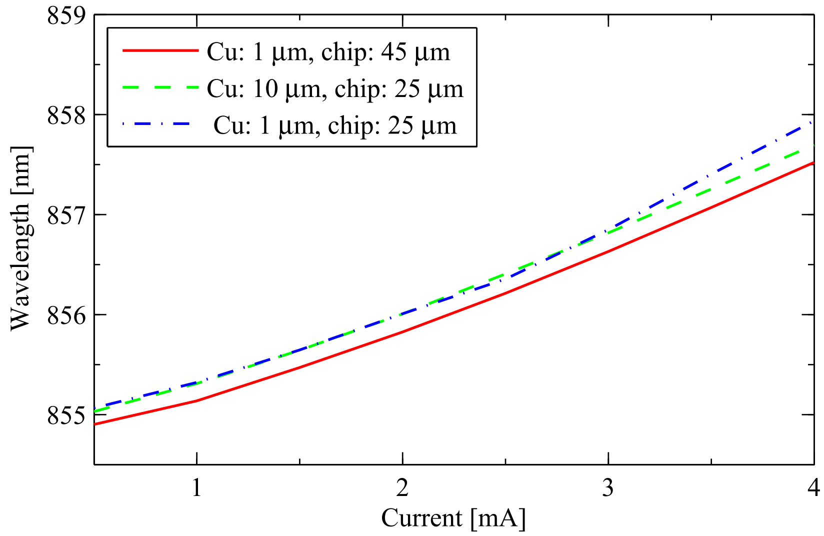

Figure 4.19 – Wavelength tuning of SU-8 embedded optoelectronic single-mode VCSELs on a PI ground layer with varying Cu heatsink thickness and chip thickness.

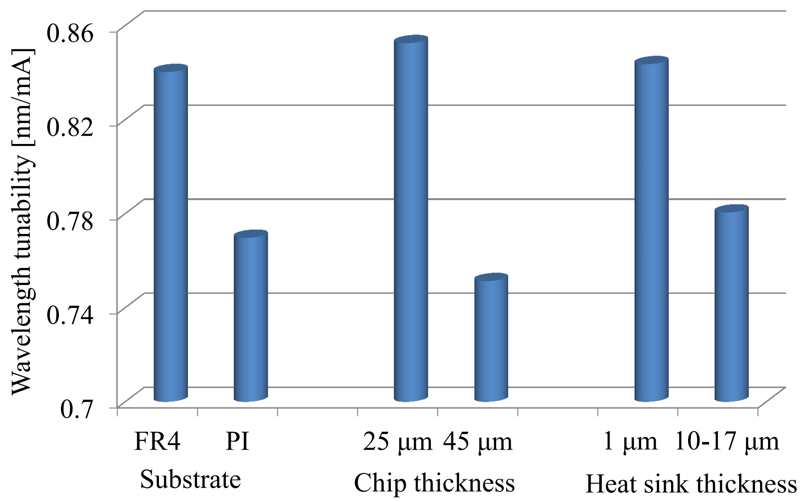

Figure 4.20 – Wavelength tuning of SU-8 embedded optoelectronic single-mode VCSELs. Average values depending of substrate, chip thickness and heatsink thickness.

4.5 PI based low-stress optoelectronic package

Because of the difference in the Coefficient of Thermal Expansion (CTE, listed in Table 4.3), the PI-2525/SU-8 based ultra-thin polymer stack can suffer from a considerable amount of mechanical stress. This can be an issue when a released package is used for fiber coupling and further embedding. The alternative which is presented here is based on a single polyimide embedding material (PI-2611, HD Microsystems [9]) with a CTE close to the semiconductor materials resulting in a low-stress optoelectronic package. A potential drawback is the non-flatness of the polymer stack introducing different step coverages, for example of the optoelectronic chip. Another challenge is the higher curing temperature (> 300 °C) of the PI-2611 vs. the PI-2525/SU-8 embedding stack. The OE components considered in this chapter prove to be compatible with the proposed embedding flow and according process temperatures but this is not guaranteed when changing the type of component. This process flow is strongly inspired by the work of Rik Verplancke ([10], Chapter 4). Within his PhD, a stretchable electronics platform using thin dies, using different polymers including PI-2611, was developed.

Table 4.3 – Overview of the coefficients of thermal expansion of different semiconductor (left) and polymer embedding (right) materials.

Material	CTE (ppm/°C)
Si	3
InP	4.5
GaAs	6

Material	CTE (ppm/°C)
PI-2611	3
PI-2525	40
SU-8	52

4.5.1 Process flow

Figure 4.21 shows a schematic overview of the fabrication of this low-stress optoelectronic package. Processing for this type of package again starts on a rigid temporary glass carrier with selectively applied adhesion promoter (Pyralin VM652) on which a polyimide (PI-2611, HD Microsystems) is spin-coated (6 µm thickness). A 1 µm copper layer is sputtered on top. Heatsinks which can simultaneously act as bottom contact layers are patterned using a wet etching ($CuCl_2$) process (a). The dimensions of the copper heatsinks are 4.5 mm x 4.5 mm, providing sufficient heat spreading capabilities with only a limited influence on the mechanical flexibility. Next, a PI-2611 layer (6 µm thickness) is spin-coated on top and a chip embedding cavity is ablated (b) using a 248 nm KrF Excimer laser combined with the parameters listed in Table 4.4. Then, an ultra-thin (20 µm) chip is placed (c), leveled and fixed (d) in the cavity using a thermally conductive glue (U 8449-9, Namics Corporation) or an ICA (thermally and electrically conductive), CE3103 WLV from Emerson & Cuming Isotropic. Leveling of the chips is again measured using a non-contact optical profilometer. Measuring 25 embedded components, an average of 0.46° with a standard deviation of 0.22° is obtained after leveling before glue curing and an average of 0.57° with a standard deviation of 0.31° is found after thermal curing of the adhesive. The optoelectronic chip is subsequently covered by spin-coating a PI-2611 layer (6 µm thickness) and microvias (diameter 40 µm) are drilled (e) using a 248 nm KrF Excimer laser (200 mJ/cm^2, 100 Hz, static: 50-70 pulses/location) to reach the chip top contacts. Top metalization is performed by sputtering and patterning a 1 µm Cu layer (f). This copper layer is protected by a top covering PI-2611 layer (6 µm thickness), again applied by spin-coating (g). To make contact with the outside world, the polymer layers covering the chip contact fan-out pads are locally removed using laser ablation (CO_2 and KrF Excimer). The optoelectronic package with a total thickness of 40 µm is then ready for release (h). **To the best of our knowledge, such PI based ultra-thin flexible optoelectronic packages including single-mode and back contacted laser chips are reported for the first time.**

Table 4.4 – Chip embedding cavity in PI-2611: laser ablation parameters.

Parameter	Value
Laser	Excimer, $\lambda = 248$ nm
Projection mask	2000 µm x 2000 µm
Spot size	200 µm x 200 µm
Pulse energy	80 µJ
Pulse repetition frequency	100 Hz
Fluence	200 mJ/cm^2
Dynamic: stage translation speed	1 mm/s
Static: # pulses	20 pulses/location

Before each polyimide spin-coating step (except for the starting PI layer), the underlying PI surface is slightly roughened after hard bake by exposing it for 1 min to an oxygen (O_2) plasma. A System VII Batchtop RIE (Plasma-Therm) was used for this purpose with following parameters: RF power 150 W, O_2 flow rate 25 sccm and chamber pressure 150 mTorr. This Reactive Ion Etching (RIE) step is performed to improve the adhesion with the covering layer.

Resulting PI-2525/SU-8 packages with embedded photodetector arrays (4 active areas) are shown in Figure 4.22. Figure 4.22b includes a special fan-out copper design which will ease the alignment of the fiber coupling plug (Chapter 5).

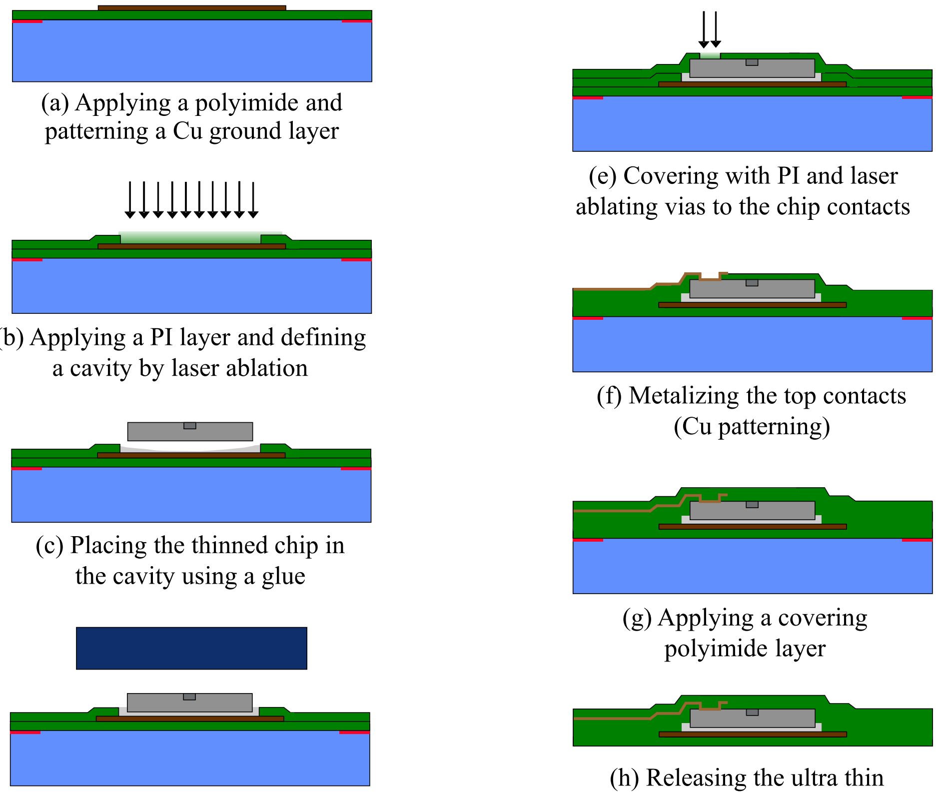

(a) Applying a polyimide and patterning a Cu ground layer

(b) Applying a PI layer and defining a cavity by laser ablation

(c) Placing the thinned chip in the cavity using a glue

(d) Leveling the chip in the cavity

(e) Covering with PI and laser ablating vias to the chip contacts

(f) Metalizing the top contacts (Cu patterning)

(g) Applying a covering polyimide layer

(h) Releasing the ultra thin optical package

Figure 4.21 – Schematic overview of the PI based low-stress optoelectronic package process flow.

4.5.2 Critical points

In order to avoid early failure (decreasing optical power, electrical degradation or breakdown) of the embedded components, following guidelines have to be taken into account during the process flow:

- Although limiting the electrothermal wavelength tuning effect, the dimensions of the heatsinks should be sufficiently large to spread the generated heat.
- The electrically conductive adhesive should be cured under vacuum conditions to avoid the inclusion of air holes.

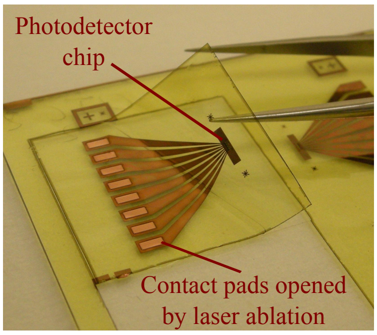

(a) Releasing a PI-2611 embedded photodetector after opening contact pads.

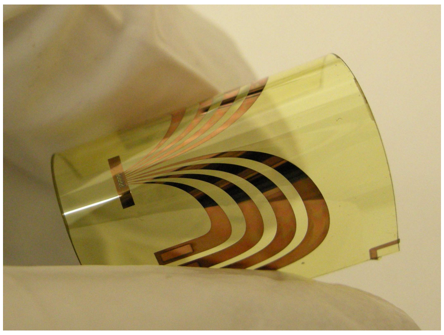

(b) Released photodetector package with dedicated "butterfly" contact fan-out design.

Figure 4.22 – Result of the PI-2611 embedding process flow.

- The sample should be exposed to the highest processing temperature, typically during glue curing, before applying the chip covering layer.

4.5.3 Characterization

The electrical and optical characterization results are similar to the SU-8 based process flow results and are therefore not repeated in this section.

In Figure 4.23, a cross-sectional investigation of a PI-2611 embedded single-mode VCSEL is shown. Figure 4.23a is showing the areas which are investigated in more detail in Figures 4.23b-4.23e. A good step coverage of the different layers stacked on the optoelectronic chip can be observed. The electrical top contacting interface does not show any delamination. In the Scanning Electron Microscope (SEM) images however, one can observe a few potential inclusions of air holes in the electrically conductive adhesive layer.

Figure 4.24 is showing an embedded chip with a thickness of only 10 µm. Because of increasing mechanical stresses, the chip itself starts to bend hindering a proper layer build-up of the polymer package.

4.5.4 Reliability

Thinning and embedding unpackaged (opto)electronic chips in ultra-thin packages with a guaranteed performance level is a huge challenge. The well established traditional packages and according reliability standards do not apply and especially the combination with polymers can be an issue. Moisture can slowly penetrate the system, causing oxidation of galvanic interconnects and swelling of polymer material, resulting in stresses and - in the end - defects. The best

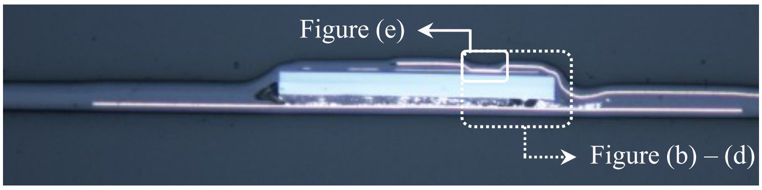

(a) Overview microscope image.

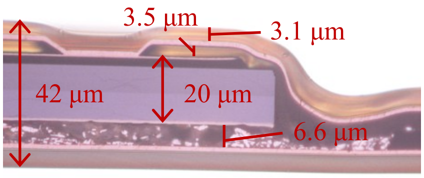

(b) Edge of the chip and PI/Cu step coverage (back illumination).

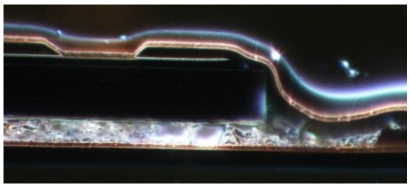

(c) Edge of the chip and PI/Cu step coverage (dark field image).

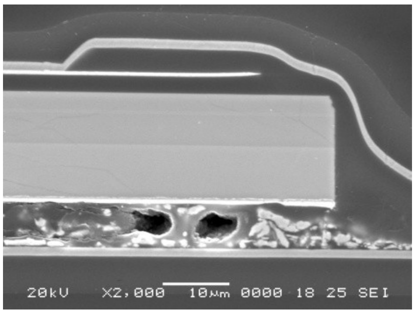

(d) SEM image - potential air hole inclusion.

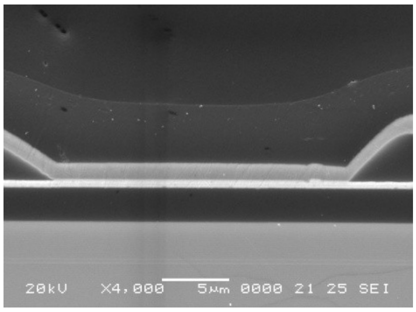

(e) SEM image - detailed view on microvia and top metalization.

Figure 4.23 – Cross-section of a PI-2611 embedded VCSEL.

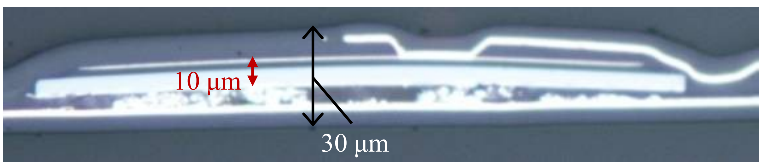

Figure 4.24 – 30 µm chip package with an embedded 10 µm VCSEL.

way to estimate the life time of a system is to put it through accelerated aging tests. Therefore, initial reliability 85/85 (temperature-humidity) tests have been performed on 10 single-mode 850 nm VCSELs embedded in a PI-2611 stack. The samples were stored for 1000 h in a climate chamber under controlled temperature and humidity conditions. The selected temperature/humidity profile consisted of the well-known 85 °C/85 % RH parameters. Each time before measuring the electrical and optical characteristics, the environmental conditions are gradually changed to 30 °C/30 % RH for 30 min.

The results are shown in Figure 4.25. During the first 500 hour, the electrical DC impedance (V_{VCSEL}/I_{VCSEL} @ I_{VCSEL} = 6 mA) and optical power is monitored each 50 h. Between 500 h and 1000 h, the measurement interval is changed to 100 h. After 500 h, the packages are consequently exposed for the first time to an uninterrupted period of 100 h at 85° and 85 % RH. This can explain the unexpected drop of optical power (extra loss of 0.36 dB) at t = 600 h. Another observation is the gradual increase of the electrical impedance, which is less pronounced towards the end of the reliability measurements. All optical and electrical measurements are however within a 10 % range indicating that the effect of accelerated aging might be limited.

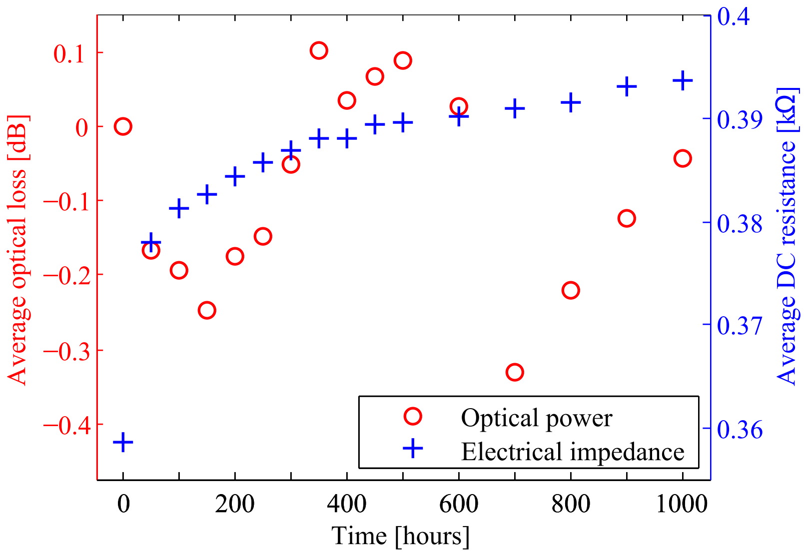

Figure 4.25 – 85/85 reliability test performed on embedded 850 nm single-mode VCSELs monitoring both electrical and optical properties. All measurements are performed using a DC driving VCSEL current, I_{VCSEL} = 6 mA.

4.6 Conclusion

Within this chapter, a polymer integration technology is developed to integrate laser and detector chips within polymer packages. The electrical interconnection is provided through sputtered thin-film copper layers. As a polymer embedding layer, different spin-on polyimide and epoxy materials are used. To limit the thickness of the total chip package, individual optoelectronic chips are thinned down to 20 µm and, if necessary, back-contacts are reapplied and alloyed. The result is an ultra-thin optoelectronic chip package incorporating single- or multi-mode sources or detectors in the 850 nm or 1550 nm wavelength range. This mechanically flexible optoelectronic package has a typical thickness of only 40 µm. Furthermore, the packaging approach based on a PI-2525/SU-8 or PI-2611 embedding stack was shown to have a limited influence on the operation of the devices.

From an embedding point of view, the GaAs 850 nm components are preferred over the InP 1550 nm components, because of a more robust substrate material in terms of handling and thinning. In terms of cost, beam divergence, optical power generation and electrical power consumption, the VCSEL components turned out to be the ideal candidates as a driving source for the fiber sensing systems.

Applying this integration technology using SM VCSELs and PDs on fiber sensing applications, the interrogation system will be based on the electrothermal red-shift observed in the VCSEL wavelength when varying the driving current. A typical wavelength range of 3 nm can be covered using the embedded VCSELs. This is offering only limited possibilities to exploit the multiplexing features of optical fiber sensors, but provides a cost-effective and highly accurate way to read out the optical sensors. Moreover, using this ultra-thin integration technology enables the fabrication of fully embedded interrogation systems with an unprecedented degree of miniaturization.

A fiber sensing system based on the integrated optoelectronic components as well as a detailed discussion on the interrogation principles is included in Chapter 6. But before doing so, the final technology chapter is describing the coupling of the integrated optoelectronic components and optical fiber(s) (sensors).

References

[1] Universal Enterprise - leading distributor of semiconductor bare die, wafer and packaging in China/Asia. (Accessed 2013) Company website. [Online]. Available: http://www.ue.com.hk/

[2] Roithner LaserTechnik. (Accessed 2013) Products. [Online]. Available: http://www.roithner-laser.com/

[3] EXALOS: Superluminescent Light Emitting Diodes (SLEDs) Manufacturer. (Accessed 2013) Products. [Online]. Available: http://www.exalos.com/

[4] BeamExpress. (Accessed 2012) Products. [Online]. Available: http://www.beamexpress.com/

[5] Ulm-Photonics. (Accessed 2012) Products. [Online]. Available: http://www.ulm-photonics.com/

[6] W. Christiaens, "Active and passive component integration in polyimide interconnection substrates," Ph.D. dissertation, Ghent University, 2009.

[7] E. Bosman, "Integration of optical interconnections and opto-electronic components in flexible substrates," Ph.D. dissertation, Ghent University, 2010.

[8] MicroChem - Innovative Chemical Solutions for MEMS and Microelectronics. (Accessed 2013) Company website. [Online]. Available: http://microchem.com/

[9] HD MicroSystems, an enterprise of Hitachi Chemical and DuPont. (Accessed 2013) Company website. [Online]. Available: http://hdmicrosystems.com/

[10] R. Verplancke, "Generic technology platform for the integration of microelectronics and microfluidics on stretchable substrates," Ph.D. dissertation, Ghent University, 2013.

5
Coupling integrated optoelectronic components

The embedding technology and the characterization of embedded fiber sensors and optoelectronics have been described extensively in previous chapters. To combine several of these building blocks into a functional sensing system, a dedicated coupling technology is needed to integrate the optoelectronic driving and read-out units combined with the sensor structures. This technology should provide a low-loss, robust, small, skin compatible (i.e. enabling embedding in thin planar sensing skins), low-cost solution for coupling single and multimode optoelectronic sources to optical waveguiding (typically fiber sensing) structures. A generic compact coupling technology accommodating these needs is developed within this chapter.

5.1 Introduction

Laser diode packages can generally be divided in three categories: butterfly, TO-can (coaxial) and dual in-line. The common configuration for laser diode transmitters in optical communications is the butterfly configuration. Most of the cost of these modules is due to the process of packaging, which includes the coupling of the laser diode to an optical (single-mode or multimode) fiber via certain optical coupling schemes and the firm attachment of all components at their optimum positions inside the module [1].

A rather outdated but still very relevant statistic [2] shows that the commercial market for optical telecommunication components had reached $5 billion in 2001. And more importantly, about 60 % to 80 % of the manufacturing cost of these components comprises fiber pigtailing and packaging (see Figure 5.1). A major portion of the packaging cost is associated with active alignment and attachment of chip-to-chip and single-mode fibers to chips. Active alignment involves lighting up input fibers and active components and maximizing light throughput before attachment. It is clear that the coupling scheme and resulting fiber pigtailing technology are of major importance and have to be chosen judiciously.

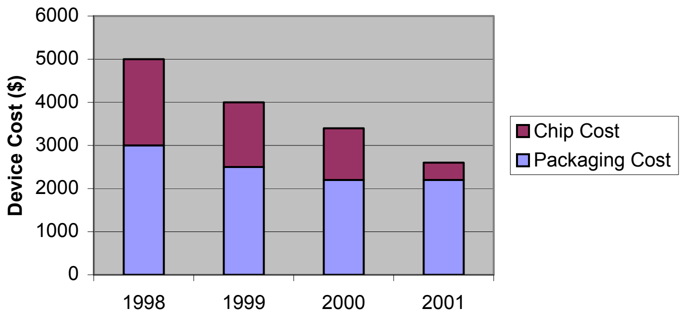

Figure 5.1 – Packaging as a fraction of the total manufacture cost of an optical modulator during the millennium transition.

Within this chapter, a generic compact fiber coupling technology is developed. The specific application which is driving this technology is an optical fiber sensing system, fabricated as flat and small as possible enabling embedding in thin optical skins. The coupling technology will therefore be used to deliver integrated and skin-compliant fiber-coupled optoelectronic components. Like the embedding host material, the material used in the coupling scheme is preferably a (biocompatible) polymer. The coupling scheme itself is based on existing configurations using V-groove technologies, micro-mirrors and intermediate waveguides but combined to yield a fiber-coupled ultra-thin package. This chapter includes design, modeling and fabrication of the coupling technology, as well as evaluation of the alignment accuracy.

Throughout this chapter, several technology choices have to be made to narrow down the options both in terms of the optoelectronic components and the coupling technology. Starting from the conclusions of Chapter 4, only SLEDs and VCSELs are withheld as optoelectronic driving sources in Section 5.2. In Section 5.3, a VCSEL is selected as the final optoelectronic source and initial coupling simulations prove a direct coupling approach to be more efficient compared to an integrated intermediate waveguide approach. Finally, in Sections 5.4-5.6, a dedicated planar coupling technology for single-mode VCSELs is developed. The structure of this chapter is schematically shown in Figure 5.2.

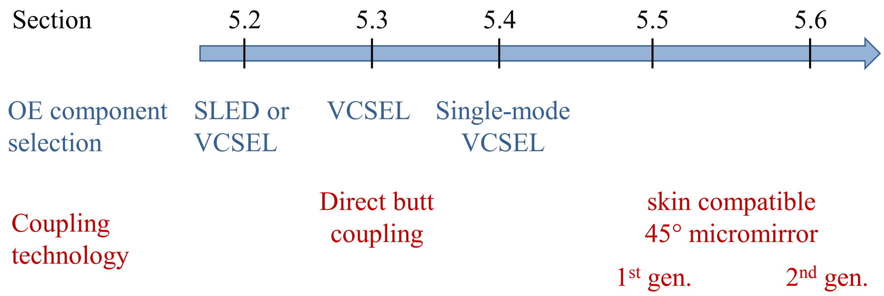

Figure 5.2 – Technology choices within Chapter 5.

The optical simulations (Lumerical and ASAP) performed within this chapter were defined in close collaboration with and carried out by B-Phot, VUB within the framework of the European project Phosfos [3]. It is also important to mention that, although the coupling medium is different (waveguides versus fibers), the coupling concepts and associated technologies are strongly inspired by the work of dr. Erwin Bosman. Within his PhD dissertation [4] (Chapter 7, and more specifically Sections 7.4.2 and 7.5), a polyimide based 90° optical mirror insert for flexible polymer optical interconnects was developed based on a dedicated 45° clamping tool to lap and polish mirror facets. For the final (VCSEL-fiber-PD) coupling schemes in this dissertation, a similar clamping tool is used albeit with different materials and processing steps.

5.2 Optoelectronic component selection

Before fiber pigtailing, the optoelectronic components are packaged by embedding them in ultra-thin optical packages. Several types of semiconductor lasers were looked into, both in the 850 nm and 1550 nm wavelength range. An overview of the optoelectronic components (bare die), available for embedding and coupling, is again provided and combined with the conclusions from Chapter 4 in Table 5.1.

All optoelectronic sources have a different lay-out, wavelength, emitting direction/angle, degree of polarization and modal structure. For the fiber coupling work, a selection of the most promising source(s) was consequently imposed. As discussed in Chapter 4, the Roithner LED and LD suffer from several disadvantages (high beam divergence, modal structure not compatible with fiber sensors). They will therefore not be included in the coupling simulations and technology. Furthermore, embedding the Exalos SLED source revealed several technology challenges (limited heatsinking for a driving current of 300 mA, optical feedback)

Table 5.1 – Overview of the available (bare die) optoelectronic sources.

	edge-emitting		*top-emitting*			
	LD	SLED	LED	VCSEL	VCSEL	VCSEL
	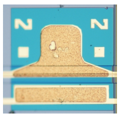		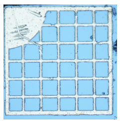		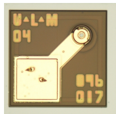	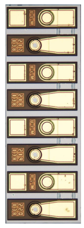
Company	Roithner	Exalos	Roithner	BeamExpress	ULM Photonics	ULM Photonics
Reference	[5]	[6]	[5]	[7]	[8]	[8]
Price/die	€ 10	€ 250	€ 2	€ 50	€ 11	€ 6
λ_{central}	1550 nm	850 nm 1550 nm	1550 nm	1550 nm	850 nm	850 nm
Modes	SM/MM	SM	MM	SM	SM	MM
$P_{\text{optical, total}}$	6 mW	10.5 mW 20 mW	2.5-5 mW	1.2 mW	2.5 mW	1.5 mW
Bandwidth	3-5 nm	50 nm 65 nm	130 nm	0.15 nm	0.1 nm	0.3 nm
Chapter 4 remarks	Modal structure problem	Optimized thermal design indispensable	Integrated coupling not feasible	Brittle substrate	Back-contact	
Chapter 4 conclusion	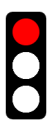		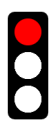			

and moreover, the SLED is an expensive chip to start from. Because of its broad spectral range and associated fiber sensor multiplexing possibilities, the SLED will nevertheless be included in the coupling simulation models. Alternatively, the Vertical-Cavity Surface-Emitting Laser (VCSEL) sources offer a cost-effective, single-mode alternative with a limited beam angle divergence. Furthermore, the electrothermal red shifting of the VCSEL wavelength can be used to track fiber Bragg grating sensors (elaborated in Chapter 6). Therefore the top-emitting VCSELs are chosen as the main component throughout this chapter, to describe the coupling technology. Main disadvantages of these components are the wavelength variation from chip-to-chip (up to a few nm), restricting the use of fiber Bragg gratings with fixed wavelengths, and the limited fiber sensor multiplexing possibilities because of the tuning range comprising only a few nm.

5.3 Intermediate waveguides vs. direct butt coupling

Initial coupling simulations were performed to determine the feasibility of different technological possibilities to couple the packaged optoelectronic sources to optical fibers. These initial simulations do not yet include the flexible optoelectronic package but are based on the unpackaged chip characteristics and the most generally used optical fiber, silica single-mode (SMF-28).

Two general coupling structures have been investigated:

- An intermediate waveguiding structure to couple the source to a silica single-mode fiber.
- Direct butt coupling of the optical source to a silica single-mode fiber.

5.3.1 SLED coupling

The first candidate source we consider is the Exalos SLED chip ($\lambda_{central}$ = 1550 nm). The far field Full Width at Half Maximum (FWHM) divergence angles of the Exalos SLED are respectively $\theta_{\parallel} = 46°$ and $\theta_{\perp} = 22°$. Given these large divergence, coupling to a single-mode fiber is not straightforward (NA of a silica SMF is typically between 0.12 and 0.14). The initially proposed coupling structure consists of an intermediate tapered waveguide, as illustrated in Figure 5.3, to avoid damaging the SLED facet when directly coupling to SMF and to ease the coupling procedure through increased coupling alignment tolerances.

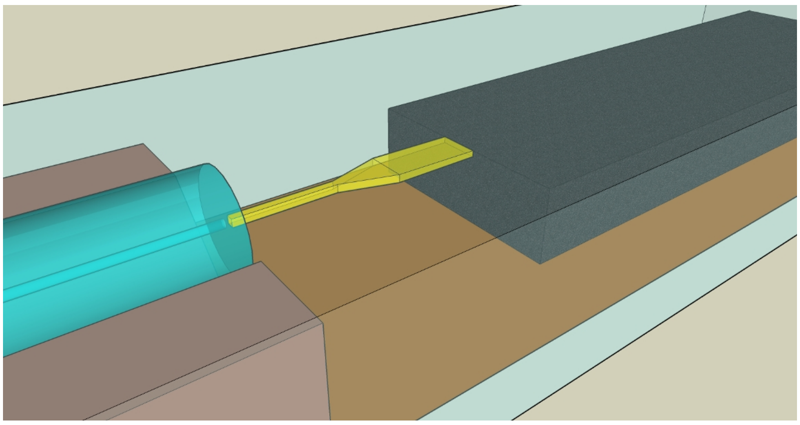

Figure 5.3 – Schematic view of an intermediate tapered waveguide as a coupling structure between the SMF (left) and the SLED (right), mounted on a carrier and embedded in a host material.

Tapered waveguide

To calculate the waveguide modes of the tapered waveguide, Lumerical MODE Solutions [9] was used. Before optimizing the taper shape, we investigate the coupling of the SLED to the tapered waveguide. From practical considerations, the large end of the waveguide (at the interface with the SLED) is targeted to be 34 µm x 8 µm. The former is chosen in view of providing some tolerance during the packaging and fiber pigtailing, whereas the latter (the 8 µm height) is chosen in correspondence to the core size of the SMF. The tapered waveguide would be fabricated in LightLink XP-6701A, a polymer optical core material with a refractive index of 1.506, surrounded by LightLink XP-5202A, a polymer optical cladding with a refractive index of 1.481 (both at a wavelength of 1550 nm, NA = 0.27) [10, 11]. To generate the beam emitted by the SLED, we suppose that it emits a Gaussian beam. Because Lumerical MODE Solutions does not allow the definition of asymmetrical Gaussian beams, we generate two separate Gaussian beams, where the first one has a divergence of 46° and the second one has a divergence of 22°. For both these beams, the coupling transfer to the simulated mode profile of the tapered waveguide was calculated by evaluating the overlap integral.

The resulting coupling efficiencies are given in Table 5.2. The effective coupling efficiency between the SLED and the waveguide, taking into account the SLED beam asymmetry, will be in between both simulated coupling efficiencies. Nonetheless, we notice that the achievable coupling efficiency is very low, especially in view of the fact that the coupling from the waveguide to the SMF will induce additional losses.

Table 5.2 – Calculated coupling efficiency between the SLED and the tapered waveguide.

Divergence	Overlap	Coupling loss
46°	2.17 %	−16.64 dB
22°	10.24 %	−9.90 dB

Direct butt coupling

Given the very low efficiencies in Table 5.2, the direct coupling of the SLED to an SMF, without the use of an intermediate waveguide, is also investigated. A standard SMF-28 with a 4.15 µm radius GeO_2-doped core to calculate the SMF's fundamental mode [12] is used. The resulting coupling efficiencies between the SLED and the SMF are given in Table 5.3.

Given the relatively large difference in-coupling efficiency in Table 5.3, further simulations are performed in the Advanced System Analysis Program (ASAP)

Table 5.3 – Calculated coupling efficiency between the SLED and the directly coupled SMF.

Divergence	Overlap	Coupling loss
46°	4.89 %	−13.11 dB
22°	22.70 %	−6.44 dB

by Breault Inc. [13], which allows the definition of asymmetric Gaussian beams (as opposed to Lumerical MODE Solutions). The coupling efficiency resulting from the overlap integral is 14.7 % or −8.33 dB, which indeed lies in between the values calculated in Table 5.3.

At least as important as the maximum achievable coupling efficiency is the tolerance for mechanical misalignments during the assembly (packaging) process. To evaluate the lateral misalignment tolerance, the SMF mode profile is shifted along the X- and Y-axis respectively, and the coupling efficiency at each position is calculated. The results of these simulations show a −1 dB lateral alignment tolerance of +/- 1.5 µm along both axes.

Because the maximum achievable coupling efficiency is still rather low, the possibility of using lensed single-mode fibers instead of normal SMF is investigated. Lensed fibers are commercially available with various mode field diameters. Therefore, the coupling efficiency between SLED and lensed SMF is calculated as a function of the Mode Field Diameter (MFD) of the lensed fiber. The results are shown in Figure 5.4a. This graph clearly shows that using a lensed fiber allows improving the coupling efficiency when the SLED and lensed SMF are perfectly aligned. However, as mentioned earlier, the tolerance for misalignments should again be taken into account.

We select two different lensed fibers to perform this tolerancing analysis, with a mode field diameter of respectively 2.2 µm and 5.6 µm. From the tolerancing simulations for the lensed SMF with MFD = 2.2 µm, the −1 dB tolerance for lateral misalignments can be determined to be +/- 0.6 µm in X and +/- 0.5 µm in Y. This illustrates that in comparison to the standard SMF, the lensed SMF with MFD = 2.2 µm allows achieving a much higher coupling efficiency (87.35 % versus 14.7 %), but at the expense of a tighter alignment tolerance (+/- 0.5 µm versus +/- 1.5 µm), hence requiring a higher alignment accuracy during the packaging.

The tolerancing simulations for the lensed SMF with MFD = 5.6 µm yield a −1 dB alignment tolerance of +/- 1.1 µm in X and +/- 1.0 µm in Y. Whereas the alignment tolerance is more relaxed for this lensed SMF than for the previous one, the maximum achievable coupling efficiency is also lower (40.52 % in this case). When using a lensed SMF for the coupling to the SLED, it is clear that one should take the trade-off between maximum coupling efficiency and tolerance for misalignments into account. Figure 5.4b shows a graphical comparison between the lateral misalignment tolerance in Y for standard SMF, and the two previously selected lensed SMFs.

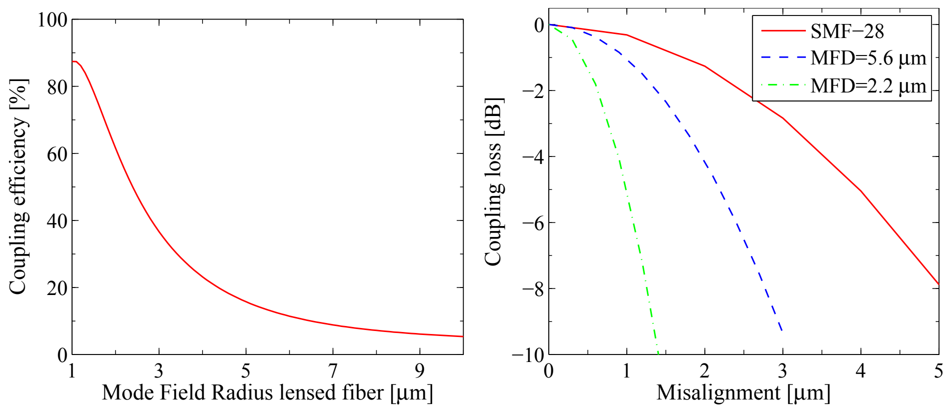

(a) Coupling efficiency between SLED and lensed fiber with varying mode field radius.

(b) Comparison of the lateral misalignment in Y (most stringent axis) for standard SMF and two selected lensed SMFs.

Figure 5.4 – SLED direct butt coupling results. Note that unlensed (standard) SMF-28 has a mode field radius of 5.2 µm.

5.3.2 VCSEL coupling

The second optoelectronic source we look into is the BeamExpress VCSEL (λ = 1550 nm). The main advantage of this source is the small divergence angle ($\theta_{\parallel} = 9°$ and $\theta_{\perp} = 9°$ FWHM) compared to the superluminescent LED. The fundamental mode profile of this source is again simulated as a Gaussian beam.

The coupling efficiency between the BeamExpress VCSEL and standard SMF is 89.13 % or −0.5 dB at the optimal position. The variation of the coupling efficiency as a function of the MFD of the receiving fiber is also calculated. For a lensed fiber with MFD = 2.2 µm and MFD = 5.6 µm, the coupling efficiency changes to respectively 28.18 % and 93.33 %.

A tolerance analysis is again performed on coupling with an unlensed SMF-28, a lensed SMF with MFD = 2.2 µm and a lensed SMF with MFD = 5.6 µm. The −1 dB tolerances for lateral misalignments are listed in Table 5.4. The practical implementation of the aligning and coupling process will be done using a Dr. Tresky T3200 semi-automatic bonder. An alignment accuracy less than 3 µm can be achieved using this bonder. Monitoring the optical power during alignment of the optical fiber(s) (active coupling) can further enhance the alignment accuracies likely achievable.

Table 5.4 – Coupling efficiencies and aligning tolerances for VCSEL coupling.

Fiber type	MFD	Coupling efficiency	1 dB tolerance (X)	1 dB tolerance (Y)
Unlensed (SMF-28)	10.4 μm	89.1 %	+/- 2.2 μm	+/- 2.2 μm
Lensed	5.6 μm	93.3 %	+/- 1.6 μm	+/- 1.6 μm
Lensed	2.2 μm	28.2 %	+/- 1.3 μm	+/- 1.3 μm

The conclusion here is different from the previous optoelectronic component. The coupling efficiency is already high for the unlensed single-mode fiber. In combination with the best results for the alignment tolerances, the unlensed fiber is the best option to couple with in this case. A lensed fiber with a MFD of 5.6 μm maximizes the absolute coupling but the overall result will be worse because of the lower alignment tolerances. A lensed fiber with a MFD of 2.2 μm yields the worst results both on coupling efficiency and alignment tolerances.

5.3.3 Conclusion

Simulations for the intermediate waveguide approach, using a tapered waveguide and an SLED, indicate high coupling losses introduced by the mode field diameter mismatch of the optical source and the waveguide. The alternative, using direct butt coupling of the optical fiber, still provides quite low coupling efficiency (less than 15 %) for the SLED. A solution can be the introduction of lensed fibers providing a good mode field diameter match and yielding coupling efficiencies of 80 % and more. For the long wavelength VCSEL, direct coupling to an unlensed fiber results in high coupling efficiencies (89 %). It is important to note that the above-mentioned VCSEL simulations, performed for 1550 nm VCSELs, also apply as indicative coupling results for the 850 nm VCSELs as the beam divergence angles are in the same order of magnitude.

Because of the higher coupling efficiencies in combination with better alignment tolerances - especially for the standard unlensed SMF, cheaper components, possibility to fabricate simple fiber sensor interrogation systems (based on thermal wavelength shifting, see Chapter 2, Section 2.2.1), **the VCSEL component is selected as a final optoelectronic source for the remainder of this chapter. Fiber coupling is performed based on a direct butt coupling scheme, without the use of an intermediate waveguide structure.**

5.4 VCSEL wavelength and modal structure

To further limit the selection of eligible optoelectronic components, we turn our focus to the requirements for VCSELs as fiber sensing interrogation units.

5.4.1 VCSEL requirements

Using the embedded VCSELs from Chapter 4, the fully embedded (using integrated VCSELs and detectors) fiber sensing system can be used in two variants to interrogate fiber Bragg gratings:

- On-off peak detecting interrogation scheme *(constant current mode)*. In this interrogation scheme, the VCSEL is driven at a fixed DC current and the optical power on the integrated photodetector is monitored as a function of time. Each time the Bragg grating is coinciding with the VCSEL spectral peak, a maximum will be detected in the photocurrent through the integrated photodetector. This current is then a measure of the degree of overlap of the VCSEL spectrum and the Bragg grating spectrum. This interrogation scheme can for example be used for respiration monitoring.
- Full reconstruction of the Bragg grating shape *(modulation mode)*. In this interrogation scheme, the VCSEL is driven at a modulated (for example a sawtooth) current at a certain frequency, f. The photocurrent is read out continuously and each 1/f seconds a plot of intensity versus current can be extracted to show the intensity of the power, transmitted or reflected by the Bragg grating, versus the wavelength. This interrogation scheme is fully exploiting the embedded system possibilities and provides a low-cost high-speed (upper bound is determined by the red-shift dynamics of the VCSEL driving unit) read-out.

It is clear that, regardless of the interrogation scheme which is used, the FWHM of the VCSEL should be as narrow as possible and ideally there should be only one spectral peak. The intensity versus wavelength of the VCSEL has therefore preferably a Gaussian profile:

$$I_{\mathrm{VCSEL}} = \frac{P_{\mathrm{total}}}{a\sqrt{\pi}}\, e^{-(\lambda-\lambda_{\mathrm{central}})^2/a^2}$$

- I_{VCSEL} is the VCSEL intensity profile.
- P_{total} is the total power emitted by the VCSEL.
- a is linked to the FWHM: FWHM = 2 a $\sqrt{\ln(2)}$

- λ_{central} is the VCSEL central emitting wavelength.
- The value of a should be as small as possible:

$$\lim_{a \to 0} I_{\text{VCSEL}} = P_{\text{total}}\, \delta(\lambda - \lambda_{\text{central}})$$

The smaller a, the higher the resolution of the spectral analysis will be.

The technology developed in this chapter is applied for 850 nm devices. This 850 nm route was given priority over the 1550 nm route because of a higher component workability in terms of temperature budget, robustness and cost. Without going into details, the 1550 nm devices typically involve the use of InP as a more fragile substrate material imposing more restrictions [14]. When interrogating *polymer* or *plastic* optical fiber or waveguide sensors, 850 nm is also the preferred wavelength because of significantly lower propagation losses (see Section 2.3). A drawback however is related to the strain sensitivity of Bragg gratings in silica and polymer fibers at 850 nm, which is lower than at 1550 nm [15, 16].

A key parameter is the modal structure of the driving optoelectronic source. Both a multimode and single-mode variant of the 850 nm VCSEL are available. The far-field beam profile of these devices for several driving currents is measured with a goniometric radiometer, available at B-Phot (VUB). The results are shown in Figure 5.5 and 5.6. We conclude that the multimode VCSEL is not suited for fiber sensing as the modal structure varies as function of the driving current. A comparison of the spectral output of the multimode and single-mode VCSEL using a driving current of 5 mA is shown in Figure 5.7. At the detector side, it is impossible to distinguish between an extra peak in the multimode VCSEL spectrum and a shifted Bragg grating peak.

5.4.2 Conclusion

When selecting a VCSEL to be integrated with a fiber sensor element, wavelength and modal compatibility of the laser source and Bragg grating sensor is crucial. From an embedding point of view, the 850 nm laser source offers the most reliable, robust and cost-effective driving optoelectronic element. Therefore, **the** 850 nm **single-mode VCSEL component from ULM Photonics [8] (Table 5.1) is selected as the final optoelectronic source.**

The remainder of this chapter focuses on the coupling of integrated VCSEL components to optical fiber sensors. The general coupling approach consists of a 500 µm thick micromirror coupling plug including different types of silica single-mode (5 to 6 µm diameter at 850 nm, 9 µm at 1550 nm) or multimode (50 µm diameter) optical fiber and a 45° micromirror facet enabling 90° deflection of the light from a VCSEL into a fiber. This coupling scheme results in a thin, planar coupling module which can be integrated in flexible and stretchable sensing foils of 1 mm thickness.

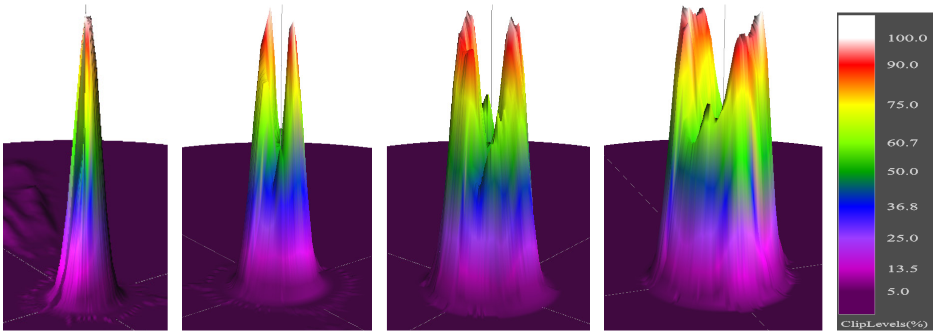

(a) 1 mA **(b)** 2 mA **(c)** 5 mA **(d)** 10 mA

Figure 5.5 – 3D far-field radiation pattern for a multimode 850 nm VCSEL.

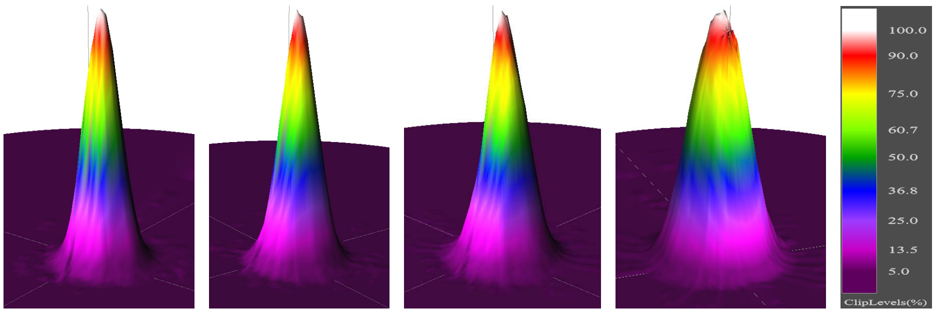

(a) 1 mA **(b)** 2 mA **(c)** 3 mA **(d)** 5 mA

Figure 5.6 – 3D far-field radiation pattern for a single-mode 850 nm VCSEL.

5.5 VCSEL-fiber coupling scheme: initial design

Starting from simulations in ASAP (Advanced Systems Analysis Program), different coupling structures are now looked into in detail and theoretical upper limits for the coupling efficiencies are calculated. Similar coupling schemes can be used for integrated photodetectors. The active emitting area of a VCSEL typically has a 9 µm diameter whereas the active area of the photodetector is 100 µm in diameter. Alignment tolerances are consequently less restrictive for the photodetector. Further detailed simulations are consequently only carried out for the source to fiber coupling problem.

To come up with a skin compatible fiber coupling scheme, a planar (flat), thin and integrated fiber in- and out-coupling technique is required. The coupling scheme therefore consists of a PMMA plug (500 µm thickness) with a U- or V-

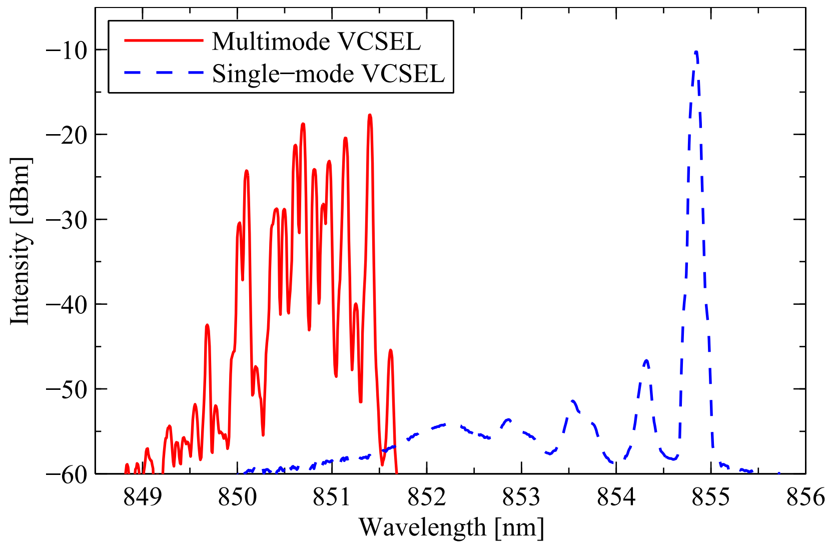

Figure 5.7 – Spectral output comparison of a multimode and single-mode VCSEL ($I_{driving} = 5\,mA$).

groove track to clamp the fiber (Figure 5.8). A 45° mirror facet can be introduced on the PMMA plug by using a dedicated 45° clamping master tool and different lapping/polishing techniques. The reflecting layer is applied by evaporating a thin (few 100 nm) layer of gold. A cleaved fiber can then be inserted in the groove and fixed with an index-matched UV glue. When the coupling plug is mounted on top of the VCSEL package, the vertically emitted light is reflected on the gold surface through the coupling plug in the optical fiber.

The base material of the fiber coupling plug is polymethyl methacrylate (PMMA). This transparent and low-cost polymer material is compatible with flexible and stretchable skin embedding materials and offers several advantages for fixing and aligning optical fibers. The choice of a transparent material such as PMMA instead of polyimide (used for the micromirrors in [4]) reduces the optical losses introduced by the optical path through the coupling plug material.

5.5.1 Simulations in ASAP

To validate this initial coupling scheme model, simulations have been performed in Advanced Systems Analysis Program (ASAP). Following parameters were simulated:

- Lateral misalignment losses

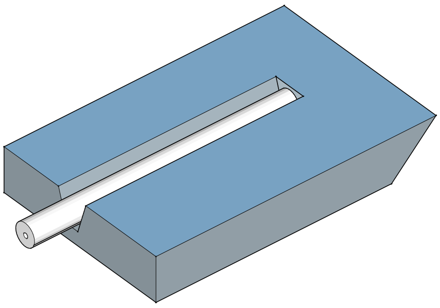

(a) Top side (U-/V-groove ablation).

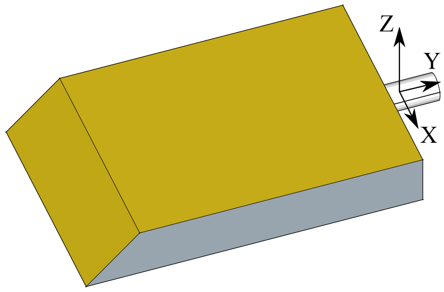

(b) Backside (metalized).

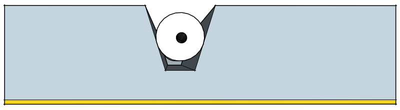

(c) Cross-section of the top side view, metalization on bottom.

Figure 5.8 – Schematic view of the initial coupling scheme.

- Longitudinal misalignment losses
- Influence of the fiber type (single-mode versus multimode)
- Influence of the VCSEL driving current
- Influence of the thickness of the chip covering layer (as part of the optoelectronic chip package)
- Influence of the optical package top polyimide layer (as part of the optoelectronic chip package)

The embedded optoelectronic component is the single-mode 850 nm VCSEL from ULM Photonics (Table 5.1). Beam profiles of the bare VCSEL dies and the embedded VCSEL dies have been measured using a far-field profiler. An example of the far-field intensity of a bare die VCSEL was shown in Figure 5.6.

Based on the information provided by the goniometric radiometer (beam profile, source divergence), the lateral and longitudinal misalignment losses are simulated and the results are shown in Figure 5.9. The applied simulation parameters are listed in Table 5.5, case "Fiber detector 1". The longitudinal direction (Y) is oriented along the fiber axis. The lateral misalignments are located perpendicular to the fiber axis (X and Z). To achieve a total loss in multimode fiber below 1 dB, an alignment accuracy of 5 µm is needed. During assembly of the fiber coupling plug, a theoretical alignment accuracy below 3 µm is achievable using the Dr. Tresky T3200 semi-automatic bonder.

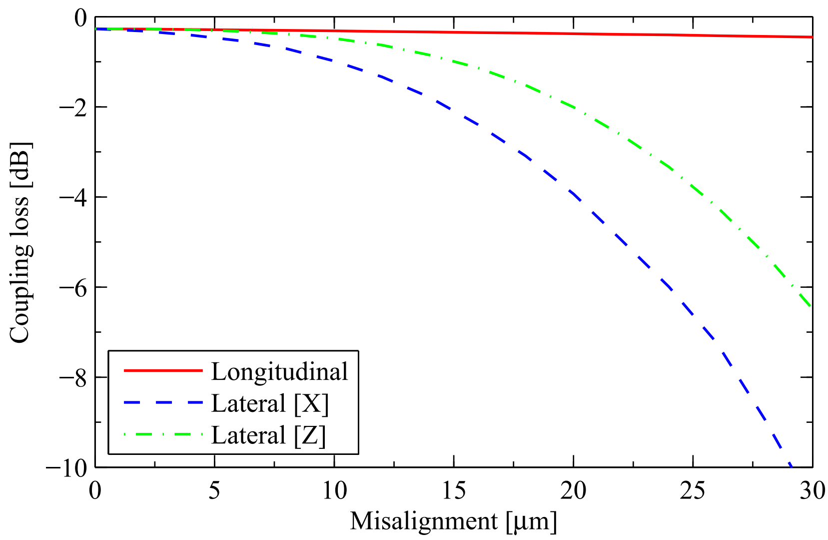

Figure 5.9 – Misalignment losses for the 1st coupling scheme using a MM 50 µm fiber.

Table 5.5 – Simulation parameters initial coupling scheme, multimode and single-mode fiber detector.

Simulation parameter	Value
Fiber detector 1	50 µm multimode fiber NA = 0.2
Fiber detector 2	9 µm single-mode fiber NA = 0.13
Goniometric radiometer input	Non-embedded bare die VCSEL, I = 1 mA
Fiber - PMMA interface	NOA 81
VCSEL package - coupling plug interface	NOA 81
Optoelectronic package	SU-8 based
↪ Top SU-8 layer thickness	18 µm
↪ Top SU-8 layer refractive index	1.593
↪ Top PI layer thickness	10 µm
↪ Top PI layer refractive index	n_x,n_y = 1.678, n_z = 1.664

The next simulation case is identical to the previous one, except for the fiber detector which is now single-mode (full parameter list in Table 5.5, case "Fiber detector 2"). Lateral and longitudinal alignment tolerances are shown in Figure 5.10. The optical path is too long for efficient single-mode coupling: a minimal coupling loss of 10 dB was obtained.

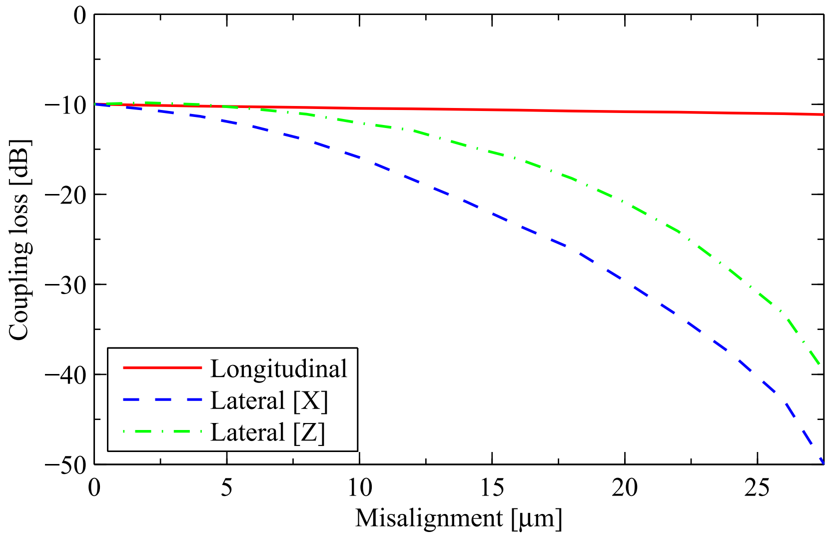

Figure 5.10 – Misalignment losses for the 1st coupling scheme using a SM 9 µm fiber.

The top layer of the flexible OE package typically consists of a HD MicroSystems PI-2525 or PI-2611 polyimide layer with a thickness up to 10 µm. The influence of this layer for the multimode fiber coupling scheme in combination with higher VCSEL driving currents is shown in Figure 5.11a assuming a perfect alignment of the coupling plug and a 10 µm PI-2525 top covering layer. There is no significant influence of the top PI layer and the coupling losses are increasing for higher driving currents because of the slight increase in beam divergence for higher driving currents (Figure 5.6).

Another important parameter of the optoelectronic package is the thickness of the polymer layer which is applied on top of the chip before via drilling and top metalization. This chip covering layer can be SU-8 or PI-2611 (more details and the full build-up of the package can be found in Chapter 4). The influence on the coupling efficiency using an SU-8 chip covering layer, is shown in Figure 5.11b. This parameter only has a significant influence in the case of a single-mode coupling fiber.

5.5.2 Experimental results

One of the assumptions of the simulation model is a perfectly smooth interface in between the coupling fiber and the PMMA material (this interface can be an

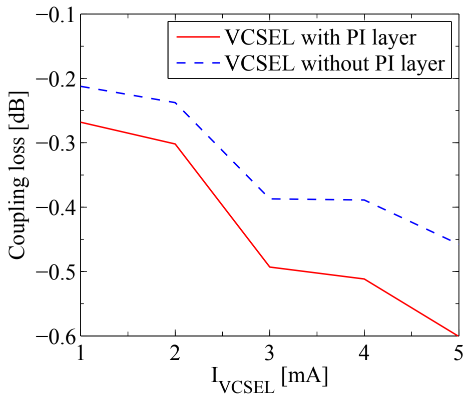

(a) Theoretical upper limit coupling loss (coupling to multimode fiber): increasing VCSEL current and influence of the optical package top PI layer.

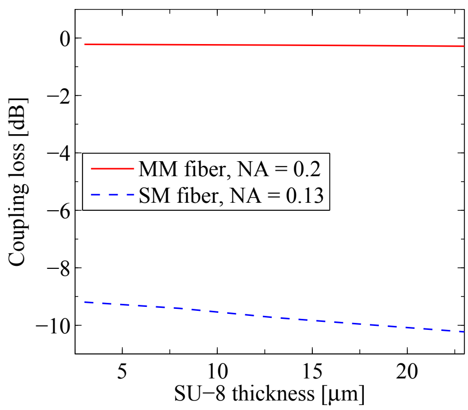

(b) Influence of the chip covering SU-8 layer thickness on the coupling efficiencies.

Figure 5.11 – Influence of SU-8 and PI chip embedding material.

air gap or filled with index matching gel). A first step to fabricate these coupling plugs is consequently the definition of a fiber clamping groove with low sidewall roughness resulting in a smooth fiber-PMMA interface. A fast and easy approach is the use of laser ablation to define structures in the PMMA material. Figure 5.12 shows the ablation rate of PMMA using a CO_2 laser ($\lambda = 10.6\,\mu m$). Useful ablation depths are obtained starting from $4\,J/cm^2$. After cross-section investigation, following parameters are selected:

$$F = 12\,\frac{J}{cm^2}$$

$$N = 10 \text{ pulses}$$

F is the fluence, N is the number of pulses. An example of such a fiber clamping groove is shown in Figure 5.13 (cross-section view). The sidewall of these ablated grooves is however too rough and not optically transparent. For obtaining high quality optical structures, an rms roughness below $\lambda/20$ is required in theory. In a practical situation, a surface roughness in the order of 20 nm (measured over a 50 µm x 50 µm area) or below is desired.

Alternative techniques to create V-grooves in optically transparent polymers such as PMMA have also been looked into, for example Reactive Ion Etching (RIE) using O_2 and CHF_3 gas mixtures. The sidewall roughness can be accurately controlled this way but the etching rate is below 1 µm/min leading to etching times of a few hours. The quality of the hard mask for the RIE process is in this case very important. Because of the time-consuming and expensive process, an alternative coupling scheme was developed as described in the next section.

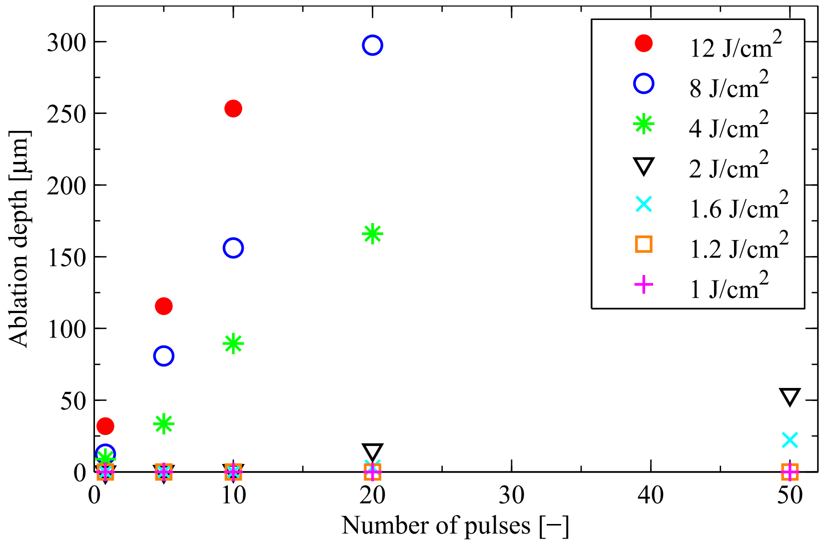

Figure 5.12 – Ablation rate of PMMA using a CO_2 (10.6 µm) laser for different fluences.

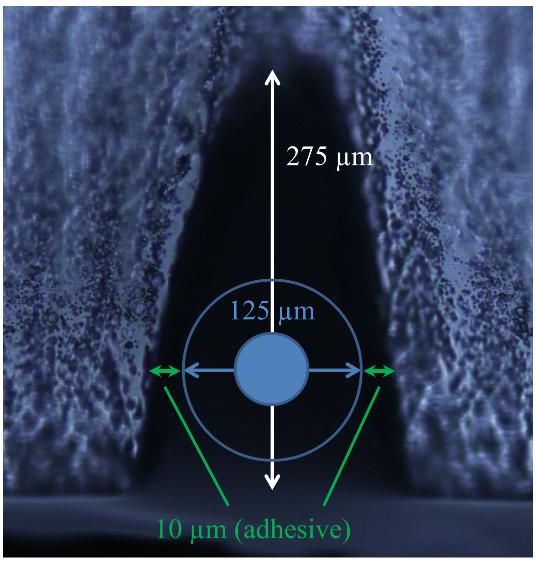

Figure 5.13 – Cross-section of CO_2 ablated groove: 10 pulses @ 12 J/cm^2.

5.6 VCSEL-fiber coupling scheme: second design

The second version of the coupling scheme consists of the same coupling plug but now the reflecting micromirror facet is applied directly on the coupling fiber. This is schematically shown in Figure 5.14. The need for PMMA sidewalls of optical quality is consequently avoided and the optical path is further reduced.

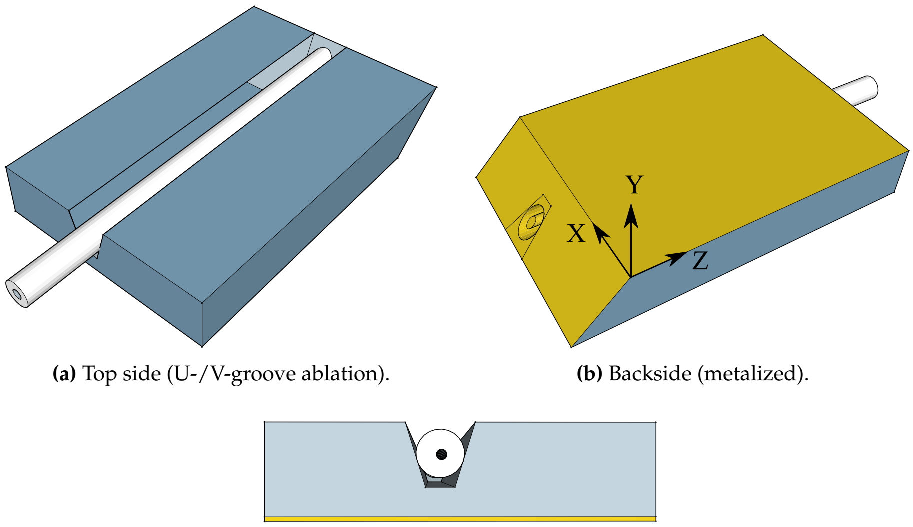

(a) Top side (U-/V-groove ablation). **(b)** Backside (metalized).

(c) Cross-section of the top side view, metalization on bottom.

Figure 5.14 – Schematic view of the second coupling scheme.

5.6.1 Simulations in ASAP

Similar simulations as for the initially designed coupling scheme are now performed for the second coupling scheme. Figure 5.15 shows the coupling losses as a function of lateral and longitudinal mismatches for the multimode fiber coupling scheme and Figure 5.16 shows the coupling losses for the single-mode fiber coupling scheme. Comparing the results to the initial coupling scheme, similar trends are visible. There is a significant difference however in the absolute coupling losses; a comparison is shown in Table 5.6. The alignment tolerances in this table are referring to the alignment of the coupling plug (and not to the fiber as such), consequently including the optical path length between the source and the fiber (beam broadening). The second coupling scheme provides a higher alignment tolerance for the multimode coupling fiber and half the coupling loss for single-mode fibers compared to the initial coupling scheme. The second coupling scheme is consequently more efficient, both in terms of fabrication and performance. The influence of other parameters (related to the chip embedding layers) is also simulated indicating similar trends as in the initial coupling scheme and are therefore not shown here.

Table 5.6 – First (initial) and second coupling scheme: comparison of coupling losses. 3 dB tolerances are measured with respect to the minimal loss numbers (perfect alignment).

Fiber type	Axis	1st scheme Min. loss	2nd scheme Min. loss	1st scheme −3 dB tol.	2nd scheme −3 dB tol.
50 µm core MM fiber	Longit.	0.3 dB	0.3 dB	≫ 50 µm	≫ 50 µm
	Lateral X	0.3 dB	0.3 dB	18 µm	21 µm
	Lateral Z	0.3 dB	0.3 dB	23 µm	25 µm
9 µm core SM fiber	Longit.	10 dB	6.4 dB	> 50 µm	53 µm
	Lateral X	10 dB	6.4 dB	7 µm	5 µm
	Lateral Z	10 dB	6.4 dB	13 µm	7 µm

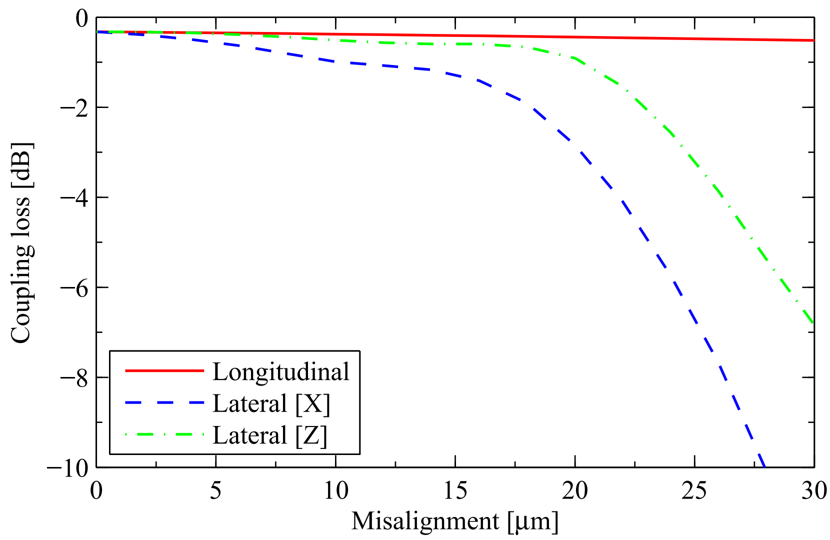

Figure 5.15 – Misalignment losses for the 2nd coupling scheme using a MM 50 µm fiber.

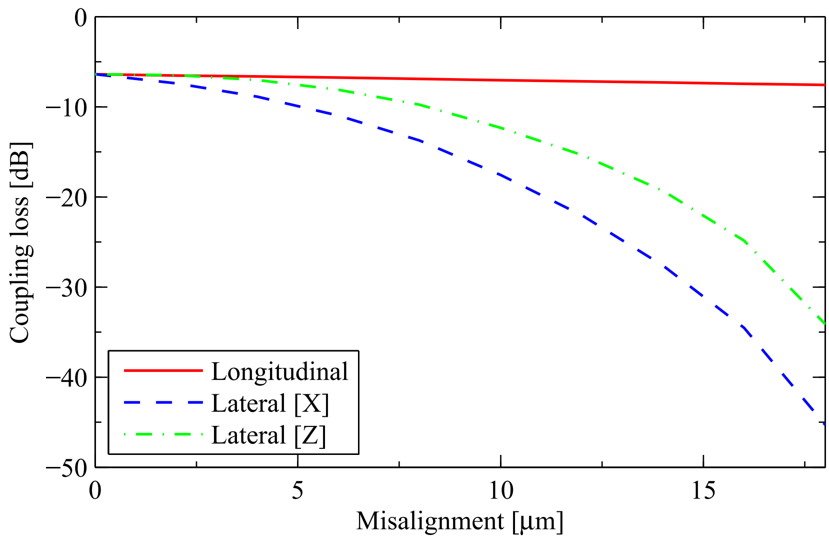

Figure 5.16 – Misalignment losses for the 2nd coupling scheme using a SM 9 μm fiber.

5.6.2 Experimental results

Mirror plug fabrication

A similar laser process as for the first coupling plug is used to fabricate the fiber alignment grooves. The technological manufacturing process for the coupling plugs is schematically shown in Figure 5.17a-c; several PMMA plugs can be fabricated in one laser ablation step.

After ablating fiber alignment grooves and fixing the coupling fibers in the grooves using UV curable NOA 68 (referred to as *glue layer 1*), a lapping and polishing process (Figure 5.17e) is applied to obtain a 45° micromirror on the fiber facet. This process consists of subsequent mechanical grinding and polishing steps of the coupling plug. A dedicated PMMA coupling plug clamping tool is used for this process, shown in Figure 5.18. In Figure 5.19, microscope images are shown of the fiber facet after mechanical lapping (P1200 and P4000 grinding foils) and after polishing with different grain size suspensions (1 μm diamond and 0.3 μm alumina powder). The end result is a flat fiber facet of optical quality with an average surface roughness of 23 nm on a 50 μm x 50 μm area, measured with a non-contact optical profilometer (WYKO NT3300).

Because of the manual fixing of the fiber in the alignment groove, laser ablation debris and glue residuals can be present on the fiber (at the back of the mirror plug). This is clearly visible in Figure 5.20.

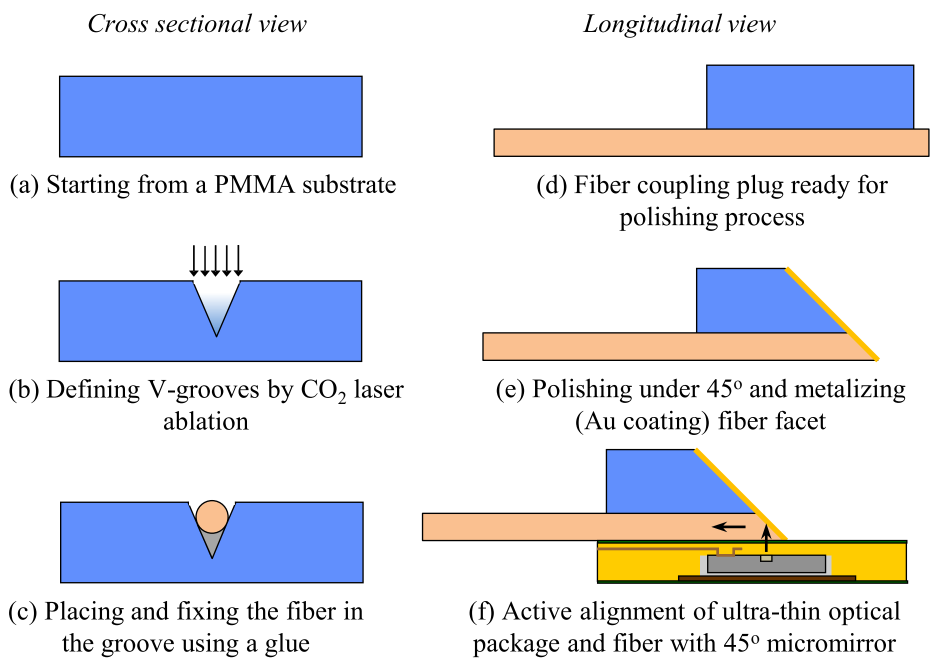

(a) Starting from a PMMA substrate

(b) Defining V-grooves by CO_2 laser ablation

(c) Placing and fixing the fiber in the groove using a glue

(d) Fiber coupling plug ready for polishing process

(e) Polishing under 45º and metalizing (Au coating) fiber facet

(f) Active alignment of ultra-thin optical package and fiber with 45º micromirror

Figure 5.17 – Overview fabrication process of the fiber micromirror (2nd coupling scheme).

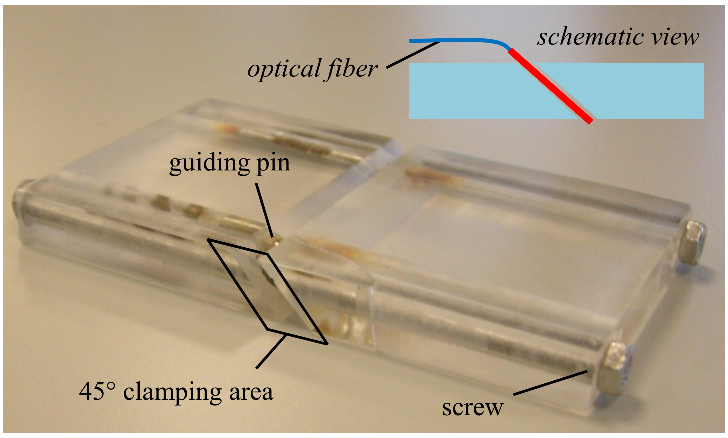

Figure 5.18 – Clamping, lapping, polishing under 45°: dedicated tool.

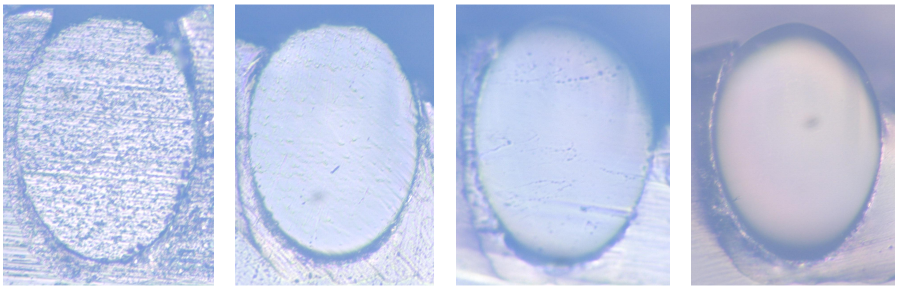

(a) P4000 grinding **(b)** 1 µm diamond suspension **(c)** 0.3 µm diluted alumina powder **(d)** After cleaning.

Figure 5.19 – 45° facet (microscope top view) of the fiber during mechanical lapping (a) and polishing (b-c).

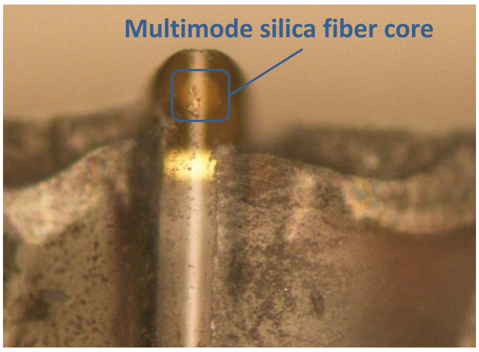

Figure 5.20 – Debris on the back of the micromirror fiber facet.

An Excimer laser cleaning step is consequently applied to clean the fiber light out-coupling surface. Parameters for this cleaning step are depicted in Table 5.7.

The final step in the production of the fiber coupling plug is the deposition of a thin (few 100 nm) reflective Au layer. Therefore the coupling plug is mounted with the 45° facet facing upwards in the evaporation device.

Some examples of resulting mirror plugs are shown in Figure 5.21; a 635 nm red laser is used to illuminate the optical fiber and show the optical path.

Coupling losses inherent to the fiber coupling plugs are measured using a commercial laser diode at 850 nm and a Newport 818 series photodiode. A resulting inherent coupling loss of maximum 1 dB (total insertion loss) is measured over different samples indicating good fiber mirror quality comparable to state-of-the-art mirror plugs.

Table 5.7 – Laser ablation parameters to clean the fiber mirrors (back - light out-coupling - side).

Parameter	Value
Laser	Excimer, $\lambda = 248\,\text{nm}$
Projection mask	2000 µm x 2000 µm
Spot size	200 µm x 200 µm
Pulse energy	80 µJ
Pulse repetition frequency	100 Hz
Fluence	200 mJ/cm^2
Stage translation speed	0.4 mm/s

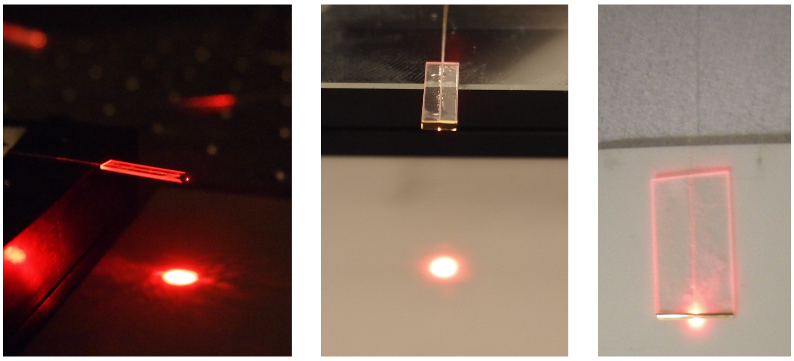

Figure 5.21 – Final coupling plugs, ready for active alignment.

Mirror plug aligning

To maximize the fiber-coupled power, the alignment process of the coupling plug is done actively. This implies a real-time monitoring of the optical power coupled in the fiber during the alignment and fixing process. The alignment procedure is shown in detail in Figure 5.22.

The coupling plug bonding is performed using a Dr. Tresky T3200 semi-automatic bonder. First, the plug is aligned on top of the VCSEL package while monitoring and maximizing the fiber-coupled power. The height between the coupling plug and the embedded optoelectronic component is gradually reduced and the optical power is continuously maximized by varying the position of the Dr. Tresky vacuum chuck in X and Y. Then, a UV curable adhesive (NOA 68 or 81) is dispensed along the sides of the plug while the pressure of the bonding chuck on the coupling plug is preserved. The adhesive (referred to as *glue layer 2*)

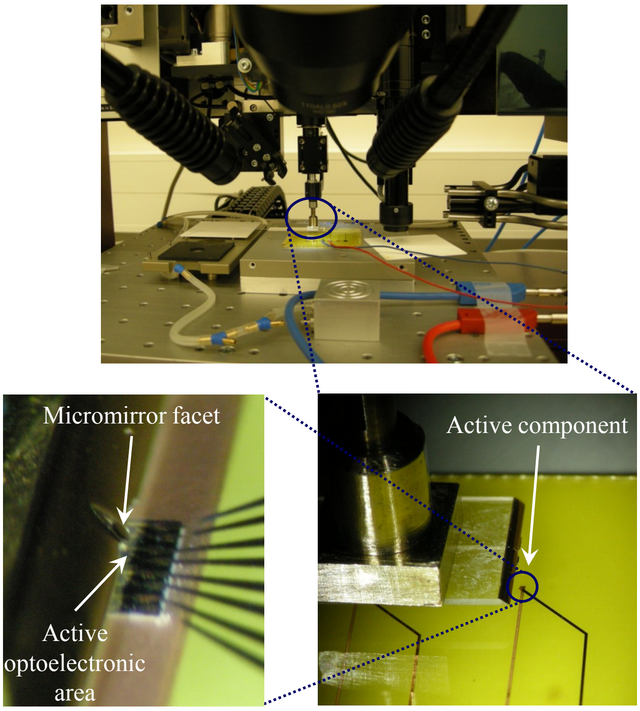

Figure 5.22 – Active alignment process of a coupling plug on an embedded optoelectronic component with the Dr. Tresky T3200 semi-automatic bonder.

is underfilling the coupling plug and the curing is initiated during a short (typically 30 s) UV exposure. After this exposure, the bonding pressure is released. Finally, a top sealing UV glue layer (again NOA 68 or 81) is applied covering all the edges of the fiber coupling plug (referred to as *glue layer 3*). Full curing of glue layer 2 and 3 is guaranteed by a long (typically 2 min) UV exposure step. A similar technique is used to pigtail (i.e. fiber coupling using a short, usually uncoated, optical fiber that mostly has an optical connector pre-installed at one end) integrated photodetectors. For active alignment, the fiber coupling plug is first connected to a fiber pigtailed VCSEL.

Examples of the resulting flexible optical packages based on PI-2525/SU-8 polymer embedding layers, coupled to an optical fiber are shown in Figure 5.23. An example of two ultra-thin (VCSEL and photodetector) packages based on a full PI2626 embedding stack and coupled to the same optical fiber, is shown in Figure 5.24. Electrical interconnections are provided by simple wires. Depending on the application and the potential need for further encapsulation, these wires can easily be replaced by mechanically flexible connectors.

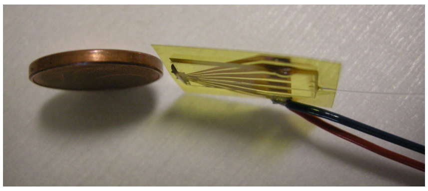

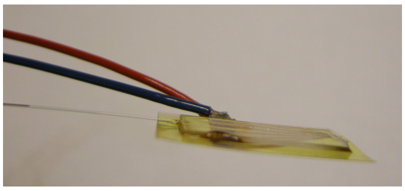

Figure 5.23 – Ultra-thin flexible optical packages bonded to thin PMMA micromirror plugs for fiber pigtailing.

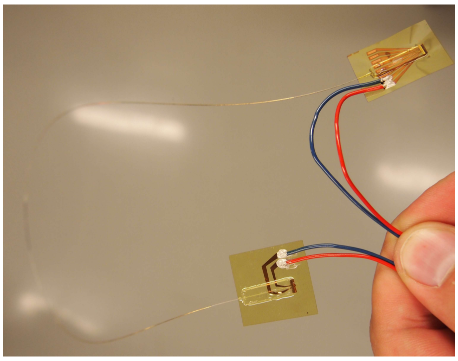

(a)

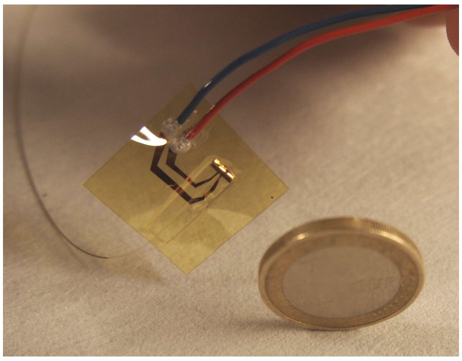

(b)

Figure 5.24 – Ultra-thin flexible optical packages bonded to thin PMMA micromirror plugs.

Cross-sectional investigation

Cross-sectional investigation is performed on the final PI-2611 embedded and fiber pigtailed components to gain insight into the real inner structure of the fiber-coupled optoelectronic packages. In Figure 5.25, a cross-section at the level of the VCSEL emitting area is shown. Figure 5.25a depicts a backlighted microscopic view of the fiber-coupled optoelectronic chip package showing the fiber diameter and core. In Figure 5.25b, the same view is shown with front light illumination. One can recognize the PMMA coupling plug material (1), coupling fiber (2), cured glue layer (3), ultra-thin VCSEL chip (4) with the laser light emitting area and the intermediate glue layer in between the chip package and silica fiber (5). Figure 5.25c depicts a zoomed microscopic view at the same cross-sectional location, showing the VCSEL top metalization layer (6), chip package Cu ground layer acting as a heatsink and ground contact layer (7) and Isotropic (thermally and electrically) Conductive Adhesive (ICA) (8). The thinned VCSEL chip has a thickness of 20 µm and the total chip package thickness is 39 µm.

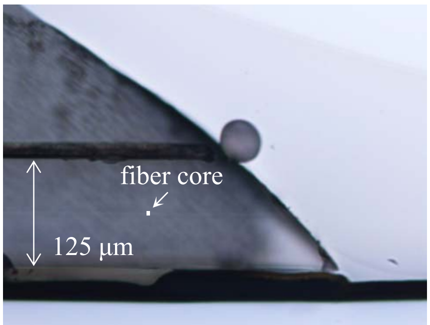

(a) Back illumination.

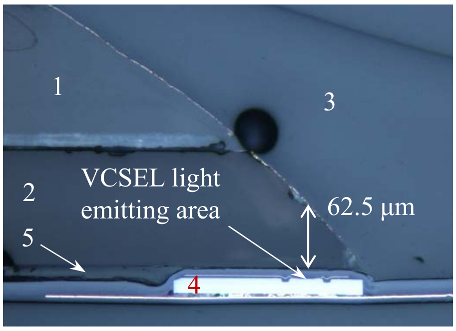

(b) Front illumination.

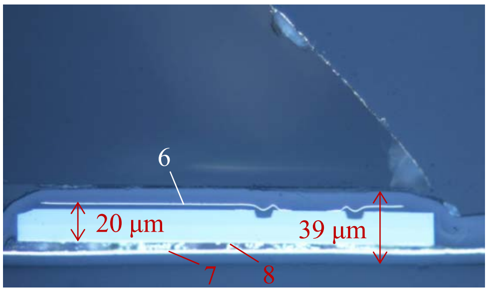

(c) Detailed view.

Figure 5.25 – Cross-section of a PI-2611 embedded and fiber pigtailed VCSEL: position 1. *1: PMMA coupling plug. 2: Coupling fiber. 3: Cured NOA glue layer. 4: Ultra-thin VCSEL chip. 5: Glue layer between chip package and silica fiber. 6: VCSEL top metalization layer. 7: chip package Cu ground layer. 8: Isotropic conductive adhesive.*

In Figure 5.26, a cross-section at a second position beyond the VCSEL light emitting area is shown. Figure 5.26a is again depicting the 45° metalized fiber facet. The interface between the glue layer to fix the coupling plug at the maximum optical power position *(glue layer 2)* and the top covering glue layer which is dispensed afterwards *(glue layer 3)*, is indicated. In Figure 5.26b, the edge side (opposite end of the fiber coupling plug) of the fiber-coupled optoelectronic package is shown. The different glue layers are again visible. *Glue layer 1* is used to perform the initial fixing process of the fiber in the PMMA V-groove. The protective coating from the fiber was therefore stripped along the length of the PMMA substrate. The transition from the PMMA plug to the outside world is clearly visible at the edge of *glue layer 3*, coinciding with the start of the fiber coating. Figures 5.26c and 5.26d are showing a zoomed microscopic (front and backlight illumination) view on the edge of the embedded chip. These figure are also depicting the good PI-2611 step coverage of the VCSEL chip.

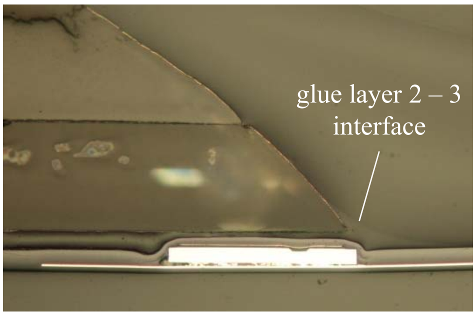

(a) 45° fiber facet on top of the VCSEL.

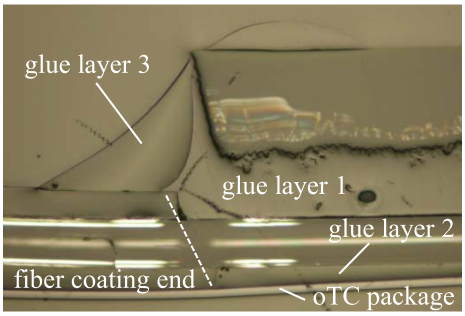

(b) Rear of the pigtailed optoelectronic package.

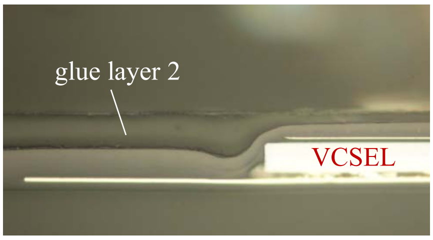

(c) Detailed view on the chip edge and polyimide step coverage (front illumination).

(d) Detailed view on the chip edge and polyimide step coverage (back illumination).

Figure 5.26 – Cross-section of a PI-2611 embedded and fiber pigtailed VCSEL: position 2.

Characterization

The performance of the fiber-coupled VCSEL and PD packages is now investigated, both electrically and optically. It is important to mention that all the coupling losses in this section include a fiber fusion splice and a certain fiber length (up to several meters) to connect the coupling plug to an optical power meter. After aligning, coupling and fixing of the micromirror, the pigtailed devices are characterized by measuring the LI (W/A) or IL (A/W) curve. VCSEL coupling results indicated a coupling loss of 2.8 dB after glue dispensing (single-mode VCSEL, multimode silica fiber). Detailed coupling results are shown in Figure 5.27a and 5.27b for the VCSELs (optical power in multimode and single-mode coupling fiber) and Figure 5.27c for the PDs. "Total power" within Figure 5.27 is referring to the total power emitted by the VCSEL directly measured with a calibrated Newport power detector. Comparing the graphs in Figure 5.27 to the simulated values in Table 5.6, an additional coupling loss of 2-2.5 dB on top of the minimal coupling loss is obtained.

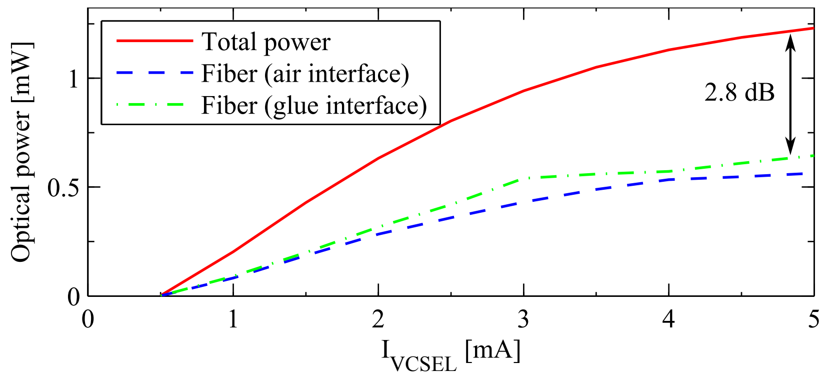

(a) Fiber pigtailing single-mode embedded VCSELs to multimode coupling fibers.

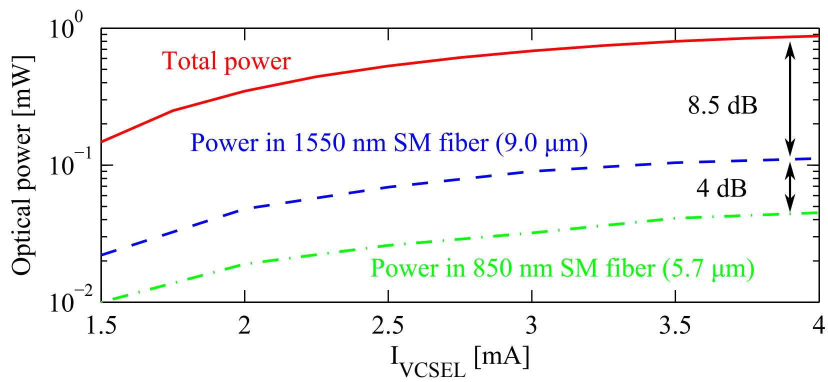

(b) Fiber pigtailing single-mode embedded VCSELs to single-mode coupling fibers.

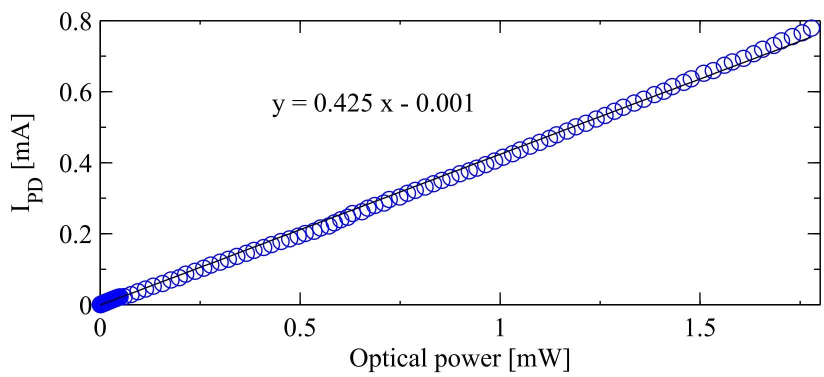

(c) Fiber pigtailing embedded PDs to multimode coupling fibers.

Figure 5.27 – Characterization of the fiber-coupled VCSEL and photodetector packages.

The accumulated X-Y-Z alignment accuracies are therefore well within the 3 dB tolerance values.

By making small adjustments to the coupling set-up (flatness of the sample, roughness of the coupling plug, pressure applied to the coupling during glue dispensing), the VCSEL coupling loss is further limited to 2 dB for the multimode fiber case. Initial coupling tests using single-mode 1550 nm 9 µm and 850 nm 5.7 µm fibers indicated coupling losses around 8.5 dB for the first case and an extra 4 dB for the second case (Figure 5.27b). These first results were however obtained with the SU-8/PI-2525 optoelectronic packages with a chip covering layer having a total thickness of 10 µm.

As mentioned before, integrated photodetectors are pigtailed using the same technique as for the VCSELs. The alignment restrictions are less critical in this case because the active area diameter is 100 µm (vs. 9 µm for the VCSEL). Coupling losses are typically limited to 1 dB. An example response of a pigtailed integrated photodetector is shown in Figure 5.27c. A slope of 0.425 A/W is found for the pigtailed integrated photodetector (power in-fiber versus PD current) whereas the slope of a bare die photodetector is 0.550 A/W [17]. This implies a coupling loss of 1.1 dB in this case.

In Chapter 6, we will show a fully single-mode 850 nm fiber link with an overall loss number of 7 dB including VCSEL and PD coupling. These low losses are obtained using PI-2611 VCSEL and PD packages significantly reducing the optical power losses. Optical spectrum analyzer measurements showing the electrothermal tuning characteristics of the embedded VCSELs and proving their potential to drive fiber sensors were shown in Chapter 4. Similar measurements for the fiber pigtailed devices will also be shown in Chapter 6 (Figure 6.11).

5.7 Advanced coupling schemes

The coupling technology which is described within this chapter is a generic technology and therefore not limited to single silica fibers.

5.7.1 VCSEL/PD array coupling

Similar coupling plugs have been fabricated to couple VCSEL or PD *arrays* to single-mode or multimode optical fibers [18]. An example of such a coupling plug is shown in Figure 5.28. In Figure 5.28a, a microscopic view is shown and the black dots are indicating light in-coupling spots providing a rough estimation of the fiber in-coupling positions. Figure 5.28b shows a detailed top view of the coupling plug including the horizontal fiber spacing (250 µm) and the lower and upper boundaries for the vertical fiber spacing (193 µm). The latter adds 16 µm to the theoretical best case of $\sqrt{2}\cdot 125$ µm = 177 µm.

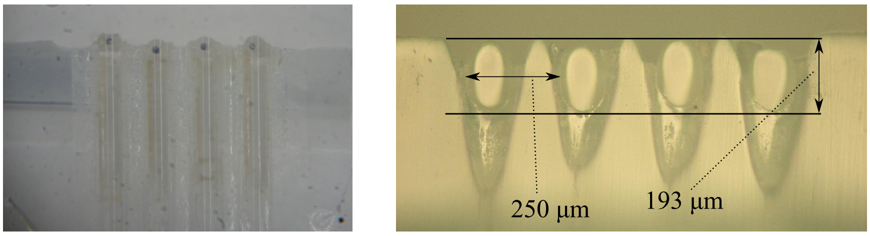

(a) Microscopic view (bottom side multiplexed coupling plug). **(b)** Detailed microscopic view (top side multiplexed coupling plug).

Figure 5.28 – Multiplexed multimode fiber coupling plug.

These plugs can for example be used to multiplex the coupling process to fiber couple chip arrays of 4 multimode VCSELs to 4 multimode fibers. Typical spacing between two VCSEL emitting areas on a single chip is indeed 250 µm [8]. Initial coupling tests provide coupling losses of 7 dB, averaged over 4 multiplexed coupling fibers. Fine-tuning the fiber positioning in the V-groove channels can decrease this loss number.

5.7.2 Specialty silica fiber

Alternatively, special silica fibers can be used, broadening the application domain of this coupling technology to sensing platforms other than fiber Bragg gratings or even extending the application domain to for example optical communication systems. The fiber coupling technology can in this case provide an alternative for the traditional fiber cleaving units typically having limited core diameter variation possibilities. Figure 5.29 shows two examples of straight polished facets on unconventional silica fibers.

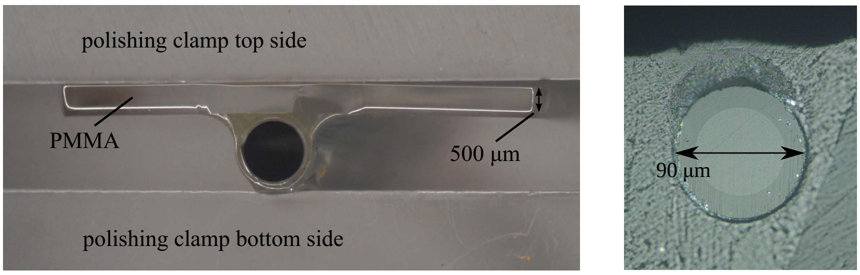

(a) Large-core fiber. **(b)** Multicore fiber.

Figure 5.29 – Polishing straight fiber facets on special silica fibers.

5.7.3 Polymer fiber coupling

When targeting sensing applications based on fiber Bragg gratings, one is not limited to the traditional silica fiber Bragg gratings. Polymer fiber sensors offer many advantages over their silica counterparts such as a higher sensitivity, the outlook towards inherent biocompatibility and potentially also a lower cost (see Chapters 2 and 3). Because of their small core size (core diameter $\leq 50\,\mu m$), the polymer fibers which are used to inscribe Bragg gratings are not straightforward to make and to interconnect. Traditionally, a polymer fiber sensor is connected through a silica fiber pigtail limiting the polymer fiber length and consequently minimizing the optical losses. A special glue joint is then needed to couple the silica fiber to the polymer fiber [19, 20]. This way, the commercially available silica fiber connectors can be used and the need for special polymer fiber connectors is avoided. Directly coupling a polymer fiber sensor could however radically simplify the coupling process. The silica pigtail and the delicate silica-polymer transition is avoided consequently limiting the losses and reducing the cost. This will lead to an optical power budget which can be sufficient to have a fully embedded fiber sensor system with integrated source and detector based on polymer fiber sensors. In Figure 5.30, two examples are shown of 45° polished POF in PMMA coupling plugs. Both the use of 1550 nm single-mode polymer fiber (Figure 5.30a) and 850 nm multimode microstructured polymer fiber (Figure 5.30b) were successfully investigated. These are the same types of fibers used for the polymer fiber embedding work (both planar and tubular) reported in Chapter 3.

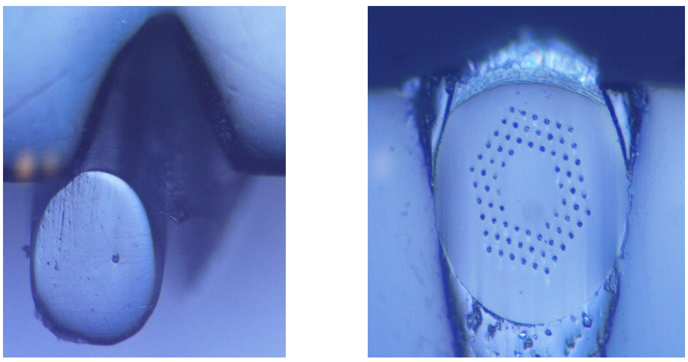

(a) 1550 nm SM POF. **(b)** 850 nm MM microstructured POF.

Figure 5.30 – Creating 45° micromirrors directly on polymer fiber sensors, avoiding a silica fiber interface and consequently minimizing the optical losses.

5.7.4 Polymer waveguide coupling

The next step towards the integration of optical sensing structures with integrated read-out units in polymer materials is the use of Bragg gratings in polymer waveguides. This was discussed in detail in Chapter 2, Section 2.3.2. Using traditional waveguide patterning techniques (lithography, embossing) and grating inscription techniques similar to the polymer fiber sensors, polymer waveguide sensors can indeed serve as an alternative for the polymer fiber sensors.

To increase the flexibility of the sensor structure even further and to add a degree of stretchability to the sensor itself, it is possible to use polydimethylsiloxane (PDMS) waveguides fabricated based on an embossing or micromolding in capillaries (MIMIC) process. These fabrication technologies were investigated and optimized within the PhD research of Jeroen Missinne [21] (Chapter 3, and more specifically Sections 3.4 and 3.5). Coupling integrated sources and detectors to the polymer waveguides can be done using similar 45° coupling plugs mounted on the ultra-thin optoelectronic packages. Figure 5.31 shows an example of a polymer stretchable waveguide with an integrated coupling plug providing direct coupling of the VCSEL and PD to the polymer waveguide. More details on the fabrication and characterization of the coupling technology applied on flexible and stretchable waveguides can be found in [18, 22]. It is important to mention that the stretchable polymer waveguides do not (yet) include Bragg grating structures. The application of the coupling process is limited to stretchable polymer optical interconnects at this moment.

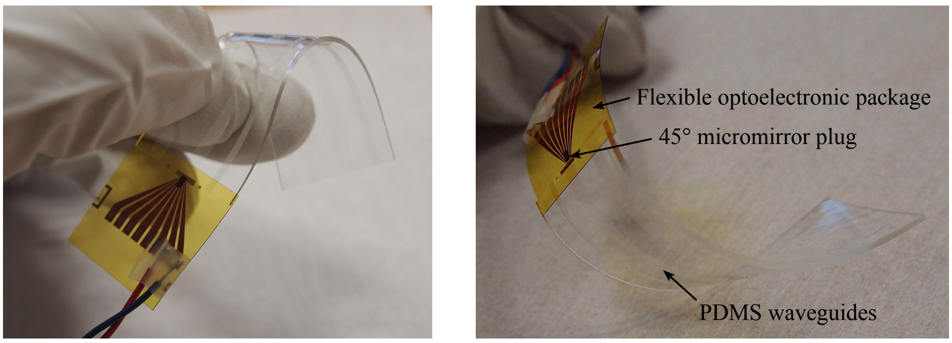

Figure 5.31 – Array of 4 PDMS stretchable waveguides coupled to a flexible optoelectronic package.

The fabrication of Bragg grating structures in flexible and stretchable polymer waveguide structures will be further investigated within the IWT-SBO project Self Sensing Composites, as discussed in Chapter 1, Section 1.8.

The coupling of integrated optoelectronic components with sensing structures in polymer waveguides, not limited to Bragg grating structures, will be further developed within the scope of the PhD research of Sandeep Kalathimekkad.

5.8 Conclusion

In this chapter, an optical (fiber) coupling technology was designed, fabricated and characterized. More specifically, a compact coupling technology to interconnect ultra-thin optoelectronic packages and optical fiber sensors has been developed and optimized. Starting from a broad range of available optoelectronic components, initial simulations were carried out to narrow the light sources selection and to eliminate theoretically infeasible solutions. The resulting fiber-coupled module consists of a single-mode 850 nm VCSEL and a direct butt-coupled silica fiber. A 45° micromirror facet is applied directly on the fiber end, minimizing the optical path length and simplifying the alignment procedure ("one-step alignment"). This generic technology provides a robust and permanent coupling structure between optoelectronic components (for example VCSELs, photodetectors) and optical fiber sensors.

The coupling plug itself consists of PMMA. The total thickness of the coupling plug, including the fiber, is 500 µm enabling embedding of this structure in thin planar sensing sheets. It is thus compatible with the flexible and stretchable optical skins (thickness of 1 to 4 mm) from Chapter 3. The resulting optical package consists of an integrated optoelectronic device (thickness of 20 to 40 µm) and the PMMA plug (thickness of 500 µm), and provides a thin, 90° coupling structure for vertical emitting lasers and detectors.

Theoretical coupling losses of 0.3 dB (single-mode VCSEL to 50 µm multimode fiber) and 6.4 dB (single-mode VCSEL to 9 µm single-mode fiber) are reported. Effective loss numbers after aligning and fixing the mirror plug range from 2 dB for the multimode case (including a fusion splice) to 8.5 dB for the single-mode case. Pigtailing integrated detectors has resulted in coupling losses of 1 dB. In Chapter 6, also 850 nm single-mode fibers (5-6 µm core diameter) are used to couple lasers and detectors directly to fiber sensors (without fusion splices or excessive fiber length) yielding even lower losses.

Next to the traditional silica fibers, also *polymer* fibers or waveguide structures can be coupled to optoelectronic driving components using similar coupling plugs. These polymer sensing alternatives take the artificial optical sensing skin concepts to the next level. The resulting sensing system itself can be fully polymer and no longer be embedded in a polymer host material.

The coupling technology developed within this PhD allows to achieve efficient optical coupling through a minimized optical path length. Using different types of fibers, this approach constitutes a novel fiber coupling platform with integration and miniaturization possibilities beyond the state-of-the-art.

References

[1] M. Fadhali, J. Zainal, Y. Munajat, J. Ali, and R. A. Rahman, "Efficient coupling and relaxed alignment tolerances in pigtailing of a laser diode using dual ball lenses," *Optik*, vol. 120, no. 8, pp. 384–389, 2009.

[2] A. Mahapatra and R. Mansfield, "Optoelectronic packaging using passive optical coupling," in *Optoelectronics Packaging and MOEMS Topical Workshop, IMAPS, Bethlehem, PA*, 2002, Conference Paper.

[3] Phosfos Consortium. (2008) Photonic skins for optical sensing. [Online]. Available: http://www.phosfos.eu/

[4] E. Bosman, "Integration of optical interconnections and opto-electronic components in flexible substrates," Ph.D. dissertation, Ghent University, 2010.

[5] Roithner LaserTechnik. (Accessed 2013) Products. [Online]. Available: http://www.roithner-laser.com/

[6] EXALOS: Superluminescent Light Emitting Diodes (SLEDs) Manufacturer. (Accessed 2013) Products. [Online]. Available: http://www.exalos.com/

[7] BeamExpress. (Accessed 2012) Products. [Online]. Available: http://www.beamexpress.com/

[8] Ulm-Photonics. (Accessed 2012) Products. [Online]. Available: http://www.ulm-photonics.com/

[9] Lumerical MODE Solutions. (Accessed 2013) Product website. [Online]. Available: http://www.lumerical.com/tcad-products/mode/

[10] Rohm & Haas. (Accessed 2013) Lightlink™clad and core datasheet. [Online]. Available: http://www.dow.com/products/product_line_detail.page?product-line=1120529&application=1120778

[11] E. Anzures, R. Dangel, R. Beyeler, A. Cannon, F. Horst, C. Kiarie, P. Knudsen, N. Meier, M. Moynihan, and B. J. Offrein, "Flexible optical interconnects based on silicon-containing polymers," in *PHOTONICS PACKAGING, INTEGRATION, AND INTERCONNECTS IX*, ser. Proceedings of SPIE, A. Glebov and R. Chen, Eds., vol. 7221, 2009, conference on Photonics Packaging, Integration, and Interconnects IX, San Jose, CA, JAN 2009.

[12] J. Van Erps, C. Debaes, T. Nasilowski, J. Watte, J. Wojcik, and H. Thienpont, "Design and tolerance analysis of a low bending loss hole-assisted fiber using statistical design methodology," *Optics Express*, vol. 16, no. 7, pp. 5061–5074, Mar. 2008.

[13] Advanced System Analysis Program by the Breault Research Organization. (Accessed 2013) Product website. [Online]. Available: http://www.breault.com/software/asap.php

[14] M. Mueller, W. Hofmann, T. Gruendl, M. Horn, P. Wolf, R. D. Nagel, E. Roenneberg, G. Boehm, D. Bimberg, and M.-C. Amann, "1550-nm high-speed short-cavity vcsels," *IEEE Journal of Selected Topics in Quantum Electronics*, vol. 17, no. 5, pp. 1158–1166, 2011.

[15] K. Hill and G. Meltz, "Fiber bragg grating technology fundamentals and overview," *Journal of Lightwave Technology*, vol. 15, no. 8, pp. 1263–1276, Aug. 1997.

[16] A. Stefani, W. Yuan, C. Markos, and O. Bang, "Narrow bandwidth 850-nm fiber bragg gratings in few-mode polymer optical fibers," *IEEE Photonics Technology Letters*, vol. 23, no. 10, pp. 660–662, May 2011.

[17] Enablence. (Accessed 2013) Photodiode products. [Online]. Available: http://www.enablence.com/components/solutions/transmission/photodiodes

[18] B. Van Hoe, E. Bosman, J. Missinne, S. Kalathimekkad, G. Van Steenberge, and P. Van Daele, "Novel coupling and packaging approaches for optical interconnects," ser. Proceedings of SPIE, A. Glebov and R. Chen, Eds., vol. 8267, 2012, conference on Optoelectronic Interconnects XII, San Francisco, CA, JAN 2012.

[19] C. C. Ye, J. M. Dulleu-Barton, D. J. Webb, C. Zhang, G. D. Peng, A. R. Chambers, F. J. Lennard, and D. D. Eastop, "Applications of polymer optical fibre grating sensors to condition monitoring of textiles," in *Sensors & their Applications XV*, ser. Journal of Physics Conference Series, A. Augousti and G. McConnell, Eds., vol. 178, 2009, 15th Conference on Sensors and Their Application, Edinburgh, Scotland, OCT 2008.

[20] I. P. Johnson, K. Kalli, and D. J. Webb, "827 nm bragg grating sensor in multimode microstructured polymer optical fibre," *Electronics Letters*, vol. 46, no. 17, pp. 1217–U74, Aug. 2010.

[21] J. Missinne, "Development of conformable optical and optoelectronic based tactile sensors," Ph.D. dissertation, Ghent University, 2011.

[22] J. Missinne, B. Van Hoe, E. Bosman, S. Kalathimekkad, G. Van Steenberge, and P. Van Daele, "Compact coupling and packaging concepts for flexible and stretchable polymer optical interconnects," 2012, Conference Paper, pp. 129–30, 2012 IEEE Optical Interconnects Conference, Santa Fe, NM, USA, MAY 2012.

6 Ultra-compact optical fiber sensing system

This chapter tackles the fully embedded sensing concept based on fiber Bragg gratings and integrated optoelectronic components. The sensor system which is presented and characterized in this chapter can be considered as the culmination of this dissertation. The sensing and interrogation concepts introduced in Chapter 2 are combined with the component and sensor integration technologies developed within Chapters 3, 4 and 5 creating a portable dynamic fiber sensing system as an alternative for the traditionally bulky and expensive fiber sensor and interrogation systems. The main part of this chapter is based on [1].

6.1 Introduction

As already frequently discussed within this dissertation, optical sensors offer specific advantages over their electrical counterparts. Optical fiber sensors have additional advantages such as the (quasi-)distributed sensing capabilities, the possibility to perform absolute measurements and the sensor stability reflected in excellent fatigue resistance under high load and repeatable cycles [2]. The sensors can potentially also be fabricated in a low-cost manner as the sensor base material is typically a silica fiber. As shown in Chapter 3, optical fiber sensors also offer high integration and embedding capabilities. The *polymer* embedding materials used in Chapter 3 enable mechanically flexible and stretchable applications but also other embedding host materials are possible. The integration of fiber Bragg grating in *composite* materials for example is another popular embedding example enabling structural health monitoring in for example air plane wings or wind turbines [3].

However, using optical fiber sensors requires a spectral read-out unit, as the sensing information is encoded in the shift, deformation or split of the optical Bragg wavelength. Commercially available types of spectral read-out units are mostly based on a broadband light source, for example a superluminescent LED, spectrometer or reference grating. They are therefore typically bulky (therefore not mechanically flexible) and expensive (see Chapter 2, Section 2.2.1). In this chapter a unique fiber sensor interrogation system is presented, based on electrothermal wavelength tuning of an optoelectronic source, which can be fabricated low-cost and with an ultra-small form factor. By using simple optoelectronic components (VCSELs and photodetectors), an ultra-thin optical chip package is fabricated to embed laser and detector chips in flexible polymer foils with a thickness of only 40 µm. An integrated fiber coupling technique, based on a 45° micromirror, is used to ensure compatibility of the pigtailed optoelectronic components with planar flexible sensing sheets of only 1 mm thick, incorporating both driving and read-out optoelectronics as well as the optical sensor elements.

The result is a fully embedded flexible sensing system with a thickness of only 1 mm including integrated planar fiber pigtails, based on a single VCSEL, fiber sensor and photodetector chip. Temperature, strain and electrodynamic shaking tests have been performed on our system, not limited to static read-out measurements but dynamically reconstructing full spectral information datasets.

6.2 Optical fiber sensor selection

Within Chapter 3, several special types of fiber sensors were used, each possessing their specific advantages. Particularly polymer fiber sensors constitute an interesting alternative because it can pave the way towards a fully polymer fiber sensing system. Nevertheless for this chapter, a traditional silica fiber Bragg grating was chosen. This choice allows maximizing the optical power budget and also ensures the availability of sensors at different wavelengths matching the optical sources. To maintain compatibility with the polymer embedded and fiber-coupled optoelectronic components (Chapter 4 and 5), the wavelength range around 850 nm is selected for the fiber sensors. It further exploits the advantage of low-cost semiconductor laser and detector chips available around 850 nm compared to the more expensive 1550 nm wavelength range.

The FBG sensors for this work were inscribed in Fibercore SM800, a B/Ge co-doped optical silica fiber, with a 244 nm UV laser using a holographic technique [4]. Prior to UV inscription, the fibers were submitted to hydrogenation at 200 bar and 80 °C for 48 h and stored for a short period at −40 °C. This fiber type has a very high photosensitivity to enable rapid fabrication of gratings. The gratings were fabricated with a center wavelength at 855 nm to match the wavelength tuning range of the VCSEL devices used to drive the fiber sensors. A typical FBG transmission spectrum fabricated using this type of fiber is illustrated in Figure 6.1. The 3 dB wavelength range, measured in transmission as depicted in Figure 6.1b, is 0.15 nm. A broadband source (superluminescent LED) and an optical spectrum analyzer were used to perform these initial spectral measurements.

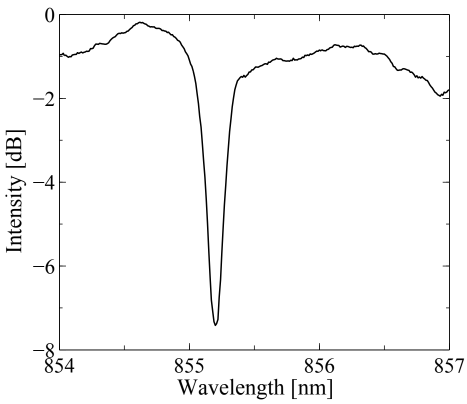

(a) Normalized transmission spectrum of the grating.

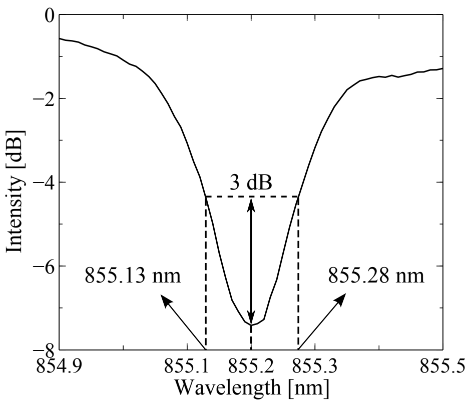

(b) Detailed view indicating the 3 dB wavelength range in transmission.

Figure 6.1 – Typical spectral response of the fabricated fiber Bragg gratings in the 850 nm range, measured in transmission with an optical spectrum analyzer.

6.3 Interrogation principle

The interrogation scheme is schematically shown in Figure 6.2. A single-mode VCSEL is used as a fiber optic driving unit and a photodiode is used to read out the transmitted power. The electrothermal effect (electrical current causes heating due to Joule dissipation and the temperature rise causes red shift of the emission wavelength due to the thermo-optic effect) causes the emitting wavelength to shift when tuning the VCSEL driving current. Higher driving currents correspond to higher red-shifts in the VCSEL wavelength. An electrical driving unit is needed to modulate the electrical current in the VCSEL, consequently activating the VCSEL wavelength red shifting. Depending on the separation of the different

Bragg gratings, this interrogation system even has limited possibility to read out multiplexed fiber sensing points. A data acquisition board linked to a computer is typically used to store and visualize the photocurrent through the photodiode.

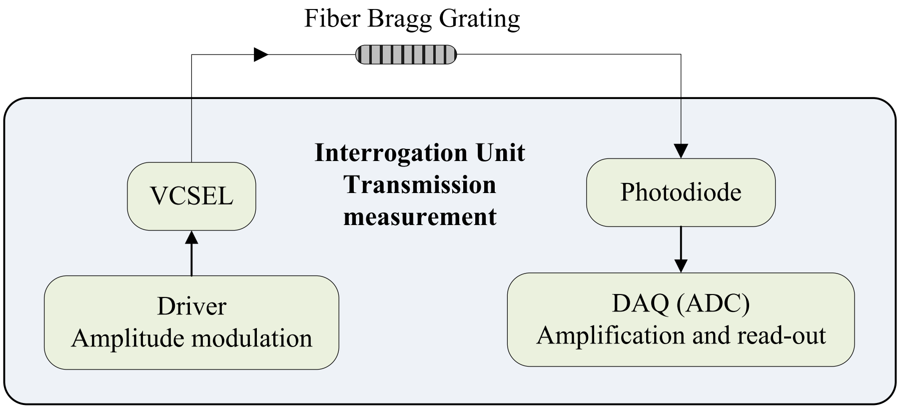

Figure 6.2 – Schematic view of the sensor interrogation system.

Fiber sensing systems based on a similar VCSEL wavelength red shifting interrogation technique have been reported by other institutes and include vibration [5] and temperature [6] sensing systems. Using MEMS technology, it is possible to extend the tuning range of the VCSEL increasing the number of addressable multiplexed sensing points [7, 8]. Other types of laser diodes can also be used to perform wavelength tuning enabling fiber sensor interrogation [9]. Alternatively, tunable optical filters have been applied on broadband light sources or detectors, such as a driving superluminescent LED [10] or a read-out photodetector [11].

As already introduced in Section 5.4.1, the presented interrogation system has two operating modes: *modulation mode* and *constant current mode*. Figure 6.3 shows a basic schematic example of the dynamic interrogation scheme *(modulation mode)*. In Figure 6.3a and 6.3b, the VCSEL is modulated with a sawtooth signal and the optical power and wavelength are varying accordingly. Figure 6.3c shows the response of the photodetector current when a Bragg grating is measured in transmission. The photocurrent is depicting the sawtooth driving signal and the grating filter characteristic. Combining the data in Figure 6.3c with the data from a VCSEL calibration measurement enables filtering the sawtooth signal and isolating the grating response in the photocurrent signal (Figure 6.3d). Assuming the VCSEL is modulated using a frequency f, a new full spectrum reconstruction is available each 1/f seconds. Assigning a color to the relative wavelength intensity results in a complete spectral reconstruction (Figure 6.3e) in which the intensity is depicted for each wavelength, every 1/f seconds.

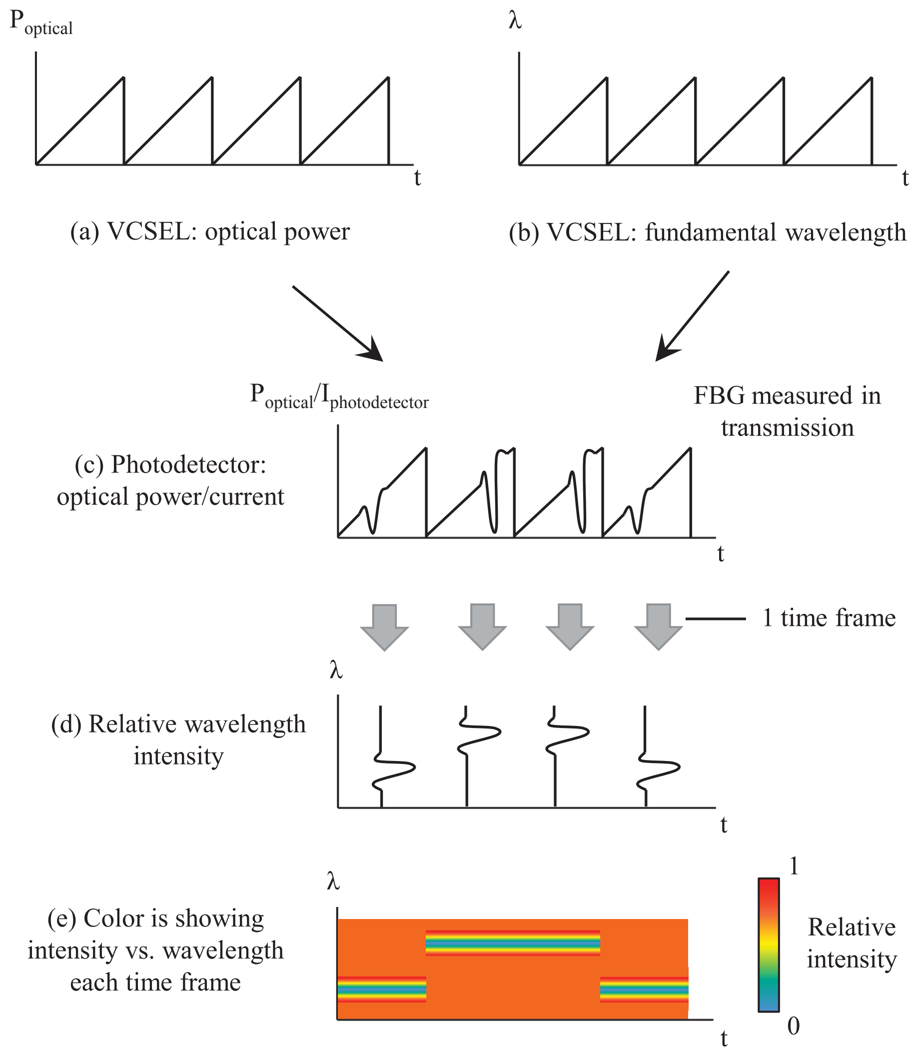

Figure 6.3 – Schematic example of the fiber sensor interrogation principle *(modulation mode).*

Figure 6.4 shows the dynamic reconstruction (f = 1 kHz) of the 855 nm FBG using an integrated and fiber pigtailed VCSEL and photodetector, perfectly corresponding to the initial characterization results from Figure 6.1.

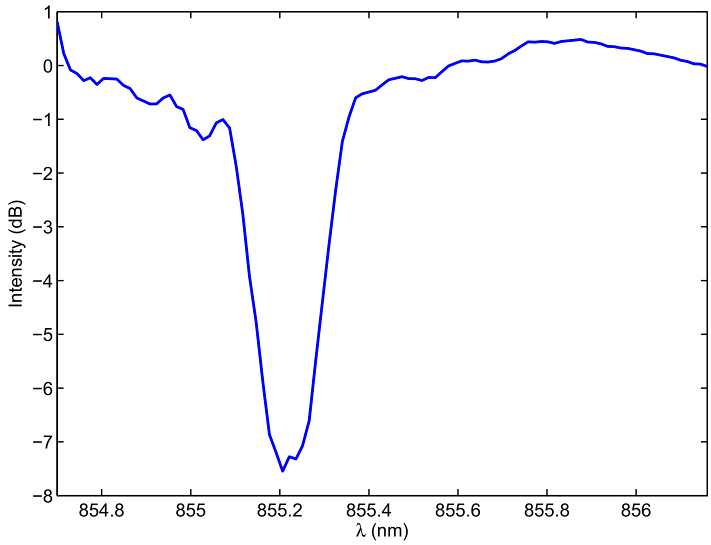

Figure 6.4 – Full spectral FBG reconstruction using integrated VCSEL and photodetector.

Alternatively, a fixed VCSEL driving current can be used. The varying transmitted optical power intensity is then monitored at a well-defined wavelength *(constant current mode)*. This wavelength is preferably on the edge of the grating characteristic, enabling the distinction between blue and red shifting of the fiber sensor. In this static interrogation scheme, one is limited to the detection of the amount of Bragg wavelength shift and consequently losing the dynamic sensing information such as peak broadening, splitting or deformation.

The remainder of this chapter is divided in two parts: the first part is devoted to the interrogation system to come up with a low-cost, portable system and the second part is taking the technology one step further by integrating the opto-electronic components in thin, flexible packages and consequently limiting the thickness of the total sensing system to one millimeter.

6.4 Proof-of-concept: system with discrete components

This section illustrates the sensor system using conventionally packaged opto-electronic components. To demonstrate the capabilities of the interrogation principle, an FBG was set up in transmission mode using a VCSEL light source and a GaAs photodetector as shown in Figure 6.5. Note that it is also possible to configure a grating in reflection mode by adding a coupler. This enables higher signal-to-noise ratio measurements of the grating but with the trade-off in having to include a coupler.

This proof-of-concept interrogation unit was largely developed by the Aston Institute of Photonic Technologies (Aston University) and Astasense within the framework of Phosfos [12] and tested using the photonic skins from Chapter 3.

6.4.1 Inside the Interrogation Unit

The interrogation unit is shown in Figure 6.6, has a dimension of 160 mm x 116 mm x 35 mm and weighs 520 g with a lithium-ion battery. The unit can run up to 24 h on a single charge or indefinitely when plugged into a power outlet. The interrogation unit was built around an Atmel ATMEGA644 microcontroller running a custom written program. The Atmel ATMEGA family of microcontrollers were chosen for their low-power consumption, low-cost and high-performance. The Atmel ATMEGA644 microcontroller features 64 KB ISP flash memory, 2 KB EEPROM, 4 KB SRAM, selectable 8 or 10-bit Analogue to Digital Converters (ADC), 2 USARTs and 32 general purpose I/O channels. The primary method used to control and configure the interrogation unit is through a graphical user interface in the form of an application (app) built on the Android platform which communicates wirelessly over Bluetooth to a tablet or smartphone device. The system can also be set up using a computer terminal using the serial RS232/Bluetooth connection.

The microcontroller directly controls a current source (Wavelength Electronics LDD P series) which was used to drive a VCSEL (or other light source). The photodetector was connected through a low noise transimpedance amplifier with a variable gain which converts the photocurrent into a voltage signal which is then read by the on-board microcontroller ADC. The variable gain in the transimpedance amplifier offers additional flexibility to allow the system to be fine-tuned and adapted to suit different strength gratings and light sources.

As discussed in the previous section, the interrogation unit has two modes of operation: constant current mode and modulation mode. Under constant current mode, the interrogation unit sweeps the drive current of the VCSEL using a user configured step size to reconstruct the profile of the FBG. Once the grating profile has been established, the system automatically chooses the VCSEL driving current which matches the source wavelength with the most sensitive edge of the FBG. With a static drive current, the interrogation unit then monitors the amplitude of the light received by the photodetector. The system can sample the photodetector up to a rate of 5 kHz; moving point averages and other math calculations can be computed directly on the microcontroller. In modulation mode,

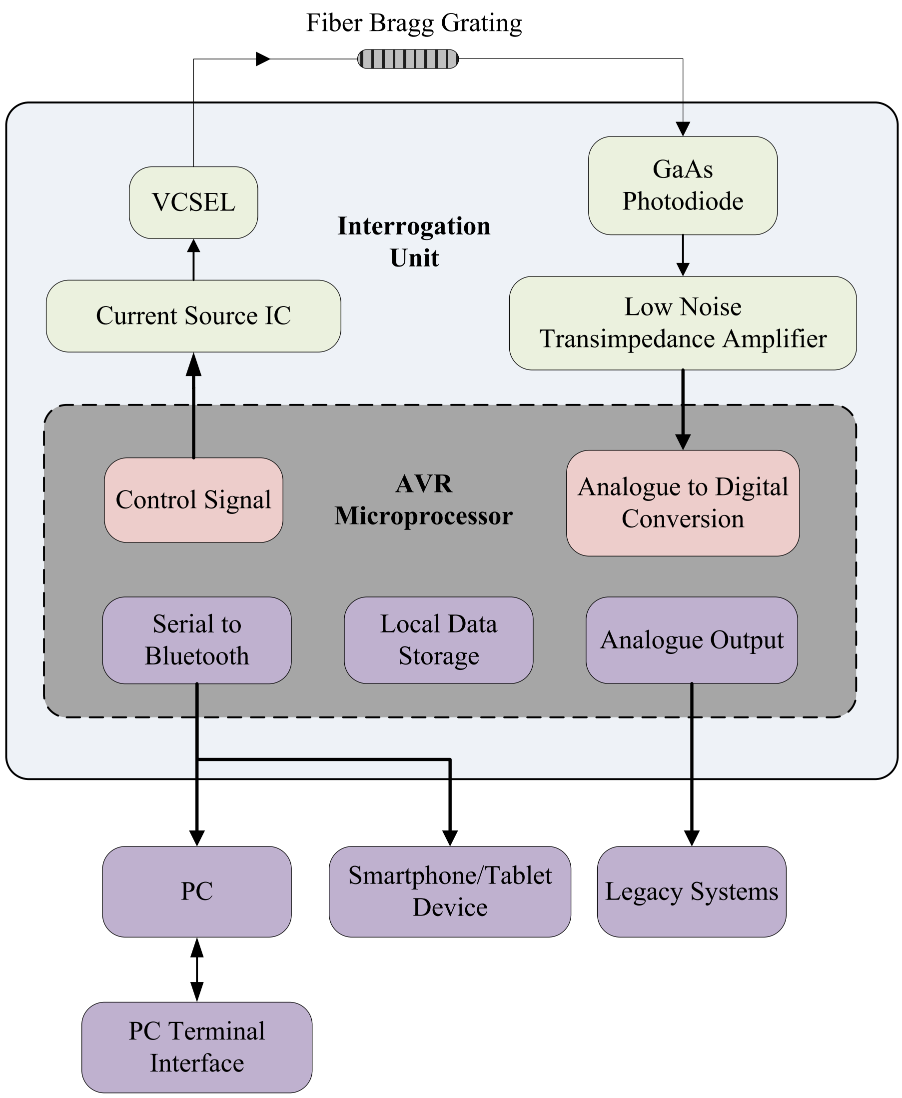

Figure 6.5 – Detailed schematic view of the proof-of-concept sensor interrogation system.

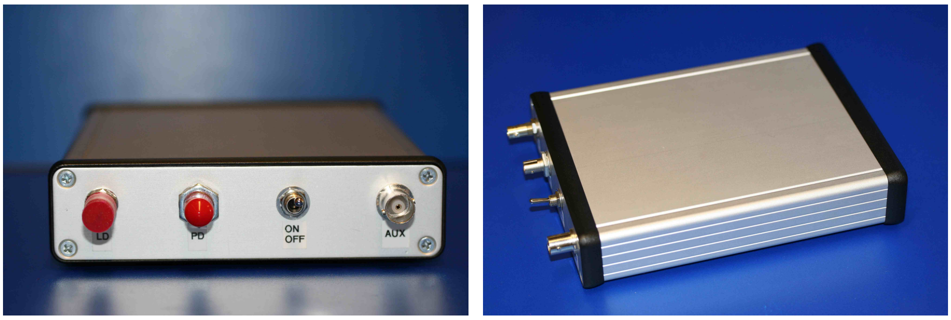

(a) Front panel view. Ports from left-to-right: laser diode (fiber out), photodetector (fiber in), on/off switch, analogue auxiliary port.

(b) Side view. Power inlet port is situated at the rear.

Figure 6.6 – Interrogation system incorporating all elements schematically shown in Figure 6.5.

the Android app is used to select a modulation signal such as a sine or sawtooth signal to drive the current source. The microcontroller is able to modulate the current source at a frequency up to 1 kHz. A higher sensing sensitivity can be achieved in modulation mode due to the higher signal-to-noise ratio and therefore much smaller perturbations on the FBG can be detected compared to constant current mode. More detailed test results of the electronics in combination with a fiber sensor element can be found in [13].

6.4.2 Read-Out Android app

The Android app (Figure 6.7a) used to configure the interrogation unit also acts as a data logger and live data plotter for perturbations experienced by the FBG. It is also possible to recall data plots collected in past sessions. Alternatively, data can be logged and plotted through a PC terminal connected through the RS232/Bluetooth serial interface. The Android device automatically connects wirelessly over Bluetooth to the interrogation unit on startup. When a connection has been established, a prompt is displayed to allow the user to select the mode of operation, configure the maximum drive current limit, modulation type and modulation frequency. Once the settings are saved, a new measurement session is displayed in the form of a live graph with the photodetector intensity plotted against a data reading identifier code. Incoming data is automatically logged and saved to the internal memory of the tablet or smartphone device which can later be retrieved and replotted. In addition, the 2 KB EEPROM microcontroller on-board memory can provide ample space to store up to 500 data points. The analogue auxiliary output port can be used simultaneously with the Android app and the on-board memory. The analogue port provides a quick and easy to use interface to connect to an oscilloscope or other legacy equipment to view live data at high modulation rates.

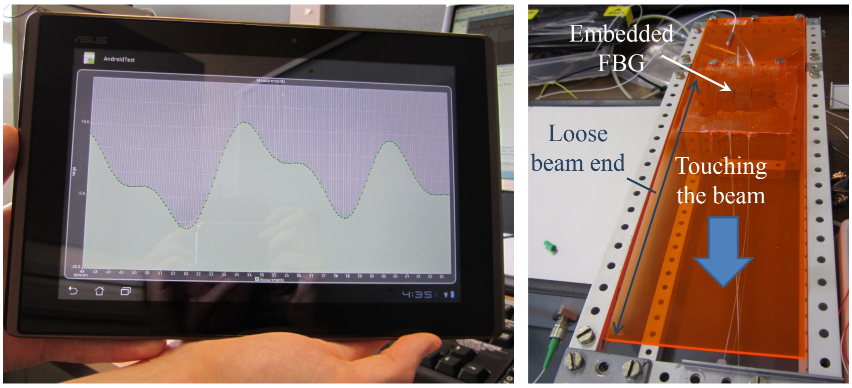

(a) Android read-out system.

(b) Beam test set-up with one end free to oscillate.

Figure 6.7 – Proof-of-concept characterization set-up.

6.4.3 Proof-of-concept demonstration

The interrogation unit was tested with a commercially available pigtailed VCSEL and photodetector from Honeywell in the interrogation box. An FBG was used as the sensor device which was embedded in a flexible and stretchable polymer host material and taped to a beam secured at one end so that the beam was free to oscillate when a downward force was applied (Figure 6.7b). For the first test, the interrogation unit was set to constant current mode and the microcontroller swept the VCSEL drive current from 0.1 mA to 0.4 mA with a step size of 0.01 mA which corresponded to a wavelength tuning range of 855.877 nm to 857.660 nm. During the sweep, the photodetector was sampled at 5 kHz with every 50 readings averaged and plotted onto a real-time graph on the Android device. Once the sweep completed, the microcontroller automatically selected the VCSEL drive current that corresponded to the most sensitive edge of the FBG. After the setup sequence, the beam with the grating was made to oscillate to demonstrate the speed and type of read-out that is possible with the interrogation unit. A screen capture of the live graph (transmitted optical power) is shown in Figure 6.8a. Both blue (decreasing optical power) and red shifting (increasing optical power) effects of the FBG are visible. Figure 6.8b shows the system response when mimicking breathing movements on the embedded fiber. Next to the constant current mode, also the modulation mode was successfully tested using similar driving parameters but with continuous current sweeping.

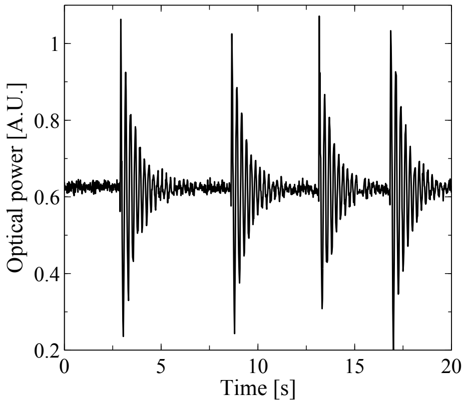

(a) Transmitted power oscillations resulting from a downward touching force at 2.9 s, 8.7 s, 13.2 s and 16.9 s.

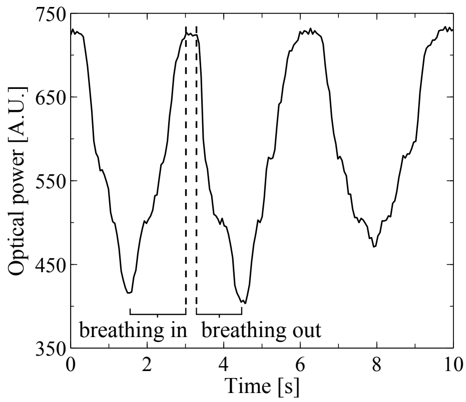

(b) Breathing movement system response.

Figure 6.8 – Proof-of-concept characterization results.

6.5 Fully embedded system: building blocks

The fully embedded system consists of three building blocks:

- A single-mode VCSEL embedded in an ultra-thin chip package (Chapter 4) and fiber pigtailed to a multimode or single-mode coupling fiber (Chapter 5). The result is shown in Figure 6.9a.
- A single-mode silica fiber Bragg grating sensor embedded in a polymer host material (Chapter 3). This fiber can be the same fiber as the coupling fiber(s). The result is shown in Figure 6.9b.
- A photodetector chip embedded in an ultra-thin chip package (Chapter 4) and fiber pigtailed to a multimode or single-mode coupling fiber (Chapter 5). The result is shown in Figure 6.9c.

Figure 6.10a is depicting a fully single-mode system (the fiber sensor is not embedded). The coupling plugs have been fabricated directly on the sensing fiber on both sides. All intermediate splicing transitions are consequently avoided. Figure 6.10b depicts the auxiliary read-out equipment (power supply, microscope) needed to visualize the electrical signals.

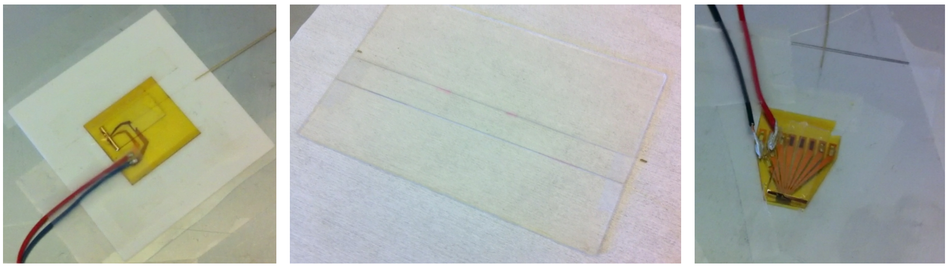

(a) Fiber-coupled embedded VCSEL.
(b) Polymer embedded fiber Bragg grating.
(c) Fiber-coupled embedded photodetector.

Figure 6.9 – Fully embedded system building blocks.

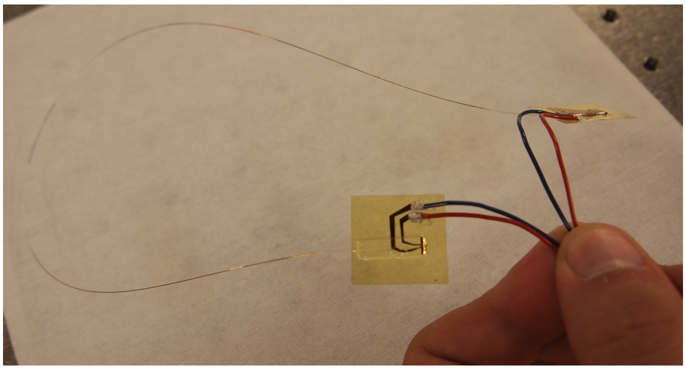

(a) Fully single-mode system.

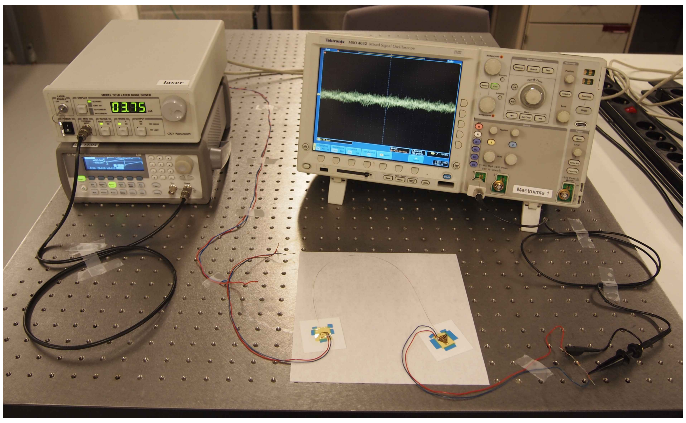

(b) Auxiliary read-out equipment.

Figure 6.10 – Fully integrated fiber sensing system.

6.6 Fully embedded system: characterization

A fully embedded sensor system, consisting of a fiber-coupled integrated single-mode VCSEL (available as bare chip from ULM Photonics), a fiber-coupled integrated photodetector (available as bare chip from Enablence) and a silica fiber sensor with Bragg grating at 855 nm, was characterized under varying temperature and axial strain. Also tactile sensing and vibration measurements were performed on the system to prove the high-speed dynamic read-out capabilities of the sensing system. To characterize the fully embedded system, modulation mode was used. This allows to obtain full spectral reconstruction of the fiber sensor. Note that only relevant wavelength ranges are shown in the characterization graphs.

6.6.1 Electrothermal tuning effect

To interrogate the fiber sensor, the electrical current through the VCSEL was driven using an analog sawtooth signal between 4 mA and 8 mA at 100 Hz. The fiber sensor was read out in transmission mode and the photodetector current was amplified and sampled at 100 kHz yielding 1000 data points each tuning cycle of 10 ms.

Figure 6.11 shows the electrothermal tuning effect of the integrated fiber pigtailed VCSEL as a function of different DC driving currents and a sawtooth signal at different frequencies.

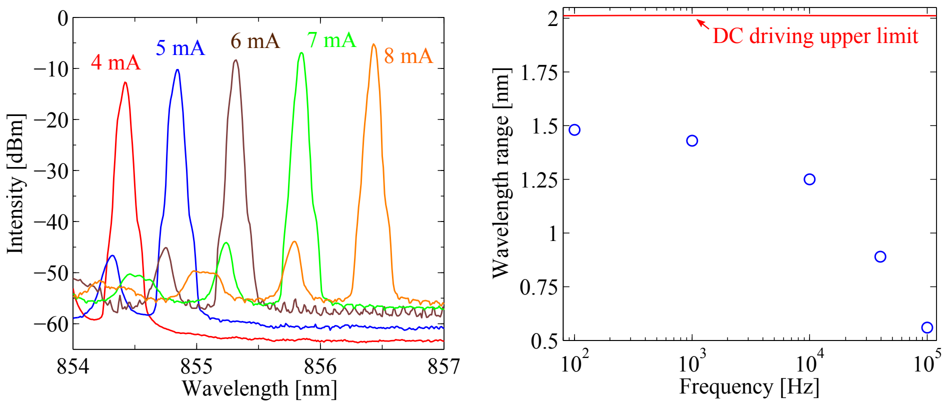

(a) Spectral intensity measured with varying DC driving current using an Optical Spectrum Analyzer.

(b) Wavelength tuning characteristics of the embedded and fiber pigtailed VCSEL.

Figure 6.11 – Dynamic wavelength range of the fiber pigtailed single-mode VCSEL.

At 100 Hz, the heating effect and the corresponding dynamic wavelength range is limited to 1.46 nm when using the sawtooth driving signal versus 2.01 nm when using the DC driving mode. A theoretical spectral resolution of 1.5 pm and a response time of 10 ms are consequently obtained. The accuracy of the interrogation system is limited by the VCSEL bandwidth. Figure 6.11a also indicates that single-mode behavior of the embedded and fiber-coupled VCSEL is preserved even for higher driving currents. The same parameters were used to perform the initial spectral reconstruction measurements (modulation mode), as was shown in Figure 6.4.

6.6.2 Temperature measurements

Temperature tests were carried out using a Thermoelectric Cooler (TEC) set-up on which the FBG was positioned next to the heating elements (Figure 6.12a). Before the actual experiments, a calibration measurement was performed to obtain relative (referenced) spectral measurements.

(a) Temperature characterization set-up.

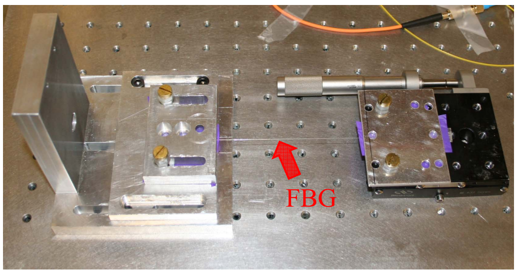

(b) Axial strain characterization set-up.

Figure 6.12 – Fully embedded system tests.

Temperature characterization was carried out by first heating up the fiber from room temperature (Figure 6.13a, measurement 1) to 75 °C (Figure 6.13a, measurement 2) and subsequently cooling it down. A limited set of spectral measurements is shown in Figure 6.13a. The central wavelength for all the measurements is plotted versus temperature in Figure 6.13b. A linear temperature response is obtained yielding a sensitivity of 3.0 ± 0.1 pm/°C. The slope of this curve is deviating from the theoretical sensitivity of 5.7 pm/°C for 855 nm silica fiber Bragg gratings [14]. This difference can be explained by the heat loss during the heat transfer from the TEC to the fiber.

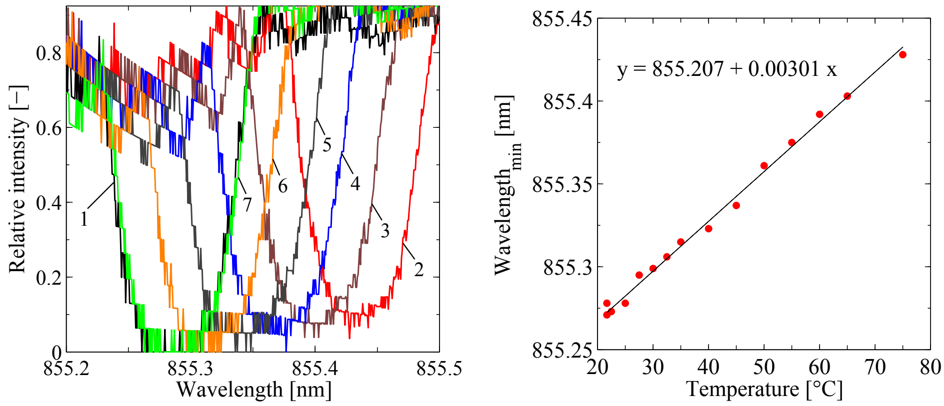

(a) Measured transmission spectra using the integrated VCSEL and photodetector system.

(b) Wavelength extremum versus temperature.

Figure 6.13 – Temperature characterization of the fully embedded system. 1: 21.7 °C (RT), 2: 75 °C, 3: 65 °C, 4: 55 °C, 5: 45 °C, 6: 35 °C, 7: 25 °C.

6.6.3 Axial strain measurements

The axial strain tests were performed on a fiber clamping set-up with microscrews to accurately control the applied displacement (Figure 6.12b). The fiber system is set up using similar test parameters as for the temperature characterization. Before the actual experiments, a calibration measurement was performed to obtain relative (referenced) spectral measurements.

Axial strain characterization tests were performed by applying different displacements on one end of the fiber and monitoring the corresponding spectra (Figure 6.14a). The central wavelength for all the measurements is plotted versus strain in Figure 6.14b. A linear axial strain response is achieved yielding a sensitivity of $0.25 \pm 0.01\,\mathrm{nm/m}\epsilon$. This slope is lower than the theoretical sensitivity of $0.67\,\mathrm{nm/m}\epsilon$ for 855 nm silica fiber Bragg gratings [14]. The difference can be explained by partial slippage of the fiber in the fiber clamping set-up and partial slippage of the fiber in the acrylate fiber coating.

6.6.4 Tactile sensing

Dynamic characterization tests were performed to prove the feasibility of fast full spectral reconstruction measurements, not limited to a fixed monitoring wavelength. Therefore, the system was operated using a sawtooth signal of 1 kHz and driving currents between 4 mA and 8 mA. The corresponding wavelength range is limited to 1.39 nm in this case and a response time of 1 ms is consequently ob-

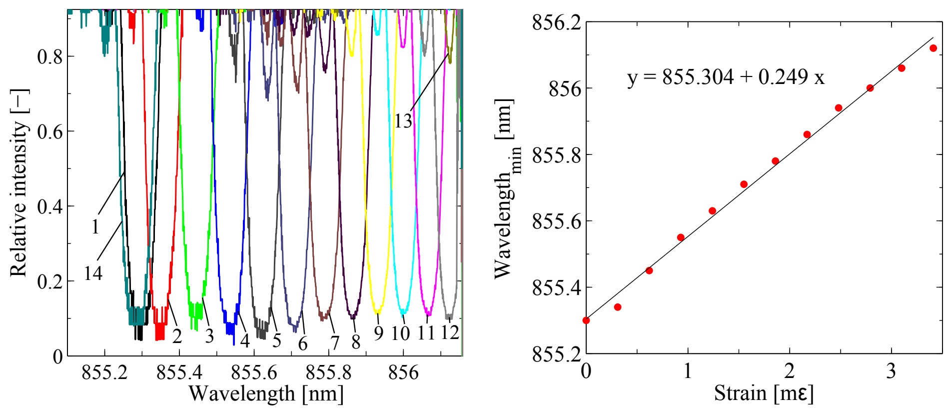

(a) Measured transmission spectra using the integrated VCSEL and photodetector system.

(b) Wavelength extremum versus axial strain.

Figure 6.14 – Strain characterization of the fully embedded system.
1: 0 mϵ, 2: 0.31 mϵ, 3: 0.62 mϵ, 4: 0.93 mϵ, 5: 1.24 mϵ, 6: 1.55 mϵ, 7: 1.86 mϵ, 8: 2.17 mϵ, 9: 2.48 mϵ, 10: 2.79 mϵ, 11: 3.10 mϵ, 12: 3.41 mϵ, 13: 3.72 mϵ, 14: 0 mϵ.

tained. Data acquisition rates are varying between 100 kHz and 10 MHz, depending on the required measurement detail and associated resolution. For the tactile sensing measurements, the fiber sensor is embedded in an artificial sensing skin as discussed in Chapter 3 and [15, 16].

To demonstrate the tactile "touch" sensing capabilities, the operation of the sensing system was qualitatively proven by manually touching and releasing the fiber sensing skin and dynamically monitoring the system (modulation mode as schematically shown in Figure 6.3). The resulting tactile sensing measurements are shown in Figure 6.15.

6.6.5 Vibration

Next to the tactile sensing tests, an electrodynamic shaker test was set up to dynamically characterize the system in a repeatable and controllable way. Therefore, the fiber system was set up using similar test parameters as for the tactile sensing characterization tests. This set-up was available at the Department Material Science and Engineering of Ghent University. In Figure 6.16, the electrodynamic shaker set-up is shown, as well as the driving and read-out equipment, connecting fibers and data acquisition unit. The fiber sensor was fixed on a metal resonating plate with a resonance frequency of 50 Hz. A logarithmic frequency sweep between 20 Hz and 300 Hz during 60 s was applied on the shaker set-up.

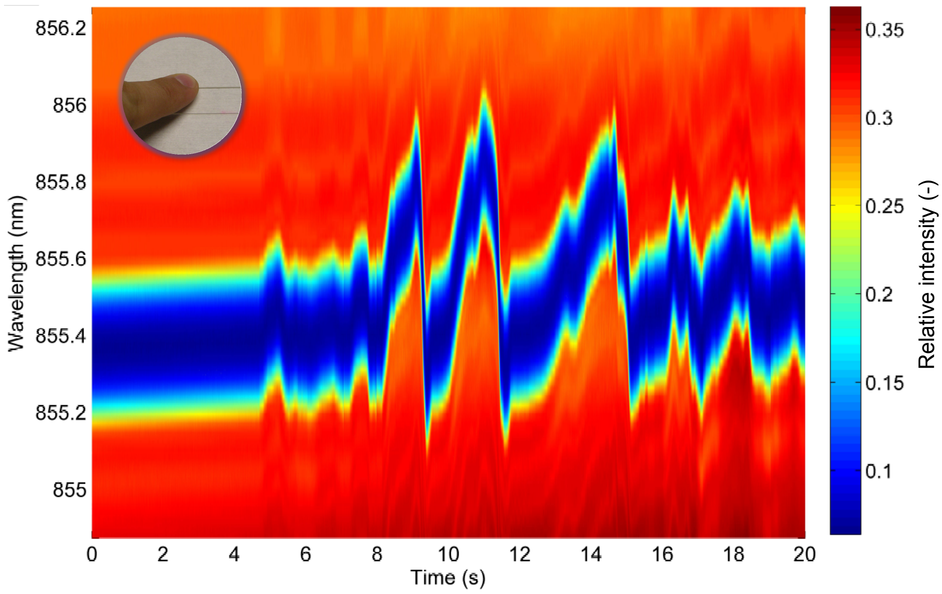

Figure 6.15 – Tactile sensing demonstration: relative wavelength intensity variations when touching the embedded fiber sensor.

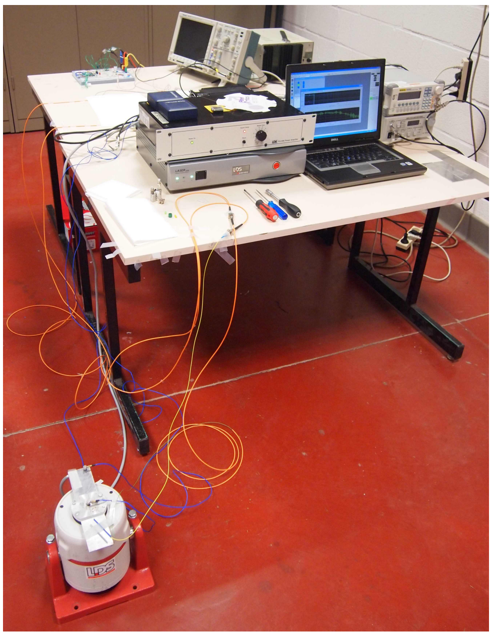

Figure 6.16 – Electrodynamic shaker set-up.

Part of the resulting dynamic measurement (wavelength resolution of 4 pm) is shown in Figure 6.17 and more detailed views are depicted in Figures 6.18 and 6.19.

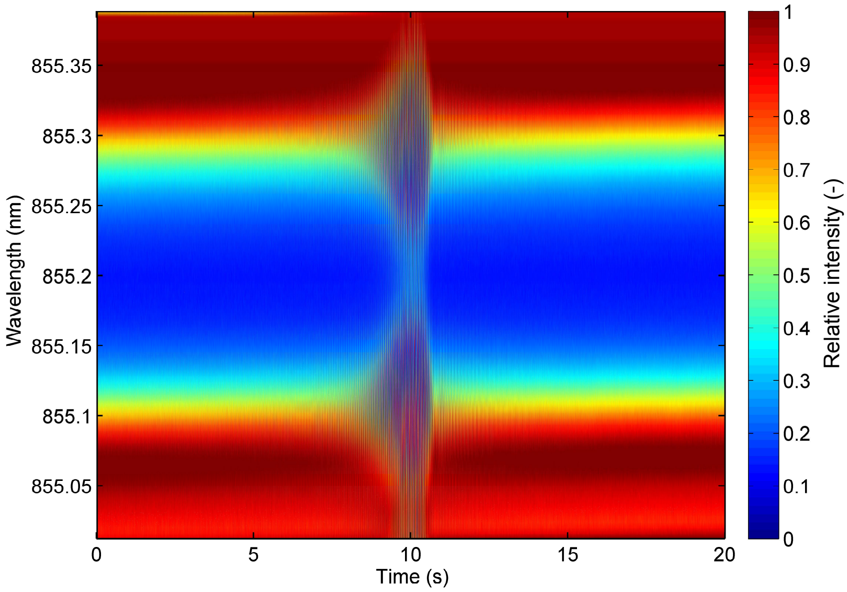

Figure 6.17 – Electrodynamic shaker characterization of the fully embedded system (relative wavelength intensities). Full spectral reconstruction of the resonance effect.

In Figure 6.20, a time domain plot (at a fixed wavelength, λ = 855.104 nm), focusing on the lower edge of the grating response, is depicting the periodic signal without shaking (labeled "Reference") and during resonance (labeled "Experiment").

Without resonance, there is partial overlap of the VCSEL emitting power spectrum and the grating filter characteristic, transmitting about 75 % of the optical power. During resonance, the Bragg grating filter characteristic overlap is completely eliminated when reaching a 100 % relative transmitted power intensity. After analyzing this graph, a frequency of 50 Hz is obtained confirming that the spectral information can indeed be reconstructed correctly.

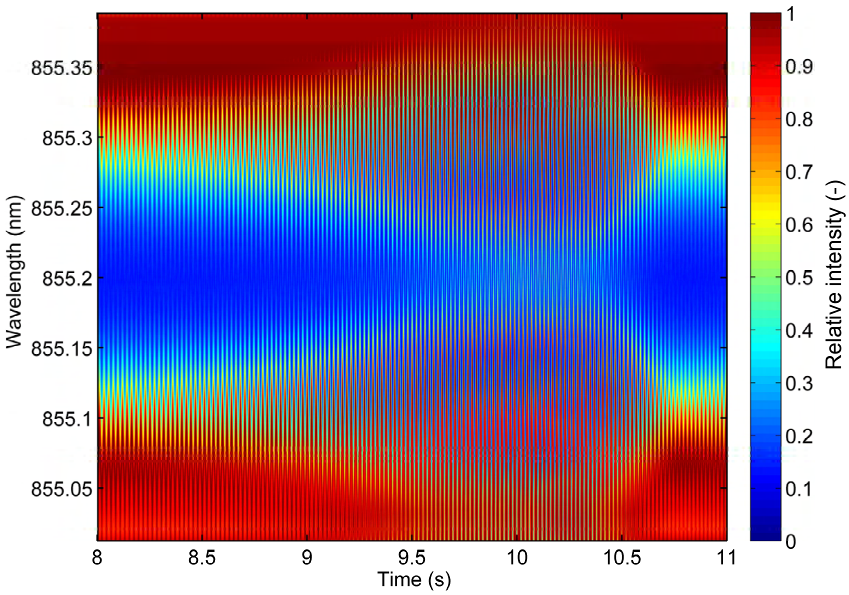

Figure 6.18 – Electrodynamic shaker characterization of the fully embedded system (relative wavelength intensities). Zoomed view of the full spectral reconstruction.

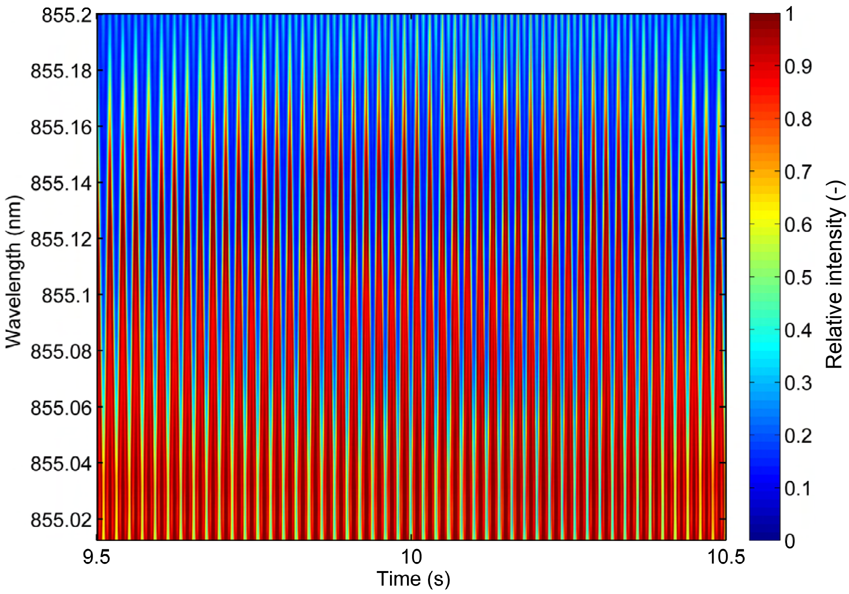

Figure 6.19 – Detailed analysis of the electrodynamic shaker characterization (full spectral reconstruction with relative wavelength intensities).

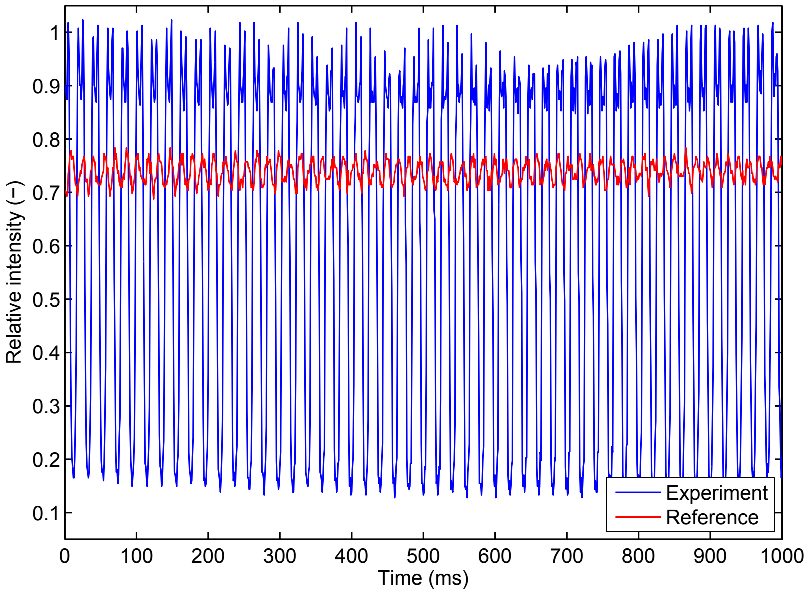

Figure 6.20 – Electrodynamic shaker characterization: time domain analysis (relative intensity at a fixed wavelength of 855.104 nm) during resonance. Reference measurement is stable around 75 %.

6.6.6 Asymmetric deformation

As mentioned before, to fully exploit the benefits of fiber Bragg gratings, full spectral reconstruction of the fiber sensor signal is needed. In this section, an example will be given of an asymmetric deformation of a fiber Bragg grating leading to peak deformation and birefringence [17, 18]. In optical communication systems, this is typically an unwanted effect deteriorating the signal quality and reducing the data connection speed. In structural health monitoring applications however, this effect can provide a very useful source of information. Analyzing these spectral distortions can provide important information on for example residual stresses or transverse cracks in composite laminates [19, 20]. Another application was already discussed in Section 3.4. Shrinkage of the embedding polymer host material in combination with a good fiber adhesion was in this case causing spectral peak deformation after completion of the embedding process or during temperature variation. To measure these kinds of special distortions, spectral analysis is performed on a few-mode silica fiber with a Bragg grating around 850 nm.

This grating is fabricated in a different fiber (single-mode at 1550 nm but few-mode at 850 nm). As a reference, the transmission spectrum of this few-mode silica fiber with Bragg grating is recorded using a compact fiber pigtailed Exalos [21]

SLED and an Agilent 86142B OSA, shown in Figure 6.21.

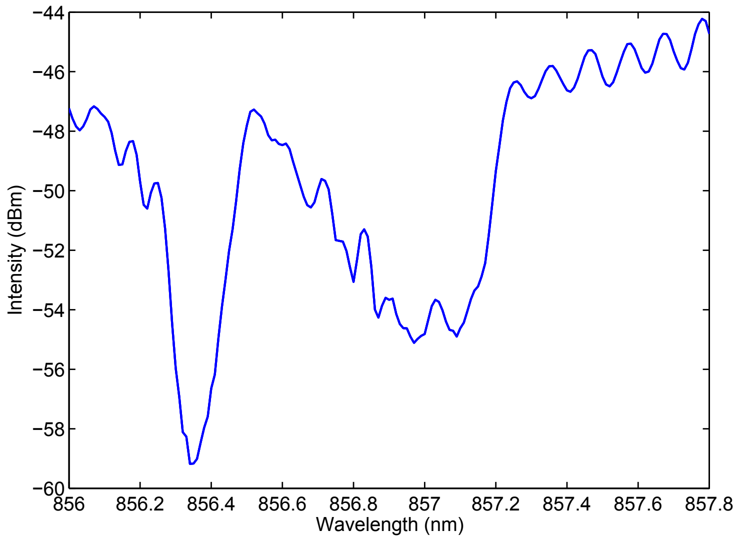

Figure 6.21 – Fiber Bragg grating in transmission using an SLED and an OSA.

The sensing fiber is then clamped between two stages accommodated with micro-screws to apply a strain on the Bragg grating. The fully embedded interrogation scheme is again using the modulation mode, as discussed in Section 6.3. Driving the VCSEL is done using a 1 kHz sawtooth current signal and the VCSEL is modulated between 2 mA and 4 mA. A linear relation between electrical current and VCSEL wavelength is assumed. The photocurrent signal (a measure of the transmitted optical power) is amplified in a negative feedback loop and filtered (read-out filter cut-off frequency = 1 MHz) to clear the signal from high-frequency noise. A National Instruments data acquisition (DAQ) board is used to read out and store the functional photocurrent data and the DAQ read-out frequency is set at 10^5 samples per second. Consequently, every millisecond a new spectral waveform is available and each waveform consists of 100 data points.

The total VCSEL tuning range is 1.783 nm yielding a spectral resolution accuracy of 17.83 pm. This wavelength tuning range is deviating from previously mentioned wavelength ranges at 1 kHz. This is because the VCSEL used for these tests was originating from a different batch and, as mentioned before, one of the drawbacks of the VCSELs are the chip-to-chip and batch-to-batch varying optical characteristics. Increasing the VCSEL modulation or photodetector sampling frequency can further enhance time and spectral resolution of the system. The upper limit for the modulation frequency in this simple approach was experimentally determined around 20 kHz. Beyond this limit, the wavelength-current relationship of the VCSEL starts to fade. By using pulse width modulation or other more advanced signal processing techniques, one could further enhance the resolution values.

A calibration measurement is necessary in order to filter the optical power fluctuations and to come up with relative wavelength intensities. During the functional test, a manual strain of 0.954 mϵ is applied by loading the fiber with a microscrew with a resolution of 10 µm. The relative wavelength intensities are color plotted as a function of time in Figure 6.22. This figure displays a dynamic measurement of the fiber Bragg grating during manual straining and releasing of the fiber. The different straining and releasing steps are clearly visible.

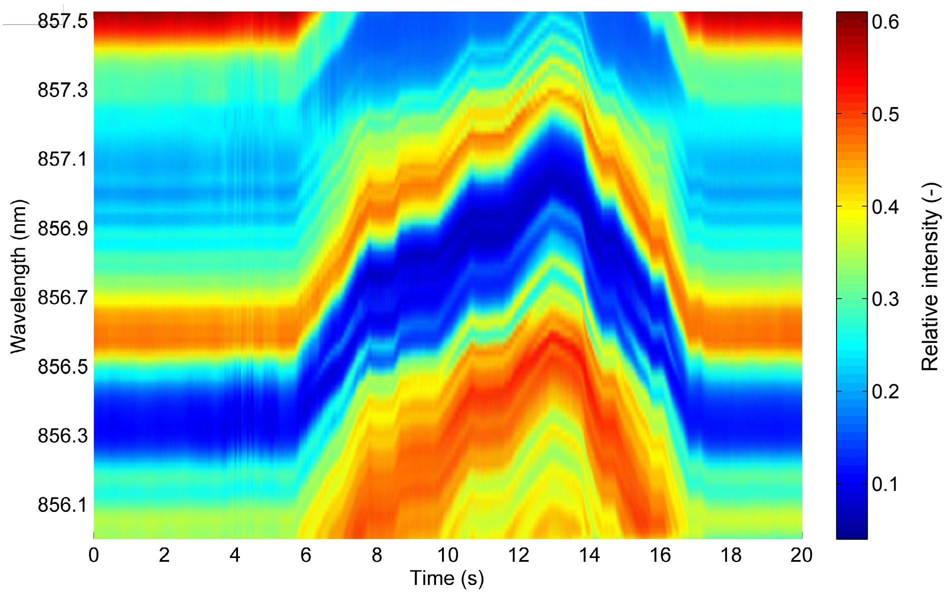

Figure 6.22 – Dynamic measurement of the fiber Bragg grating using the fully embedded system (wavelength intensity versus time).

In order to experimentally verify the strain which is applied, the minimum wavelength intensity is tracked. A maximum wavelength shift of $\approx$ 0.7 nm is obtained at t = 12.96 s. Comparing this value to the theoretical strain of 0.954 mϵ indicates an almost perfect transfer of the applied displacement to strain on the fiber. More advanced analysis of the spectral response of the fiber Bragg grating is now possible on a very accurate scale, both in time and wavelength domain. A snapshot of the optical spectrum is shown in Figure 6.23. One can extract the shift in peak wavelength but also other information, not measurable with traditional peak-tracking systems, such as peak deformation or the introduction of birefringence leading to the two different dips in the optical spectrum (Figure 6.22, t = 7 s and snapshot in Figure 6.23) is visible. This effect is due to an asymmetrical deformation of the fiber core leading to a difference in effective refractive index when changing the polarization and propagation direction of light. A double refraction effect is the result. Using microstructured optical fibers possessing a high degree of inherent birefringence (Chapter 3), one can tune the sensitivity of fiber sensors to certain parameters and distinguish between axial and transverse loading effects. The fiber interrogation system presented here can consequently also be used on these advanced fiber sensors.

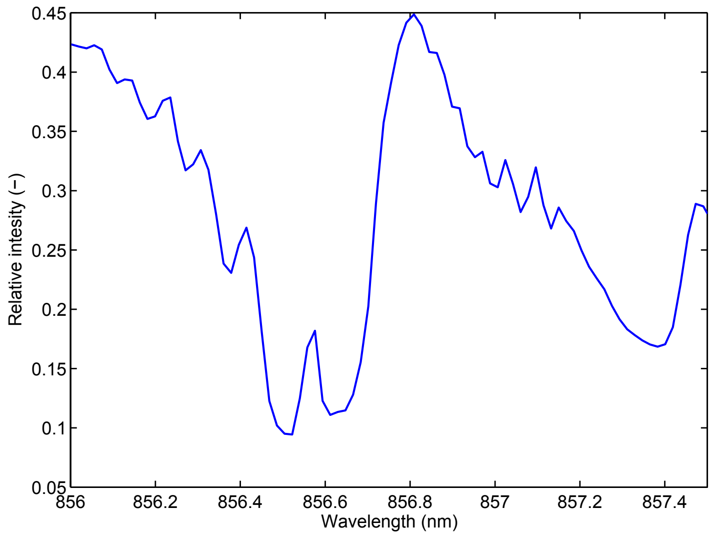

Figure 6.23 – Snapshot of the spectral information at t = 7s (intensity vs. wavelength).

6.6.7 Complete single-mode system

In this section, a fully single-mode system is discussed. Figure 6.24 shows the comparison of an optical spectrum analyzer measurement with the fully embedded read-out result. The two graphs nicely coincide. At $\lambda = 856.5$ nm, an extra dip in the dynamically reconstructed spectrum is visible. This is possibly due to a second mode present in the VCSEL emission spectrum. The total loss of the single-mode VCSEL - fiber - photodiode link is about 7 dB.

Figure 6.25 is depicting a basic characterization graph in which strain is manually applied on the fiber sensor. The x-axis is now showing both time and data point values (5000 acquired optical power transmission values over 1 ms) over 1 spectral reconstruction period. The y-axis is showing linear (photocurrent) intensity values. This graph is depicting 1 round trip of the driving VCSEL and the rela-

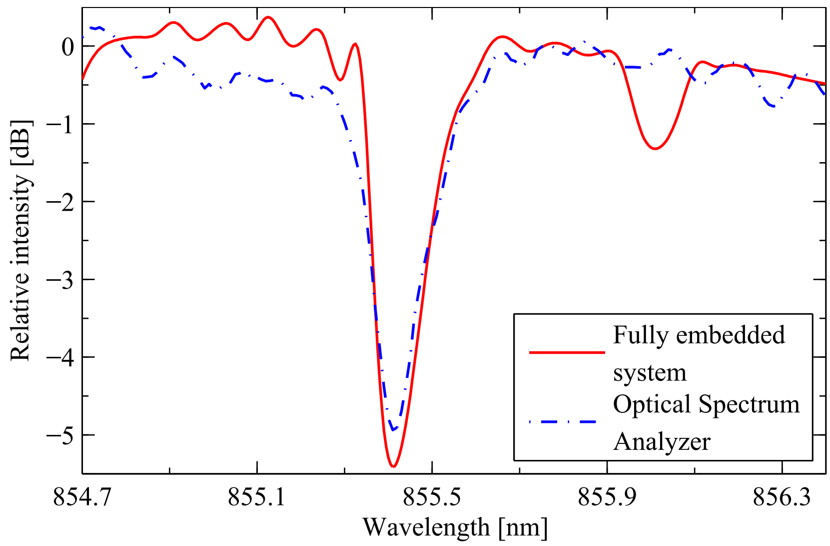

Figure 6.24 – Measuring a single-mode fiber Bragg grating: OSA vs. fully embedded system.

tive intensity values start to saturate from t = 0.3 ms. This effect has nothing to do with the fiber sensor but can be attributed to the fact that higher time values correspond with increasing VCSEL driving currents (Figure 6.3). These increasing driving currents are in this case causing an increasing but flattening optical power (rather than a linear increase, probably due to thermal effects) explaining the saturated relative intensity values.

6.6.8 Temperature influence

As discussed in Chapter 2, one of the important advantages associated with sensors based on fiber Bragg gratings is their insensitivity to optical intensity fluctuations caused by aging effects, deteriorating coupling alignments or differences in electrical driving currents. Unwanted wavelength fluctuations, for example of the driving VCSEL source, can however influence and potentially also compromise the sensor measurements. The main reason for these unwanted wavelength fluctuations is to be found in ambient temperature variations. To check the vulnerability of the embedded single-mode VCSELs to such ambient temperature changes, the emitting wavelength was monitored between 20 °C and 70 °C using different driving currents (2.5 mA and 6 mA). An ultra-thin VCSEL package was therefore mounted on a hot plate and the wavelength was monitored using an Agilent 86142B OSA. The results are shown in Figure 6.26.

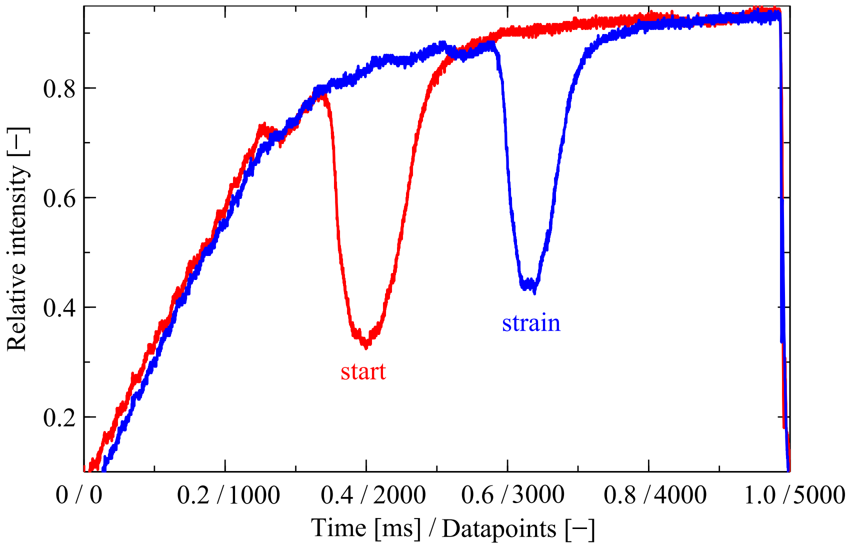

Figure 6.25 – Characterization of the fully single-mode system: initial measurement vs. strain.

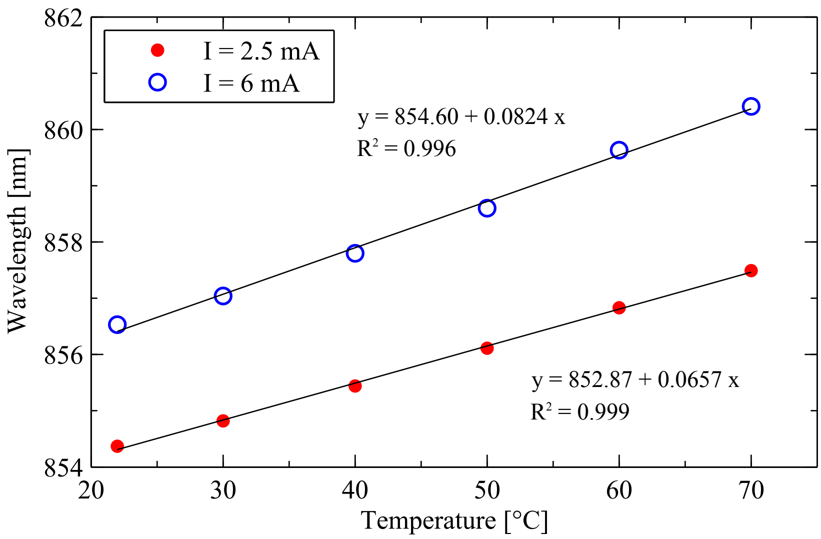

Figure 6.26 – Wavelength - temperature sensitivity of the single-mode VCSEL source.

Sensitivities of respectively 66 ± 1.2 pm/°C and 82 ± 2.7 pm/°C are extracted. The typical temperature dependency of the emitting wavelength is 60 pm/°C according to the manufacturer datasheet. An elegant way to circumvent this temperature sensitivity could be matching the temperature sensitivity of the embedded fiber sensor(s) (Table 3.13) to the sensitivity of the driving VCSEL.

6.7 Conclusion

This chapter described a new fiber sensor interrogation system which can be fabricated ultra-small and fully embedded in a thin polymer stack. The sensing elements are manufactured using mature and commercially available Bragg grating inscription technology. Driving and read-out electronics and optoelectronics were combined with an Android based acquisition unit resulting in a portable and compact sensing system. Furthermore, technology was provided to take the integration a step further and embed the optoelectronics on a chip level to obtain a wearable system with a thickness below 1 mm. A broad range of new applications, including tactile sensing, structural health monitoring and biomedical systems, can be targeted with this unique sensing concept.

The interrogation technique is based on an intelligent VCSEL-photodiode combination. Two interrogation modes are available: constant current mode and modulation mode. In constant current mode, the transmitted optical power is monitored at a fixed wavelength with a maximum acquisition rate of 5 kHz. Using the modulation mode offers full spectral reconstruction. The corresponding wavelength resolution is depending on the driving frequency and data acquisition rate, and demonstrated at, but not limited to, 1.5 pm and 4 pm. The wavelength accuracy is limited by the VCSEL bandwidth and the associated response time varies between 1 ms and 10 ms. In terms of resolution and measurement speed, the only limit on the sensing system is the driving laser (VCSEL) chip. Increasing the sensing system speed will narrow the wavelength range. There is however only one signal containing full spectral datasets which has to be read out. Compared to conventional spectrometers and other state-of-the-art fiber Bragg grating interrogation systems this yields a significant advantage as no optical mirrors have to be turned or multiple CCD elements read out.

References

[1] B. Van Hoe, G. Lee, E. Bosman, J. Missinne, S. Kalathimekkad, O. Maskery, D. J. Webb, K. Sugden, P. Van Daele, and G. Van Steenberge, "Ultra small integrated optical fiber sensing system," *Sensors*, vol. 12, no. 9, pp. 12 052–12 069, Sept. 2012.

[2] E. J. Voet, G. Luyckx, I. De Baere, J. Degrieck, J. Vlekken, E. Jacobs, and H. Bartelt, "High strain monitoring during fatigue loading of thermoplastic composites using imbedded draw tower fibre bragg grating sensors," in *Emboding Intelligence in Structures and Integrated Systems*, ser. Advances in Science and Technology, P. Vincenzini and F. Casciati, Eds., vol. 56, 2009, pp. 441–446, 3rd International Conference on Smart Materials, Structures and Systems, Acireale, Italy, JUN 2008.

[3] G. Luyckx, E. Voet, N. Lammens, and J. Degrieck, "Strain measurements of composite laminates with embedded fibre bragg gratings: Criticism and opportunities for research," *Sensors*, vol. 11, no. 1, pp. 384–408, Jan. 2011.

[4] G. Meltz, W. Morey, and W. Glenn, "Formation of bragg gratings in optical fibers by a transverse holographic method," *Optics Letters*, vol. 14, no. 15, pp. 823–825, Aug. 1989.

[5] Y. Huang, T. Guo, C. Lu, and H.-Y. Tam, "Vcsel-based tilted fiber grating vibration sensing system," *IEEE Photonics Technology Letters*, vol. 22, no. 16, pp. 1235–1237, Aug. 2010.

[6] C. F. R. Mateus and C. L. Barbosa, "Harsh environment temperature and strain sensor using tunable vcsel and multiple fiber bragg gratings," in *2007 SBMO/IEEE MTT-S INTERNATIONAL MICROWAVE AND OPTOELECTRONICS CONFERENCE, VOLS 1 AND 2*, 2007, pp. 496–498, sBMO/IEEE MTT-S International Microwave and Optoelectronics Conference, Salvador, Brazil, OCT-NOV 2007.

[7] F. Koyama, "Recent advances of vcsel photonics," *Journal of Lightwave Technology*, vol. 24, no. 12, pp. 4502–4513, Dec. 2006.

[8] K. Zogal, T. Gruendl, H. A. Davani, C. Gierl, S. Jatta, C. Grasse, M. C. Amann, and P. Meissner, "High speed modulation of a 1.55-mu m mems-tunable vcsel," in *CONFERENCE ON LASERS AND ELECTRO-OPTICS (CLEO)*, 2011, conference on Lasers and Electro-Optics (CLEO), Baltimore, MD, MAY 2011.

[9] M. Njegovec and D. Donlagic, "High-resolution spectrally-resolved fiber optic sensor interrogation system based on a standard dwdm laser module," *Optics Express*, vol. 18, no. 23, pp. 24 195–24 205, Nov. 2010.

[10] S. Schultz, W. Kunzler, Z. Zhu, M. Wirthlin, R. Selfridge, A. Propst, M. Zikry, and K. Peters, "Full-spectrum interrogation of fiber bragg grating sensors for dynamic measurements in composite laminates," *Smart Materials & Structures*, vol. 18, no. 11, Nov. 2009.

[11] T. Vella, S. Chadderdon, R. Selfridge, S. Schultz, S. Webb, C. Park, K. Peters, and M. Zikry, "Full-spectrum interrogation of fiber bragg gratings at 100 khz for detection of impact loading," *Measurement Science & Technology*, vol. 21, no. 9, SI, Sept. 2010.

[12] Phosfos Consortium. (2008) Photonic skins for optical sensing. [Online]. Available: http://www.phosfos.eu/

[13] G. C. B. Lee, B. Van Hoe, Z. Yan, O. Maskery, K. Sugden, D. Webb, and G. Van Steenberge, "A compact, portable and low cost generic interrogation strain sensor system using an embedded vcsel, detector and fibre bragg grating," ser. Proceedings of SPIE, C. Lei and K. Choquette, Eds., vol. 8276, 2012, conference on Vertical-Cavity Surface-Emitting Lasers XVI (VCSELs)/SPIE Photonics West Symposium, San Francisco, CA, JAN 2012.

[14] K. Hill and G. Meltz, "Fiber bragg grating technology fundamentals and overview," *Journal of Lightwave Technology*, vol. 15, no. 8, pp. 1263–1276, Aug. 1997.

[15] X. Chen, C. Zhang, B. Van Hoe, D. J. Webb, K. Kalli, G. Van Steenberge, and G. D. Peng, "Photonic skin for pressure and strain sensing," ser. Proceedings of SPIE-The International Society for Optical Engineering, F. Berghmans, A. Mignani, and C. Hoof, Eds., vol. 7726, 2010, conference on Optical Sensing and Detection, Brussels, Belgium, APR 2010.

[16] B. Van Hoe, G. Van Steenberge, E. Bosman, J. Missinne, T. Geernaert, F. Berghmans, D. Webb, and P. Van Daele, "Optical fiber sensors embedded in polymer flexible foils," ser. Proceedings of SPIE-The International Society for Optical Engineering, F. Berghmans, A. Mignani, and C. Hoof, Eds., vol. 7726, 2010, conference on Optical Sensing and Detection, Brussels, Belgium, APR 2010.

[17] R. Gafsi and M. El-Sherif, "Analysis of induced-birefringence effects on fiber bragg gratings," *Optical Fiber Technology*, vol. 6, no. 3, pp. 299–323, July 2000.

[18] R. Wagreich, W. Atia, H. Singh, and J. Sirkis, "Effects of diametric load on fibre bragg gratings fabricated in low birefringent fibre," *Electronics Letters*, vol. 32, no. 13, pp. 1223–1224, June 1996.

[19] Y. Okabe, S. Yashiro, T. Kosaka, and N. Takeda, "Detection of transverse cracks in cfrp composites using embedded fiber bragg grating sensors," *Smart Materials & Structures*, vol. 9, no. 6, pp. 832–838, Dec. 2000.

[20] Y. Okabe, S. Yashiro, R. Tsuji, T. Mizutani, and N. Takeda, "Effect of thermal residual stress on the reflection spectrum from fiber bragg grating sensors embedded in cfrp laminates," *Composites Part A - Applied Science and Manufacturing*, vol. 33, no. 7, pp. 991–999, 2002.

[21] EXALOS: Superluminescent Light Emitting Diodes (SLEDs) Manufacturer. (Accessed 2013) Products. [Online]. Available: http://www.exalos.com/

7
High resolution pressure sensor based on optical feedback in a VCSEL

This final technology chapter is reaching out for optical sensor principles which are inherent to the optoelectronic sources avoiding the use of any Bragg grating structure. These sensors can pave the way towards further sensor miniaturization and integration. Within this chapter a highly accurate integrated incremental pressure sensor, based on optical feedback in a VCSEL, is developed. This laser chip is again embedded as an unpackaged optoelectronic component in a polymer host material. A compressible polymer sensing layer is acting simultaneously as an external laser cavity and as a transducer material, converting the pressure which is applied into a change in the laser cavity length.

7.1 Introduction

As already discussed in Chapter 1, pressure sensors are becoming increasingly important in different areas, such as the automotive industry, the structural health sector and biomedical engineering. These markets are demanding for technologies which allow to miniaturize sensors and, at the same time, to integrate sensor elements with microelectronic functions in minimal space. Within the medical application domain additional requirements apply such as biocompatibility, mechanical flexibility and sensor insensitivity to electromagnetic interference.

The existing Microelectromechanical Systems (MEMS) pressure sensors are mostly based on piezoresistive or capacitive force sensing technologies [1]. Optical alternatives, mostly based on fiber sensors, have been developed by several institutes [2]. Polymer and polymer embedded optical fiber sensors as well as ultra-small fiber sensing systems have been discussed in Chapters 3 and 6. These sensors can perform absolute pressure measurements and offer unique advantages such as immunity to electromagnetic interference and capability of operating in harsh environments. In this chapter, an optical, incremental, VCSEL based sensor is presented based on self-mixing interferometry in an external laser cavity. Using unpackaged laser chips, one can embed this sensor element in an ultra-thin flexible package (an optical sensing foil) which can be mounted on a non-planar surface or even irregularly shaped objects, such as a the human body. These laser chips typically contain arrays of VCSELs (pitch between the light emitting areas of 250 µm for example) enabling high-density measurements in small areas. In this respect the VCSEL sensing approach is clearly distinguishable from the (multiplexed) optical fiber sensors, typically covering larger areas but with lower density.

The working principles of optical sensors based on self-mixing interferometry were discussed in Chapter 2, Section 2.1.2. In the next paragraph, these working principles are applied on VCSEL array chips. This VCSEL based pressure sensor combines the specific advantages of sensors based on an optical sensing mechanism with extensive integration capabilities. The pressure sensor which is developed within this chapter namely relies on optical feedback in the optoelectronic component itself. Expensive and delicate fiber coupling or free-space light coupling technology blocks are consequently avoided.

7.2 Principle of operation

The pressure sensing mechanism is based on a displacement measurement of an external target on a VCSEL chip. The underlying mechanism for this displacement measurement is based on the self-mixing interference effect in VCSELs which is observed when a fraction of light emitted from the laser is injected back into the laser cavity. This back reflection is performed by an external target on a distance L_{ext} from the VCSEL emitting area [3]. As a result, an external cavity is created between the VCSEL and the external reflector (Figure 7.1).

The VCSEL resonator itself consists of two Distributed Bragg Reflector (DBR) mirrors parallel to the wafer surface with an active region consisting of one or more quantum wells for the laser light generation in between. The planar DBR-mirrors (reflectance R_{int}, Figure 7.1) consist of layers with alternating high and low refractive indices. Each layer has a thickness of a quarter of the laser wavelength in the material, yielding intensity reflectivities above 99 %. High reflectivity mirrors are required in VCSELs to balance the short axial length of the gain region.

The external target has a reflecting layer with a reflectance R_{ext} and is typically consisting of a thin metal layer.

Due to the coherence of the emitted laser light, the recoupled light mixes in a deterministic way with the light in the internal laser cavity. The phase shift introduced by the round trip travel to and from the target, influences the optoelectronic characteristics of the laser. Depending on the delay and the phase of the back-reflected light, the VCSEL threshold condition is varied; thus the emitted optical power changes as the pump current is held constant. The change in the threshold implies a change in the actual VCSEL carrier density; as a consequence, the wavelength emitted by the VCSEL subject to back reflections is also slightly varied [3, 4]. Because of this phase shift dependency, increasing or decreasing L_{ext} results in a periodic variation of laser wavelength, optical power and electrical resistance, all with period $\lambda/2$ (λ being the emitting wavelength of the VCSEL, in this chapter 850 nm). This means that the target displacement can be calculated by monitoring the periodic signal between the initial and the final position of the target, where the spacing between the two consecutive peaks corresponds to the distance of $\lambda/2$. Similar interferometric effects in VCSELs can be used to sense other parameters or even perform multi-parametric sensing [5].

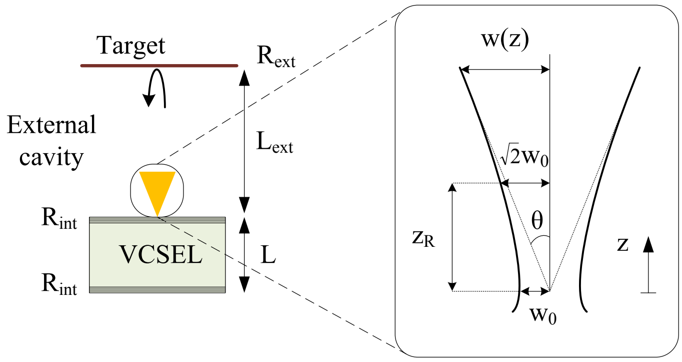

Figure 7.1 – Schematic overview of the VCSEL sensor principle.

7.2.1 Transducer layer parameters

A parameter of major importance for the sensor discussed in this chapter is the external cavity material (Figure 7.1). Most existing sensors based on self-mixing interference working principles are based on air as an external cavity material between the light source and the target. Light is in this case propagating free-space and optical elements (lenses) are typically needed to observe self-mixing interferometry. In the first part of this chapter, a free-space optical path is indeed used as an external cavity for discrete experiments producing proof-of-principle results and demonstrating the sensor capabilities. In this case displacement measurements are performed rather than real pressure measurements.

The sensing mechanism of the integrated pressure sensor discussed in the second part of this chapter is based on a conversion of the applied pressure to a certain displacement of the external target mirror layer. This target reflecting layer itself typically consists of a thin, little compressible, metal structure. Therefore, a key sensor parameter determining to a large extent the sensing range and the according accuracy, is the external cavity material. This transducer material is situated between the VCSEL (internal laser cavity) and the external target (Figure 7.2). Its mechanical properties are tuning the sensor characteristics (sensing range, accuracy, sensitivity, etc.).

The reason why unpackaged VCSEL components and extensive integration processes are used, is the possibility to integrate the sensor component (VCSEL) in an ultra-thin polymer package. To preserve the advantages associated with this integrated approach in terms of size and flexibility, an integrated polymer transducer layer is replacing the air gap. It is clear that without this integration technology, the sensor concept from Figure 7.2 would not be possible.

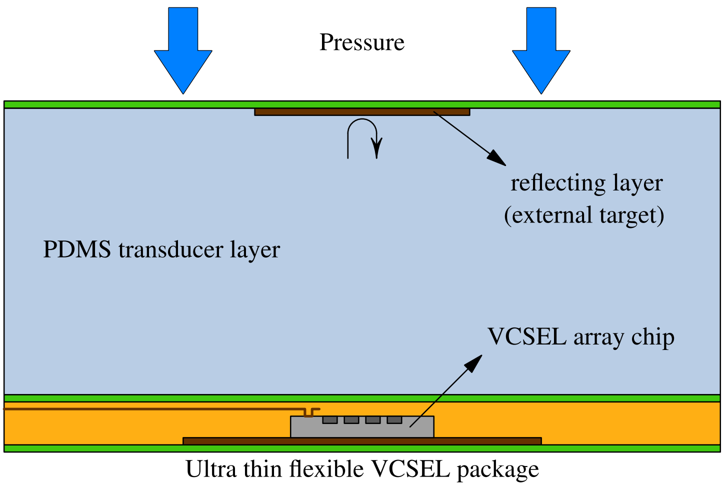

Figure 7.2 – Schematic overview of the integrated VCSEL sensor principle.

The transducer material for the integrated sensor approach is a compressible polydimethylsiloxane (PDMS) material, Sylgard®184, throughout the entire chapter. As mentioned before (Chapter 3, Section 3.3), it is difficult to list exact mechanical properties of PDMS as they are depending on the preparation conditions of the material but also the application methods and curing parameters. As a guideline, the Young's modulus E typically varies between 0.7 and 3.7 MPa and Poisson's ratio $\nu \approx 0.5$. Next to its mechanical flex- and stretchability, PDMS exhibits good environmental and thermal stability up to 300 °C [6]. Furthermore, the material shows a relatively low moisture absorption and is resistant to a large range of commonly used chemicals [7]. For a detailed discussion on the mechanical and optical properties of PDMS, the reader is again referred to the PhD dissertation of Jeroen Missinne [8] (Chapter 2, Section 2.4).

7.2.2 Interferometric parameters

During all experiments based on self-mixing interferometry the following important interferometric parameters, determining the working regime of the VCSEL sensor, have to be monitored:

- *The recoupled optical power $P_{coupled}$.* This value is depending on several VCSEL parameters such as the aperture, divergence angle and Rayleigh length, but also external cavity parameters such as the cavity length and material, as well as the reflecting layer hedging the external cavity.
- *The feedback parameter C.* This value is determined by the (internal) VCSEL linewidth enhancement factor, the laser internal DBR reflectance, cavity length and effective refractive index as well as the external cavity length, effective refractive index and external mirror reflectance.

Recoupled optical power

The power P_{coupled} which is coupled back in the internal laser cavity after propagation through the external cavity length can be estimated assuming the VCSEL output beam has a Gaussian spatial profile. A schematic view was shown in Figure 7.1. The optical power P passing through a circle of radius r in the transverse plane at position z is

$$P(r,z) = P_0\left(1 - e^{-2r^2/w^2(z)}\right)$$

where P_0 is the total power transmitted by the beam. For a Gaussian beam propagating in free-space, the spot size radius w(z) will be at a minimum value w_0 at one place along the beam axis, known as the beam waist. For a beam of wavelength λ at a distance z along the beam from the beam waist, the variation of the spot size is given by [9]

$$w(z) = w_0\sqrt{1 + \left(\frac{z}{z_{\mathrm{R}}}\right)^2}$$

where the origin of the z-axis is defined, without loss of generality, to coincide with the beam waist, and where [9]

$$z_R = \frac{\pi \, w_0^2}{\lambda}$$

is called the Rayleigh range. The VCSEL which is used as a sensor element is a multimode 850 nm component from ULM Photonics [10]. From Chapter 4, the following VCSEL parameters are obtained

$$\lambda = 850\,\text{nm}$$

$$P_0|_{V=1.5\,\text{V}} = 0.5\,\text{mW}$$

$$w_0 \approx 5\,\mu\text{m}$$

$$\frac{\mathrm{d}P_0}{\mathrm{d}V} \approx 11.3\,\frac{\text{mW}}{\text{V}}$$

Based on these values and under the assumption that the light is traveling one round trip ($2\,L_{ext}$) to recouple into the internal laser cavity, $P_{coupled}$ can be calculated as a function of the external cavity length L_{ext} using $n_{eff,ext}$ = 1.41 @ 850 nm. This is shown graphically for different VCSEL driving voltages in Figure 7.3.

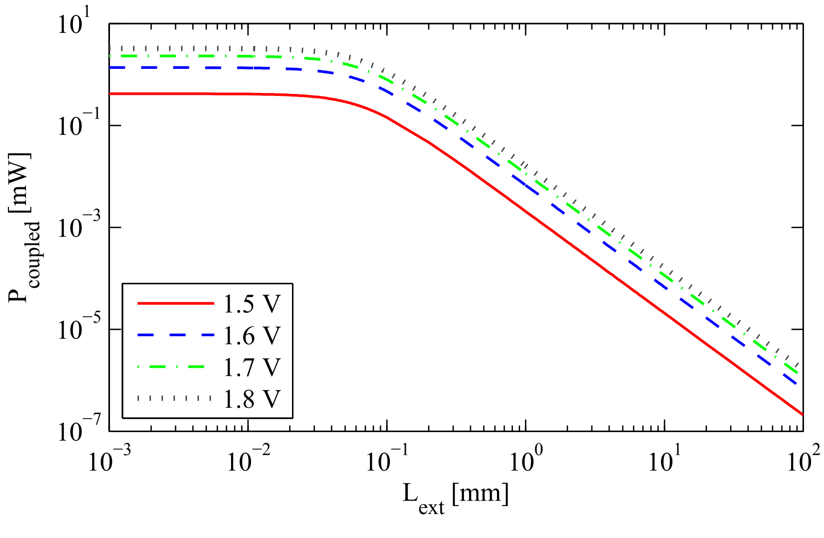

Figure 7.3 – Optical power coupled back into the laser cavity versus the external cavity length for varying VCSEL driving voltages.

A first observation from Figure 7.3 is that starting from 100 µm, the recoupled optical power is dropping drastically. From Chapter 2, Section 2.1.2, we know that the VCSEL parameters are dynamically modulated because of the self-mixing effect starting from a recoupled optical power of $P_{coupled}$ = 0.01 P_0, leading to the following condition for observing self-mixing interferometry effects:

$$L_{\mathrm{ext}} < 901\,\mu\mathrm{m}$$

Optical feedback parameter

A conventional VCSEL interferometric self-mixing configuration was shown in Figure 7.1. This configuration is equivalent to a three-mirror cavity, where the back-diffused or back-reflected power by the remote target can be calculated as a fraction R_{ext} of the emitted optical power P_0. An analytical steady-state solution describing the optical power in this three-mirror laser cavity can be found in [4, 11, 12], and is leading to the following general expression for the optical power emitted by the total VCSEL structure (including the external cavity)

$$P(\phi) = P_0(1 + m\,F(\phi))$$

where again P_0 is the power emitted by the unperturbed VCSEL, m is the modulation index and $F(\phi)$ is a periodic function of the interferometric phase $\phi = 2\,k\,L_{\mathrm{ext}}$ ($k = 2\pi\ \lambda$), of period 2π [3]. The modulation index m and the shape of the function $F(\phi)$ depend on the so-called feedback parameter C.

This feedback parameter is defined as follows [3, 4]

$$C = \frac{\kappa}{\tau}\,\tau_{\mathrm{ext}}\,\sqrt{1+\alpha^2}$$

α is the VCSEL linewidth enhancement factor and κ is the feedback coefficient given by

$$\kappa = (1 - R_{\mathrm{int}})\,\sqrt{\frac{R_{\mathrm{ext}}}{R_{\mathrm{int}}}}.$$

R_{int} is the reflectance for the internal DBR VCSEL layers and R_{ext} is the reflectance of external cavity reflecting layer (as shown in Figure 7.1). τ and τ_{ext} are the round-trip propagation time in the laser cavity (length L) and the external cavity (length L_{ext}) respectively

$$\tau = \frac{2\,n_{\mathrm{eff}}\,L}{c}$$

$$\tau_{\mathrm{ext}} = \frac{2\,n_{\mathrm{eff,ext}}\,L_{\mathrm{ext}}}{c}.$$

n_{eff} and $n_{eff,ext}$ are the effective refractive indexes in respectively the internal and external laser cavity and c is the speed of light.

Thus, the value of the C parameter depends on both the amount of feedback and, interestingly, on target distance L_{ext}. The feedback parameter is of great importance, because it discriminates between different feedback regimes:

- For $C \ll 1$, we have the very weak feedback regime. $F(\phi)$ is a cosine function and the modulation index m is proportional to $\sqrt{R_{ext}}$.
- For $0.1 < C < 1$, we have the weak feedback regime. The function $F(\phi)$ gets distorted, showing a non-symmetrical shape; the modulation index m is again proportional to $\sqrt{R_{ext}}$.
- For $1 < C < 4.6$, we have the moderate feedback regime. The function $F(\phi)$ becomes three-valued for certain values of the phase ϕ, i.e. the system is bistable, with two stable states and one unstable. The modulation index m increases for increasing $\sqrt{R_{ext}}$, but it is no longer proportional to it. The interferometric signal becomes sawtooth-like and exhibits hysteresis.
- For $C > 4.6$, we have the strong feedback regime. The function $F(\phi)$ may become five-valued, not all the specimens of VCSELs remain in the self-mixing regime; rather, in some cases the VCSEL enters the mode-hopping regime and interferometric measurements are no longer possible.

Introducing asymmetry in the VCSEL interference enables the determination of the displacement direction. Therefore, the feedback parameter is preferably larger than 0.1. Together with the restriction at the upper side of the feedback parameter, a functional range of $0.1 < C < 4.6$ is obtained.

The feedback parameter is calculated as a function of the external cavity length (Figure 7.4) in the case of air as an external cavity and in the case of Sylgard®184 as an external cavity, each time with a gold reflecting layer on top (Au coating > skin depth). The conversion of external pressure into displacement will be guaranteed by the use of this compressible PDMS layer as an external cavity which is applied on top of an ultra-thin flexible VCSEL package (Figure 7.2).

To end up with a feedback parameter within the functional range between 0.1 and 4.6, the following condition is obtained for air acting as an external cavity material:

$$18\,\mu\text{m} < L_{ext} < 800\,\mu\text{m}$$

To end up with a feedback parameter between 0.1 and 4.6, the following condition is obtained for Sylgard®184 acting as an external cavity material:

$$13\,\mu\text{m} < L_{ext} < 570\,\mu\text{m}$$

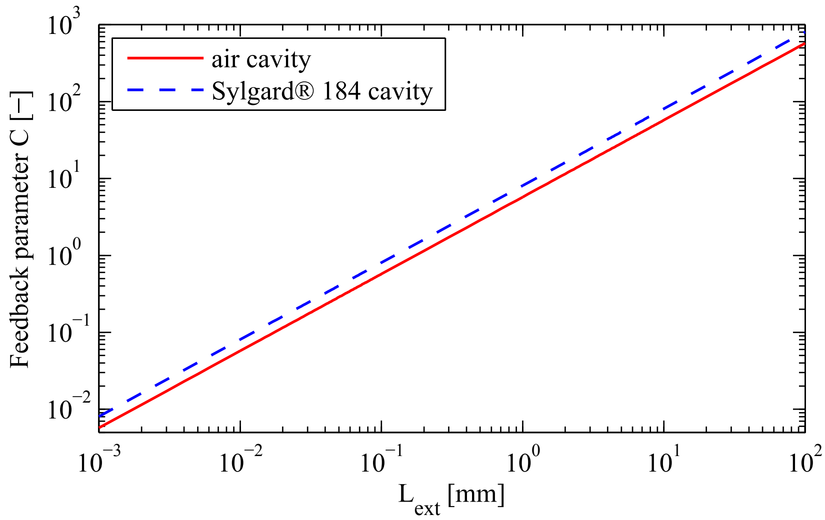

Figure 7.4 – Optical feedback parameter for different external cavity lengths and different external cavity materials.

7.3 Discrete proof-of-principle set-up

A discrete set-up was developed to mimic and prove the working principle of this new integrated sensing mechanism. This proof-of-principle set-up is schematically shown in Figure 7.5 and consists of different building blocks which are read out in parallel by a PC through GPIB. An unpackaged wire bonded VCSEL was put on a fixed location and a movable reflector acting as the external target (R_{ext}) was positioned close to the active area. This movable reflector consisted of a coating layer of evaporated gold on top of a multimode silica fiber with a 62.5 µm core diameter. This fiber was clamped on a precision microstage and connected to an optical power meter. The external cavity consequently consisted of an air gap between the light emitting area of the VCSEL ($\Delta z = 0$) and the movable reflector ($\Delta z = L_{ext}$). The electrical parameters of the VCSEL were driven and read out through a Source Measure Unit (SMU).

Figure 7.6 is showing an overview of the full measurement set-up *(top)*, a detailed view on the fiber alignment on top of the VCSEL light emitting area using CCD cameras *(middle)* and the actual view of the cameras on the wire bonded VCSEL and Au coated fiber facet *(bottom)*.

It is important to mention that the ULM Photonics VCSEL which is used for the remainder of this chapter is a 850 nm multimode VCSEL array with top-top contacts. These VCSELs typically emit only one mode up to a driving current of

1 mA. Increasing the VCSEL current will induce a higher number of modes being emitted by the VCSEL [13, 14].

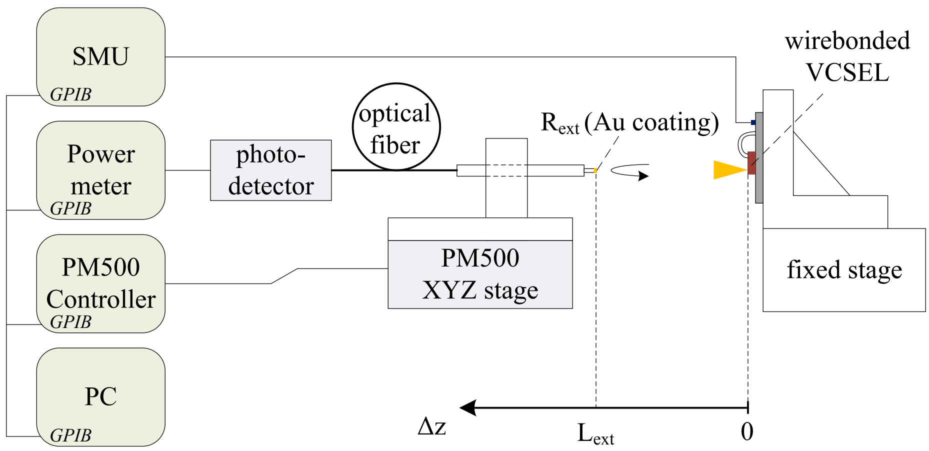

Figure 7.5 – Schematic view of the discrete proof-of-principle set-up.

7.3.1 Time domain results

Moving the fiber reflector 4 times over 5 µm using displacement steps of 50 nm results in a periodic variation of both the monitored optical power and electrical VCSEL driving current while the VCSEL voltage is kept constant. A Keithley 2400 SMU is used to control the VCSEL junction voltage and read out the VCSEL driving current. The resulting electrical and optical power fluctuations for a VCSEL driving voltage of 1.5 V are shown in Figure 7.7. A reference measurement (reflector is not moving) is included for all measurements. From Figure 7.7b, the first trend we observe in the experimental signal is a slow optical power variation coinciding with the displacement variation shown in Figure 7.7a. The larger the external cavity length is, the less power is coupled to the optical fiber. The second trend we observe is a fast periodical variation due to the optical feedback effect and superimposed on the slower optical power variation. A total of roughly 48 periods can be observed, demonstrating the 425 nm ($\lambda/2$) periodicity. The optical power signal is oscillating with a peak-to-peak variation of 10 nW. The information we can extract on the exact periodical shape of the waveform is rather limited as the data acquisition speed is limited to roughly 7 points each interferometric period. The electrical current signal (Figure 7.7c) is not showing any significant difference between the reference and the experimental measurement. Probably the optical feedback power is too low to modulate the electrical parameters.

The same measurement is repeated with a driving VCSEL voltage of 1.6 V (Figure 7.8). Variations in the optical power (Figure 7.8b) show a similar behavior as for the previous measurements although some higher harmonic effects are visible, possibly due to the multimodal behavior of the VCSEL. The electrical current measurement (Figure 7.8c) however now exhibits a similar modulated behavior confirming the ability to read out the VCSEL interference effect through the electrical current.

When further increasing the VCSEL driving voltage to 1.7 V (Figure 7.9), a similar VCSEL behavior is observed both for the optical power and electrical current. The peak-to-peak variation is 8 µW for the experimental measurements in Figure 7.8b and 7.9b, and 8 µA for the experimental measurements in Figure 7.8c and 7.9c.

7.3.2 Frequency domain results

To evaluate in detail how the experimental optical power and electrical current variations relate to the theoretical periodicity of 425 nm, frequency analysis is performed on the time domain results. Therefore the optical power/electrical current values corresponding to the same displacement position are averaged out resulting in unambiguous power and current versus displacement values. The linear trend is removed from the experimental signals and zero-padding (2^{10}) is applied to increase the resolution in the frequency domain. The sample frequency is the inverse of one displacement step of the stage in the time domain ($f_s = 1/50\,\text{nm}$). A Fast Fourier Transform (FFT) operation is applied on the resulting datasets and the power spectral density information is consequently extracted. The results are shown in Figure 7.10. The Full Width at Half Maximum (FWHM) is similar for all measurements, $\approx 0.24\,\mu\text{m}^{-1}$. Determining the maximum values for all the averaged measurements yields the reciprocal interferometric signal period. These calculated periods of the analyzed interferometric signals at different driving voltages are depicted in Table 7.1 and are varying between 403 nm and 410 nm, slightly lower than the expected 425 nm. Because of the low sample frequency and the translation stage inaccuracies, these values are definitely acceptable.

Table 7.1 – Frequency analysis of the discrete proof-of-principle results.

Measured quantity	Driving voltage	Reciprocal interferometric signal period
Optical power	1.5 V	406 nm
Electrical current	1.5 V	-
Optical power	1.6 V	403 nm
Electrical current	1.6 V	406 nm
Optical power	1.7 V	406 nm
Electrical current	1.7 V	410 nm

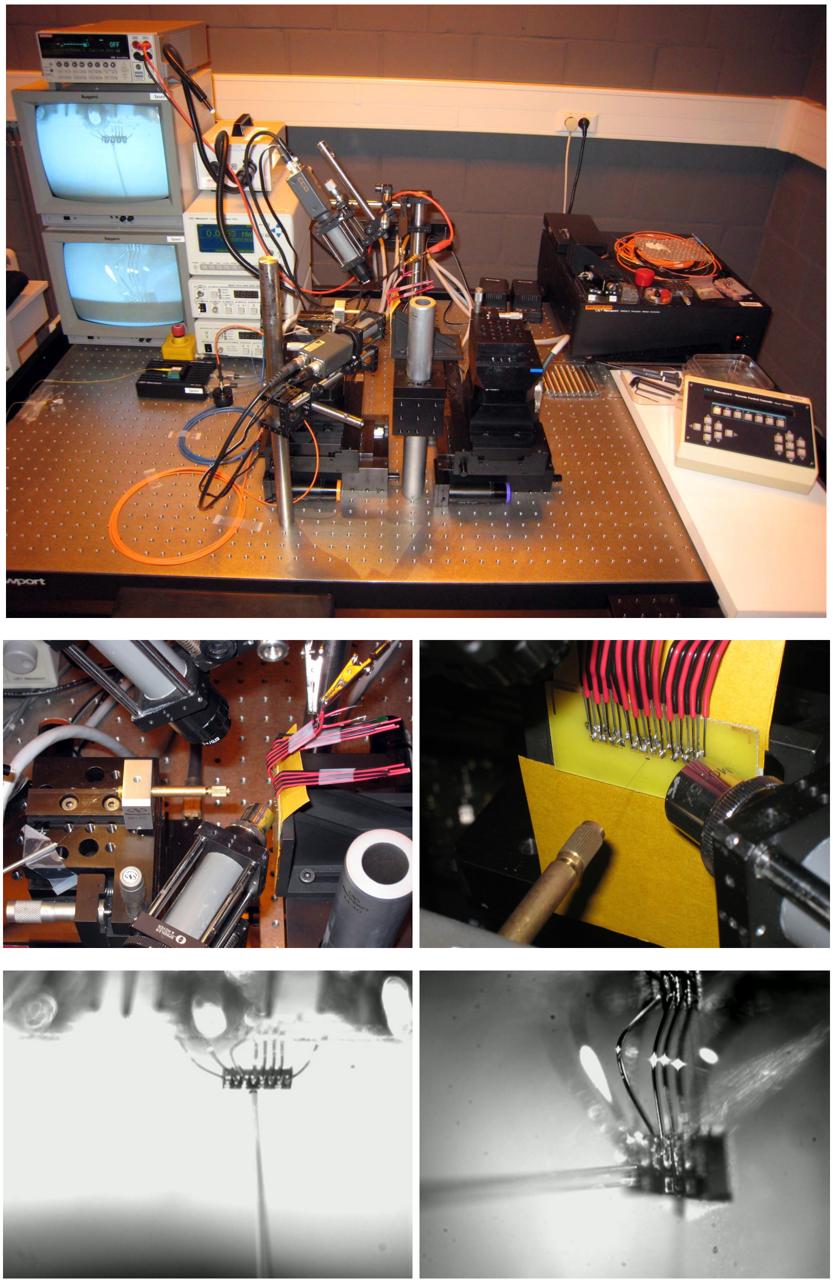

Figure 7.6 – Discrete proof-of-principle set-up. *(top)* Overview of the full measurement set-up. *(middle)* Fiber alignment on light emitting area of the vertically mounted VCSEL. *(bottom)* Camera view on the wire bonded VCSEL and fiber mirror facet.

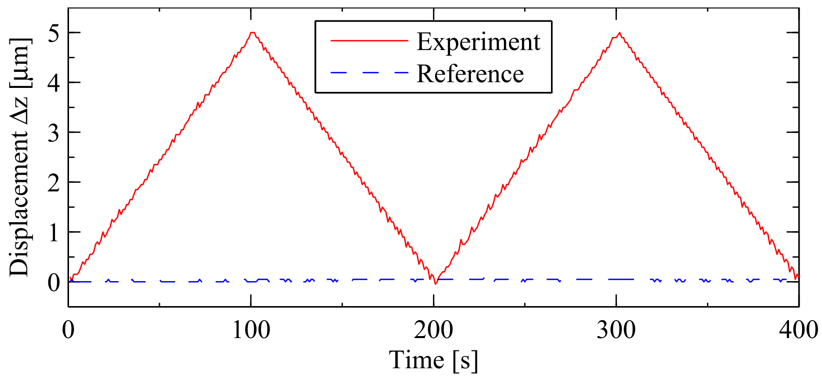

(a) Position of the movable reflector which was mounted on a microstage.

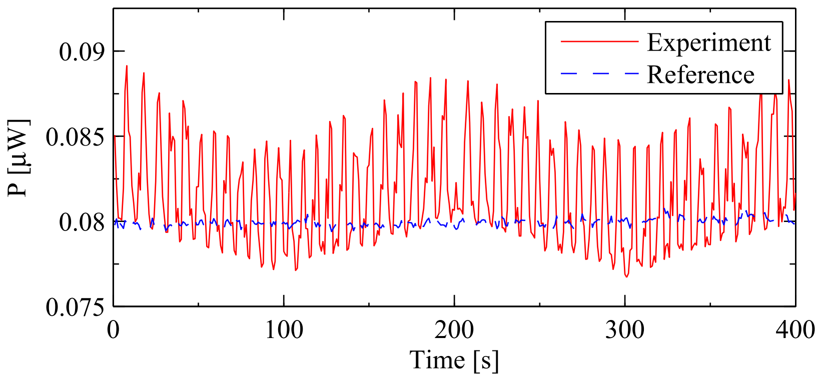

(b) Variations in the optical power.

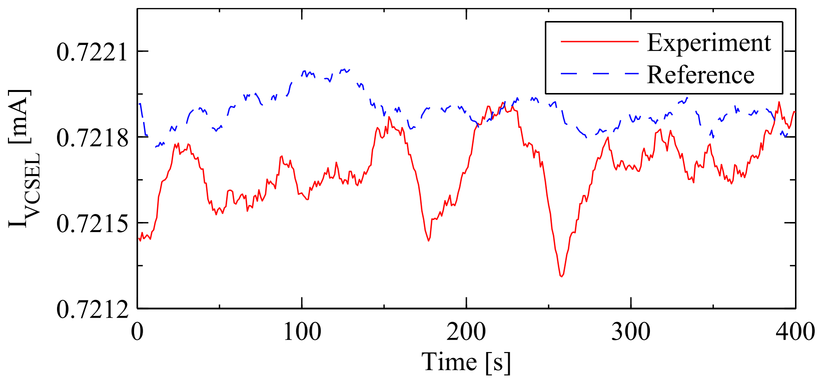

(c) Variations in the electrical current.

Figure 7.7 – Discrete proof-of-principle result with a VCSEL driving voltage of 1.5 V.

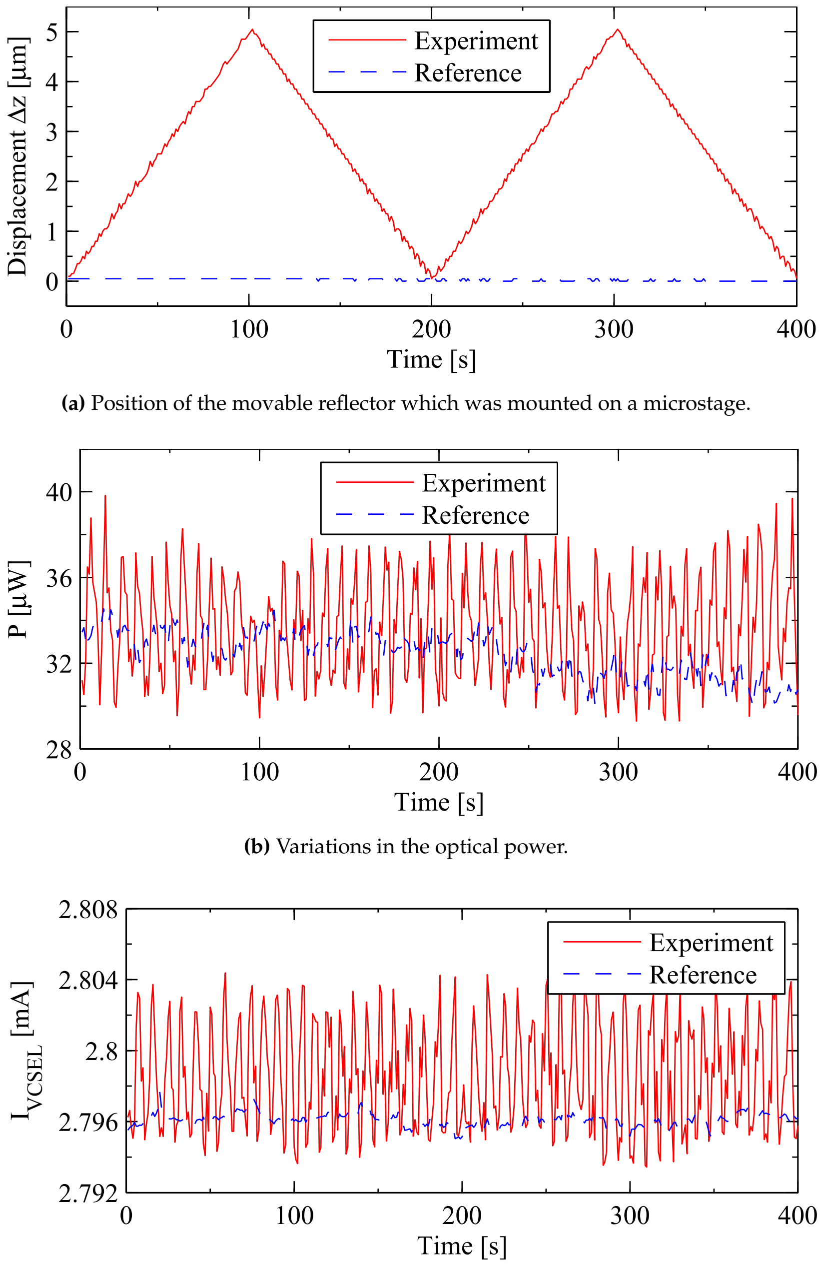

(a) Position of the movable reflector which was mounted on a microstage.

(b) Variations in the optical power.

(c) Variations in the electrical current.

Figure 7.8 – Discrete proof-of-principle result with a VCSEL driving voltage of 1.6 V.

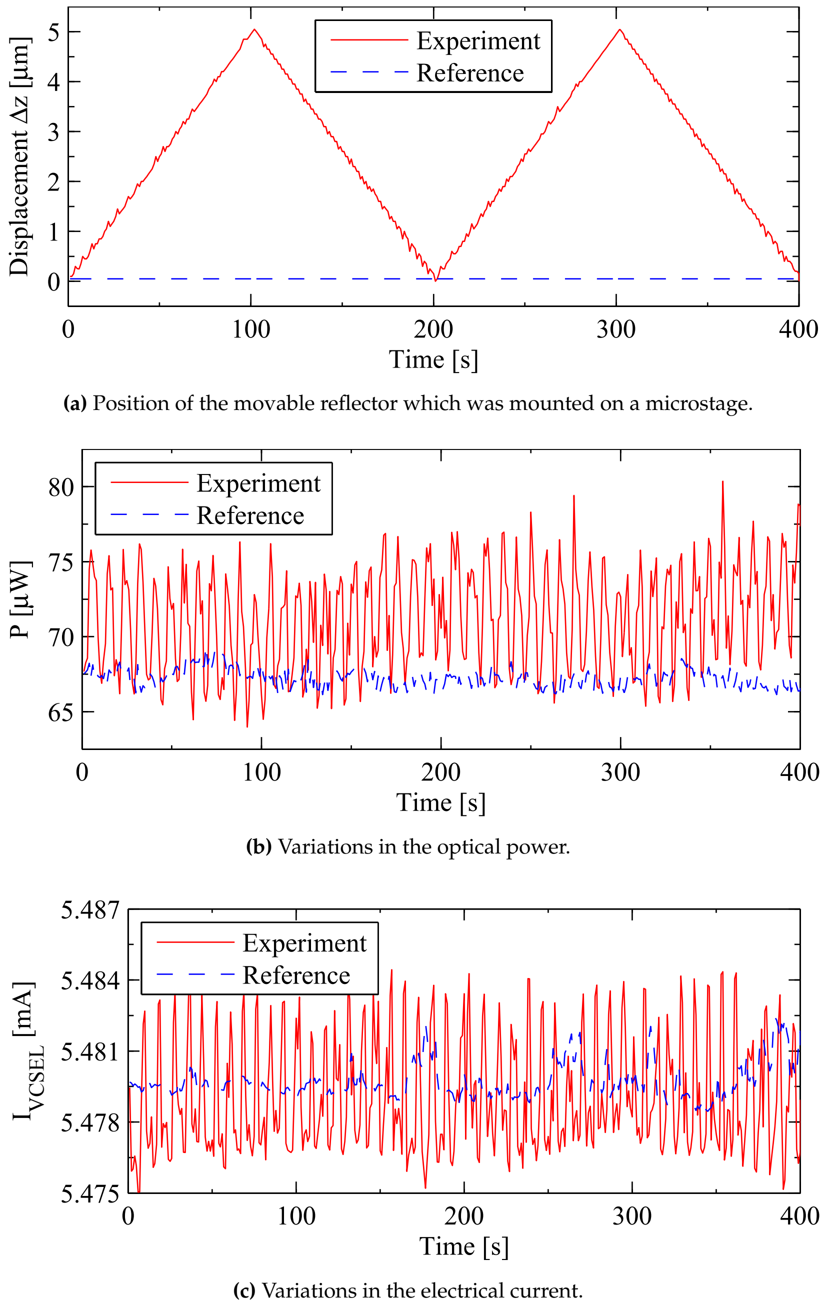

(a) Position of the movable reflector which was mounted on a microstage.

(b) Variations in the optical power.

(c) Variations in the electrical current.

Figure 7.9 – Discrete proof-of-principle result with a VCSEL driving voltage of 1.7 V.

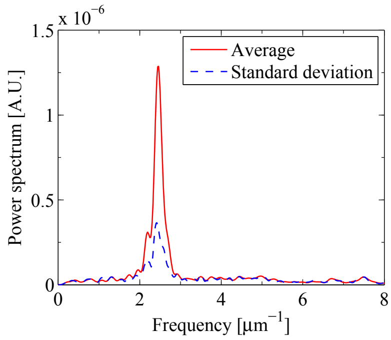

(a) Optical power at 1.5 V: power spectral density.

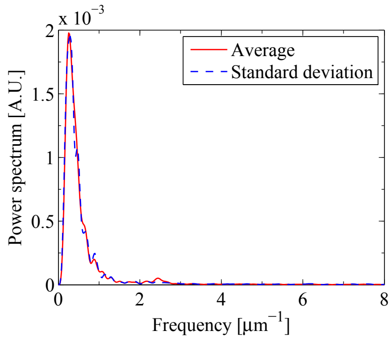

(b) Electrical current at 1.5 V: power spectral density.

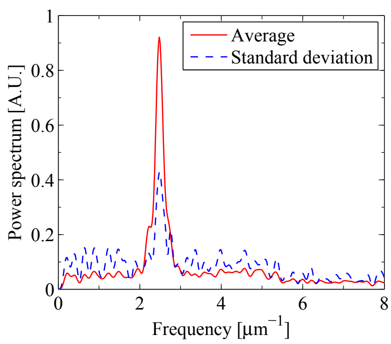

(c) Optical power at 1.6 V: power spectral density.

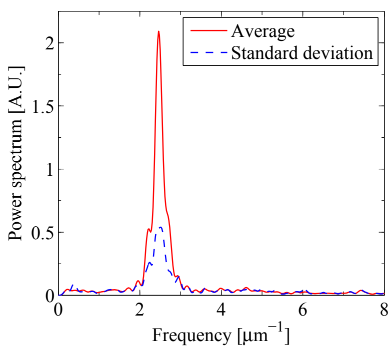

(d) Electrical current at 1.6 V: power spectral density.

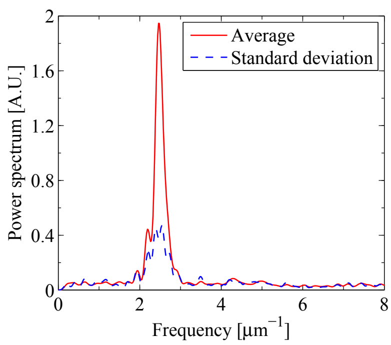

(e) Optical power at 1.7 V: power spectral density.

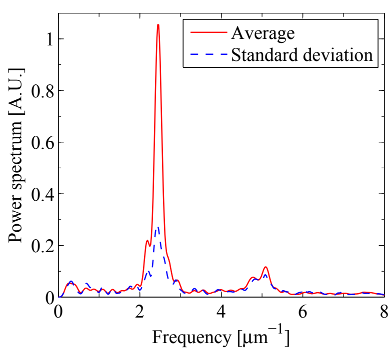

(f) Electrical current at 1.7 V: power spectral density.

Figure 7.10 – Frequency analysis of the interferometric read-out signals at different VCSEL driving voltages.

7.4 Integrated VCSEL sensor approach

7.4.1 Fabrication

The proposed integrated optical pressure sensor consists of a flexible optoelectronic package (an ultra-thin flexible VCSEL package), a deformable PDMS layer acting as an external cavity and a reflecting top layer providing optical feedback, as illustrated in Figure 7.2. To fabricate a flexible and ultra-thin package, the 850 nm multimode GaAs VCSEL die (1x4 array with top-top contacts, 250 μm pitch, ULM Photonics) was thinned down to 20 μm and embedded in a flexible polymer package of 40 μm thick using a dedicated integration process which was extensively optimized and characterized in Chapter 4 and [15].

This VCSEL package was fabricated on a temporary glass substrate and on the VCSEL package a 50 μm thick PDMS layer, Sylgard®184 from Dow Corning, was spin-coated (Figure 7.11, package A). To enhance the mechanical robustness, the reflecting copper layer was sputtered on a non-functional flexible package. After patterning the metal layer, a 50 μm thick PDMS layer, Sylgard®184 was spin-coated on top (Figure 7.11, package B). Finally, both the VCSEL and mirror package were released from the glass substrate and the PDMS layers were treated with an air plasma (Diener Pico, 0.8 mbar, 24 s, 190 W, 40 kHz generator). After aligning the reflecting layers with the VCSEL active areas, both packages were brought into contact, creating an irreversible bond and a total transducer layer thickness of 100 μm, perfectly within the functional range of the transducer thickness values derived in Section 7.2. A similar approach can be used to create other types of sensors measuring other parameters such as shear force [8, 16].

7.4.2 Characterization of the sensor

The pressure sensor was mechanically characterized by applying a controlled displacement with a microtip and simultaneously reading out the corresponding force experienced by the tip. During sensing operation, the VCSEL driving current was held constant and the VCSEL voltage was read out. Monitoring the optical power and wavelength changes requires additional read-out equipment effacing the integration advantages and is therefore avoided. An example of a characterization set-up is depicted in Figure 7.12 (for illustration purposes only, the integrated reflecting layer is not shown). Characterization tests were performed using a nanoindenter Asmec UNAT-M set-up with spherical indentation tips, located at Flamac [17], a division of SIM vzw. Also manual loading and unloading was used to characterize the VCSEL sensor.

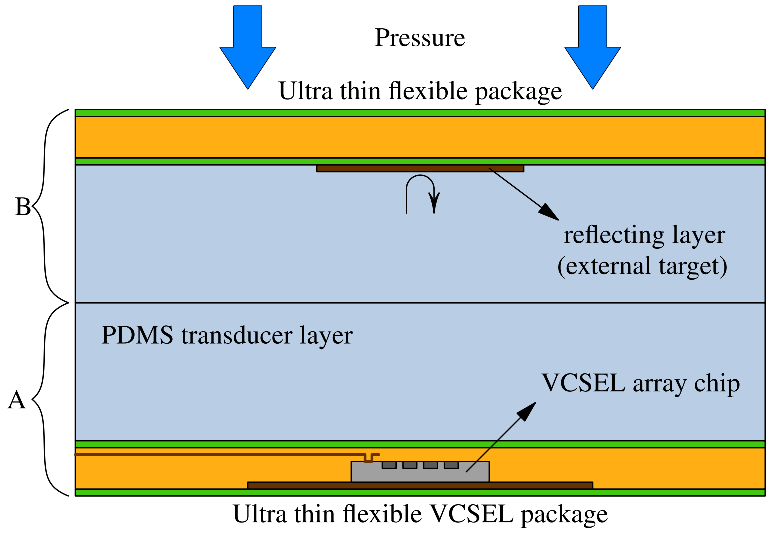

Figure 7.11 – Schematic overview of the integrated VCSEL sensor principle.

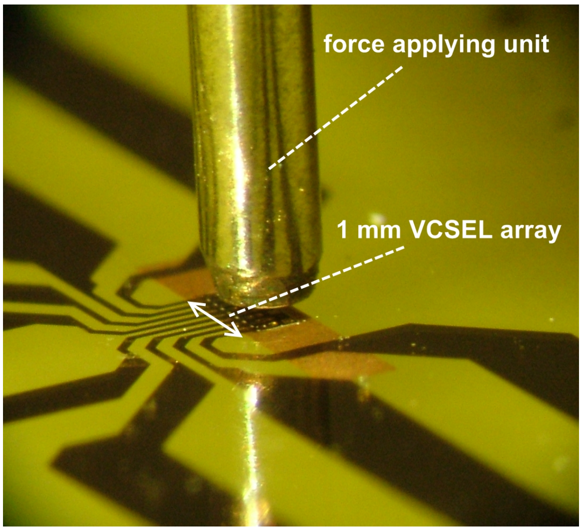

Figure 7.12 – Microscope view of a force applying unit of top of the integrated pressure sensor (reflecting layer not shown).

7.5 Integrated VCSEL sensor results

7.5.1 Linear displacement variation

Embedded VCSEL arrays are subjected to a linear displacement variation. The spherical indentation tip (10 µm or 150 µm radius) is actively aligned on top of the VCSEL light emitting area. The applied displacement and corresponding measured force values for the different indentation tips are shown in Figure 7.13 during the indentation and release of the tip. There is a clear difference in material behavior when using different indentation tips on the compressible sensing layers.

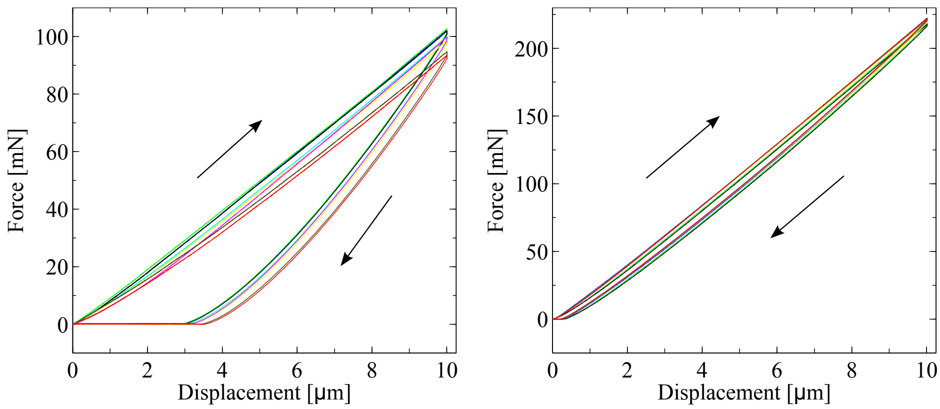

(a) Force-displacement curve with a 10 µm spherical indentation tip.

(b) Force-displacement curve with a 150 µm spherical indentation tip.

Figure 7.13 – Linear displacement and corresponding force applied on the integrated pressure sensor.

For the initial characterization tests, the 10 µm spherical tip was used and the measurements were limited to the indentation. The release was not taken into account. Table 7.2 summarizes the relevant integrated measurement parameters.

The detailed force-displacement curve is depicted in Figure 7.14. The electrical current is kept constant at 1 mA and the variations in the electrical VCSEL junction voltage were monitored through a Keithley 2400 Source Measure Unit (Figure 7.15a).

Roughly 22 periods are visible in the time domain signal and given that 1 period corresponds to a change in external cavity length of 301 nm ($n_{eff,ext}$ = 1.41 @ 850 nm), an experimentally measured displacement of 6.6 µm is obtained. The difference between the actual displacement and the experimentally measured

Table 7.2 – Test parameters for the linear displacement experiments.

Parameter	Value
Indentation set-up	Asmec UNAT-M nanoindenter
Indentation tip diameter	10 µm
Indentation depth	10 µm
Indentation position	Alignment of indent tip on the VCSEL active area
VCSEL driving current	1.0 mA
Multiplexing	Off
Sampling rate	64 Hz

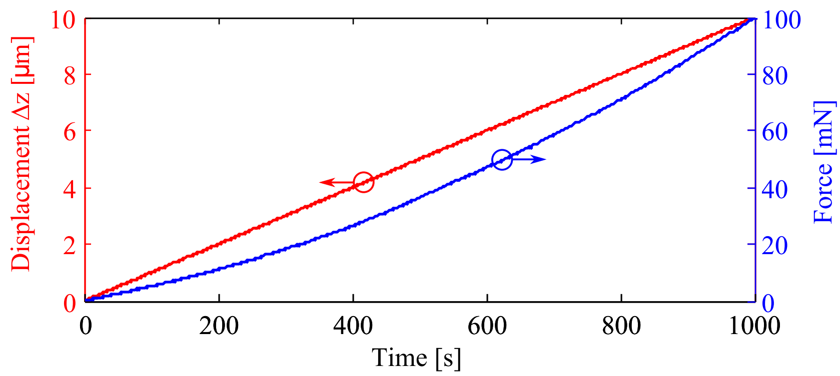

Figure 7.14 – Linear displacement and corresponding force applied on the integrated pressure sensor.

value can be explained by a 3.4 µm compression of the polymer embedding layers, including the mirror package with the reflecting layer (Figure 7.11). This effect becomes more important for higher force values.

Signal processing, including a low-pass 3th order Butterworth filter and a FFT (details were described in Section 7.3.2) to determine the spatial frequency of the signal, yields a peak frequency in the power spectrum at 2.27 μm^{-1} (Figure 7.15b). This spatial peak frequency corresponds to a reciprocal interferometric signal period of 441 nm whereas the expected theoretical value is 301 nm.

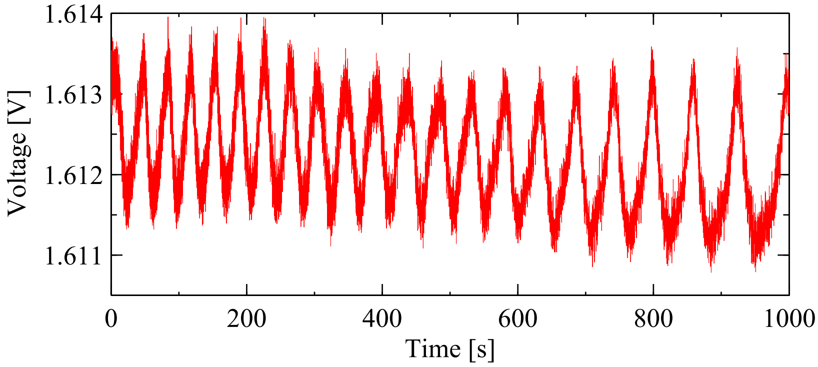

(a) Measuring the electrical voltage variation (2 mV peak-to-peak) while keeping the driving current constant at 1 mA during a 10 µm indentation.

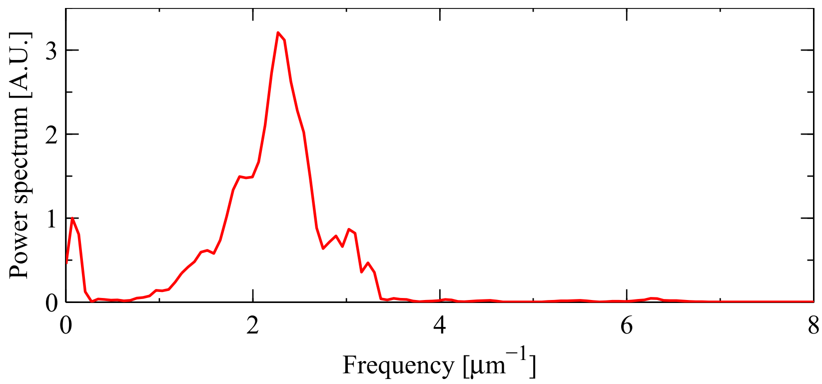

(b) Result of frequency analysis performed on the measured VCSEL voltage variation.

Figure 7.15 – Time domain and frequency domain result during a linear displacement variation experiment on the integrated VCSEL sensor.

From further analysis of the results in Figure 7.15a, a 2 mV peak-to-peak signal variation can be derived. This yields a displacement responsivity of 4.71 µV/nm. Through the Sylgard®184 Young's modulus, a pressure reponsivity of 26.2 µV/mbar is obtained.

State-of-the-art ultra-thin *electronic* pressure sensors can for example be based on organic transistor active matrixes [18], having a typical pressure responsivity of 0.022 µA/mbar.

7.5.2 Spatial sensing range

The spatial responsivity of the sensor was checked by scanning an indentation matrix of 7 x 7 sensing points on a total area of 240 µm x 240 µm on the VCSEL emitting area (Figure 7.16, *left*) and using the indentation sphere with a radius of 150 µm and forces up to 300 mN. The driving current was kept constant at 1 mA, the electrical voltage variations were monitored and frequency analysis was performed as described in the previous section. The resulting spatial peak frequencies are shown in Figure 7.16, *right* (linearly interpolated between the 49 measuring points) and a peak frequency of 2.52 μm^{-1} is obtained on top of the light emitting area. The sensor responsivity has dropped to 50 % at 200 µm from the central area.

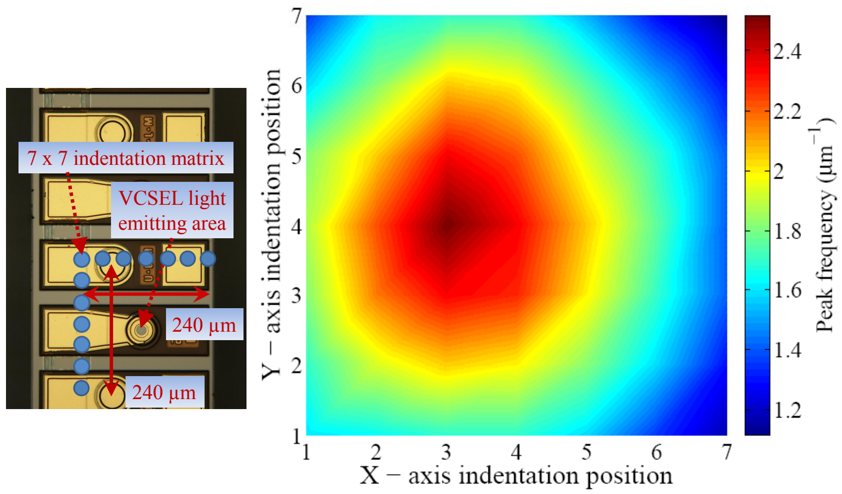

Figure 7.16 – Measuring the spatial dependency of the VCSEL sensor.
(left) Top view of the VCSEL array with schematic representation of the indentation matrix.
(right) Frequency analysis performed on each indentation point.

7.5.3 Resolution doubling

An interesting phenomenon has been observed during experiments involving a discrete external mirror instead of the integrated reflecting layer (deposited on a non-functional flexible package, Figure 7.11). This external mirror consists of a rigid glass substrate with an evaporated gold layer (10 to 20 nm). Manual loading and unloading of different weights on the glass substrate (roughly 1 cm by 1 cm) is applied. The multimode VCSEL is driven using voltage steering (1.8 V) and the current is monitored through a GPIB connection with a 11.7 Hz sampling frequency. One measurement consists of 2500 samples.

The resulting graphs (Figure 7.17) clearly show the time at which pressure is applied ($t \approx 15\,s$) and the time at which pressure is released ($t \approx 105\,s$). Due to aging effects of the embedded chips and interconnecting copper tracks, the total resistance value is also considerably higher than during previous measurements. The first trend which can be observed in Figure 7.17a is a significant increase in the mean current level after pressure is applied and a slow returning process towards its initial value after pressure release. This influence on the VCSEL current ($< 1\,\%$) is probably due to a changing resistance when applying a certain pressure and through this action compressing the different layers of the VCSEL stack.

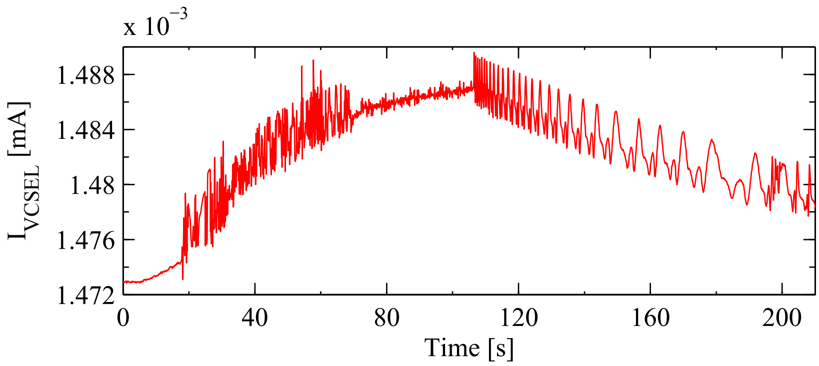

(a) Full measurement.

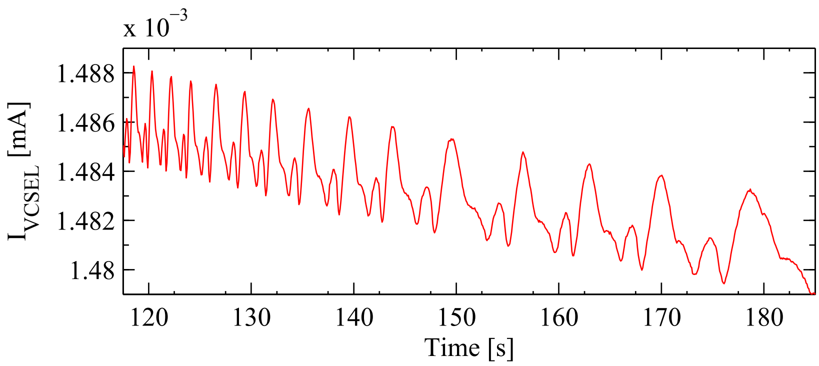

(b) Detailed view.

Figure 7.17 – VCSEL sensor current response to a pressure step function of 73.53 kPa applied at $t \approx 15\,s$ and released at $t \approx 105\,s$. The VCSEL driving voltage is 1.8 V.

Next to these changes in the DC current level, there are also interferometric effects occurring during the experiment. These effects are hardly visible in the first part of the measurement. This is probably due to a high noise level in combination with the fact that the pressure is not applied gradually, but rather imposed as a step function. During pressure release, an interferometric signal is visible (detailed view in Figure 7.17b) with a double periodicity. The spacing between 2 periods is gradually increasing after pressure release indicating a hysteresis (memory) effect of the transducer layer. This effect is due to the viscoelastic character of the PDMS layer preventing a fast recovery of the sensor. The sensing layer consequently has a certain time constant which has to be taken into account, this effect will be further explained in Section 7.5.5. The double periodicity effect can be explained by the multimodal behavior of the VCSEL (starting from $I_{VCSEL} \approx 1$ mA). The signal consists of ≈ 30 double periods, corresponding with ≈ 12.75 µm.

7.5.4 Multiplexing

One of the major advantages associated with the use of VCSEL *array* chips, is the possibility to address several VCSELs in parallel enabling different multiplexed sensing nodes on a small area (VCSEL chip size is typically 1 mm by 0.35 mm). Using even larger VCSEL arrays or extending the sensing area to a matrix can lead to extensive multiplexing resulting in distributed pressure sensing. The typical spatial resolution (spacing between 2 sensing points or light emitting areas on the chip) is 250 µm.

The size of traditional piezoresistive or capacitive tactile sensors in literature typically comprises several millimeters [8] (Chapter 1, Tables 1.3 and 1.5, size of 1 sensor). State-of-the-art ultra-thin electronic pressure sensors [18] have a typical spatial sensing resolution of a few mm.

In this paragraph, the 1 x 4 ULM Photonics VCSEL arrays are used to prove the multiplexing principle of operation. To do so, an array of 250 (10 x 25) pressure sensing points with a 50 µm spacing is indented and the corresponding electrical signals of all VCSELs are monitored simultaneously. The 4 VCSELs are driven in parallel using an electrical current of 6 mA (1.5 mA each) and a resistive load, with a resistance roughly 10 times the resistance of a VCSEL, is put in parallel with all 4 optoelectronic components to equally distribute the current. The voltage variation of the different VCSELs is read out. An overview of the different test parameters is shown in Table 7.3.

The result is a collection of 1000 measurements for a 10 µm indentation. An FFT calculation is again performed to obtain the information in the frequency domain. The power spectrum graphs are analyzed afterwards and the first peak in the frequency domain is recorded. These peak frequency points are then plotted in a graph containing the indentation reference number on the x-axis and the obtained peak frequency on the y-axis. An example for the second VCSEL of the array is

Table 7.3 – Test parameters for the multiplexing measurements.

Parameter	Value
Indentation set-up	Asmec UNAT-M nanoindenter
Indentation tip diameter	300 µm
Indentation depth	10 µm
Indentation position	Matrix of 10 x 25 points ensuring a good coverage of the VCSEL active area
VCSEL driving current	1.5 mA
Multiplexing	4 points
Sampling rate	64 Hz

shown in Figure 7.18. The 25 different measurement columns (each column contains 10 data points) are plotted in one graph showing increased peak frequencies between indent number 25 and 150, coinciding with the region around the second laser emitting area. The evolution of the magnitude of the peak frequency is again a measurand for the spatial responsivity of this one VCSEL sensor (see Section 7.5.2).

The data from Figure 7.18 is now plotted in a three-dimensional plot, again showing the indent numbers versus the peak frequency values. Figure 7.19 clearly shows a Gaussian shape determining the influence of a pressure applied on a location at a certain distance from the VCSEL light emitting area. The light emitting area is located at the center of the Gaussian beam, close to coordinate (9,6).

Analyzing the data from Figure 7.19, we find that the peak frequency drops to 50 % of its maximum value after 3 to 4 measurement points (both in X and Y). This corresponds to a spatial sensitivity range ranging between 150 µm and 200 µm, perfectly in line with Section 7.5.2.

In the case of multiplexing, four power spectrum graphs similar to Figure 7.18 are obtained. A three-dimensional graph incorporating the maximum frequency values of all 4 VCSELs (plotted on top of each other) is shown in Figure 7.20.

Using the information from Figure 7.20 as a calibration input for the VCSEL sensor, it is now possible to determine the location and the magnitude of a certain pressure applied on a location within the sensing range of the total VCSEL array (at this moment 1.25 mm x 0.5 mm, but easily expendable to larger areas).

Every VCSEL has a radial sensing range of about 400 µm diameter with respect to its emitting middle. The profile of the distribution is nicely Gaussian, meaning that it can easily be interpolated by software to further enhance the measurement

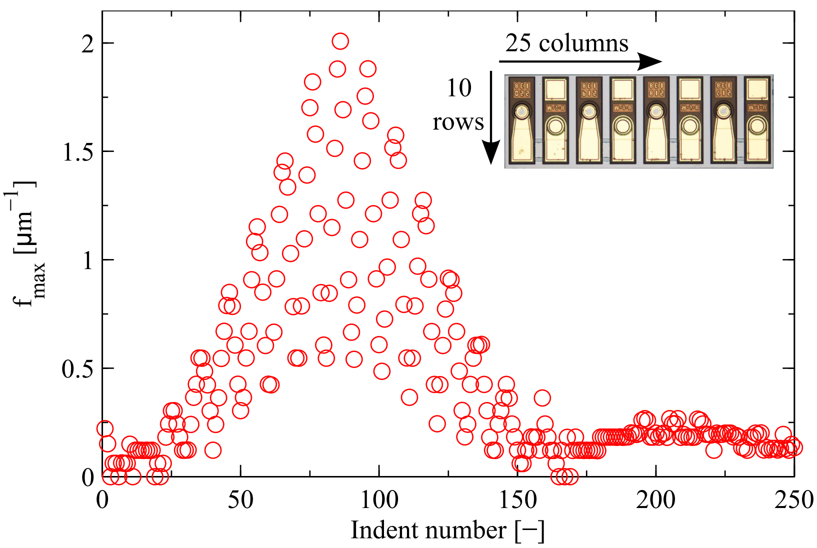

Figure 7.18 – Peak frequencies for the second VCSEL. The columns of the indentation matrix are plotted next to each other: column 1 comprises Indent number 1 - 10, column 2 Indent number 11 - 20, etc.

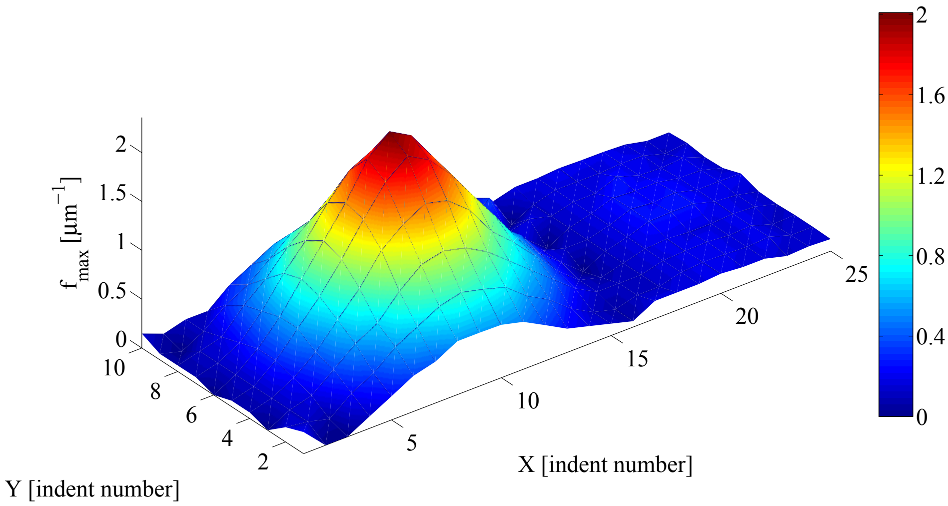

Figure 7.19 – Peak frequencies for the second VCSEL plotted as an overlay on the indentation matrix.

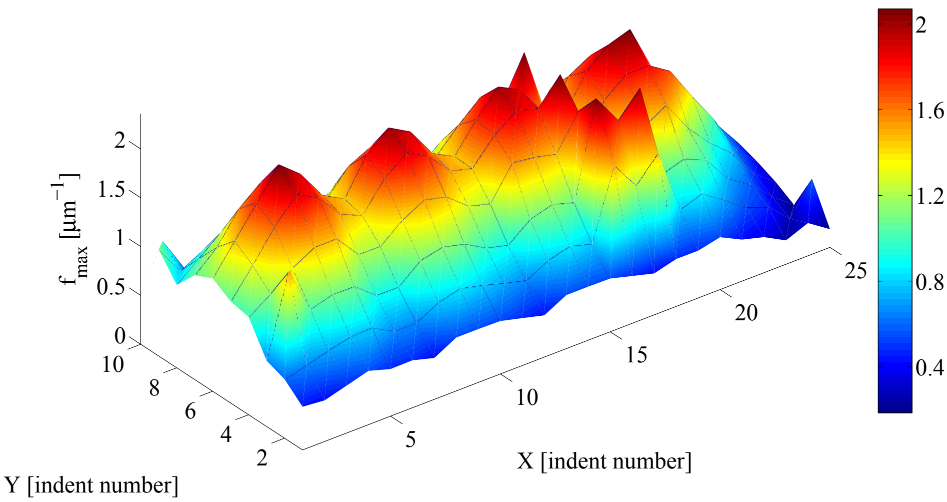

Figure 7.20 – Peak frequencies for all 4 VCSELs plotted as an overlay on the indentation matrix.

accuracy. Knowing the middle and a couple of points around it can fully reconstruct the beam shape.

7.5.5 Indentation speed

The reaction speed and the time response of the sensor are important parameters when using the sensor in real-life applications. The PDMS transducer material largely determines the dynamic behavior of the sensor. Because of the PDMS memory effect (hysteresis) observed in earlier measurements, it is interesting to investigate the step response to indentations with varying displacement application speed. All relevant testing parameters are summarized in Table 7.4 and a typical characterization result including both the indentation and release process is shown in Figure 7.21. Figure 7.22 depicts a detailed view on the 50 s and 100 s measurements.

From Figure 7.21 it can be seen that for the lower indentation speeds, the signal gives proper and repeatable results. At an indentation time of 20 s, the signal starts to deform with respect to the previously obtained signals. The 10 s indentation speed does not at all resemble the first two measurements (100 s and 50 s respectively). This distortion can be partially attributed to a sampling rate which is too low as the sampling frequency is not over the Nyquist criterion minimum for the complete signal power spectrum.

Table 7.4 – Test parameters for the measurements with varying indentation speed.

Parameter	Value
Indentation set-up	Asmec UNAT-M nanoindenter
Indentation tip diameter	300 µm
Indentation depth	10 µm
Indentation position	Array of points ensuring a good coverage of the VCSEL active area
Indentation time	100 s, 50 s, 20 s, 10 s
VCSEL driving current	1.0 mA
Multiplexing	Off
Sampling rate	64 Hz

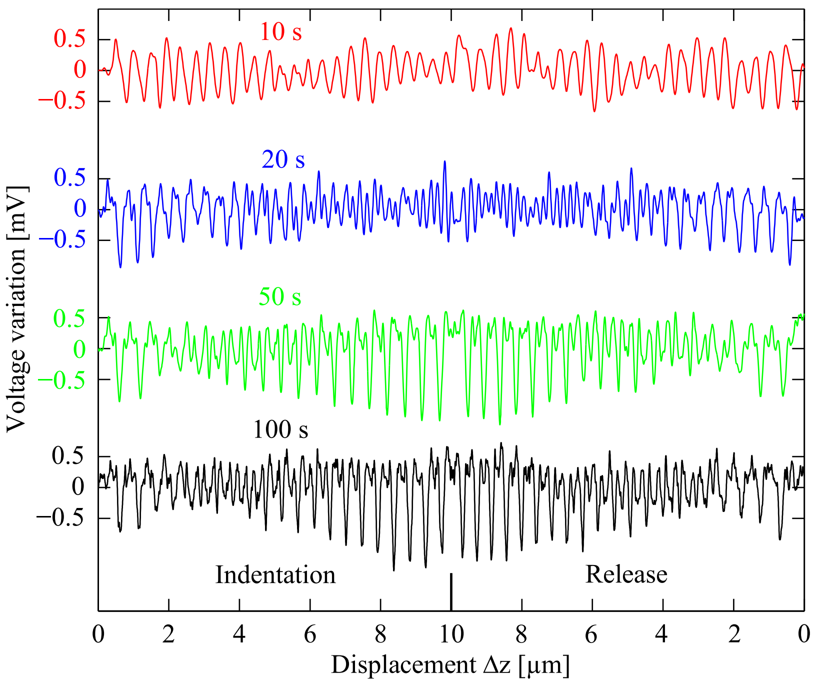

Figure 7.21 – Sensor response for a 10 µm indentation with varying indentation times, respectively 100 s, 50 s, 20 s, 10 s.

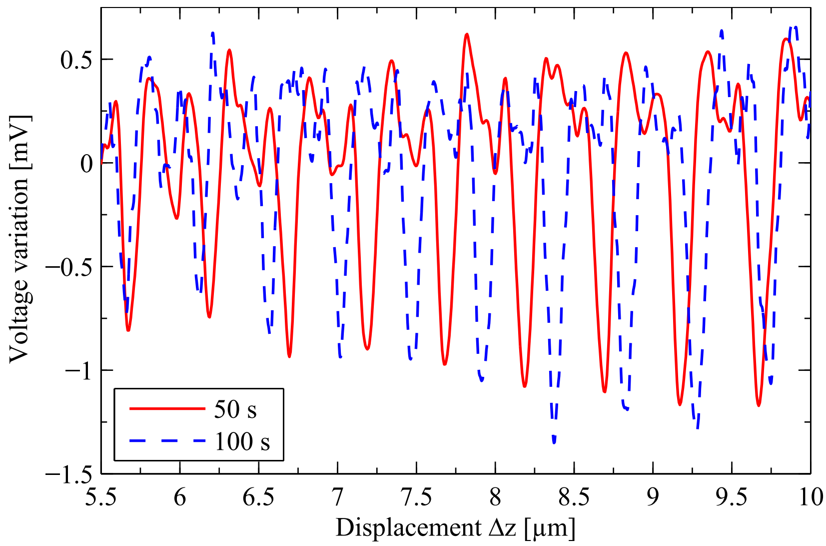

Figure 7.22 – Detailed sensor response for a 10 µm indentation with varying indentation times, respectively 100 s and 50 s.

There might be an influence of plastic deformation or creep of the transducer material. In the force-displacement curves of the full sensor stack at the higher indentation speeds however, no large deformations can be found. Therefore plastic deformation of the PDMS transducer will not be the speed limiting factor.

Looking back to the detailed structure of the incremental pressure sensor stack (Figure 7.11), the answer probably lies within the distribution of the total displacement within the polymer stack. This sensing stack consists of an ultra-thin PI/SU-8 VCSEL package, a PDMS transducer layer and a an ultra-thin PI/SU-8 (non-functional) package acting as a support stack for the external cavity reflecting layer. Both SU-8 and PDMS are elastomer materials, belong to the group of materials called viscoelastic polymers and have been used as mechanical springs in sensors and actuators. These materials behave partly as an elastic solid at short time range and partly as a viscous liquid at long time range [19]. PDMS is famous for its excellent elasticity and flexibility among other types of elastomer [20]. However, by nature PDMS also possesses some small amount of viscous liquid behavior, and exhibits a creeping behavior with time, which may result in hysteresis up to 3 - 7 % of full signal scale. Also SU-8 shows these viscoelastic properties by measuring the creep (up to 10 %) [21, 22]. Although the creep is in first order reversible, this hysteresis effect can significantly influence the device performance.

Because of this creep time effect, one should always take the possibility into account that the sensor does not fully adapt to the actual deformation. Especially in the case of fast changes in the deformation, the applied force is not translated into deformation of the underlying VCSEL embedding layers, but rather in energy storage in the material or plastic deformation. We can conclude that for fast applications the top layer of the VCSEL sensor is not yet stiff enough. Other protective layers, such as harder polymers which have a higher stiffness, should be used to investigate higher indentation speeds.

7.6 Conclusion

A highly accurate integrated incremental pressure sensor sensor was developed based on optical feedback in an embedded Vertical-Cavity Surface-Emitting laser. This laser chip can be embedded in a polymer host material and an external cavity, consisting of a compressible transducer material and a reflecting layer, is applied on top. The transducer layer consists of an external laser cavity of 100 µm on top of the VCSEL light emitting area. The reflecting layer is coupling part of the emitted laser light back into the internal VCSEL cavity introducing optical feedback and causing self-mixing interferometry. This interference signal adopts a periodic shape corresponding to half the VCSEL wavelength.

By applying pressure and consequently compressing the external cavity and thus changing the external cavity length, the optical and electrical VCSEL parameters are modulated. The sensing mechanism was first proven using a discrete proof-of-principle set-up and the integrated sensing principle has been demonstrated using a PDMS transducer layer. Characterization test on this integrated sample were performed using a nanoindenter. Starting from a 850 nm VCSEL, a sensing displacement resolution in the nanometer range was achieved and the responsivity to forces up to 300 mN in a 240 x 240 μm^2 matrix was measured resulting in a 2 mV peak-to-peak variation of the electrical driving voltage. More advanced signal reconstruction techniques can enhance the sensor read-out accuracy.

The use of unpackaged VCSELs reduces the sensor dimensions and minimizes the distance between two adjacent sensing points. By choosing the appropriate transducer material, a wide range of tactile sensing applications can be targeted with this sensor. The use of multimode VCSELs is introducing higher-order mode effects and offers the possibility to further enhance the sensing resolution. The VCSEL chip arrays have a typical separation distance of 250 µm between two adjacent emitting arrays. Scanning multiplexed or even distributed sensing points is enabled when reading out several electrical current values in parallel. The spatial responsivity of a VCSEL sensor typically shows a Gaussian profile with a sensing radius of 200 µm.

When using the compressible PDMS layer as a flexible transducer interface, one has to be careful to take into account the viscoelastic effect of this polymer material. Particularly the memory effect of the material is limiting the possibility to read out fast varying forces and according deformations, especially during release of pressure.

References

[1] W. Eaton and J. Smith, "Micromachined pressure sensors: Review and recent developments," *Smart Materials & Structures*, vol. 6, no. 5, pp. 530–539, Oct. 1997.

[2] B. Culshaw and A. Kersey, "Fiber-optic sensing: A historical perspective," *Journal of Lightwave Technology*, vol. 26, no. 9-12, pp. 1064–1078, 2008.

[3] G. Giuliani, M. Norgia, S. Donati, and T. Bosch, "Laser diode self-mixing technique for sensing applications," *Journal of Optics A-Pure and Applied Optics*, vol. 4, no. 6, pp. S283–S294, Nov. 2002.

[4] G. Acket, D. Lenstra, A. Denboef, and B. Verbeek, "The influence of feedback intensity on longitudinal mode properties and optical noise in index-guided semiconductor-lasers," *IEEE Journal of Quantum Electronics*, vol. 20, no. 10, pp. 1163–1169, 1984.

[5] L. Columbo, M. Brambilla, M. Dabbicco, and G. Scamarcio, "Self-mixing in multi-transverse mode semiconductor lasers: model and potential application to multi-parametric sensing," *Optics Express*, vol. 20, no. 6, pp. 6286–6305, Mar. 2012.

[6] J. DeGroot, A. Norris, S. Glover, and T. Clapp, "Highly transparent silicone materials," in *LINEAR AND NONLINEAR OPTICS OF ORGANIC MATERIALS IV*, ser. PROCEEDINGS OF THE SOCIETY OF PHOTO-OPTICAL INSTRUMENTATION ENGINEERS (SPIE), R. Norwood, M. Eich, and M. Kuzyk, Eds., vol. 5517, 2004, pp. 116–123, conference on Linear and Nonlinear Optics of Organic Materials IV, Denver, CO, AUG 2004.

[7] J. Lee, C. Park, and G. Whitesides, "Solvent compatibility of poly(dimethylsiloxane)-based microfluidic devices," *Analytical Chemistry*, vol. 75, no. 23, pp. 6544–6554, Dec. 2003.

[8] J. Missinne, "Development of conformable optical and optoelectronic based tactile sensors," Ph.D. dissertation, Ghent University, 2011.

[9] B. E. A. Saleh and M. C. Teich, *Fundamentals of Photonics, Chapter 3, Beam Optics*. New York: John Wiley & Sons, 1991.

[10] Ulm-Photonics. (Accessed 2012) Products. [Online]. Available: http://www.ulm-photonics.com/

[11] S. Donati, G. Giuliani, and S. Merlo, "Laser-diode feedback interferometer for measurement of displacements without ambiguity," *IEEE Journal of Quantum Electronics*, vol. 31, no. 1, pp. 113–119, Jan. 1995.

[12] K. Petermann, *Laser Diode Modulation and Noise*. Dordrecht: Kluwer, 1988.

[13] E. Bosman, J. Missinne, B. Van Hoe, G. Van Steenberge, S. Kalathimekkad, J. Van Erps, I. Milenkov, K. Panajotov, T. Van Gijseghem, P. Dubruel, H. Thienpont, and P. Van Daele, "Ultrathin optoelectronic device packaging in flexible carriers," *IEEE Journal of Selected Topics in Quantum Electronics*, vol. 17, no. 3, pp. 617–628, 2011.

[14] E. Bosman, "Integration of optical interconnections and opto-electronic components in flexible substrates," Ph.D. dissertation, Ghent University, 2010.

[15] E. Bosman, J. Missinne, B. Van Hoe, G. Van Steenberge, S. Kalathimekkad, J. Van Erps, I. Milenkov, K. Panajotov, T. Van Gijseghem, P. Dubruel, H. Thienpont, and P. Van Daele, "Ultrathin optoelectronic device packaging in flexible carriers," *IEEE Journal of Selected Topics in Quantum Electronics*, vol. 17, no. 3, pp. 617–628, 2011.

[16] J. Missinne, E. Bosman, B. Van Hoe, G. Van Steenberge, S. Kalathimekkad, P. Van Daele, and J. Vanfleteren, "Flexible shear sensor based on embedded optoelectronic components," *IEEE Photonics Technology Letters*, vol. 23, no. 12, pp. 771–773, June 2011.

[17] Flamac. (Accessed 2013) Flamac, flanders materials centre, a division of sim vzw. [Online]. Available: http://www.flamac.be/

[18] T. Someya, Y. Kato, T. Sekitani, S. Iba, Y. Noguchi, Y. Murase, H. Kawaguchi, and T. Sakurai, "Conformable, flexible, large-area networks of pressure and thermal sensors with organic transistor active matrixes," *Proceedings of the National Academy of Sciences of the United States of America*, vol. 102, no. 35, pp. 12 321–12 325, Aug. 2005.

[19] K. L. Phan, "Methods to correct for creep in elastomer-based sensors," in *IEEE Sensors*, 2008, Conference Paper, pp. 1119–22, IEEE Sensors, Lecce, Italy, OCT 2008.

[20] J. Lotters, W. Olthuis, P. Veltink, and P. Bergveld, "The mechanical properties of the rubber elastic polymer polydimethylsiloxane for sensor applications," *Journal of Micromechanics and Microengineering*, vol. 7, no. 3, pp. 145–147, Sept. 1997, 7th Workshop on Micromachining, Micromechanics and Microsystems in Europe (MME 96), Barcelona, Spain, OCT 1996.

[21] K. Wouters and R. Puers, "Determining the young's modulus and creep effects in three different photo definable epoxies for mems applications," *Sensors and Actuators A-Physical*, vol. 156, no. 1, pp. 196–200, Nov. 2009, 22nd Eurosensors Conference, Dresden, Germany, SEP 2008.

[22] B. Schoeberle, M. Wendlandt, and C. Hierold, "Long-term creep behavior of su-8 membranes: Application of the time-stress superposition principle to determine the master creep compliance curve," *Sensors and Actuators A-Physical*, vol. 142, no. 1, SI, pp. 242–249, Mar. 2008, 20th Eurosensors Conference, Chalmers Univ Technol, Göteborg, Sweden, SEP 2006.

8 Conclusion

It's fine to celebrate success but it is more important to heed the lessons of failure
–Theodore Maiman (1927 - 2007)

8.1 Main contributions to the field of optical fiber sensors

This dissertation significantly contributed to the emerging field of optical sensors. More specifically, major steps have been taken to increase the usability of optical fiber sensing applications and to take away some of the traditional showstoppers of these sensing systems. The challenges within this field of optical fiber sensors mainly include the cost effectiveness, size and sensitivity. Within this PhD, several technology building blocks were developed to cope with these challenges.

8.1.1 Fiber embedding in polymer host materials

Chapter 3 reported on the development of fiber embedding techniques to integrate optical fiber(s) (sensors) in polymer flexible and stretchable host materials. The resulting optical sensing skins can be used in a wide range of applications, for example in robotics, wearable applications or structural health monitoring.

Next to the possibility of applying the sensors on irregularly shaped objects, additional advantages include the responsivity tuning of the sensors because of the polymer host material acting as a transducer layer.

The embedding techniques were applied on standard silica fiber sensors, specialty microstructured silica fibers and polymer fiber sensors each possessing their specific advantages and challenges. All fiber sensors are based on Bragg gratings reflecting a narrowband spectral range. Highly birefringent microstructured fibers offer the possibility to perform measurements with limited temperature - transverse strain cross-sensitivity combined with an increased pressure sensitivity through advanced fiber design. Rather than a change in the absolute reflected wavelength, the sensing signal is in this case based on the peak separation between the wavelengths reflected by the two fundamental modes propagating in the fiber. Polymer fiber sensors have the main advantage of being more safe and more sensitive. Draw Tower Gratings are an off-the-shelf ready-to-use product commercially available through FBGS International [1].

Optical fiber sensors have been embedded in planar foils and cylindrical tubes. There is a clear trend of embedded polymer fiber sensors being more sensitive than silica. Depending on the embedding material and technique, it is possible to tune the sensor response. In the case of the microstructured silica fibers, further experimental work is needed to fully exploit the advantages of this sensor approach. Therefore macrostructuring and detailed interface analysis is under investigation (see Section 8.5.1).

The experimental verification of the tubular sensor devices yielded pressure sensitivities compatible with the requirements of the typical esophageal calibration measurements.

8.1.2 Integrating optoelectronic components

Chapter 4 described the technology to integrate the necessary driving and read-out optoelectronic components (lasers and photodiodes) to interrogate the optical fiber sensors. Integrating the optoelectronic components starts on a chip level by thinning them down to 20 μm. Depending on the contact pads structure and substrate material, the thinning parameters vary. Then, they are embedded in an ultra-thin polymer stack of 40 μm. The electrical and optical characteristics of all the investigated components are preserved after thinning and embedding.

SLEDs offer a broadband spectral range of several tens of nm. Spectral analysis is in this case needed at the read-out side. As an alternative, VCSELs offer a tuning range of a few nm but provide an interesting approach to circumvent the need for a spectral analysis tool. A photodetector is in that case sufficient to read out the optical fiber sensors.

Two types of optoelectronic packages were considered. SU-8 epoxy serves as the main embedding material for the first package type resulting in a flat embedded component. The second approach yields a PI based package offering a low-stress alternative with a CTE close to the semiconductor values. On this PI package, initial reliability (85/85) tests have indicated a limited effect on the characteristics of the embedded components.

8.1.3 Coupling of integrated optoelectronic components

Fiber coupling is the most tricky part when building a system based on optical fibers and optoelectronic components. Within Chapter 5, an optical coupling technology was developed which is combining an efficient coupling strategy (losses down to 7 dB for fully single-mode systems) and a planarly integrated, "optical skin compatible" approach. The result is a 500 µm thick PMMA fiber coupling plug with integrated 45° micromirror. This coupling plug can be attached to an ultra-thin optical package using a one-step alignment procedure maximizing the optical power budget both at source and detector side of the optical sensing system.

The combination of these three building blocks into a functional sensing system as well as a discussion on the cost effectiveness is included in Section 8.4.

8.2 Main contributions to the field of interferometry based optical sensors

Optical sensors based on self-mixing interferometry in optoelectronic components have a working principle inherent to the light generating sources themselves. The Achilles' heel of the integrated fiber based, i.e. fiber coupling optoelectronic sources and detectors, is consequently avoided. However, this sensing principle is mainly used for free-space (for example displacement) measurements. External optical components (lenses, mirrors, etc.) are needed in this case to confine the light and to couple a sufficient amount of optical power back into the laser cavity.

Within this dissertation (Chapter 7), the optoelectronic integration technology is used to embed VCSEL components combined with an integrated transducer material and a thin reflecting layer. The external cavity is consequently limited to typically 100 µm, providing an unobtrusive and ultra-small pressure sensing unit. By using laser component arrays, this sensing principle is easily extendable to multiplexed sensing points. The proposed sensing mechanism has also proven to be readable through the electrical properties of the sensor. Separate optical power or wavelength detecting units are therefore not needed.

The spatial range of one sensing point is typically 200 µm (FWHM).

8.3 Overview of the proof-of-principle systems

Two proof-of-principle integrated optical sensing systems were developed within this PhD. An integrated sensing *system* refers to the integrated combination of all optical and optoelectronic components. The extensive characterization results of embedded optical fiber sensors (Chapter 3) is therefore not considered as an integrated sensing system in this section.

8.3.1 Ultra-small integrated optical fiber sensing system

In Chapter 6, a new fiber sensor interrogation system was presented which can be fabricated ultra-small and fully embedded in a thin polymer stack. The sensing elements are manufactured using mature and commercially available Bragg grating inscription technology. Driving and read-out electronics and optoelectronics were combined with an Android based acquisition unit resulting in a portable and compact sensing system. Furthermore, technology was provided to take the integration a step further and embed the optoelectronics on a chip level to come up for the first time with a wearable, mechanically flexible optical fiber sensing system with a thickness below 1 mm. A broad range of new applications, including tactile sensing, structural health monitoring and biomedical systems, can be targeted with this unique sensing concept. The interrogation technique is based on an intelligent VCSEL-photodiode combination. Two interrogation modes are available: constant current mode and modulation mode. In constant current mode, the transmitted optical power is monitored at a fixed wavelength with a maximum acquisition rate (typically 5 kHz). Using the modulation mode offers full spectral reconstruction. The corresponding wavelength resolution is depending on the driving frequency and data acquisition rate, and demonstrated at, but definitely not limited to, 1.5 pm and 4 pm. The wavelength accuracy is limited by the VCSEL bandwidth and the associated response time varies between 1 and 10 ms.

The optical fiber sensor approach is ideally suited for applications requiring large-area sensing foils. The embedded optical fiber sensing system enables (quasi-)distributed measurements based on multiple or multiplexed fiber Bragg gratings. It offers an elegant way to detect large-scale movements such as respiration or impact.

8.3.2 Photonic incremental pressure sensor based on optical feedback in a polymer embedded VCSEL

A new pressure sensor was developed based on optical feedback in an embedded Vertical-Cavity Surface-Emitting laser (Chapter 7). The traditional free-space external cavity was replaced by an integrated external cavity transducer material, eliminating the need for additional optical elements. To introduce this feedback, an external cavity of 100 µm is created on top of the light emitting area. By compressing this cavity and thus changing the external cavity length, the optical and electrical VCSEL parameters are modulated. The sensing mechanism was first proven using a discrete set-up and integrated samples were subsequently characterized using a nanoindenter. A sensing displacement resolution in the nanometer range was achieved and a responsivity to forces up to 300 mN in a 240 x 240 μm^2 matrix was measured. More advanced signal reconstruction techniques can enhance the sensor read-out accuracy. By choosing the appropriate transducer material, a wide range of tactile sensing applications can be targeted with this sensor.

This sensor approach is best suited for applications requiring high-density tactile sensors. The integrated VCSEL sensor offers the possibility to perform highly accurate multiplexed pressure measurements.

8.4 Conclusion on the PhD objectives

A conclusion on the PhD objectives as defined in Chapter 1, Section 1.6 is presented in the following paragraph.

- *Polymer fiber embedding* Broaden the application domain of fiber sensors by working towards mechanically flexible and stretchable, typically polymer based, sensor host materials. Combining these materials with optical fiber sensors results in a photonic skin for optical sensing.

  > Different embedding technologies to integrate optical fiber sensors in polymer host materials are available. Characterizing the embedded sensors yielded a range of sensitivities depending on the different fiber - material combinations. Reliability and cross-sensitivity are remaining challenges.

- *Integration and coupling of optoelectronic chips* By miniaturizing and integrating optoelectronic components on a chip level, ultra-small laser and detector packages are created. These packages can be fiber-coupled when using them in combination with optical fiber sensors or serve as stand-alone sensing units (intrinsic sensor).

  > Several types of optoelectronic sources have been thinned down and integrated in ultra-thin packages. For different optoelectronic components (LED, LD, SLED), several integration challenges remain. VCSELs, single- and multimode, were successfully embedded as driving optoelectronic sources for fiber sensors or as sensing elements.

- *Simple and cost-effective optical sensor interrogation systems* By simplifying and downsizing the sensing interrogation schemes, the usability and applicability of optical sensors can significantly increase.

  > A dedicated VCSEL - PD interrogation scheme was developed enabling fully integrated, cost-effective and highly accurate fiber sensing measurements. Cost effectiveness is one the most important challenges related to optical sensing systems. Within this PhD, important steps have been taken to drastically limit the cost of the fiber sensor interrogation units through the use of simple and low-cost optoelectronic components. The embedding of these components in ultra-thin packages however is a labor-intensive process requiring a multitude of processing steps. The ongoing research on foil based alternatives using low-cost polymer substrate materials instead of spin-coatable layers and roll-to-roll laminating steps will play a crucial role within the commercialization process of this technology. Many applications however do not require or do not allow for a fully embedded sensing system. The interrogation scheme can then be deployed outside the polymer host material. The interrogation techniques described in this dissertation can in this case be applied using standard OE packages.

- *Ultra-small integrated pressure sensors* A sensing alternative for highly accurate pressure measurements can be based on self-mixing interferometry in a laser consequently avoiding fiber sensors, coupling structures and photodetectors. By pushing the limits of the optoelectronic integration process, one can include the necessary polymer transducer layers and reflective coatings.

  > An ultra-small and highly accurate pressure sensor was created based on optical feedback in a multimode integrated 850 nm VCSEL. One interferometric period corresponds to half this VCSEL wavelength. Using VCSEL chip arrays, it is possible to multiplex high-density pressure sensing points.

8.5 Outlook and future work

8.5.1 Optical skins: macrostructuring and interface properties

The polymer embedding of microstructured silica fiber sensors is further investigated within the PhD research of Sanne Sulejmani (including macrostructuring polymer optical sensing skins) and Camille Sonnenfeld (including interface properties fiber - polymer host material) at B-Phot, VUB.

8.5.2 Multiplexing FBG sensors using tunable VCSELs

The recent progress towards tunable VCSELs, typically fabricated by adding movable MEMS based top membranes on the VCSEL active region, is yielding dynamic tuning ranges of severals tens of nm [2]. These tunable VCSELs were developed within the EU-FP7 project SUBTUNE [3]. Combining these next-generation VCSELs with the proposed integration and fiber coupling technology could enable an elegant way to interrogate multiplexed fiber Bragg gratings in a single optical fiber.

8.5.3 Polymer waveguide gratings

The ultimate photonic skin consists of a fully polymer based optical sensing foil. This type of system was created by replacing the silica optical fiber sensors with polymer fiber sensor alternatives. Several difficulties however, such as rapidly increasing optical losses and the lack of off-the-shelf interfacing equipment, are currently limiting the application domain. In order to avoid fiber coupling structures and increase the compatibility of the sensor structure with the optoelectronic packages, the next step is to use planar sensing layers consisting of polymer waveguide stacks. Adding sensing features to these waveguides (polymer waveguide Bragg gratings) enables the use of spin-coated sensing layers replacing the discrete optical fibers. As discussed in Chapter 2, Section 2.3.2, the combination of Bragg gratings and polymer optical waveguides offers the promising prospect to combine the advantages of higher sensitivities with acceptable losses and integration possibilities. First trials to include Bragg gratings in polymer waveguide materials, similar to the polymer embedding materials used for the optoelectronic packages, have been started. Figure 8.1 shows a first grating structure in LightLink material with a grating pitch of ≈1 µm.

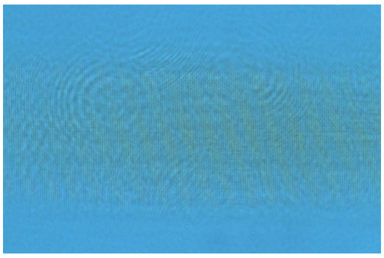

Figure 8.1 – Microscopic image of a LightLink polymer waveguide grating structure.

8.5.4 Composite integration

Next to polymer embedding materials, the use of composite materials (combination of two or more constituent materials with significantly different physical or chemical properties) is becoming another key host material for optical (fiber) sensing systems. The combination of optical fiber sensors and composites is under investigation within different research institutes. Introducing polymer waveguides within composite materials can be a next step towards a highly sensitive mechanical structure which can be monitored through measurements of the mechanical strain, pressure etc. Combining the optical sensing structures in composite materials enables to anticipate problems and avoid failures, and consequently significantly prolongs the composite life time. Typical application domains include aerospace engineering, green energy development and structural health monitoring in general.

Monitoring multi-axial strain during composite fabrication, usage and servicing, is exactly what the Self Sensing Composites project [4] is aiming for. A first integrating test for epoxy based polymer optical waveguides (Epocore/Epoclad stack) is shown in Figure 8.2, depicting a waveguide stack embedded in a carbon-fiber-reinforced polymer host material, fabricated using an autoclave technique.

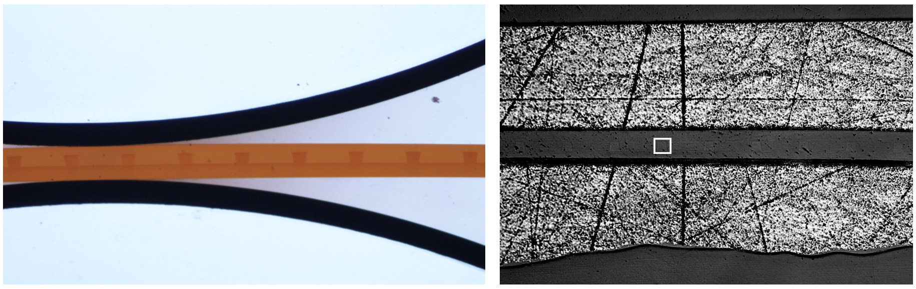

(a) Stand-alone waveguide foil. **(b)** After composite embedding.

Figure 8.2 – Cross-sections of polymer optical waveguides: Epocore/Epoclad stack.

References

[1] FBGS International. (Accessed 2012) Company website. [Online]. Available: http://www.fbgs.com/

[2] M. Maute, G. Bohm, and M. Amann, "Long-wavelength tunable vertical-cavity surface-emitting lasers and the influence of coupled cavities," *Optics Express*, vol. 13, no. 20, pp. 8008–8014, Oct. 2005.

[3] SUBTUNE Consortium. (2008) Widely tuneable vcsel using sub-wavelength gratings. [Online]. Available: http://www.subtune.org/

[4] SSC Consortium. (2013) Self sensing composites. [Online]. Available: www.selfsensingcomposites.be/